Investigation of Highly Effective and Stable Electrocatalysts for Electrochemical CO$_2$ Reduction at Room and Elevated Temperatures

by

Subiao Liu

A thesis submitted in partial fulfillment of the requirements for the degree of

Doctor of Philosophy

in

Chemical Engineering

Department of Chemical and Materials Engineering

University of Alberta

© Subiao Liu, 2017

Abstract

To effectively reduce and utilize atmospheric CO_2, electrochemically converting it to CO on an efficient and stable electrocatalyst at room and elevated temperatures has attracted extensive interests. However, present electrocatalysts usually suffer from sluggish kinetics, high overpotential, low selectivity and energy efficiency. Therefore, it is highly desirable to search for novel catalysts that can efficiently facilitate the CO_2RR at room and elevated temperatures.

I demonstrated a predominant shape-dependent electrocatalytic reduction of CO_2 to CO on triangular silver nanoplates (Tri-Ag-NPs) in 0.1 M $KHCO_3$ at room temperature. Compared with similarly sized Ag nanoparticles and bulk Ag, Tri-Ag-NPs exhibited an enhanced current density and significantly improved Faradaic efficiency and energy efficiency with a considerable durability. To further study the effects of electrocatalyst structure and employed solvent, I successfully prepared Ag_2S nanowires (NWs) using a facile one-step method and utilized it as an electrocatalyst for CO_2RR. Ag_2S NWs in ionic liquid (IL) possess a partial current density of 12.37 mA cm^{-2}, about 14 and 17.5-fold higher than those of Ag_2S NWs in $KHCO_3$ and bulk Ag. Moreover, it shows significantly higher selectivity with a value of 92.0% at η of -0.754 V. More importantly, the CO formation begins at an ultralow η of 54 mV. These studies demonstrate shape and structure influences of electrocatalysts as well as employed solvent in tuning electrocatalytic activity and selectivity of metal/non-mental catalysts for CO_2RR.

I also developed a new Ni-doped $La(Sr)FeO_{3-\delta}$ as an electrocatalyst for CO_2RR at elevated temperatures. To further increase the electrochemical performance of La(Sr)Fe(Ni), the powders were reduced in a tubular furnace in a reducing gas flow,

thus forming *in situ* exsolved Fe-Ni alloy nanospheres on the backbone of LSFN since the catalysts coated with functional metal/alloy nanoparticles can significantly improve the catalytic activity and coking resistance in hydrocarbon fuels. Additionally, I developed an electrocatalyst with *in situ* exsolved Co-Fe alloy nanoparticles embedded in an active $(Pr_{0.4}Sr_{0.6})_3(Fe_{0.85}Mo_{0.15})_2O_7$ double-layered perovskite backbone, which also acts as a more stable and efficient electrocatalyst to promote CO_2RR compared to the $Pr_{0.4}Sr_{0.6}Co_{0.2}Fe_{0.7}Mo_{0.1}O_{3-\delta}$ cubic perovskite. Therefore, these newly developed perovskites point to a new direction to develop highly efficient catalysts in the form of the perovskite oxides with uniformly *in situ* exsolved metal/bimetal nanospheres/nanoparticles.

Preface

Chapter 1 is the introduction that contains the background knowledge and principles of electrochemical CO_2 reduction at room and elevated temperatures.

Chapter 2 covers the literature survey of electrocatalysts for electrochemical CO_2 reduction at room and elevated temperatures based on the previous studies.

Chapter 3 briefly introduces the employed methodologies and characterizations.

Chapter 4 has been published as <u>**Liu S.**</u>, Tao H., Zeng L., Liu Q., Xu Z., Liu Q., Luo J.-L. Shape-dependent Electrocatalytic Reduction of CO_2 to CO on Triangular Silver Nanoplates. *Journal of the American Chemical Society*, 2017, 139, 2160-2163. Tao H worked on the DFT calculations under the guidance of Prof. Liu Q. and Prof. Xu Z., Zeng L. helped with the repair of the GC. Prof. Luo J.-L. and Prof. Liu Q. provided valuable discussions, comments, suggestions and feedbacks for manuscript writing and revision.

Chapter 5 has been submitted to Journal as <u>**Liu S.**</u>, Tao H., Liu Q., Xu Z., Liu Q., Luo J.-L. (Electrolyte, Structure)-Engineered CO_2 Electroreduction over Transition Metal Sulfide Nanowires. Tao H worked on the DFT calculations under the guidance of Prof. Liu Q. and Prof. Xu Z., Prof. Luo J.-L. and Prof. Liu Q. provided valuable discussions, comments, suggestions and feedbacks for manuscript writing and revision.

Chapter 6 has been published as <u>**Liu S.**</u>, Liu Q., Luo J.-L. The Excellence of La(Sr)Fe(Ni)O$_3$ as an Active and Efficient Cathode for Direct CO_2 Electrochemical Reduction at Elevated Temperatures. *Journal of Materials Chemistry A*. 2016, 5, 2673-2680. Prof. Luo J.-L. and Prof. Liu Q. provided valuable discussions, comments, suggestions and feedbacks for manuscript writing and revision.

Chapter 7 has been published as <u>**Liu S.**</u>, Liu Q., Luo J.-L. Highly Stable and Efficient Catalyst with In Situ Exsolved Fe-Ni Alloy Nanospheres Socketed on an Oxygen Deficient Perovskite for Direct CO_2 Electrolysis. *ACS Catalysis*. 2016, 6, 6219-6228. Prof. Luo J.-L. and Prof. Liu Q. provided valuable discussions, comments, suggestions and feedbacks for manuscript writing and revision.

Chapter 8 has been published as <u>**Liu S.**</u>, Liu Q., Luo J.-L. CO_2-to-CO conversion on layered perovskite with in situ exsolved Co-Fe alloy nanoparticles: an active and stable cathode for solid oxide electrolysis cells. *Journal of Materials Chemistry A*. 2016, 4, 17521-17528. Prof. Luo J.-L. and Prof. Liu Q. provided valuable discussions, comments, suggestions and feedbacks for manuscript writing and revision.

Chapter 9 of the thesis includes the summary and future prospects.

Acknowledgements

The completion of this thesis could not have been possible without the help from many individuals and organizations in many ways over the past four years at UofA. It has been an interesting, challenging, tough and eventually a rewarding experience to earn my Ph.D degree. It may be hard to verbally express my deep appropriations to those who contributed, directly or indirectly, to my academic success along the path of this journey.

Herein, I would like to take this opportunity to show my sincere respect and gratitude to all of them.

Firstly, I really hope to express my heartfelt thanks to my supervisor, Dr. Jing-Li Luo for all of her academic and financial supports during the past four years. She taught me how to think creatively and approach scientific explorations in the right way, which will benefit the rest of my life.

Secondly, my deep appreciation also goes to my supervisory committee members Dr. Thomas Thundat and Dr. Qingxia Liu for their valuable suggestions and guidance during my research progress.

Thirdly, my thanks are given to all the group members, including Dr. Xianzhu Fu, Dr. Hong Luo, Dr. Qinying Wang, Dr. Chen Shen, Dr. Ning Yan, Dr. Yifei Sun and Li Zeng, Xianzong Wang, Yaqian Zhang, Kaiyang Li, Tengfei Li, Jiankuan Li, Shuo Shuang for their help in my experiment design and measurements. Besides, many thanks go to Dr. Jian Chen for TEM measurements and analysis, National Institute of Nanotechnology, University of Alberta and Dr. Shihong Xu, Nancy Zhang, Anqiang He and Peng Li for their suggestions in materials characterization, Nanofab, University of Alberta.

Last but not least, my special thanks are given to my parents and my young sister who offer unconditional love and encouragement for me to overcome challenges in the past four years.

Table of Contents

List of Tables

List of Figures

List of Symbols

η	Overpotential
j	Current density
ΔG	Gibbs free energy
i_o	Exchange current density
δ	Oxygen vacancy
Rs	Ohmic resistance
Rp	Polarization resistance

List of Abbreviations

CO_2RR	CO_2 reduction reaction
HER	Hydrogen evolution reaction
RHE	Reversible hydrogen electrode
Tri-Ag-NPs	Triangular silver nanoplates
SS-Ag-NPs	Similarly sized nanoparticles
CB	Carbon black
GCE	Glassy carbon electrode
FE	Faraday efficiency
EE	Energy efficiency
BE	Binding energy
DFT	Density functional theory
LSV	Linear sweep voltammetry

GC	Gas chromatograph
TCD	Thermal conductivity detector
FID	Flame ionization detector
NW	Nanowire
IL	Ionic liquid
EMIM-BF$_4$	1-ethyl-3-methylimidazoliumtetrafluoroborate
MAA	Mercaptoacetic acid
CV	Cyclic voltammetry
AFM	Atomic force microscope
TEM	Transmission electron microscopy
FFT	Fast Fourier transformation
PDOS	Partial density of states
NMR	Nuclear Magnetic Resonance
UPS	Ultraviolet photoelectron spectroscopy
XRD	X-ray diffractometer
XPS	X-ray photoelectron spectroscopy
SEM	Scanning Electron Microscope
EDX	Energy-dispersive X-ray spectroscopy
EELS	Electron energy loss spectrometer
TGA	Thermogravimetric analysis
SOEC	Solid oxide electrolysis cell

SOFC	Solid oxide fuel cell
MEA	Membrane electrode assembly
EIS	Electrochemical impedance spectra
ASR	Area-specific resistance
TPB	Triple phase boundary
OCV	Open circuit voltage
EDTA	Ethylenediaminetetraacetic acid
LSFN	$La_{0.6}Sr_{0.4}Fe_{0.8}Ni_{0.2}O_{3-\delta}$
Fe-Ni-LSFN	LSFN socketed with *in situ* exsolved Fe-Ni alloy nanospheres
LSCF	$(La_{0.60}Sr_{0.40})_{0.95}Co_{0.20}Fe_{0.80}O_{3-\delta}$
GDC	$Gd_{0.2}Ce_{0.8}O_{2-\delta}$
YSZ	Yttria-stabilized zirconia
PSFM	$(Pr_{0.4}Sr_{0.6})_3(Fe_{0.85}Mo_{0.15})_2O_7$
Co-Fe-PSFM	PSFM socketed with *in situ* exsolved Co-Fe alloy nanoparticles
PSCFM	$Pr_{0.4}Sr_{0.6}Co_{0.2}Fe_{0.7}Mo_{0.1}O_{3-\delta}$

List of Publications

Refereed Journals (published or accepted)

1) **Liu S.**, Tao H., Zeng L., Liu Q., Xu Z., Liu Q., Luo J.-L. Shape-dependent Electrocatalytic Reduction of CO_2 to CO on Triangular Silver Nanoplates. *Journal of the American Chemical Society*. 2017 Feb, 139, 2160-2163.

2) **Liu S.**, Liu Q., Luo J.-L. The Excellence of La(Sr)Fe(Ni)O_3 as an Active and Efficient Cathode for Direct CO_2 Electrochemical Reduction at Elevated Temperatures. *Journal of Materials Chemistry A*. 2016 Dec, 5, 2673-2680

3) **Liu S.**, Liu Q., Luo J.-L. CO_2-to-CO conversion on layered perovskite with in situ exsolved Co-Fe alloy nanoparticles: an active and stable cathode for solid oxide electrolysis cells. *Journal of Materials Chemistry A*. 2016 Oct, 4, 17521-17528.

4) **Liu S.**, Liu Q., Luo J.-L. Highly Stable and Efficient Catalyst with In Situ Exsolved Fe-Ni Alloy Nanospheres Socketed on an Oxygen Deficient Perovskite for Direct CO_2 Electrolysis. *ACS Catalysis*. 2016 Aug, 6, 6219-6228.

5) **Liu S.**, Chuang K.T., Luo J.-L. Double-Layered Perovskite Anode with in Situ Exsolution of a Co-Fe Alloy To Cogenerate Ethylene and Electricity in a Proton-Conducting Ethane Fuel Cell. *ACS Catalysis*. 2015 Dec,6, 760-768.

6) **Liu S.**, Behnamian Y., Chuang K.T., Liu Q., Luo J.-L. A-site deficient $La_{0.2}Sr_{0.7}TiO_{3-\delta}$ anode material for proton conducting ethane fuel cell to cogenerate ethylene and electricity. *Journal of Power Sources*. 2015 Dec, 298,23-29.

7) **Liu S.**, Yang C., Liu R., Xie X., Zhou T. Sodium ligninsulfonate as electrolyte additive for vanadium redox flow battery. *CIESC Journal*. 2012.

8) Behnamian Y., Mostafaei A., Kohandehghan A., Amirkhiz B.S., Serate D., Sun Y., **Liu S.**, Aghaie E., Zeng Y., Chmielus M., Zheng W.. A comparative study of oxide scales grown on stainless steel and nickel-based superalloys in ultra-high temperature supercritical water at 800 C. *Corrosion Science*. 2016 May, 106,188-207.

Refereed Journals (under review)

9) **Liu S.**, Tao H., Liu Q., Xu Z., Liu Q., Luo J.-L. (Electrolyte, Structure)-Engineered CO_2 Electroreduction over Transition Metal Sulfide Nanowires. (Under review in ***Journal of the American Chemical Society***)

10) **Liu S.**, Luo H., Li Y., Xia C., Liu Q., Luo J.-L. Layered Perovskite: Structure-Engineered Electrocatalyst Enables Highly Active and Stable Oxygen Evolution Reaction. (Under review in ***Advanced Materials***)

11) **Liu S.**, Liu Q., Fu X., Luo J.-L. Cogeneration of Ethylene and Energy in Protonic Fuel cell with an Efficient and Stable Anode Anchored with *in-situ* Exsolved Functional Metal Nanoparticles. (Under review in ***Chemistry of Materials***)

12) Sui Y., **Liu S.**, Li T., Liu Q., Jiang T., Guo Y., Luo J.-L. Atomically and Selectively Dispersed Pt on Specific TiO_2 Facets for Photocatalytic H_2 Evolution. (Under review in ***ACS Catalysis***)

Unrefereed Journals

13) **Liu S.**, Liu Q., Luo J.-L. *In Situ* Exsolved Alloy Nanoparticles on Perovskite for Direct CO_2 Reduction. ***ECS Transactions***. 2017 Jan, 75,1-6.

14) **Liu S.**, Chuang K.T., Luo J.-L. *In Situ* Exsolved Alloy Nanoparticles on Perovskite for the Cogeneration of Ethylene and Electricity in Proton Conducting Fuel Cell. ***ECS Transactions***. 2017 Jan, 75, 53-58.

List of Presentations

1) **Liu S.**, Liu Q., Luo J.-L. "*In Situ* Exsolved Alloy Nanoparticles on Perovskite for Direct CO_2 Reduction", 230th Meeting of The Electrochemical Society/PRiME 2016, Oct. 2-7, Honolulu, Hawaii. (Oral)

2) **Liu S.**, Chuang K.T., Luo J.-L. "*In Situ* Exsolved Alloy Nanoparticles on Perovskite for the Cogeneration of Ethylene and Electricity in Proton Conducting Fuel Cell", 230th Meeting of The Electrochemical Society/PRiME 2016, Oct.2-7, Honolulu, Hawaii. (Poster).

Chapter 1. Introduction

1.1 Motivation

1.1.1 The supply and demand of global energy

As the world populations grow, the demand for energy is increasing tremendously. Figure 1.1 shows the annual and estimated world population and energy demand (MBDOE: million of barrels per day of oil equivalent).[1] The increasing energy demand has sparked the need to seek alternative energy sources.
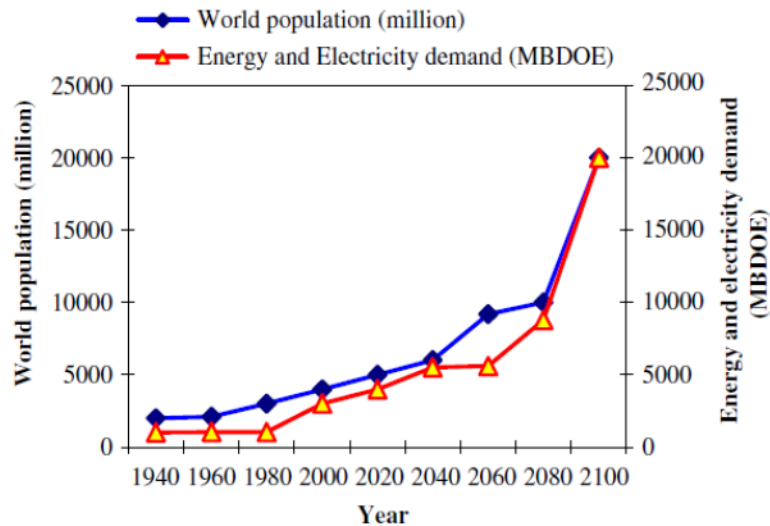
Figure 1.1 Annual and estimated world population and energy demand (MBDOE: million of barrels per day of oil equivalent).[1]

Despite the rapid development of clean energy (e.g., hydroelectric power and nuclear power) and renewable energy sources (e.g., solar energy and wind power) to generate energy, approximately 85% of the world energy consumption today still comes from the combustion of fossil fuels (i.e. natural gas, coal and oil) (Figure 1.2),[2,3] which subsequently leaves its wake destructive cumulative effects, particularly greenhouse effect.[4] The climate change and environmental issues derived from the consumption of fossil fuel are one of the great challenges today.[5]

1
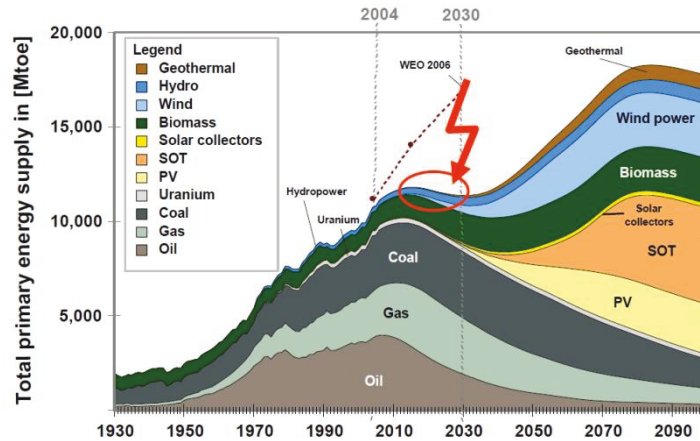
Figure 1.2 Total primary energy supply.[6]

1.1.2 The consequence: the accumulation of CO_2

The emission of CO_2 from the combustion of fossil fuels increases at a rising rate each year.[7] As a result, the global warming issue gradually changes the ecological system and irreversibly damages our environment worldwide.[8,9] In recent years, the increase of global CO_2 emission has caused serious concerns because the rising temperature has resulted in the melting glacier and rising sea level.[6] As we know, the CO_2 emission from burning fossil fuels grows significantly since the beginning of the industrial revolution and the growth rate ratcheted up from less than 1% each year in the 1990s to almost 3% annually in the first decade of this century.[10] Assuming CO_2 emission follows projected GDP growth and accounting for improvement in carbon intensity, it is predicted that the total CO_2 emission reach 43.2 Gt by 2019 (see Figure 1.3).[11]

According to Figure 1.3., human activities largely contribute to the global warming, as confirmed by the Fourth Assessment Report of the United Nations Intergovernmental Panel on Climate Change.[12,13] Anthropogenic influences, particularly the emissions of greenhouse gases, are the most remarkable causes for the current global warming trend.[14]
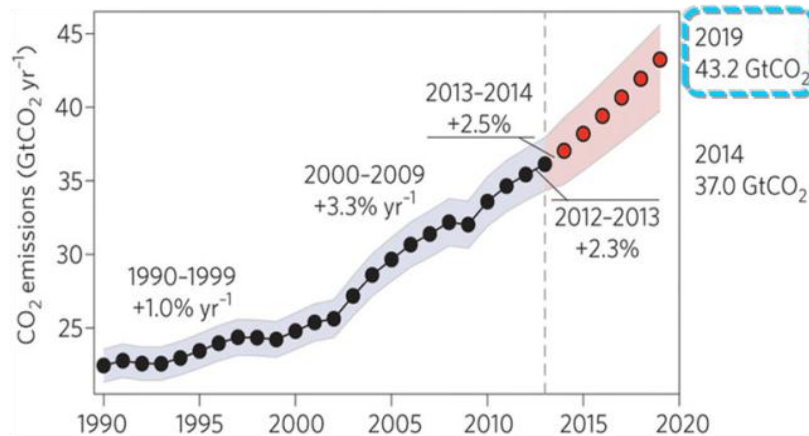
Figure 1.3 The projected global CO_2 emission (CDIAC: Friedlingstein et al 2014).[11]

Figure 1.4 shows the annual greenhouse gas emissions by sector, relative contributions of manmade greenhouse gases for the year 2000 as estimated by the emission database for the Global Atmospheric Research.[15] It is found that the energy production and consumption are the main sources of CO_2 emissions (http://www.globalwarmingart.com/wiki/Image:Greenhouse_Gas_by_Sector.png), with transportation (14%), agricultural activities (12.5%) and industrial activities (16.8%) also making a contribution.
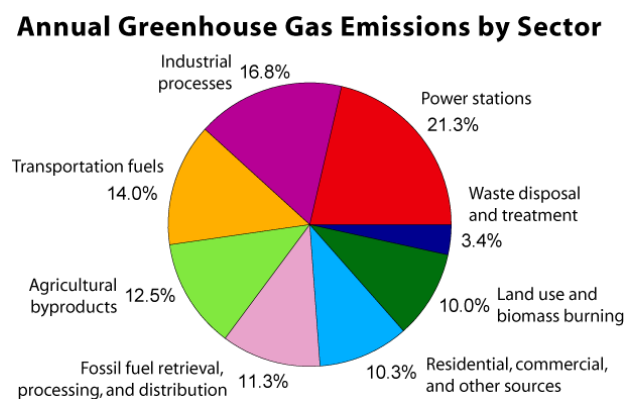
Figure 1.4 Annual greenhouse gas emissions by sector.[16]

1.2 Technologies to reduce CO_2

1.2.1 CO_2 capture and storage

Carbon capture and storage (CCS) refers to technologies which can capture CO_2 released from some processes, such as combustion, especially power generation and

3

gasification.[17,18] CCS has been proposed to allow the utilization of fossil-fueled power stations whilst preventing CO_2 emissions from reaching the atmosphere. The captured CO_2 is pressurized and transported to a storage site where it is injected into some stable geological textures to avoid subsequent emission into the atmosphere and trapped for hundreds or thousands of years.[19,20]

1.2.2 The utilization of CO_2

CO_2 utilization has been recognized as a potential approach to reduce atmospheric CO_2 concentration in an economical manner.[21,22] Normally, CO_2 can be utilized in three major pathways,[23-25] as shown in Figure 1.5.
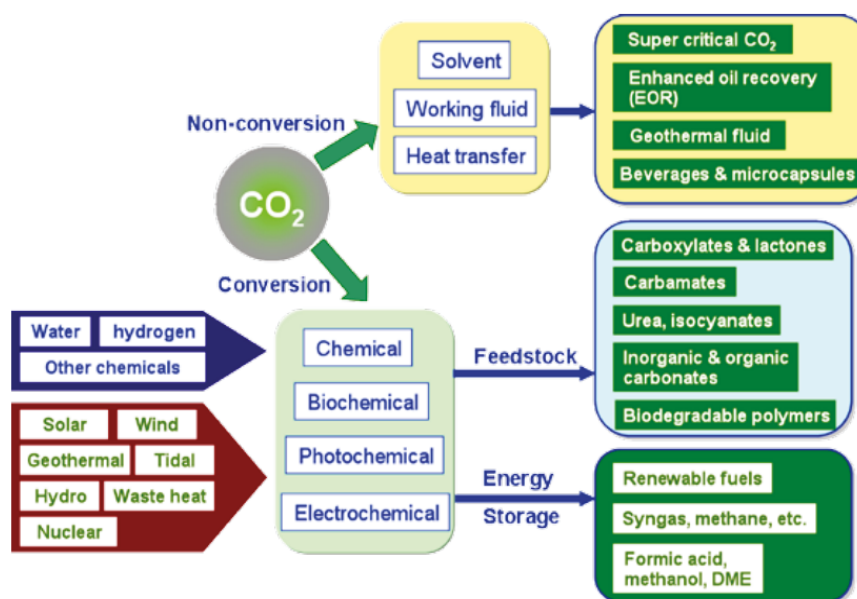
Figure 1.5 Different pathways for utilizing CO_2.[26]

1) As a solvent or working fluid: CO_2 can be utilized via non-conversion methods (e.g., solvent, working fluid and heat transfer) without being transformed to the other chemical forms. The only commercially viable technology currently used is the injection of supercritical CO_2 into depleted oil wells for the purpose of further enhancing the oil recovery, which has been well studied.[27] Figure 1.6 shows the process of CO_2 enhanced oil recovery. The CO_2 injection can significantly enhance

the oil recovery from a depleting well by 10~20 %. Figure 1.7 shows the application of CO_2 in geothermal heat extraction.
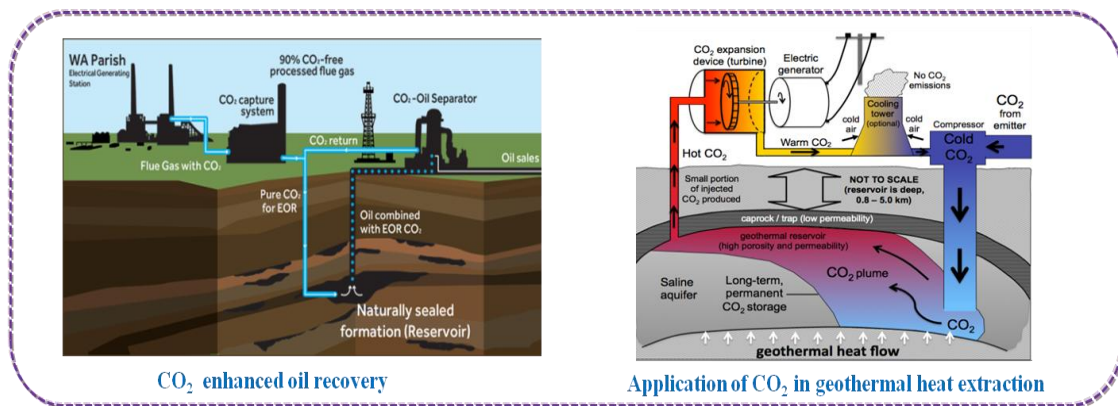
Figure 1.6 the process of CO_2 enhanced oil recovery (left);[28] Figure 1.7 the application of CO_2 in geothermal heat extraction (right).[29]

2) As a storage medium for renewable energy: The utilization of CO_2 for the conversion of solar energy to biomass and subsequently to different renewable fuels is a promising way to guarantee future energy supplies and the reduction of CO_2 emissions.[30,31]

3) As a feedstock for different chemicals: CO_2 can be photochemically and/or electrochemically converted to energy-intensive chemicals (e.g., syngas, formic acid, methane, ethylene and methanol) (see Figures 1.8 and 1.9) which can be further used in fuel cells or burned directly.[32-34] Electrochemical CO_2 reduction reaction (CO_2RR) can not only decrease CO_2 accumulation, but also convert intermittent renewable electricity into energy-dense fuels.[32,35] This points to a promising direction to recycle CO_2 and close the anthropogenic carbon cycle, an ultimate goal to reduce CO_2 emissions.
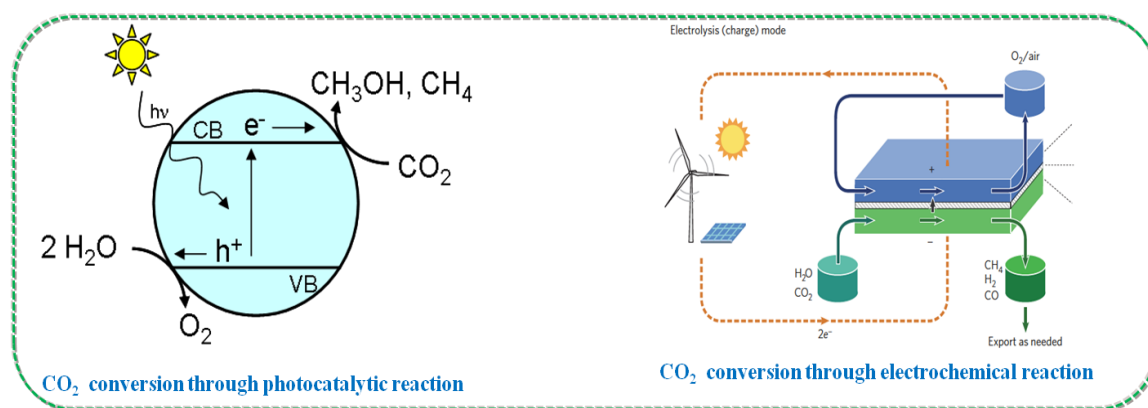
Figure 1.8 the CO_2 conversion through photocatalytic reaction (left);[36] Figure 1.9 the CO_2 conversion through electrochemical reaction (right).[37]

1.3 Opportunity: the incorporation of intermittent energy storage and CO_2RR

In the course of finding alternative fuels for fossil fuels, other energy forms (e.g., hydroelectric, geothermal, wind and solar) have drawn extensive studies in the past few decades.[38-40] As commonly known, the solar energy and wind power are the most abundant and geographically widespread, however, both of them suffer from intermittency due to the highly variable wind strength and the sunlight intensity throughout the day.[41,42] Obviously, the most energy-dense systems are not stored in physical or electrical forms but in chemical bonds.[43] The production of chemicals from CO_2 reduction utilizing renewable energy makes it possible that these chemicals are commercially available for many industrial applications and as fuels in a net carbon-neutral cycle.[33,43] The production of those chemicals by combining the use of renewable energy and electrochemical CO_2RR provides a great potential for the reduction of CO_2 emission, the main topic of this dissertation.

1.4 An overview of electrochemical CO_2 reduction (CO_2RR)

1.4.1 Thermodynamics of CO_2RR at room temperature

The electrochemical CO_2RR is thermodynamically endergonic and as such, additional

energy is required for the process to proceed spontaneously. More importantly, the Gibbs energy of the relevant reaction can be precisely controlled by changing the potential. Since CO_2RR is endergonic, the required potentials to different products are all in negative range. The potentials presented are all at neutral conditions with unit activities of all species.

$$\Delta G^0 = -nFE^0$$

Where E^0 is the standard potential for a specific reaction, ΔG^0 is the standard change in Gibbs free energy, n is the number of electrons involved, F (96485 C·mol^{-1}) is the Faraday constant.

Table 1.1 Selected standard potentials (vs reversible hydrogen electrode, RHE) of CO_2RR at 1.0 atm and 25 °C.

Electrochemical thermodynamic half reactions	Standard potential (vs RHE)
$CO_2(g) + 4H^+ + 4e^- = C(s) + 2H_2O(l)$	0.210
$CO_2(g) + 2H^+ + 2e^- = HCOOH(l)$	-0.250
$CO_2(g) + 2H^+ + 2e^- = CO(g) + H_2O(l)$	-0.106
$CO_2(g) + 4H^+ + 4e^- = CH_2O(l) + H_2O(l)$	-0.070
$CO_2(g) + 6H^+ + 6e^- = CH_3OH(l) + H_2O(l)$	0.016
$CO_2(g) + 8H^+ + 8e^- = CH_4(g) + 2H_2O(l)$	0.169
$2CO_2(g) + 2H^+ + 2e^- = H_2C_2O_4(aq)$	-0.200
$2CO_2(g) + 12H^+ + 12e^- = CH_2CH_2(g) + 4H_2O(l)$	0.064
$2CO_2(g) + 12H^+ + 12e^- = CH_3CH_3(g) + 3H_2O(l)$	0.084

Electrochemical CO_2RR can occur via two-, four-, six- and eight-electron transfer processes;[34,44,45] the corresponding thermodynamic electrochemical half-reactions of CO_2RR, the number of electrons transferred, and the associated standard electrode

potential are summarized in Table 1.1.

Based on Table 1-1, various aimed products can be formed via different reaction pathways. The main products include gases (e.g., CO, CH_4, and C_2H_4) and liquids (e.g., HCCOH or $HCOO^-$ in basic media, $H_2C_2O_4$ or $C_2O_4^{2-}$ in basic media, CH_2O and CH_3CH_2OH).[46,47]

1.4.2 Thermodynamics of CO_2RR at elevated temperatures

E_{rev} is the minimum voltage required for CO_2RR and is related to the standard Gibbs energy for CO_2 formation. Under standard conditions (25 °C and 1 atm), the E_{rev} is

$$E_{rev}^0 = \frac{\Delta G^0}{nF}$$

The standard Gibbs free energy for the formation of CO_2, $\Delta G_f^0(CO_2) = -250.1 \; kJ \; mol^{-1}$, At 25 °C, the reversible voltage at standard conditions is 1.33 V for CO_2RR.[48] The thermodynamic data for CO_2RR at different temperatures were calculated using HSC software, as shown in Table 1.2.

Table 1.2 Thermodynamic data for CO_2RR at different temperatures.

CO_2RR: $CO(g) + 0.5 \, O_2(g) \rightarrow CO_2(g)$			
T (°C)	**ΔH (kJ)**	**ΔG (kJ)**	**Reversible potential E (V)**
800	-282.316	-189.206	0.980
850	-282.111	-184.873	0.957
900	-281.899	-180.548	0.936

The reversible voltage at any pressure and temperature can be expressed by the Nernst equation, which provides the relationship between the standard potential (E_{rev}^0) for the cell reaction and the reversible potential (E_{rev}) at different partial pressures of reactants and products:

$$E_{rev} = \frac{\Delta G^0}{nF} - \frac{RTlnQ}{nF}$$

$$Q = \frac{P_{CO_2}}{P_{CO} + P_{O_2}^{1/2}}$$

Where, Q is the reaction coefficient for CO_2RR. At standard conditions, all reactants and products are 1, thus Q = 1 and lnQ = 0. It is clearly seen that an increase in temperature reduces the reversible potential substantially, as shown in Figure 1.10. Thus, it is advantageous to operate the CO_2RR at elevated temperatures.[48]
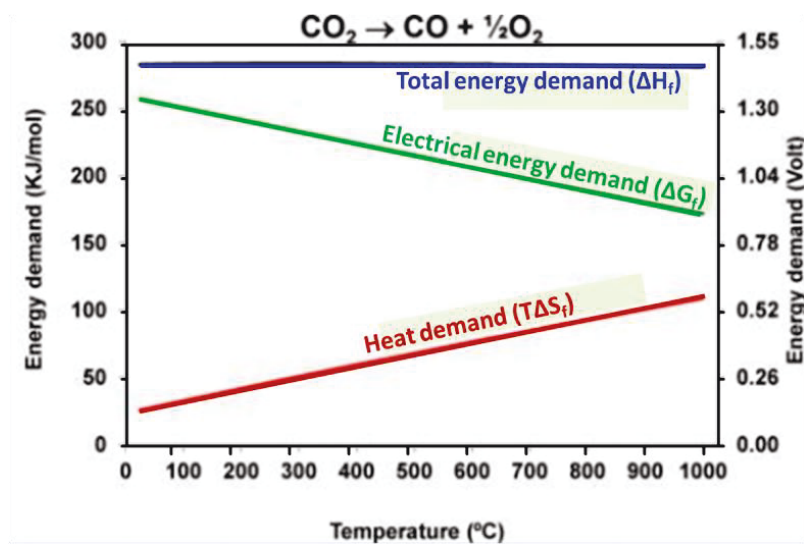
Figure 1.10 Relationships between enthalpy change (ΔH), Gibbs free energy change (ΔG) and entropy change (ΔS) for CO_2RR.[49]

1.5 Merits for CO_2RR

1.5.1 Current density

As a measure of the reaction rate for CO_2RR, the current density (j) reflects the electrons flowing through the electrochemical cell per unit surface area. Moreover, it's related to the catalytic surface, applied potential, concentrations and diffusion coefficients of the relevant species.

The partial current density of aimed product (j_m) is a direct measure of the generation rate for a certain product. It can be expressed as

9

$$j_m = j \times FE_m$$

For a superior electrocatalyst, a high partial current density at specific applied potential will be obtained for desired products for CO_2RR. On the contrary, a low partial current density for hydrogen formation will be achieved for the competitive side reaction (i.e. hydrogen evolution reaction).

1.5.2 Faraday efficiency and energy efficiency

Faraday efficiency (FE) reflects the selectivity of aimed product for CO_2RR. FE is the ratio of the electrochemical equivalent current density for a aimed product of CO_2RR to the total applied current density.[50,51] Measured electronic current through an external potentiostat cannot distinguish where the charges come and go, so only the direct measurement of reducing products can confirm FE. The FEs can be experimentally measured by running a set of electrolysis experiments at a fixed applied potential. It can be expressed by the following equation:[52-55]

$$FE_j = \frac{2FVvp_0}{RT_0 I_{total}} \times 100\%$$

$$FE_{CO} = \frac{2 \times 96,485 \left(\frac{C}{mol}\right) \times V\left(\frac{m^3}{s}\right) \times v(vol\%) \times 1.01 \times 10^5 \left(\frac{N}{m^2}\right)}{8.314 \left(\frac{N\,m}{mol\,K}\right) \times 298.15(K) \times I_{total}\left(\frac{C}{s}\right)} \times 100\%$$

$$FE_{CO} = \frac{2 \times 96,485 \left(\frac{C}{mol}\right) \times V\left(\frac{mL}{min}\right) \times 10^{-6}\left(\frac{m^3}{mL}\right) \times v(vol\%) \times 1.01 \times 10^5\left(\frac{N}{m^2}\right)}{8.314\left(\frac{N\,m}{mol\,K}\right) \times 298.15(K) \times I_{total}\left(\frac{C}{s}\right) \times 60\left(\frac{s}{min}\right)} \times 100\%,$$

where the unit of V is mL/min. then

$$FE_{CO} = \frac{0.1315 \times V\left(\frac{mL}{min}\right) \times v(vol\%)}{I_{total}(A)} \times 100\%$$

v (Vol%) = volume concentration of CO in the exhaust gas from the cell (GC data).

V (mL/min) = Gas flow rate measured by a flow meter at the exit of the cell at room temperature and under ambient pressure.

I_{total}(A) = steady-state cell current.

The FE of a product ranges from 0% to 100%. Despite the competitive hydrogen evolution reaction for the H_2 production, especially in aqueous solutions, an excellent electrocatalyst shows a high FE for a desired product.[56-58]

Energy efficiency:[34,59] As a measure of the overall energy utilization toward the desired product and an evaluation parameter of electrocatalyst in renewable energy storage, the values of energy efficiency (EE) can be calculated using the following equation.

$$EE_k = \frac{E_k^0 \times FE_k}{E_k^0 + \eta} \times 100\%$$

Where E_k^0 is the equilibrium cell potential for a certain product.

For example, $E_k^0 = E_{cathode}^0 - E_{anode}^0 = -0.11\,V - 1.23\,V = -1.34\,V$ for the CO formation during CO_2RR.

FE_k is the Faradaic efficiency of the aiming product k.

η is the cell overpotential.

From this equation, it is obvious that the high EE is obtained through a combination of high FE for the desired product and low overpotentials on the cathode and anode since that will lead to a low cell potential.[59]

1.5.3 Overpotential

Overpotential (η) is a measure of the energy required to drive the reaction to occur at an appreciable reaction rate. Generally, the overpotential of an electrochemical reaction is calculated based on the difference between the minimum potential where the reaction occurs (E) and the standard potential of the CO_2RR (E^0),[60] which can be expressed with the following equation.[43,61]

$$\eta = E - E^0$$

An excellent electrocatalyst is able to reduce CO_2 to the desired product at potentials close to the standard potential of the CO_2RR. This refers to a low overpotential for CO_2RR. On the contrary, a more negative potential than the standard one points to a high overpotential for certain aimed product.

1.5.4 The stability and process cost

The stability of electrocatalyst over time for CO_2RR still remains a challenge. Therefore, stability is critical for its commercialization in the energy market and industrial applications.[34]

The process cost,[62] including material consumption costs, capital cost and electricity cost, also has to be considered when developing desirable efficient and stable electrocatalysts.

1.6 References

(1) Omer, A. M. *Renew. Sust. Energ. Rev.* **2008**, *12*, 2265.

(2) Outlook, W. E. **2009**.

(3) Asif, M.; Muneer, T. *Renew. Sust. Energ. Rev.* **2007**, *11*, 1388.

(4) Keeling, C.; Whorf, T. *Carbon Dioxide Information Analysis Center* **2009**.

(5) Liu, Z.; Guan, D.; Wei, W.; Davis, S. J.; Ciais, P.; Bai, J.; Peng, S.; Zhang, Q.; Hubacek, K.; Marland, G. *Nature* **2015**, *524*, 335.

(6)https://kodukant.kovtp.ee/documents/1727611/3730742/Käsiraamat.pdf/32b40ecd-fc0c-410a-96ff-cda1c375c7ca

(7) Goldemberg, J.; Johansson, T. B.; Reddy, A. K.; Williams, R. H. *Energy for a sustainable world*; Wiley New York, **1988**.

(8) Meinshausen, M.; Meinshausen, N.; Hare, W.; Raper, S. C.; Frieler, K.; Knutti, R.; Frame, D. J.; Allen, M. R. *Nature* **2009**, *458*, 1158.

(9) Revesz, R. L.; Howard, P. H.; Arrow, K.; Goulder, L. H.; Kopp, R. E.; Livermore, M. A.; Oppenheimer, M.; Sterner, T. *Nature* **2014**, *508*, 173.

(10) Zachos, J. C.; Dickens, G. R.; Zeebe, R. E. *Nature* **2008**, *451*, 279.

(11)http://www.globalcarbonproject.org/carbonbudget/archive/2014/GCP_budget_2014_lowres_v1.02.pdf

(12) IPCC, Climate Change. **2007**. *The Physical Science Basis*. Contribution of Working Group I to the Fourth Assessment Report of the Intergovernmental Panel on Climate Change, Cambridge University Press. Cambridge, United Kingdom and New York, NY, USA, **2007**.

(13) Molina, M. J.; Molina, L. T. *J. Air Waste Manage.* **2004**, *54*, 644.

(14) Crutzen, P. J. *Atmos. Environ.* **2004**, *38*, 3539.

(15) Hidalgo, J.; Masson, V.; Baklanov, A.; Pigeon, G.; Gimeno, L. *Ann. N.Y. Acad. Sci.* **2008**, *1146*, 354.

(16) Hidalgo, J.; Masson, V.; Baklanov, A.; Pigeon, G.; Gimeno, L. *Ann. N.Y. Acad. Sci.* **2008**, *1146*, 354.

(17) Boot-Handford, M. E.; Abanades, J. C.; Anthony, E. J.; Blunt, M. J.; Brandani, S.; Mac Dowell, N.; Fernández, J. R.; Ferrari, M.-C.; Gross, R.; Hallett, J. P.; Haszeldine, R. S.; Heptonstall, P.; Lyngfelt, A.; Makuch, Z.; Mangano, E.; Porter, R. T. J.; Pourkashanian, M.; Rochelle, G. T.; Shah, N.; Yao, J. G.; Fennell, P. S. *Energy Environ. Sci.* **2014**, *7*, 130.

(18) Leung, D. Y.; Caramanna, G.; Maroto-Valer, M. M. *Renew. Sust. Energ. Rev.* **2014**, *39*, 426.

(19) Krebs, F. C. *Energ. Environ. Sci.* **2012**, *5*, 7238.

(20) MacDowell, N.; Florin, N.; Buchard, A.; Hallett, J.; Galindo, A.; Jackson, G.; Adjiman, C. S.; Williams, C. K.; Shah, N.; Fennell, P. *Energy Environ. Sci.* **2010**, *3*, 1645.

(21) Huang, C.-H.; Tan, C.-S. *Aerosol Air Qual. Res.* **2014**, *14*, 480.

(22) Centi, G.; Perathoner, S. *Green carbon dioxide: advances in CO₂ utilization*; John Wiley & Sons, **2014**.

(23) Halmann, M. *Ann Arbor: CRC Press*.

(24) Halmann, M. M.; Steinberg, M. *Greenhouse gas carbon dioxide mitigation: science and technology*; CRC press, **1998**.

(25) Aresta, M. *Carbon dioxide as chemical feedstock*; John Wiley & Sons, **2010**.

(26) Sridhar, N.; Hill, D.; Agarwal, A.; Zhai, Y.; Hektor, E. *Det Norske Veritas* **2011**.

(27) DOE, U. *US Department of Energy, Morgantown, WV, 39,* **2006**.

(28) http://www.pennenergy.com/articles/pennenergy/2014/09/petra-nova-CO₂-emissions-capture-enhanced-oil-recovery-project-underway.html.

(29) http://www.thinkgeoenergy.com/university-spin-off-plans-on-using-co2-for-the-extraction-of-geothermal-heat/.

(30) Bauen, A.; Berndes, G.; Junginger, M.; Londo, M.; Vuille, F.; Ball, R.; Bole, T.; Chudziak, C.; Faaij, A.; Mozaffarian, H. *Bioenergy: a sustainable and reliable energy source. A review of status and prospects.* **2009**.

(31) Lanzafame, P.; Centi, G.; Perathoner, S. *Chem. Soc. Rev.* **2014**, *43*, 7562.

(32) Mao, X.; Hatton, T. A. *Ind. Eng. Chem. Res.* **2015**, *54*, 4033.

(33) Qiao, J.; Liu, Y.; Hong, F.; Zhang, J. *Chem. Soc. Rev.* **2014**, *43*, 631.

(34) Zhu, D. D.; Liu, J. L.; Qiao, S. Z. *Adv. Mater.* **2016**, *28*, 3423.

(35) Costentin, C.; Robert, M.; Savéant, J.-M. *Chem. Soc. Rev.* **2013**, *42*, 2423.

(36) Jiang, Z.; Xiao, T.; Kuznetsov, V. á.; Edwards, P. á. *Philosophical Transactions of the Royal Society of London A: Mathematical, Phys. Eng. Sci.* **2010**, *368*, 3343.

(37) Graves, C.; Ebbesen, S. D.; Jensen, S. H.; Simonsen, S. B.; Mogensen, M. B. *Nat. Mater.* **2015**, *14*, 239.

(38) Kharecha, P. A.; Hansen, J. E. *Global Biogeochem. Cy.* **2008**, *22*.

(39) Banos, R.; Manzano-Agugliaro, F.; Montoya, F.; Gil, C.; Alcayde, A.; Gómez, J. *Renew. Sust. Energ. Rev.* **2011**, *15*, 1753.

(40) Dincer, I. *Renew. Sust. Energ. Rev.* **2000**, *4*, 157.

(41) Jacobson, M. Z.; Delucchi, M. A. *Energ. Policy* **2011**, *39*, 1154.

(42) Fthenakis, V.; Mason, J. E.; Zweibel, K. *Energ. Policy* **2009**, *37*, 387.

(43) White, J. L., Princeton University, **2016**.

(44) Aresta, M.; Dibenedetto, A.; Angelini, A. *Chem. Rev.* **2013**, *114*, 1709.

(45) Lim, R. J.; Xie, M.; Sk, M. A.; Lee, J.-M.; Fisher, A.; Wang, X.; Lim, K. H. *Catal. Today* **2014**, *233*, 169.

(46) Qiao, J.; Liu, Y.; Hong, F.; Zhang, J. *Chem. Soc. Rev.* **2014**, *43*, 631.

(47) Albo, J.; Alvarez-Guerra, M.; Castaño, P.; Irabien, A. *Green Chem.* **2015**, *17*, 2304.

(48) Ebbesen, S. D.; Jensen, S. H.; Hauch, A.; Mogensen, M. B. *Chem. Rev.* **2014**, *114*, 10697.

(49) National Institute of Standards and Technology (NIST). NIST Chemistry WebBook. http://webbook.nist.gov/chemistry/.

(50) Delacourt, C.; Ridgway, P. L.; Kerr, J. B.; Newman, J. *J. Electrochem. Soc.* **2008**, *155*, B42.

(51) Kuhl, K. P.; Cave, E. R.; Abram, D. N.; Jaramillo, T. F. *Energ. Environ. Sci.* **2012**, *5*, 7050.

(52) Liu, S.; Liu, Q.; Luo, J.-L. *ACS Catal.* **2016**, 6, 6219.

(53) Liu, S.; Liu, Q.; Luo, J.-L. *J. Mater. Chem. A* **2016**, 4, 17521.

(54) Liu, S.; Liu, Q.; Luo, J.-L. *J. Mater. Chem. A* **2017**, *5*, 2673.

(55) Liu, S.; Tao, H.; Zeng, L.; Liu, Q.; Xu, Z.; Liu, Q.; Luo, J. L. *J. Am. Chem. Soc.* **2017**, *139*, 2160.

(56) Zhu, W.; Michalsky, R.; Metin, O.; Lv, H.; Guo, S.; Wright, C. J.; Sun, X.; Peterson, A. A.; Sun, S. *J. Am. Chem. Soc.* **2013**, *135*, 16833.

(57) Kumar, B.; Atla, V.; Brian, J. P.; Kumari, S.; Nguyen, T. Q.; Sunkara, M.; Spurgeon, J. M. *Angew. Chem.* **2017**.

(58) Li, F.; Chen, L.; Knowles, G. P.; MacFarlane, D. R.; Zhang, J. *Angew. Chem.* **2017**, *56*, 505.

(59) Jhong, H.-R. M.; Ma, S.; Kenis, P. J. A. *Curr. Opin. Chem Eng.* **2013**, *2*, 191.

(60) Bard, A. J.; Faulkner, L. R. *Electrochem. Methods* **2001**, *2*.

(61) Baruch, M. F. **2016**.

(62) Oloman, C.; Li, H. *ChemSusChem* **2008**, *1*, 385.

Chapter 2. Literature survey of electrocatalysts for CO_2RR

2.1 Electrocatalysts for CO_2RR at room temperature

2.1.1 Metal/metal alloy and oxide-derived metal based electrocatalysts

Metal-based materials have dominated the field of CO_2RR for achieving value-added chemicals in the past few decades. Transition metal-related materials, such as Co,[1] Pd,[2,3] Cu,[4-8] Ag,[9,10] and Au,[10-12] are the most widely utilized electrocatalysts for CO_2RR. Various other metals have also been utilized for electrochemical CO_2RR, including: In,[13,14] Sn,[13,15,16] Pb,[16-18], Bi,[15,19] alkaline metals,[20,21] and alkaline-earth metals.[22] Weizhu et al.[11] reported CO_2RR to CO on Au nanoparticles (NPs) with various sizes (4, 6, 8 ,10 nm), and found that the 8 nm Au NPs show FE up to 90% at -0.67 V. The Cheonghee group[9] reported that 5 nm Ag/C has the best CO_2RR performance and achieves a maximum FE of 79.2% at -0.75 V vs RHE. However, the quantities of metals and the associated costs, especially for noble metals (e.g., Ag, Au and Cu), hamper CO_2RR towards large-scale applications.[23] Recently, metal alloys, such as Ag-Sn,[24] Cu-Pd,[25] Ni-Ga,[26,27] and Cu-Sn,[28] have drawn much attention since alloying can significantly improve the performance of metal by tuning the stabilization of key intermediates.[29] Xu et al.[30] found that the incorporation of Au can improve the stability of Cu nanoparticles and lower the η for CO_2RR. Zhao et al.[31] also demonstrated that Au_3Cu alloy showed larger current densities than Au NPs. Guo et al. prepared monodisperse Cu-Pt NPs and found that the Cu_3Pt NPs exhibited the largest current density and highest selectivity toward CH_4 since the incorporation of Pt can accelerate the protonation of adsorbed *CO, and consequently lead to an improved FE toward CH_4.[32] Besides, In was electrodeposited on Cu by Rasul's group.[33] The Cu-In alloy achieved an improved current density and a high FE of 90%

at −0.5 V. Therefore, alloy electrocatalysts have exhibited great potential for practical applications since no precious-metal is utilized in the component.

Furthermore, oxide-derived metal based electrocatalysts (eg., Au,[34] Ag,[35] Sn,[36] and Pb[37]) have been demonstrated to provide the potential for promoting the catalytic activity for CO_2RR. Chen and Kanan reported that the electrodeposited composite of Sn/SnOx showed significantly increased current density and Faradaic efficiency for CO_2RR.[38] Moreover, the group of Baruch suggested that SnO_2 was reduced to Sn^{2+} first and subsequently reacted with CO_2 to form the intermediates, which were consequently reduced to formate.[39] These results suggest that oxide-derived metal based materials can efficiently precede the CO_2RR. In addition, Li and Kanan prepared an oxide-derived Cu material for CO_2RR by *in situ* electrochemically reducing a thermally grown Cu_2O layer.[40] This electrocatalyst efficiently converted CO_2 to CO and HCOOH at a higher current density with a lowered η as compared to polycrystalline Cu. The superior results can be contributed to the increased grain boundaries formed during the reduction of Cu_2O to Cu, which act as highly active reaction sites.[41] Kim et al.[42] demonstrated that the Cu_2O, formed on the surface of bulk Cu, also promote CO_2RR. A η of 200 mV lower and a higher selectivity toward C_2H_4 were observed as compared to those of bulk Cu. Thus, the reduction of metal oxide layers to metals is also an attractive way to increase the CO_2RR performance. Recently, Zhang et al.[43] prepared oxide-derived Sn via electrochemically reducing SnO_2 nanoparticles and found that the as-obtained oxide-derived Sn exhibited significantly improved current density with an enhanced FE (~86% for formate at −1.8 V) as compared to the electrodeposited Sn. More importantly, they found that the 5 nm SnO_2 achieved the maximum formate FEs since a smaller particle size led to a stronger surface binding.

2.1.2 Transition metal oxides/chalcogenides

Transition-metal oxides (e.g., SnO_2[44,45] and Cu_2O[46]) have been reported to be the potential materials for CO_2RR. However, only limited studies on transition-metal oxides for CO_2RR have been reported due to the possible reduction of transition-metal oxides to transition-metal. Recently, Bigandra et al.[45] investigated CO_2RR on porous SnO_2 NWs and found that SnO_2 NWs showed a high FE (80%) for formate at -0.8 V due to the increased density of grain boundaries within the porous structure, which introduce new catalytically active sites. Besides, the group of Oh reported that MoO_2 was effective for CO_2RR in organic solvent with enhanced current densities, where the major products are formate and oxalate.[47] The group of Sekimoto identified that doped Ga_2O_3 can effectively reduce CO_2 to formic acid with a high FE over 80%, where $HCOO-Ga_2O_3$ was considered to be the key intermediate for CO_2RR. This is due to the improved conductivity of Ga_2O_3 derived from the doping of Sn and Si.[48] Recently, Dunfeng et al.[49] demonstrated that $Au-CeO_2$ showed much higher activity and FE than Au or CeO_2 since the $Au-CeO_2$ interface was dominant in enhancing CO_2 adsorption and activation, which can be further promoted by the presence of hydroxyl groups.

Transition metal chalcogenides are of particular interest due to their abundance, low price and facile synthesis, but only limited studies have been reported towards CO_2RR.[50-52] The group of Chan indicated that the edge sites in MoS_2 and $MoSe_2$ could selectively bind the key intermediates and promote the subsequent elementary steps, where CO could be adsorbed on the edge metal atoms and consequently reduced to the aimed products.[53] Also, Asadi et al.[50,51] investigated CO_2RR on the Mo-terminated edges of MoS_2 in EMIM-BF4 and found that the layer-stacked bulk MoS_2 with Mo-terminated edges showed an superior current density of 65 mA cm^{-2} with a

high CO FE of 98% at -0.764 V.[50] The DFT simulations reveals that the excellent CO_2RR performance originates from the Mo-terminated edges character, low work function and the high d-electron density on the Mo-terminated edges of MoS_2.[51] These experimental and theoretical results demonstrate the potential of transition metal oxides/chalcogenides as the promising materials for CO_2RR.

2.1.3 Carbon-based materials

Doping carbon materials with electronegativity lower than that of carbon (e.g., N, B, P and S) has been demonstrated to increase electrocatalytic activity for the oxygen reduction reaction (ORR).[54-56] However, there have been very few studies for CO_2RR using carbon materials. Recently, Kumar et al.[57] have reported the nitrogen doped carbon nanofiber to reduce CO_2. A much higher current density and a very high Faradaic efficiency of 98% were observed as compared to the undoped carbon nanofiber for CO_2RR towards CO formation. The superior performance can be attributed to the electronic structure modulation by incorporating N atoms in the carbon fibers. The group of Pulickel[58] demonstrated that the nitrogen-doped 3D graphene foam required negligible onset overpotential (-0.19 V) for CO formation, and it exhibited superior activity over Au and Ag, achieving similar maximum FE for CO formation ($\sim 85\%$) at a lowered overpotential of -0.47 V and better stability for at least 5 h. The authors also verified that the nitrogen-doped carbon nanotubes effectively reduced CO_2 to CO at an unprecedented η of -0.18 V together with a selectivity of 80%.[59] The superior activity for nitrogen-doped carbon materials is mainly derived from a lowered free energy barrier for the formation of adsorbed COOH. These reports show their discovery of inexpensive, renewable and metal-free electrocatalysts via doping strategy with significantly enhanced catalytic activity.

2.2 Electrocatalysts for CO_2RR at elevated temperatures

The prerequisites for being an ideal cathode material for CO_2RR in a SOEC are as follows: (1) excellent catalytic activity for the CO_2 conversion, (2) durable reversibility and redox stability, (3) stable and good coking resistance, (4) high electrical conductivity to provide electrons for CO_2RR and high oxygen ions transportation, (5) superior porous structure for gas diffusion and (6) other factors including dispersion of metal nanoparticles, particle size distribution, mean particle diameters and even the thickness of each layer since they significantly impact the transportation of gas, ions and electrons.[60,61]

To my best knowledge, most SOECs that have been investigated are based on the currently preferred Ni-based cathodes because of their high catalytic activity for the conversion of CO_2 to CO,[62-65] low cost, excellent chemically stability and appropriate thermal expansion coefficient. However, these cathodes suffer from severe electrical conductivity loss and deactivation because of the facile re-oxidation of Ni (Ni $\rightarrow$ NiO) and carbon deposition in an atmosphere with highly concentrated CO_2/CO.[66-68] In this situation, Ni-based cathode materials fail to be directly utilized in SOEC for CO_2RR. In addition to the commonly used material Ni-YSZ, other materials, such as Ni-$Sm_{0.2}Ce_{0.8}O_{2-\delta}$ (Ni-SDC),[69] $(La_{0.75}Sr_{0.25})_{0.95}Cr_{0.5}Mn_{0.5}O_3$ (LSCM),[70-72] $La_{0.6}Sr_{0.4}VO_{3-\delta}$ (LSV),[73] $La_{0.35}Sr_{0.65}TiO_{3+\delta}/Ce_{0.8}Gd_{0.2}O_{2-\delta}$ (LST-CGO),[74] $La_{0.35}Sr_{0.65}TiO_3$-$Ce_{0.5}La_{0.5}O_{2-\delta}$ (LST-CeO$_2$),[75] $Sr_{0.5}Fe_{1.5}Mo_{0.5}O_{6-\delta}$ (SFM),[76,77] $Sr_{0.94}Ti_{0.9}Nb_{0.1}O_3$ (STNO),[78] and $(Sr_{0.94})_{0.9}(Ti_{0.9}Nb_{0.1})O_3$ (STNNO)[78] have also been developed. Besides, Du et al.[79] prepared a $FeNi_3$ bimetallic alloy nanoparticle coated on the perovskite oxide backbone by *in situ* reduction of the perovskite $Sr_2FeMo_{0.65}Ni_{0.35}O_{6-\delta}$ (SFMNi) and found that the catalyst with the in situ exsolved $FeNi_3$ showed improved electrochemical performance as compared to the one before reduction. In contrast to

Ni-YSZ, these newly developed perovskite oxides show enhanced mixed ionic and electronic conductivity, redox activity, stability and resistance to carbon deposition, which consequently lead to the improved catalytic reaction activity.[80] However, no single material or composite material has been found that can meet all of the requirements (stability, activity, flexibility and low cost) for CO_2RR.[81] More importantly, the AO termination of perovskite oxides with low oxygen vacancy concentration hinders the catalysis contact between CO_2 and highly active B-site transition elements.[82,83] To solve these issues, the following aspects can be focused on:

Firstly, the appropriate doping in the perovskite oxides: since it has been demonstrated that the electrocatalytic activity and stability of perovskite oxides can be adjusted and improved via doping strategy (e.g., Mn, Cr, Fe, Nd).[61]

Secondly, homogenously dispersing active metal/bimetal nanoparticles on the surface of perovskite oxides: the transition metal *in situ* exsolved on the surface/interface of perovskite oxides can not only accelerate the collision of CO_2 and site-B transition metals, but also enhance the oxygen vacancy concentration at the reaction interface, thus enhancing electrocatalytic activity and improving CO_2 conversion efficiency[79,84,85]. Besides the significantly enhanced electrochemical performance, an excellent structural stability and coking resistance was also achieved in carbon-enriched fuels.[86-88]

Thirdly, the degradation mechanism: insights into the degradation mechanism of perovskite oxides under high temperature may point to correct direction to design electrode materials.

2.3 Current status and remaining challenges

Room Temperature: Normally, the superior performance was judged based on three criteria: the high FE, high EE and large current density achieved at a low η for a particular product.[89] From these reports in the past few decades, we found that many electrocatalysts have been reported showing a high EE or a high FE or a high current density. However, optimizing all three merits has been a challenge. For example, a high FE as well as a high current density has been achieved for some cases of C1-C2 production (as high as 70% FE with a current density of 600 mA cm^{-2}), but these cases exhibit EEs of less than 22%.

Elevated Temperatures: Despite the remarkable progress toward CO_2RR at elevated temperature, no single materials or composite materials can meet all requirements (stability, activity, flexibility and low cost) for effective CO_2RR. The CO_2RR at elevated temperatures is still not sufficient to meet the requirements for practical application because of several major challenges (e.g., low CO_2 conversion efficiency and degradation issues). First, the activation of CO_2 is hampered due to its sluggish kinetics. Further fundamental understandings of CO_2 activation process at elevated temperatures are required. Second, serious degradation cause the increase of cell resistance, especially at high current densities. At anode side, oxygen evolution leads to the weaken of the electrolyte/electrode interface and finally results in the delamination of electrolyte and electrode. At the cathode side, the issues of poisoning and redox stability can result from the formation of nanoparticles and the loss of percolation. Therefore, the exact degradation mechanism needs further exploration to avoid degradation at high current densities. Third, the stability and the connection to energy supplies (e.g., nuclear, wind and solar) are more practical issues for CO_2RR.[61]

2.4 References

(1) Magdesieva, T.; Yamamoto, T.; Tryk, D.; Fujishima, A. *J. Electrochem. Soc.* **2002**, *149*, 89.

(2) Gao, D.; Zhou, H.; Wang, J.; Miao, S.; Yang, F.; Wang, G.; Wang, J.; Bao, X. *J. Am. Chem. Soc.* **2015**, *137*, 4288.

(3) Kortlever, R.; Balemans, C.; Kwon, Y.; Koper, M. T. M. *Catal. Today* **2015**, *244*, 58.

(4) Li, Y.; Cui, F.; Ross, M. B.; Kim, D.; Sun, Y.; Yang, P. *Nano Lett.* **2017**, *17*, 1312.

(5) Wang, Z.; Yang, G.; Zhang, Z.; Jin, M.; Yin, Y. *ACS Nano* **2016**, *10*, 4559.

(6) Mistry, H.; Varela, A. S.; Bonifacio, C. S.; Zegkinoglou, I.; Sinev, I.; Choi, Y. W.; Kisslinger, K.; Stach, E. A.; Yang, J. C.; Strasser, P.; Cuenya, B. R. *Nat. Commun.* **2016**, *7*, 12123.

(7) Loiudice, A.; Lobaccaro, P.; Kamali, E. A.; Thao, T.; Huang, B. H.; Ager, J. W.; Buonsanti, R. *Angew. Chem. In. Edit.* **2016**, *55*, 5789.

(8) Reske, R.; Mistry, H.; Behafarid, F.; Roldan Cuenya, B.; Strasser, P. *J. Am. Chem. Soc.* **2014**, *136*, 6978.

(9) Kim, C.; Jeon, H. S.; Eom, T.; Jee, M. S.; Kim, H.; Friend, C. M.; Min, B. K.; Hwang, Y. J. *J. Am. Chem. Soc.* **2015**, *137*, 13844.

(10) Back, S.; Yeom, M. S.; Jung, Y. *ACS Catal.* **2015**, *5*, 5089.

(11) Zhu, W.; Michalsky, R.; Metin, O.; Lv, H.; Guo, S.; Wright, C. J.; Sun, X.; Peterson, A. A.; Sun, S. *J. Am. Chem. Soc.* **2013**, *135*, 16833.

(12) Fang, Y.; Flake, J. C. *J. Am. Chem. Soc.* **2017**.

(13) Kapusta, S.; Hackerman, N. *J. Electrochem. Soc.* **1983**, *130*, 607.

(14) Ding, C.; Li, A.; Lu, S.-M.; Zhang, H.; Li, C. *ACS Catal.* **2016**, *6*, 6438.

(15) Medina-Ramos, J.; Pupillo, R. C.; Keane, T. P.; DiMeglio, J. L.; Rosenthal, J. *J. Am. Chem. Soc.* **2015**, *137*, 5021.

(16) Cui, C.; Wang, H.; Zhu, X.; Han, J.; Ge, Q. *Sci. China Chem.* **2015**, *58*, 607.

(17) Subramanian, K.; Asokan, K.; Jeevarathinam, D.; Chandrasekaran, M. *J. Appl. Electrochem.* **2007**, *37*, 255.

(18) Lee, C. H.; Kanan, M. W. *ACS Catal.* **2015**, *5*, 465.

(19) Zhang, Z.; Chi, M.; Veith, G. M.; Zhang, P.; Lutterman, D. A.; Rosenthal, J.; Overbury, S. H.; Dai, S.; Zhu, H. *ACS Catal.* **2016**, *6*, 6255.

(20) Murata, A.; Hori, Y. *B. Chem. Soc. Jpn.* **1991**, *64*, 123.

(21) Wu, J.; Yang, X.; He, Z.; Mao, X.; Hatton, T. A.; Jamison, T. F. *Angew. Chem. Int. Edit.* **2014**, *53*, 8416.

(22) Schizodimou, A.; Kyriacou, G. *Electrochimi. Acta* **2012**, *78*, 171.

(23) Mao, X.; Hatton, T. A. *Ind. Eng. Chem. Res.* **2015**, *54*, 4033.

(24) Luc, W.; Collins, C.; Wang, S.; Xin, H.; He, K.; Kang, Y.; Jiao, F. *J. Am. Chem. Soc.* **2017**, *139*, 1885.

(25) Ma, S.; Sadakiyo, M.; Heima, M.; Luo, R.; Haasch, R. T.; Gold, J. I.; Yamauchi, M.; Kenis, P. J. *J. Am. Chem. Soc.* **2017**, *139*, 47.

(26) Torelli, D. A.; Francis, S. A.; Crompton, J. C.; Javier, A.; Thompson, J. R.; Brunschwig, B. S.; Soriaga, M. P.; Lewis, N. S. *ACS Catal.* **2016**, *6*, 2100.

(27) Studt, F.; Sharafutdinov, I.; Abild-Pedersen, F.; Elkjaer, C. F.; Hummelshoj, J. S.; Dahl, S.; Chorkendorff, I.; Norskov, J. K. *Nat. Chem.* **2014**, *6*, 320.

(28) Sarfraz, S.; Garcia-Esparza, A. T.; Jedidi, A.; Cavallo, L.; Takanabe, K. *ACS Catal.* **2016**.

(29) Zhu, D. D.; Liu, J. L.; Qiao, S. Z. *Adv. Mater.* **2016**, *28*, 3423.

(30) Xu, Z.; Lai, E.; Shao-Horn, Y.; Hamad-Schifferli, K. *Chem. Commun.* **2012**, *48*, 5626.

(31) Zhao, W.; Yang, L.; Yin, Y.; Jin, M. *J. Mater. Chem. A* **2014**, *2*, 902.

(32) Guo, X.; Zhang, Y.; Deng, C.; Li, X.; Xue, Y.; Yan, Y.-M.; Sun, K. *Chem. Commun.* **2015**, *51*, 1345.

(33) Rasul, S.; Anjum, D. H.; Jedidi, A.; Minenkov, Y.; Cavallo, L.; Takanabe, K. *Angew. Chem. Int. Edit.* **2015**, *54*, 2146.

(34) Chen, Y.; Li, C. W.; Kanan, M. W. *J. Am. Chem. Soc.* **2012**, *134*, 19969.

(35) Ma, M.; Trzesniewski, B. J.; Xie, J.; Smith, W. A. *Angew. Chem.* **2016**, *55*, 9748.

(36) Zhang, S.; Kang, P.; Ubnoske, S.; Brennaman, M. K.; Song, N.; House, R. L.; Glass, J. T.; Meyer, T. J. *J. Am. Chem. Soc.* **2014**, *136*, 7845.

(37) Lee, C. H.; Kanan, M. W. *ACS Catal.* **2014**, *5*, 465.

(38) Chen, Y.; Kanan, M. W. *J. Am. Chem. Soc.* **2012**, *134*, 1986.

(39) Baruch, M. F.; Pander III, J. E.; White, J. L.; Bocarsly, A. B. *ACS Catal.* **2015**, *5*, 3148.

(40) Li, C. W.; Kanan, M. W. *J. Am. Chem. Soc.* **2012**, *134*, 7231.

(41) Li, C. W.; Ciston, J.; Kanan, M. W. *Nature* **2014**, *508*, 504.

(42) Kim, D.; Lee, S.; Ocon, J. D.; Jeong, B.; Lee, J. K.; Lee, J. *Phys. Chem. Chem. Phys.* **2015**, *17*, 824.

(43) Zhang, S.; Kang, P.; Meyer, T. J. *J. Am. Chem. Soc.* **2014**, *136*, 1734.

(44) Li, F.; Chen, L.; Knowles, G. P.; MacFarlane, D. R.; Zhang, J. *Angew. Chem.* **2017**, *56*, 505.

(45) Kumar, B.; Atla, V.; Brian, J. P.; Kumari, S.; Nguyen, T. Q.; Sunkara, M.; Spurgeon, J. M. *Angew. Chem.* **2017**, *56*, 3645.

(46) Ren, D.; Deng, Y.; Handoko, A. D.; Chen, C. S.; Malkhandi, S.; Yeo, B. S. *ACS Catal.* **2015**, *5*, 2814.

(47) Oh, Y.; Vrubel, H.; Guidoux, S.; Hu, X. *Chem. Commun.* **2014**, *50*, 3878.

(48) Sekimoto, T.; Deguchi, M.; Yotsuhashi, S.; Yamada, Y.; Masui, T.; Kuramata, A.; Yamakoshi, S. *Electrochem. Commun.* **2014**, *43*, 95.

(49) Gao, D.; Zhang, Y.; Zhou, Z.; Cai, F.; Zhao, X.; Huang, W.; Li, Y.; Zhu, J.; Liu, P.; Yang, F.; Wang, G.; Bao, X. *J. Am. Chem. Soc.* **2017**, *139*, 5652.

(50) Asadi, M.; Kumar, B.; Behranginia, A.; Rosen, B. A.; Baskin, A.; Repnin, N.; Pisasale, D.; Phillips, P.; Zhu, W.; Haasch, R.; Klie, R. F.; Kral, P.; Abiade, J.; Salehi-Khojin, A. *Nat. Commun.* **2014**, *5*, 4470.

(51) Asadi, M.; Kim, K.; Liu, C.; Addepalli, A. V.; Abbasi, P.; Yasaei, P.; Phillips, P.; Behranginia, A.; Cerrato, J. M.; Haasch, R. *Science* **2016**, *353*, 467.

(52) Li, F.; Zhao, S.-F.; Chen, L.; Khan, A.; MacFarlane, D. R.; Zhang, J. *Energy Environ. Sci.* **2016**, *9*, 216.

(53) Chan, K.; Tsai, C.; Hansen, H. A.; Nørskov, J. K. *ChemCatChem* **2014**, *6*, 1899.

(54) Li, R.; Wei, Z.; Gou, X.; Xu, W. *RSc Adv.* **2013**, *3*, 9978.

(55) Gong, K.; Du, F.; Xia, Z.; Durstock, M.; Dai, L. *Science* **2009**, *323*, 760.

(56) Yang, S.; Zhi, L.; Tang, K.; Feng, X.; Maier, J.; Müllen, K. *Adv. Funct. Mater.* **2012**, *22*, 3634.

(57) Kumar, B.; Asadi, M.; Pisasale, D.; Sinha-Ray, S.; Rosen, B. A.; Haasch, R.; Abiade, J.; Yarin, A. L.; Salehi-Khojin, A. *Nat. Commun.* **2013**, *4*.

(58) Wu, J.; Liu, M.; Sharma, P. P.; Yadav, R. M.; Ma, L.; Yang, Y.; Zou, X.; Zhou, X. D.; Vajtai, R.; Yakobson, B. I.; Lou, J.; Ajayan, P. M. *Nano Lett.* **2016**, *16*, 466.

(59) Wu, J.; Yadav, R. M.; Liu, M.; Sharma, P. P.; Tiwary, C. S.; Ma, L.; Zou, X.; Zhou, X.-D.; Yakobson, B. I.; Lou, J. *ACS Nano* **2015**, *9*, 5364.

(60) Usseglio-Viretta, F.; Laurencin, J.; Delette, G.; Villanova, J.; Cloetens, P.; Leguillon, D. *J. Power Sources* **2014**, *256*, 394.

(61) Zheng, Y.; Wang, J.; Yu, B.; Zhang, W.; Chen, J.; Qiao, J.; Zhang, J. *Chem. Soc. Rev.* **2017**, *46*, 1427.

(62) Jensen, S. H.; Larsen, P. H.; Mogensen, M. *Int. J. Hydrogen Energ.* **2007**, *32*, 3253.

(63) Ebbesen, S. D.; Mogensen, M. *J. Power Sources* **2009**, *193*, 349.

(64) Pihlatie, M.; Kaiser, A.; Mogensen, M.; Chen, M. *Solid State Ionics* **2011**, *189*, 82.

(65) Pihlatie, M.; Frandsen, H. L.; Kaiser, A.; Mogensen, M. *J. Power Sources* **2010**, *195*, 2677.

(66) Wang, S.; Tsuruta, H.; Asanuma, M.; Ishihara, T. *Adv. Energ. Mater.* **2015**, *5*,1401003.

(67) Yue, X.; Irvine, J. T. *J. Electrochem. Soc.* **2012**, *159*, F442.

(68) Murray, E. P.; Tsai, T.; Barnett, S. *Nature* **1999**, *400*, 649.

(69) Ishihara, T.; Kannou, T. *Solid State Ionics* **2011**, *192*, 642.

(70) Bidrawn, F.; Kim, G.; Corre, G.; Irvine, J.; Vohs, J. M.; Gorte, R. J. *Electrochem. Solid St.* **2008**, *11*, B167.

(71) Yang, X.; Irvine, J. T. *J. Mater. Chem.* **2008**, *18*, 2349.

(72) Chen, S.; Xie, K.; Dong, D.; Li, H.; Qin, Q.; Zhang, Y.; Wu, Y. *J. Power Sources* **2015**, *274*, 718.

(73) Ge, X.; Zhang, L.; Fang, Y.; Zeng, J.; Chan, S. H. *RSC Adv.* **2011**, *1*, 715.

(74) Li, S.; Li, Y.; Gan, Y.; Xie, K.; Meng, G. *J. Power Sources* **2012**, *218*, 244.

(75) Marina, O. A.; Pederson, L. R.; Williams, M. C.; Coffey, G. W.; Meinhardt, K. D.; Nguyen, C. D.; Thomsen, E. C. *J. Electrochem. Soc.* **2007**, *154*, B452.

(76) Liu, Q.; Yang, C.; Dong, X.; Chen, F. *Int J of Hydrogen Energ.* **2010**, *35*, 10039.

(77) Liu, Q.; Dong, X.; Xiao, G.; Zhao, F.; Chen, F. *Adv. Mater.* **2010**, *22*, 5478.

(78) Yang, L.; Xie, K.; Xu, S.; Wu, T.; Zhou, Q.; Xie, T.; Wu, Y. *Dalton T.* **2014**, *43*, 14147.

( ) u , .; hao, H.; i , S.; ia , .; Gong, .; ha ng, .; Cheng, .; Li, .; Gu, L.; wierc e , K. *ACS Nano* **2016**, *10*, 8660.

(80) Shao, Z.; Haile, S. M.; Ahn, J.; Ronney, P. D.; Zhan, Z.; Barnett, S. A. *Nature* **2005**, *435*, 795.

(81) Kan, W. H.; Thangadurai, V. *Ionics* **2015**, *21*, 301.

(82) Tsekouras, G.; Neagu, D.; Irvine, J. T. S. *Energy Environ. Sci.* **2013**, *6*, 256.

(83) Druce, J.; Téllez, H.; Burriel, M.; Sharp, M. D.; Fawcett, L. J.; Cook, S. N.; McPhail, D. S.; Ishihara, T.; Brongersma, H. H.; Kilner, J. A. *Energy Environ. Sci.* **2014**, *7*, 3593.

(84) Myung, J.-h.; Neagu, D.; Miller, D. N.; Irvine, J. T. *Nature* **2016**.

(85) Zhou, J.; Shin, T.-H.; Ni, C.; Chen, G.; Wu, K.; Cheng, Y.; Irvine, J. T. *Chem. Mater.* **2016**, *28*, 2981.

(86) Yang, C.; Li, J.; Lin, Y.; Liu, J.; Chen, F.; Liu, M. *Nano Energy* **2015**, *11*, 704.

(87) Wang, S.; Tsuruta, H.; Asanuma, M.; Ishihara, T. *Adv. Energ. Mater.* **2015**, *5*, 1401003.

(88) Neagu, D.; Oh, T. S.; Miller, D. N.; Menard, H.; Bukhari, S. M.; Gamble, S. R.; Gorte, R. J.; Vohs, J. M.; Irvine, J. T. *Nat. Commun.* **2015**, *6*, 8120.

(89) Jhong, H.-R. M.; Ma, S.; Kenis, P. J. A. *Curr. Opin. Chem. Eng.* **2013**, *2*, 191.

Chapter 3. Experimental Methodology

3.1 Materials synthesis

3.1.1 Syntheses of Tri-Ag-NPs and SS-Ag-NPs

In a standard synthetic approach,[1,2] the total volume of the reaction solution is fixed at 25.00 ml. Typically, a 24.75 ml aqueous solution combining silver nitrate (0.05 M, 50 μl), trisodium citrate (75 mM, 0.5 mL), and H_2O_2 (30 wt %, 60 μl) was vigorously stirred at room temperature in air. Sodium borohydride ($NaBH_4$, 100 mM, 250 μl) was rapidly injected into this mixture to initiate the reduction, immediately leading to a light-yellow solution. After ∼3 min, the colloidal solution turned to a deep yellow due to the formation of small silver nanoparticles. Within the next several seconds, the morphology started to change from particles to nanoplates accompanied by the solution color changing from deep yellow to red, green, and blue. The entire transition from nanoparticle to nanoplates typically took 2-3 min. The resulting product was collected by centrifugation and washed with deionized water for three times. For the preparation of SS-Ag-NPs, only poly(vinylpyrrolidone) (weight-average molecular weight Mw ∼ 29, 000 g/mol) was added to the solution of Ag(NO_3), this led to the formation of Ag nanoparticles.

3.1.2 One-step facile synthesis of Ag₂S NWs.

For the synthesis of Ag_2S NWs, 300 mL of MAA (5mM) was added to the 150 mL of 5 mM $AgNO_3$ solution. After shaking the mixture for 1 min and waiting another 20 min at room temperature, the mixture was centrifuged and washed three times with deionized water to remove residual acid. The products could be transformed to crystalline Ag_2S NWs without changing dimensions by a thermal anneal at ∼300 °C.

3.1.3 Syntheses of LSFN and Fe-Ni-LSFN.

Polycrystalline perovskite powders of LSFN and Fe-Ni-LSFN were prepared using a modified sol-gel method as described elsewhere.[3] Stoichiometric amounts of La(NO$_3$)$_3$·6H$_2$O, Sr(NO$_3$)$_2$, Fe(NO$_3$)$_3$·9H$_2$O and Ni(NO$_3$)$_2$·6H$_2$O were dissolved in EDTA-NH$_3$H$_2$O combined solution under continuous heating and stirring, then citric acid was introduced. The molar ratio of EDTA acid : citric acid : total metal ions was controlled to be around 1 : 1.5 : 1. Subsequently, NH$_3$H$_2$O was added to adjust the pH value to around 8. The solution was stirred and heated on a hot plate at 80 °C until the formation of organic resins containing the homogeneously distributed cations because of the slow evaporation of the solvent. The synthesized gel was decomposed at 300 °C for 4 h to remove the organic components and the nitrates. The precursor powders were then fired at 1100 °C for 10 h in air to obtain the raw materials (LSFN), followed by heating in a tubular furnace at 850 °C for 10 h in a reducing gas flow, thus forming the *in situ* exsolved Fe-Ni-LSFN.

3.1.4 Syntheses of PSCFM and Co-Fe-PSFM.

Polycrystalline perovskite powders of Pr$_{0.4}$Sr$_{0.6}$Co$_{0.2}$Fe$_{0.7}$Mo$_{0.1}$O$_{3-\delta}$ (PSCFM) were prepared using a modified sol-gel method as described elsewhere.[3] Stoichiometric amounts of Pr(NO$_3$)$_3$·5H$_2$O, Sr(NO$_3$)$_2$, Co(NO$_3$)$_2$·6H$_2$O, Fe(NO$_3$)$_3$·9H$_2$O and (NH$_4$)$_6$Mo$_7$O$_{24}$·4H$_2$O were dissolved in EDTA-NH$_3$H$_2$O combined solution under continuous heating and stirring, then citric acid was introduced. The molar ratio of EDTA acid : citric acid : total metal ions was controlled to be around 1 : 1.5 : 1. Subsequently, NH$_3$H$_2$O was added to adjust the pH value to 8~9. The solution was stirred and heated on a hot plate at 80 °C until the formation of organic resins containing the homogeneously distributed cations due to the slow evaporation of the solvent. The synthesized gel was decomposed at 300 °C for 4 h to remove the organic

components and the nitrates. The raw powders were then fired at 1100 °C for 10 h in air to obtain the raw materials, followed by heating in a tubular furnace at 850 °C for 10 h in a 5% H_2/N_2 reducing gas flow, thus forming the Co-Fe *in-situ* exsolved $(Pr_{0.4}Sr_{0.6})_3(Fe_{0.85}Mo_{0.15})_2O_7$ (Co-Fe-PSFM).

3.2 Materials characterizations

- **X-ray diffraction (XRD):** The crystalline structure of all the synthesized powders was identified by XRD with Riga u Rotaflex Cu Kα radiation (40 kV, 44 mA) and the raw data were analyzed with JADE version 6.5.

- **High resolution SEM:** Microstructures were determined with a high-resolution Zeiss Sigma FE-SEM equipped with an EDX detector and an EBSD detector.

- **Transmission electron microscopy (TEM):** The high-resolution transmission electron microscopy images of all samples were acquired by using a JEOL JEM-2100 with a 200-kV TEM. The TEM uses an electron beam as light source (Lab6 crystal in this case) and the beam goes through (transmission) the specimen. The TEM was operated at an accelerating voltage of 200 kV. Images were achieved using a Gatan digital imaging system through Digital Micrograph software.

- **N_2 adsorption/desorption:** The BET specific surface areas and pore size of all catalysts were measured by the N_2 adsorption/desorption method using an Autosorb Quantachrome 1MP apparatus.

- **X-ray photoelectron spectroscopy (XPS):** X-ray photoelectron spectroscopy (XPS, Kratos AXIS Ultra) was used to investigate the surface chemistry of the

obtained powders with the adventitious carbon (C 1s) at the binding energy (BE) of 284.6 eV as the reference.

- **Thermogravimetric analysis (TGA):** TGA (TA SDT Q600) was performed from 20 to 1000 °C at a heating/cooling rate of 10 °C min^{-1} in air or 5% H_2/N_2 to characterize the thermophysical properties.

- **Raman spectra:** Nicolet Almega XR Dispersive Raman Microscope with 532 nm laser and X50 objective was used to determine the level of coke deposition on the Fe-Ni-LSFN cathode after CO_2 electrolysis.

- **UV/vis spectrophotometer:** The measurement of optical property was conducted by using a Varian Cary 50 UV/vis spectrophotometer (190 nm -1100 nm).

- **Fourier transform infrared spectroscopy (FTIR):** To examine if PVP retains on the as-prepared Tri-Ag-NPs and SS-Ag-NPs, Fourier transform infrared spectroscopy (FTIR) measurements were conducted.

- **Atomic force microscope measurements (AFM):** The Ag_2S NWs were deposited on mica surface by spin-coating. The topologies of the Ag_2S NWs were characterized by using AFM (Dimension Icon, Bruker) in contact mode under ambient conditions.

- **Ultraviolet Photoelectron Spectroscopy (UPS):** The work functions for Ag_2S NWs and bulk Ag were measured through the use of ultraviolet photoelectron spectroscopy. UPS data were acquired with a physical Electronics PHI 5400 photoelectron spectrometer using He I (21.2 eV) ultraviolet radiation and pass energy of 8.95 eV.

3.3 Cell fabrication and measurements

3.3.1 For CO$_2$RR at room temperature

20 mg of powders (10 mg of catalyst and 10 mg of carbon black) were dispersed in 1 ml mixed solvent containing 700 µl isopropanol, 200 µl of 5 wt% Nafion solution and 100 µl deionized water to form a homogeneous ink after at least 3 hours ultrasonic treatment. Then, 5.0 µl of the catalyst ink was loaded onto a glassy carbon electrode (GCE) of 5 mm in diameter (loading ~ 0.51 mg cm^{-2}), the GCE was mechanically polished with alumina paste before loading the catalyst suspension, then the GCE was dried overnight in air at room temperature before testing. The LSV curves were obtained with a Solartron 1255 frequency response analyzer and a Solartron 1286 electrochemical interface instrument in a custom-built electrochemical cell using saturated calomel electrode as the reference electrode, a platinum gauze as the counter electrode and the catalyst coated GCE as the working electrode.
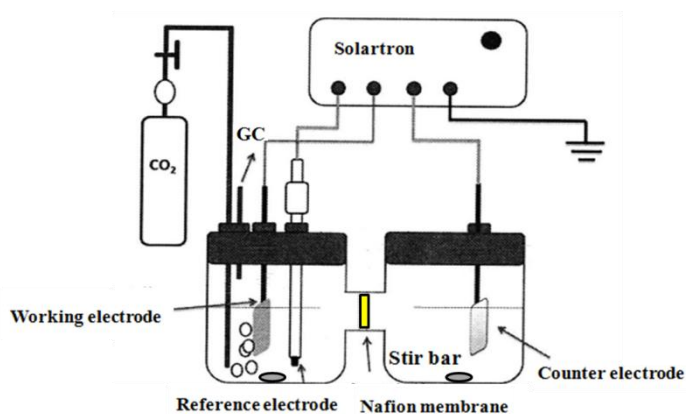
Figure 3.1 Schematic of the custom-built cell for CO$_2$RR at room temperature.

Electrolyte was saturated by bubbling CO$_2$ prior to the start of each experiment at a flow rate of 20 ml min^{-1} for 2 h until a saturated CO$_2$ condition was reached to ensure that all the oxygen was removed from the electrolyte. The flow of CO$_2$ was maintained over the solution during the recording of LSV curves in order to ensure its

continued CO_2 saturation. The working electrode was repeated at least 20 times before data were recorded at a scan rate of 20 mVs^{-1}. All potentials are reported with respect to the reversible hydrogen electrode (RHE). All measurements were independently conducted where a freshly deposited ink was used.

$$\text{Potential (V vs. RHE)} = \text{Applied potential (V vs. SCE)} + 0.241\,\text{V} + 0.0592 \times \text{pH}$$

For the product analysis of the three-electrode setup for CO_2 reduction, 25 μl of the catalyst ink was loaded onto the GCE (0.785 cm^2) (loading ~0.637 mg cm^{-2}). The gas products from the cathode compartment were analyzed using a Hewlett-Packard model Agilent 6890N gas chromatograph (GC) equipped with a packed bed column (HaySep D) operated at 80 °C with a thermal conductivity detector and a flame ionization detector. Argon (Air liquid 5.0) was employed as carrier gas with a flow rate of 30 ml min^{-1}. The gaseous products H_2, CH_4 and CO were separated in a molecular sieve column (Alltech, part no. 57732, 1.65 m × 1/8 in., molecular sieve 13X, 60/80 mesh) and hydrocarbons and CO_2 in a HaySep column (Alltech, part no. 14487, 3.5 m × 1/8 in., HaySep D, 80/100 mesh). NMR was used to quantify the concentration of liquid-phase products.

3.3.2 For CO$_2$RR at elevated temperature

The cells investigated in this work were YSZ electrolyte supported (polished before fabrication); the dimensions of the commercial YSZ discs ("fuelcellmaterials.com") are 250~300 μm in thickness and 25 mm in diameter. The GDC pastes were screen-printed on both anode and cathode sides of the YSZ electrolyte disc and co-sintered at 1300 °C for 5 h to form dense GDC buffer layers with a thickness of ~20 μm. Both the cathode pastes and anode pastes were screen-printed onto the corresponding surfaces of the YSZ disc to form a membrane electrode assembly (MEA). The MEA

was sintered at 1100 °C for 4 h in air. Gold paste was painted onto the surfaces of both anode and cathode to form current collectors. The CO_2 electrolysis cell was built by fixing the MEA between coaxial pairs of alumina tubes with a sealant, which was fastened in a vertical tubular furnace (Thermolyne F79300). Dry CO_2/CO (70:30) was fed to the cell with a flow rate of 50 ml min^{-1} via the cathode compartment located at the bottom, while the anode was placed on the top and exposed to air.

Two coaxial alumina tubes (containing an inlet and an outlet) are used as electrode compartments to place the cell, and there is a small gap between the inlet tube and the cathode. The ceramic sealant (552) is applied to seal the outer edge of the cathode side to prevent the leakage of CO_2/CO. The gold wires welded to a gold mesh that contacts the electrode go through the inlet and are connected to the testing instrument (Solartron). The CO_2/CO gas is fed to cathode compartment at a flow rate of 30 ml min^{-1} and the anode compartment is open to air directly.
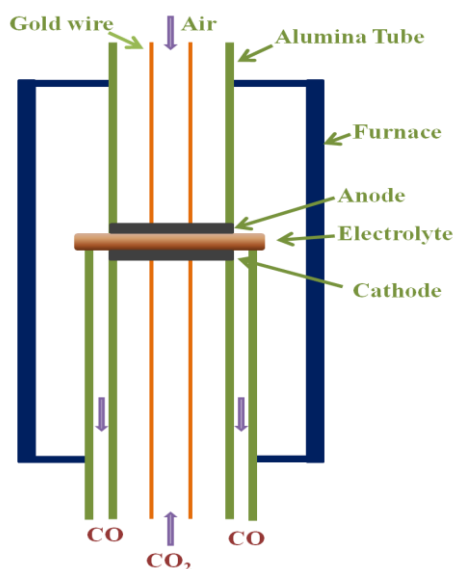
Figure 3.2 Schematic of the cell for CO_2RR at elevated temperatures.

The electrochemical performance of the CO_2 electrolysis cell was measured by employing a four-probe method with Au wires as the leads. The temperature of the

CO$_2$ electrolysis cell was slowly increased to 850 °C and a 5% H$_2$/N$_2$ reducing gas flow was continuously pumped into the cathode compartment. The temperature was maintained for 2 h to complete the further reduction and exsolution of the cathode material. The electrochemical measurements were conducted with a Solartron 1255 frequency response analyzer and a Solartron 1286 electrochemical interface instrument. The polarization resistance of the CO$_2$ electrolysis cell was determined from electrochemical impedance spectroscopy (EIS) measured under an AC potential with a frequency range of 1 MHz to 0.1 Hz and an amplitude of 10 mV at the stable open circuit voltage (OCV). Stability test in dry CO$_2$/CO (70:30) was performed under a constant applied potential of 0.6 V (vs. OCV) at 850 °C. The outlet gases from the cathode compartment were analyzed using a Hewlett-Packard model HP5890 GC equipped with a packed column (Porapak QS) operated at 80 °C with a thermal conductivity detector and a flame ionization detector. Nicolet Almega XR Dispersive Raman Microscope with 532 nm laser and X50 objective was used to determine the level of coke deposition on the Co-Fe-PSFM cathode after CO$_2$ electrolysis.

3.4 References

(1) Zhang, Q.; Li, N.; Goebl, J.; Lu, Z.; Yin, Y. *J. Am. Chem. Soc.* **2011**, *133*, 18931.

(2) Metraux, G. S.; Mirkin, C. A. *Adv. Mater.* **2005**, *17*, 412.

(3) Duan, C.; Tong, J.; Shang, M.; Nikodemski, S.; Sanders, M.; Ricote, S.; Almansoori, A.; O'Hayre, R. *Science* **2015**, *349*, 1321.

Chapter 4 Shape-dependent Electrocatalytic Reduction of CO$_2$ to CO on Triangular Silver Nanoplates

ABSTRACT: Electrochemical reduction of CO$_2$ (CO$_2$RR) provides great potentials for intermittent renewable energy storage. This study demonstrates a predominant shape-dependent electrocatalytic reduction of CO$_2$ to CO on triangular silver nanoplates (Tri-Ag-NPs) in 0.1 M KHCO$_3$.
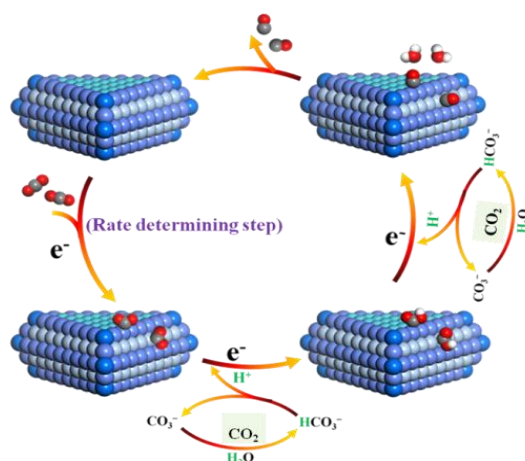
Compared with similarly sized Ag nanoparticles (SS-Ag-NPs) and bulk Ag, Tri-Ag-NPs exhibited an enhanced current density and significantly improved Faradaic efficiency (96.8%) and energy efficiency (61.7%), together with a considerable durability (7 days). Additionally, CO starts to be observed at an ultralow overpotential of 96 mV, further confirming the superiority of Tri-Ag-NPs as a catalyst for CO$_2$RR towards CO formation. Density functional theory (DFT) calculations reveal that the significantly enhanced electrocatalytic activity and selectivity at lowered overpotential originate from the shape-controlled structure. This not only provides the optimum edge-to-corner ratio, but also dominates at the facet of Ag (100) where it

requires lower energy to initiate the rate-determining step. This study demonstrates a promising approach to tune electrocatalytic activity and selectivity of metal catalysts for CO_2RR by creating optimal facet and edge site through shape-control synthesis.

4.1. Introduction

Increased utilization of fossil fuels has brought about record-breaking levels of atmospheric carbon dioxide (CO_2), which causes climate change and environmental issues.[1] To attenuate our reliance on fossil fuels, sustainable and environmentally friendly alternatives are desirable options. Electrochemical CO_2 reduction reaction (CO_2RR) points to a promising direction not only in decreasing CO_2 accumulation, but also in converting intermittent renewable electricity into energy-dense fuels.[2] However, the more kinetically preferred H_2 evolution reaction (HER) always outcompetes the CO_2RR and consequently, decreases the selectivity of target product.[3] The high overpotential (η) is also required for CO_2RR to reach substantial reaction rates.[4] Therefore, it is desirable to search for novel catalysts capable of efficiently promoting CO_2RR with high selectivity (Faraday efficiency, FE) and catalytic activity (current density, j) at low η.

Various metallic electrocatalysts have been experimentally and computationally identified for CO_2RR since the binding energy of intermediate (CO*) on the metal surface is relatively weaker than that of H* derived from HER. This leads to the selective evolution of CO rather than the competitive H_2 on these metal surfaces. The existence of optimal particle size has also been reported to strongly enhance the catalytic activity for CO_2RR over metal-based catalysts, such as Au,[5-7] and Ag[8-13], where FE and current density reach maximum values. Zhu et al.[5] reported CO_2RR on Au nanoparticles (NPs) and found that the 8 nm Au NPs show FE up to 90% at -0.67 V (vs reversible hydrogen electrode, RHE). Ag NP, an attractive alternative for noble

metal electrode, shows selectivity as high as that of Au at a lower cost. The size effects have also been observed by Cheonghee group[8] and they noted that 5 nm Ag/C has the best CO_2RR performance and achieves a maximum FE of 79.2% at -0.75 V vs RHE. It has been demonstrated that the enhanced size-dependent FE and current density are related to the ratio of edge-to-corner. Density functional theory (DFT) simulations also suggest that edge sites are more preferred for CO evolution than corner sites on sized-controlled noble metal NPs.[5, 8, 9, 14] Recently, Min Liu et al.[15] also reported a field-induced reagent concentration that enables highly efficient CO_2RR resulting from local high electric fields. Besides the effects of size and local electric filed, understanding the shape effects of metal NP on CO_2RR is also worth-noting. There have been limited studies on CO_2RR over metal NPs regarding the influence of particle shape, but further exploration is warranted since the presence of edge and corner sites varies as the shape changes.[5, 9] Shape control has received extensive attention for Ag with particular emphasis on triangular Ag nanoplate (Tri-Ag-NP) because of their unique structure-related optical properties and potential applications.[16]

In this study, Tri-Ag-NPs were synthesized using direct chemical reduction method.[17] The composite containing Tri-Ag-NPs and carbon black (CB) was fabricated on a glassy carbon electrode (GCE) for CO_2RR. It was found that Tri-Ag-NPs were particularly active for CO_2RR towards CO formation at an ultralow η. F T calculations were employed to rationalize the increased catalytic activity and selectivity of Tri-Ag-NPs towards CO_2RR.
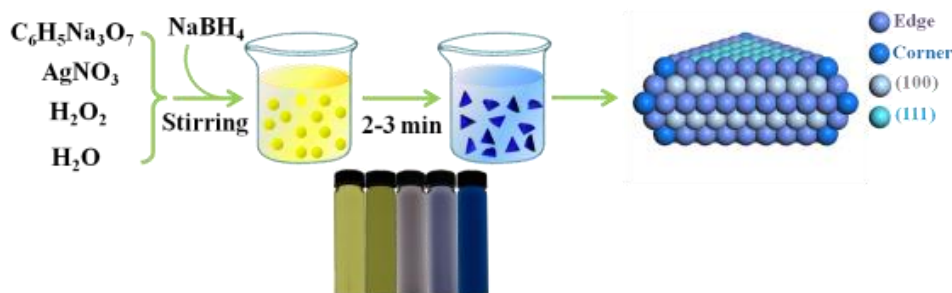
Scheme 1. The synthesis process and digital images of Tri-Ag-NPs.

4.2. Results and discussion

Tri-Ag-NPs were synthesized by chemically reducing an aqueous solution of $AgNO_3$ with $NaBH_4$ in the presence of H_2O_2 and trisodium citrate (Scheme 1). UV/vis spectra were recorded to investigate the transformation process of Tri-Ag-NPs by judging from the spectra change, as shown in Figure 4.1a. Upon the rapid injection of $NaBH_4$, the color of the original transparent solution immediately became pale yellow, suggesting the occurrence of Ag reduction. Approximately 2 min after initiation, the pale solution turned deep yellow, an indication of Ag NP formation, as evidenced in the absorbance of the characteristic peak at ~400 nm,[17] where it quickly increased to the maximum. Subsequently, the solution quickly changed to blue, where the corresponding intensity of the characteristic peak of Ag NPs at ~400 nm quickly decreased, indicating the gradual consumption of Ag NPs during the transformation process. Another peak emerged at ~600 nm and gradually red-shifted to the wavelength of 850 nm, indicative of the formation and growth of Tri-Ag-NPs, as confirmed by the TEM image in Figure 4.1b. The Ag nanoplates obtained are enclosed by two (111) facets at both top and bottom surfaces, and three (100) facets at the side faces which contain twin planes and stacking faults along the vertical direction, as demonstrated by previous studies.[16, 18]
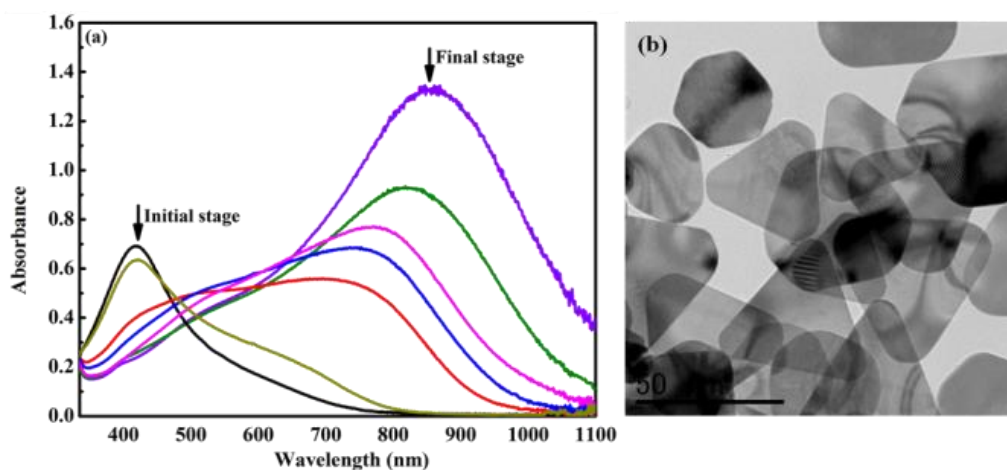
Figure 4.1 (a) UV/vis spectra; (b) TEM image of Tri-Ag-NPs.

To examine the CO_2RR activity of Tri-Ag-NPs, the mixture containing catalysts and CB was quantitatively dropped onto a GCE (0.785 cm^2). The polarization curves of all catalysts were obtained by a sweeping potential between -0.056 and -1.156 V vs RHE at a scan rate of 50 mV s^{-1}. Figure 4.2a shows the linear sweep voltammetry (LSV) results of Tri-Ag-NPs, SS-Ag-NPs and bulk Ag to distinguish the shape effects as well as CB and GCE as references to differentiate their contributions for CO_2RR. The Tri-Ag-NPs exhibited approximately 2-fold higher current densities (over 5.5 mA cm^{-2}, normalized by the geometrical surface area) relative to bulk Ag (3.0 mA cm^{-2}), and 1.0 mA cm^{-2} larger than SS-Ag-NPs. More importantly, a much more positive onset potential was observed for the Tri-Ag-NPs compared to the SS-Ag-NPs and to Bulk Ag. The increment in current density, indicative of a promoted cathodic kinetics for CO_2RR, is not conclusive evidence since HER and CO_2RR are often interconnected. To verify the occurrence of predominant CO_2RR other than HER, and the enhanced shape-dependent catalytic activity of Tri-Ag-NPs, potentiostatic electrolysis was carried out at different applied potentials. The achieved current densities are 30% less than the corresponding values in LSV measurements under the same potential load. This can be attributed to the combination of the presence of extra

42

current from the interface charging, and the formation of a CO_2 and/or CO partially depleted layer in the vicinity of the catalyst due to the mass transport limitations.[19, 20] The outlet gases were directly vented into a gas chromatography (GC) to quantitatively analyze the gas composition. To confirm that the catalytic activity is not derived from bare GCE and CB, both samples were fabricated as the cathodes. GC analyses indicated that H_2 was the major product resulting from the competitive HER on GCE and CB (see Figure S4.2).
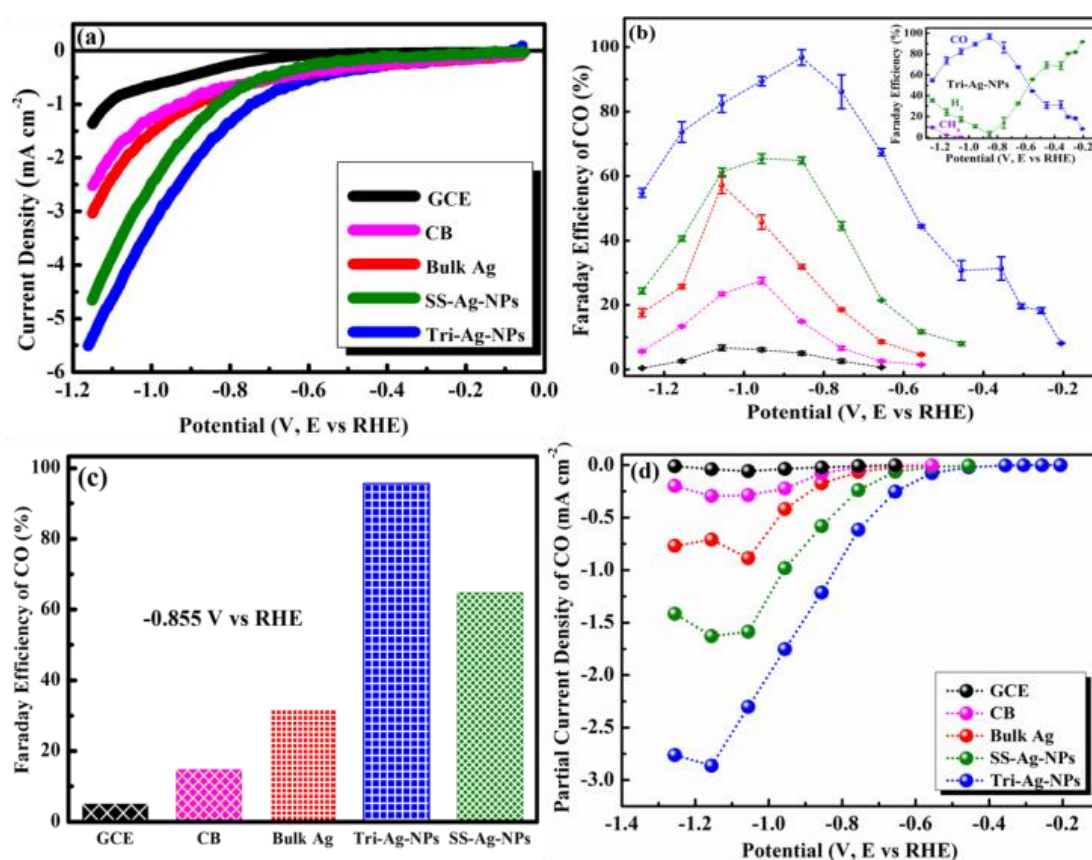
Figure 4.2 (a) Cathodic LSV results; (b) FEs of CO at various applied potentials (the inset shows the CO, CH_4 and H_2 overall FE for Tri-Ag-NPs) and (c) CO FEs at fixed potential of −0.855 V; (d) CO partial current density.

Tri-Ag-NPs, SS-Ag-NPs and bulk Ag were also performed under the same experimental conditions, and the potential-dependent FEs for CO formation were shown in Figure 4.2b. CO (FE of 8.1%) started to generate at an onset potential of

−0.206 V for Tri-Ag-NPs, which was only 96 mV lower than the theoretical equilibrium potential (−0.11 V) and remarkably lower than other reported Ag-based catalysts,[8, 21] whereas CO was not detectable under this ultralow η (96 mV) for SS-Ag-NPs and bulk Ag. To achieve the equivalent FE for CO, SS-Ag-NPs (8.0%) and bulk Ag (8.6%) required a potential of −0.456 V (η of 346 mV) and −0.656 V (η of 546 mV), respectively. The FEs of CO increased significantly for Tri-Ag-NPs, SS-Ag-NPs and bulk Ag when more negative potentials were applied. Concurrently, Tri-Ag-NPs showed the best CO_2RR performance and reached its maximum value of 96.8% with a much lower η of 0.746 V as compared to SS-Ag-NPs (65.4%, 0.846 V) and bulk Ag (57.2%, 0.946 V). When comparing the FEs of all samples at a fixed potential of −0.856 V (Figure 4.2c), Tri-Ag-NPs showed 3- and 1.5-fold higher than SS-Ag-NPs (64.9%) and bulk Ag (31.9%), respectively. This indicates that the CO_2RR is shape-dependent and the Tri-Ag-NPs are the most active for CO formation as compared to other reported Ag-based catalysts.[8, 9, 21] Figure 4.2d shows the potential-dependent CO partial current densities calculated based on the current densities from potentiostatic measurements and the corresponding CO FEs for all samples. It clearly reveals the exclusive catalytic activity of Tri-Ag-NPs for the CO_2RR towards CO formation, where a 2.2-fold increase in the CO partial current densities of Tri-Ag-NPs relative to SS-Ag-NPs further confirms the shape-dependent effects.

For comparing the reaction kinetics for CO_2RR and subsequently confirming the increased catalytic activity of Tri-Ag-NPs resulted from the shape control, Tafel plots for Tri-Ag-NPs, SS-Ag-NPs and bulk Ag are shown in Figure 4.3a.
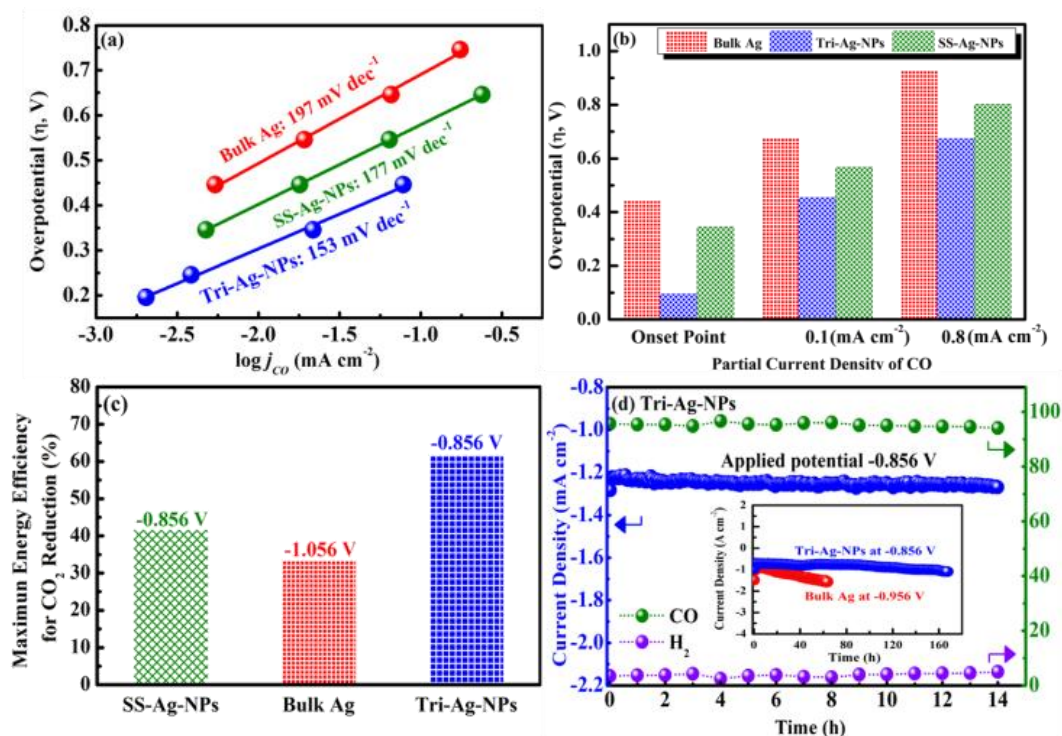
Figure 4.3 (a) Tafel plot and (b) η as a function of various current densities; (c) Maximum energy efficiencies of Tri-Ag-NPs, SS-Ag-NPs and bulk Ag; (d) long-term stability at a potential load of -0.856 V and the corresponding FEs of CO and H_2.

The Tafel slope, an indication of kinetics for CO formation, was 153 mV dec^{-1} for Tri-Ag-NPs, closer to the value of 118 mV dec^{-1} expected for rate-determining step at the electrode[22] as compared to a Tafel slope of 177 mV dec^{-1} for SS-Ag-NPs and 197 mV dec^{-1} for bulk Ag. Both values were larger than the one for Tri-Ag-NPs, indicating a poor kinetics for CO_2RR. Moreover, the formation of an adsorbed $*COO^-$ intermediate ($CO_2 + e^- \rightarrow *COO^-$) on catalyst surface exclusively determines the reaction rate for CO_2RR since the anionic radical is highly unstable. The negative reduction potential of the $CO_2/*COO^-$ redox couple, $E^o = -1.49$ vs. RHE at pH 7, not only creates a significant thermodynamic and kinetic bottleneck for the overall CO_2RR, but also promotes side reactions (e.g. HER) and consequently decreases the current efficiency for CO_2RR. However, the onset potential shifted anodically to -0.206 V on Tri-Ag-NPs (Figure 4.3b), a net decrease of 0.25 V and 0.35 V in η

compared to SS-Ag-NPs and bulk Ag, respectively. The exchange current density (i_o), a reflection of the free energy barrier required for CO_2RR at the reversible potential as well as a measure of intrinsic rate of electron transfer between the electrolyte and the electrode, was 1.1×10^{-4} mA cm^{-2} for Tri-Ag-NPs, one order of magnitude higher than that for SS-Ag-NPs (3.8×10^{-5} mA cm^{-2}) and bulk Ag (3.2×10^{-5} mA cm^{-2}). It is also comparable to a recently reported value (1.0×10^{-5} mA cm^{-2}) on 3 nm Ag/C for CO_2RR to CO,[8] further suggesting an improved shape-dependent catalytic activity. As a critical parameter in benchmarking electrocatalyst for renewable energy storage, the maximum energy conversion efficiencies of Tri-Ag-NPs, SS-Ag-NPs and bulk Ag were evaluated (Figure 4.3c). The low η together with the high FE of Tri-Ag-NPs contributed to an energy efficiency of over 61.7%, much higher than SS-Ag-NPs (42%) and bulk Ag (34%). This value is also comparable with the most efficient existing platforms for the formation of CO,[7, 23] and consequently distinguishes Tri-Ag-NPs as a promising platform for CO_2RR.

To address the stability of the developed catalyst, a major concern for CO_2RR, the long-term performance of Tri-Ag-NPs was evaluated at a constant potential load of -0.856 V for 7 days. The outlet gases were analyzed each hour over a period of 14 h by GC. The corresponding FEs of CO and H_2 were also determined (Figure 4.3d) and the inset exhibits the long-term stability test over 7 days. The current density maintained a steady value at around -1.25 mA cm^{-2} with negligible degradation and the corresponding FEs of CO only fluctuated slightly around 96% throughout the stability test. Moreover, Tri-Ag-NPs show no morphological change after CO_2 reduction (Figure S4.4), further indicating the excellent stability of Tri-Ag-NPs for CO_2RR.
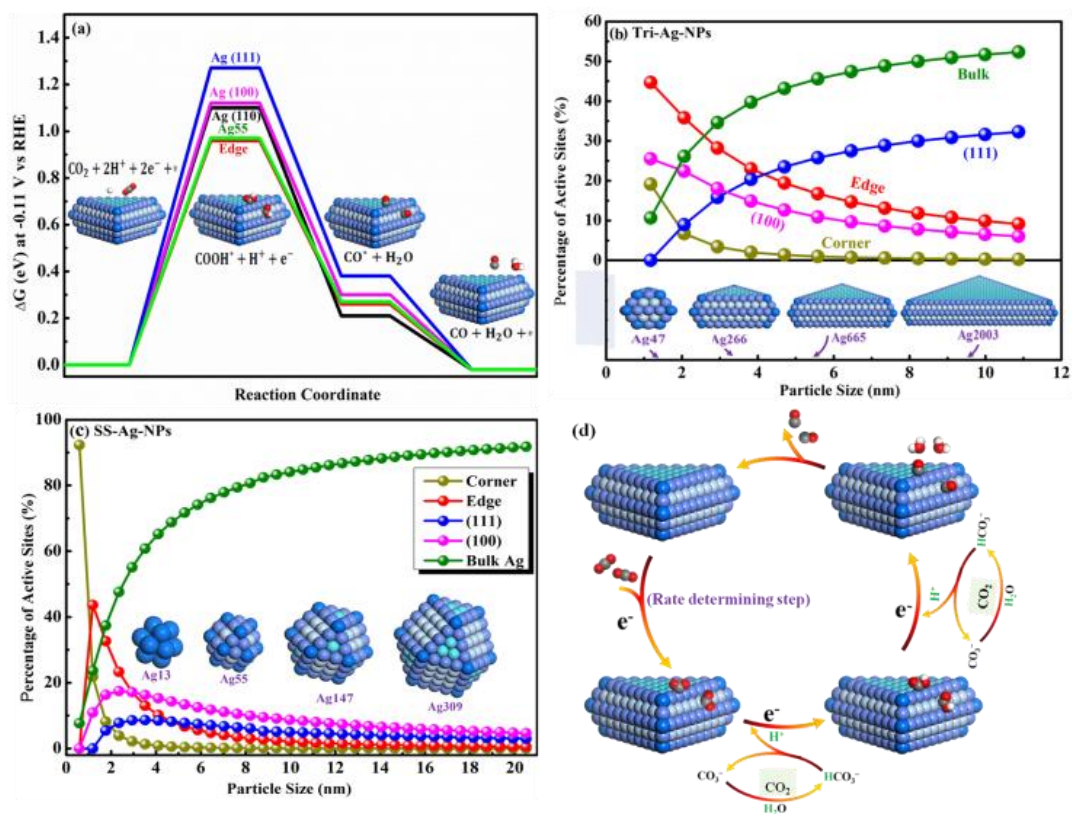
Figure 4.4 (a) Free energy diagrams for CO_2RR to CO on different facets and Ag55 cluster at -0.11 V; active adsorption site density on (b) Tri-Ag-NPs and (c) SS-Ag-NPs as a function of particle size; (d) proposed mechanism for CO_2RR to CO on Tri-Ag-NPs.

A better understanding on the origins credited for the ultralow onset potential, and the high CO selectivity at lower η for CO_2RR over shape-controlled Tri-Ag-NPs relative to SS-Ag-NPs, DFT calculations were further explored to investigate the reactivity of different Ag features based on the computational hydrogen electrode model.[5, 9, 14] Figure 4.4a shows the Gibbs free energy (ΔG) diagram for CO_2RR on different facets and Ag55 cluster, where the total ΔGs required for the proposed four elementary reaction steps were simulated and calculated (Figure 4.4d). The required η initially originates from the formation of COOH* since an uphill energy barrier of the first proton-coupled electron-transfer step for all facets and the cluster was observed. Apparently, the required ΔG to form the COOH* on Ag(100) is significantly lower than that on Ag(111) and quite close to the one on Ag(110), suggesting a higher

catalytic activity of Ag(100) for CO_2RR. More importantly, the facet of (100) is predominant in Tri-Ag-NPs as compared to that in SS-Ag-NPs since Tri-Ag-NPs are only enclosed by the facets of (100) and (111). The free-energy step subsequently becomes more thermodynamically facile for the second proton-coupled electron transfer for the adsorbed CO* at all facets. Although Ag55 cluster is slightly easier for the formation of COOH* than all facets, it tends to overbind with CO* and consequently decreases the product evolution rate. Thus, both the dominance of (100) and the ease in the CO evolution deriving from the shape-controlled effect point to the decreased η and low onset potential for CO formation. Additionally, studies have demonstrated that an increased edge-to-corner ratio yields enhanced catalytic activity and selectivity for CO_2RR since the adsorption of CO_2 and the subsequent formation of intermediate COOH* are easier on edge sites than corner sites.[5, 9, 14] Thus, the edge-to-corner ratios of Tri-Ag-NPs and SS-Ag-NPs as a function of the cluster diameter were also analyzed (Figures 4.4b and 4.4c). It is found that Tri-Ag-NPs with a diameter range from 0 to 12 nm maintain a comparably higher edge-to-corner ratio. Although the ratio difference between Tri-Ag-NPs and SS-Ag-NPs narrows gradually at larger diameters, the density of catalytically active edge sites on Tri-Ag-NPs always exceeds that on SS-Ag-NPs. This ensures sufficient active edge sites for CO_2 reduction to CO and consequently leads to superior selectivity of Tri-Ag-NPs.

In summary, we successfully synthesized Tri-Ag-NPs and investigated its shape-dependent electrocatalytic reduction of CO_2 to CO in 0.1 M $KHCO_3$. Tri-Ag-NPs exhibit considerably higher selectivity as compared to SS-Ag-NPs and bulk Ag. Moreover, CO can be detected at an ultralow onset potential, confirming the excellent catalytic activity of Tri-Ag-NPs towards CO_2RR. The durability test over 7 days further confirms the excellent performance of Tri-Ag-NPs for efficient CO_2RR. DFT

calculations indicate that the high selectivity of Tri-Ag-NPs at an ultralow overpotential is a consequence of both the optimum edge-to-corner ratio and the predominant Ag(100) facet in Tri-Ag-NPs.

4.3. References

(1) Buitenwerf, R.; Rose, L.; Higgins, S. I. *Nat. Clim. Change* **2015**, *5*, 364.

(2) Goeppert, A.; Czaun, M.; May, R. B.; Prakash, G. S.; Olah, G. A.; Narayanan, S. *J. Am. Chem. Soc.* **2011**, *133*, 20164.

(3) Qiao, J.; Liu, Y.; Hong, F.; Zhang, J. *Chem. Soc. Rev.* **2014**, *43*, 631.

(4) Costentin, C.; Robert, M.; Savéant, J.-M. *Chem. Soc. Rev.* **2013**, *42*, 2423.

(5) Zhu, W.; Michalsky, R.; Metin, O.; Lv, H.; Guo, S.; Wright, C. J.; Sun, X.; Peterson, A. A.; Sun, S. *J. Am. Chem. Soc.* **2013**, *135*, 16833.

(6) Koh, J. H.; Jeon, H. S.; Jee, M. S.; Nursanto, E. B.; Lee, H.; Hwang, Y. J.; Min, B. K. *J. Phys. Chem. C* **2015**, *119*, 883.

(7) Chen, Y.; Li, C. W.; Kanan, M. W. *J. Am. Chem. Soc.* **2012**, *134*, 19969.

(8) Kim, C.; Jeon, H. S.; Eom, T.; Jee, M. S.; Kim, H.; Friend, C. M.; Min, B. K.; Hwang, Y. J. *J. Am. Chem. Soc.* **2015**, *137*, 13844.

(9) Back, S.; Yeom, M. S.; Jung, Y. *ACS Catal.* **2015**, *5*, 5089.

(10) Hatsukade, T.; Kuhl, K. P.; Cave, E. R.; Abram, D. N.; Jaramillo, T. F. *Phys. Chem. Chem. Phys.* **2014**, *16*, 13814.

(11) Salehi-Khojin, A.; Jhong, H.-R.; Rosen, M. B. A.; Zhu, W.; Ma, S.; Kenis, P. J. A.; Masel, R. I. *J. Phys. Chem. C* **2013**, *117*, 1627.

(12) Yoon, Y.; Hall, A.S.; Surendranath, Y. *Angew. Chem. Int. Edit.* **2016**, 128, 15508.

(13) Lu, Q.; Rosen, J.; Zhou, Y.; Hutchings, G.S.; Kimmel, Y.C.; Chen, J.G.; Jiao, F. *Nat. Commun.* **2014**, *5,* 3242.

(14) Gao, D.; Zhou, H.; Wang, J.; Miao, S.; Yang, F.; Wang, G.; Wang, J.; Bao, X. *J. Am. Chem. Soc.* **2015**, *137*, 4288.

(15) Liu, M.; Pang, Y.; Zhang, B.; De Luna, P.; Voznyy, O.; Xu, J.; Zheng, X.; Dinh, C.T.; Fan, F.; Cao, C.; de Arquer, F.P. *Nature* **2016**, *537*, 382.

(16) Xia, Y.; Xiong, Y.; Lim, B.; Skrabalak, S. E. *Angew. Chem. Int. Edit.* **2009**, *48*, 60.

(17) Zhang, Q.; Li, N.; Goebl, J.; Lu, Z.; Yin, Y. *J. Am. Chem. Soc.* **2011**, *133*, 18931.

(18) Zeng, J.; Xia, X.; Rycenga, M.; Henneghan, P.; Li, Q.; Xia, Y.; *Angew. Chem.Int. Edit.* **2011**, *50*, 244.

(19) Kumar, B.; Asadi, M.; Pisasale, D.; Sinha-Ray, S.; Rosen, B. A.; Haasch, R.; Abiade, J.; Yarin, A. L.; Salehi-Khojin, A. *Nat. Commun.* **2013**, *4,* 3819.

(20) Asadi, M.; Kim, K.; Liu, C.; Addepalli, A. V.; Abbasi, P.; Yasaei, P.; Phillips, P.; Behranginia, A.; Cerrato, J. M.; Haasch, R. *Science* **2016**, *353*, 467.

(21) Hsieh, Y.C.; Senanayake, S.D.; Zhang, Y.; Xu, W.; Polyansky, D.E. *ACS Catal.* **2015**, *5*, 5349.

(22) Zhang, S.; Kang, P.; Ubnoske, S.; Brennaman, M. K.; Song, N.; House, R. L.; Glass, J. T.; Meyer, T. J. *J. Am. Chem. Soc.* **2014**, *136*, 7845.

(23) Rosen, B. A.; Salehi-Khojin, A.; Thorson, M. R.; Zhu, W.; Whipple, D. T.; Kenis, P. J.; Masel, R. I. *Science* **2011**, *334*, 643.

4.4. Supporting information

4.4.1 The specifications of chemicals and gases

Silver nitrate (AgNO$_3$), sodium borohydride (NaBH$_4$), hydrogen peroxide (H$_2$O$_2$, 30%), potassium bicarbonate (> 99.99% trace metal basis) and isopropanol were all purchased from Fisher Scientific Company. Bulk Ag were purchased from Sigma Aldrich.

Nafion perfluorinated ion-exchange resin solution (5 wt.% in mixture of lower aliphatic alcohol & H_2O) was purchased from Sigma-Aldrich. Nafion® N-117 membrane (0.18 mm thick) was purchased from Alfa Aesar; The glassy carbon electrode (GCE 10 mm) was purchased from AIDA Science Technology Company, China. Deionized water was taken from a Millipore Autopure system. All chemicals are of analytical grade and used without further purification. Hydrogen (H_2, 99.999%), argon (Ar, 99.999%), compressed air (extra dry) and carbon dioxide (CO_2, 99.999%) were purchased from Prexair;

4.4.2 Electrochemical surface area measurement.

The electrochemical surface area was performed without removal of oxygen in a flask containing 5.00 mM $Pb(NO_3)_2$, 10 mM HNO_3 and 10 mM KCl. A cyclic voltammetry curve was recorded at 10mV/s between 0 and -0.5 V vs. a Ag/AgCl electrode. The counter electrode was a 30x30 platinum mesh.

The deposited amount of lead from Pb^{2+} concentrations can be estimated from the deposited charge or from the stripped charge. The UPD peak obtained under the experimental conditions shown in Figure S4.1, at Pb^{2+} concentrations of 5 mM and higher, corresponds to a charge of 600 μC/cm^2.[1,2 3,4]
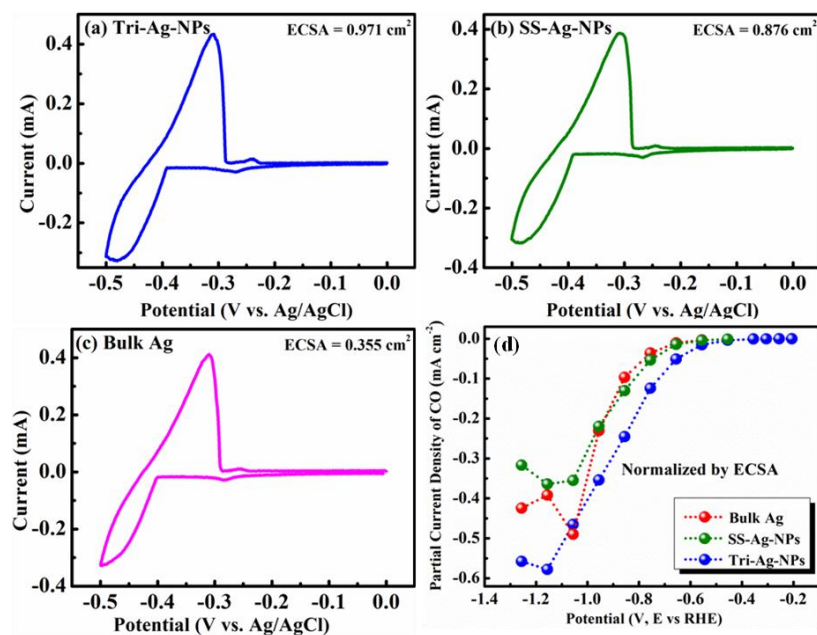
Figure S4.1 Cyclic voltammograms of UPD and bulk deposition of Pb in 5 mM Pb(NO$_3$)$_2$, 10 mM HNO$_3$ and 10 mM KCl solution for (a) Tri-Ag-NPs, (b) SS-Ag-NPs, and (c) Bulk Ag. (d) CO current density normalized by ECSA

4.4.3 DFT Calculations

The Vienna Ab initio Simulation Package (VASP)[5-8] was used to perform density functional theory (DFT) calculations. Electron-ion interactions was treated with the projector-augmented plane-wave (PAW)[9,10] method. Revised Perdew-Burke-Ernzerhof (RPBE) generalized gradient approximation (GGA)functional[11] was employed to model the exchange-correlation interactions. Plane-wave cutoff of 400 eV was set for all the computations in this study and spin-polarization was selected.

Monkhorst-Pack (15,15,15) k point sampling was set for optimization of unit cell of Ag. Based on the optimized unit cell, flat surfaces (100), (110), (111) and stepped surface (211) with 2×2×4 atom slabs and vacuum of 10 Å were built, and cuboctahedra Ag cluster models with 13, 55, 147, 309 atoms were built to simulate SS-Ag-NPs. The Ag cluster with 47 atoms was put in a box of 20 Å ×20 Å ×20 Å and was used for calculation.

During all the structure optimization calculations, top two layers of the surfaces including adsorbate were relaxed, while the bottom two layers were fixed. For Ag cluster, all the silver atoms including adsorbates were relaxed. The same density of k points as that for unit cell were set to sample the Brillouin zone for surface models, while only Gamma point was included for Ag cluster. Maximum atomic force of 0.05eV was chosen as the convergence criterion for structure relaxation. Fermi-level smearing of 0.1eV was set for surface and cluster calculations, while that of 0.01eV was set for gas-phase species. For all the adsorption models, different adsorption sites of molecule on surfaces were tested and the most stable adsorption configuration was selected.

Since purpose of this calculation was to build Gibbs free energy diagram, computational hydrogen electrode (CHE) model[11,12] was used where each electrochemical reaction step is treated as a simultaneous transfer of the proton-electron pair as a function of the applied potential. Underlying reaction mechanisms for CO_2 reduction are,

$$CO_2(g) + * + H^+(aq) + e^- \leftrightarrow COOH^*$$

$$COOH^* + e^- + H^+(aq) \leftrightarrow CO^* + H_2O(l)$$

$$CO^* \leftrightarrow CO(g) + *$$
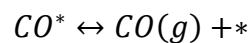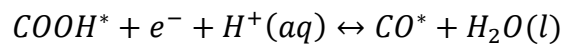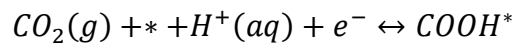
Where * means the corresponding surface where molecules or transition state species adsorbed on. Using initial state where gaseous CO_2 freely above an empty surface as the reference[12], the Gibbs free energy changes of interest can finally be represented as,

$$\Delta G[COOH^*] = G[COOH^*] - (G[*] + G[CO_2] + G[H^+ + e^-])$$

$$\Delta G[CO^*] = G[CO^*] + G[H_2O] - (G[*] + G[CO_2] + 2 \times G[H^+ + e^-])$$

$$\Delta G[CO] = G[CO] + G[H_2O] - (G[CO_2] + 2 \times G[H^+ + e^-])$$

Associated hydrogen evolution reactions and Gibbs free energy changes are shown as below,

$$H^+(aq) + e^- + * \leftrightarrow H^*$$

$$H^* + H^+(aq) + e^- \leftrightarrow H_2 + * \ \text{ or } \ H^* + H^* \leftrightarrow H_2 + 2 *$$
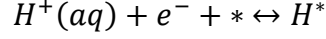
$$\Delta G[H^*] = G[H^*] - (G[*] + G[H^+ + e^-])$$

$$\Delta G[H_2] = G[H_2] - 2 \times G[H^+ + e^-]$$

To build the Gibbs free energy diagram with the computational hydrogen electrode model, Gibbs free energies for relevant species were calculated with the expression:

$$G = E_{DFT} + E_{ZPE} + \int C_p dT - TS$$

Where E_{DFT} is the DFT calculated electronic energy in VASP, E_{ZPE} is the zero-point vibrational energy, $\int C_p dT$ is the enthalpic correction and TS is the entropy contribution. Harmonic approximation where all $3N$ degrees of freedom were treated as frustrated harmonic vibrations was selected to treat the adsorbates with negligible contributions from the Ag surfaces, and PV contributions were neglected. Relevant thermodynamic data was calculated with the standard methods[13] and was transferred into Gibbs free energies at 298.15K. However, for non-adsorbed molecules, standard ideal gas[12,13] methods were employed to get the later three items from temperature, pressure, and calculated vibrational energies with VASP. As suggested[12], eU value of -0.11V was chosen to represent the approximate minimum driving force such that net free energy change from CO_2 to CO is negative. Also, to account for the overestimation of DFT calculation, +0.45eV correction was added to the CO_2

electronic energy[11,13]. All the relevant thermodynamic data used to build Gibbs free energy diagrams is listed in Table S4.1.

Table S4.1 DFT calculated electronic energies and relevant thermodynamic data with suggested fugacities for gaseous species[12].

Species/Adsorbate	Fugacity /Pa	E_{DFT} /eV	E_{ZPE} /eV	$\int C_p dT$ /eV	-TS /eV	ΔG /eV
CO (g)	91192	-15.330	0.130	0.090	-0.596	
CO_2	101325	-23.220	0.304	0.098	-0.663	
H_2	101325	-7.035	0.279	0.090	-0.403	
H_2O	3173	-14.700	0.566	0.104	-0.673	
100_CO		-106.105	0.154	0.102	-0.259	0.246
100_COOH		-117.023	0.573	0.127	-0.292	1.019
100_H		-93.793	0.051	0.042	-0.083	0.398
110_CO		-102.832	0.157	0.100	-0.279	0.161
110_COOH		-113.751	0.575	0.128	-0.322	0.925
110_H		-90.607	0.142	0.015	-0.023	0.368
111_CO		-107.162	0.152	0.104	-0.281	0.326
111_COOH		-117.958	0.571	0.131	-0.368	1.168
111_H		-95.084	0.138	0.008	-0.01	0.393
211_CO		-97.991	0.156	0.097	-0.243	0.209
211_COOH		-108.950	0.573	0.127	-0.376	0.842
211_H		-85.877	0.146	0.013	-0.021	0.279
Ag_CO		-142.276	0.154	0.099	-0.249	0.043
Ag_COOH		-152.924	0.582	0.129	-0.316	1.064
Ag_H		-129.838	0.048	0.045	-0.099	0.297

4.4.4. Supporting Figures
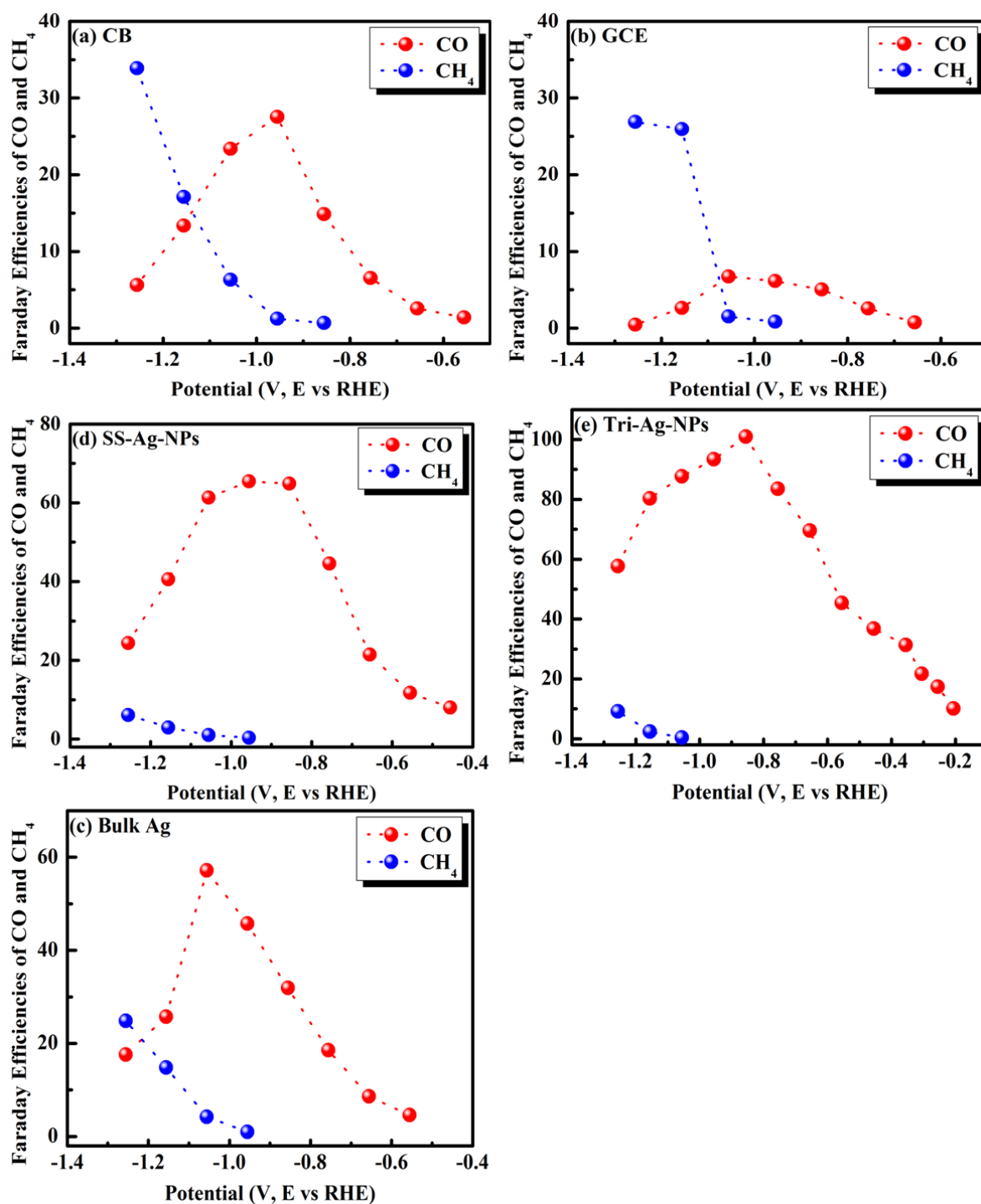
Figure S4.2 Faraday efficiencies (FEs) of different working electrodes (Bulk Ag, SS-Ag-NPs, Tri-Ag-NPs, CB and bare GCE) derived from CO_2 reduction.
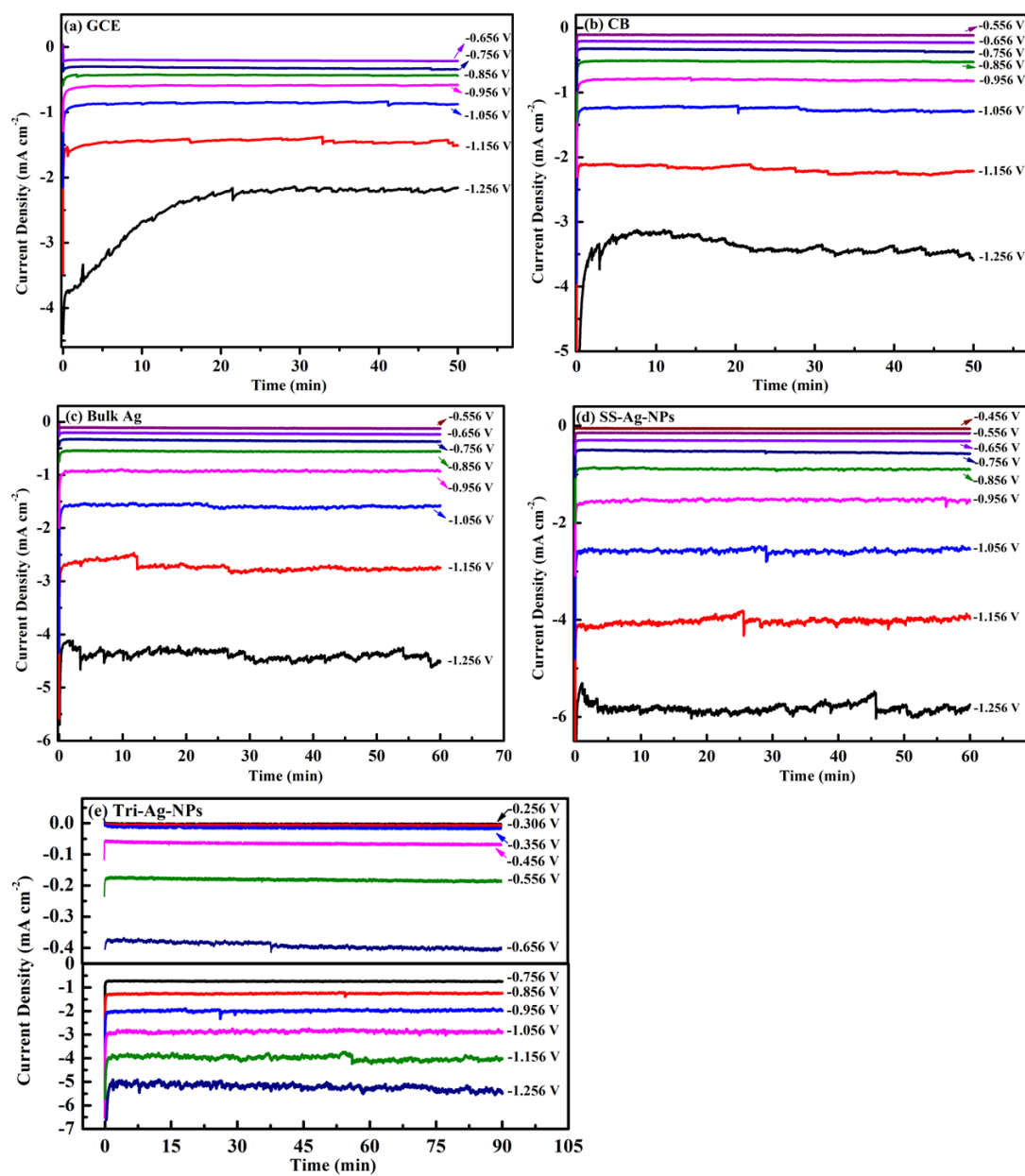
Figure S4.3 Plots of current densities over time of different catalysts (Bulk Ag, SS-Ag-NPs, Tri-Ag-NPs, CB and bare GCE) for CO_2 reduction.
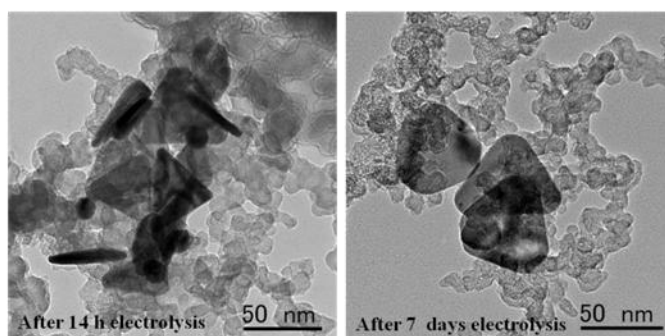
Figure S4.4 TEM images of Tri-Ag-NPs after electrolysis for CO_2RR.
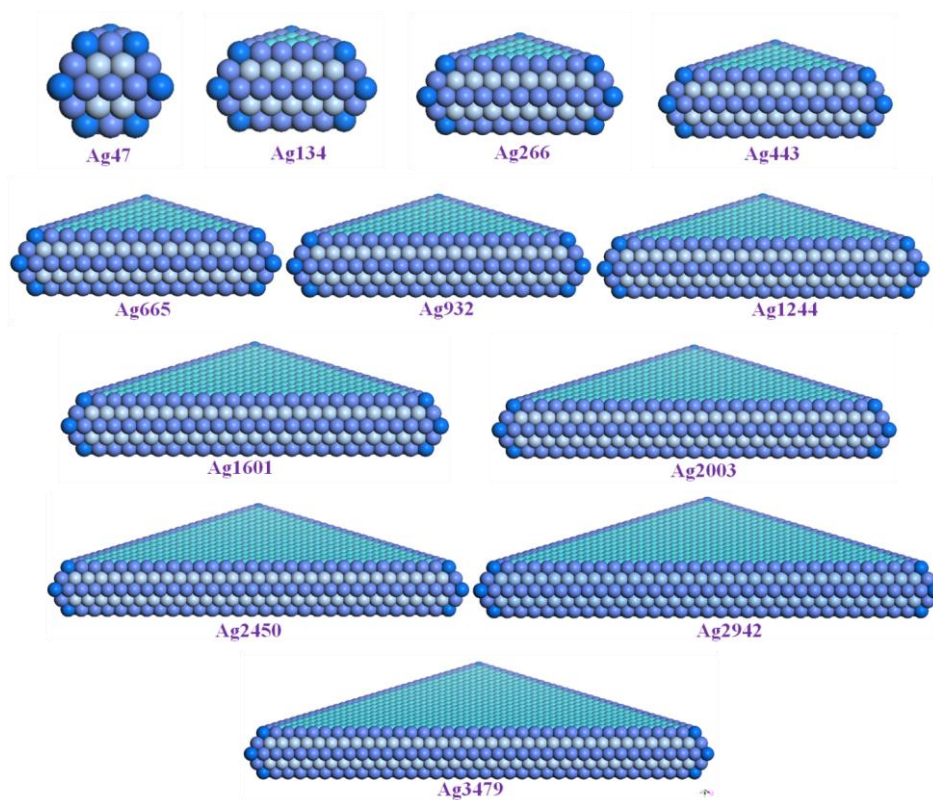
Figure S4.5 Models for Tri-Ag-NPs with different size.
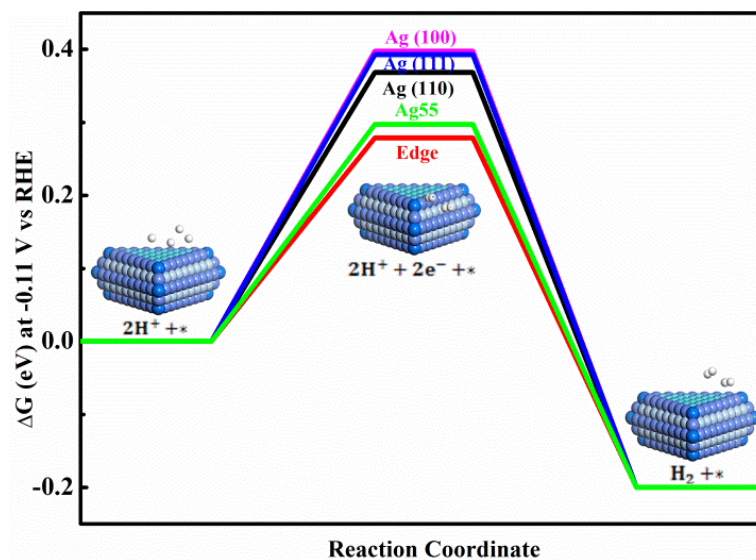
Figure S4.6 Free energy diagrams for H$^+$ to H$_2$ on different Ag sites

4.4.5 References

(1) Lu, Q.; Rosen, J.; Zhou, Y.; Hutchings, G. S.; Kimmel, Y. C.; Chen, J. G.; Jiao, F.

Nat Commun. **2014**, *5*, 3242.

(2) J. Rosen, G. S. Hutchings, Q. Lu, S. Rivera, Y. Zhou, D. G. Vlachos and F. Jiao, *ACS Catal.* **2015**, *5*, 4293.

(3) Yoon, Y.; Hall, A.S.; Surendranath, Y. *Angew. Chem.Int. Edit.* **2016**, *128*, 15508.

(4) Kim, C.; Jeon, H. S.; Eom, T.; Jee, M. S.; Kim, H.; Friend, C. M.; Min, B. K.; Hwang, Y. J. *J. Am. Chem. Soc.* **2015**, *137*, 13844.

(5) Kresse, G.; Hafner, J. *Phys. Rev. B* **1993**, *47*, 558.

(6) Kresse, G.; Hafner, J. *Phys. Rev. B* **1994**, *49*, 14251.

(7) Kresse, G.; Furthmüller, J. *Comput. Mater. Sci.* **1996**, *6*, 15.

(8) Kresse, G.; Furthmüller, J. *Phys. Rev. B* **1996**, *54*, 11169.

(5) Blöchl, P. E. *Phys. Rev. B* **1994**, *50*, 17953.

(9) Kresse, G. *Phys. Rev. B* **1999**, *59*, 1758.

(10) Hammer, B.; Hansen, L.; Nørskov, J. *Phys. Rev. B* **1999**, *59*, 7413.

(11) Durand, W. J.; Peterson, A. A.; Studt, F.; Abild-Pedersen, F.; Nørskov, J. K. *Surf. Sci.* **2011**, *605*, 1354.

 (12) Cramer, C. J. *Essentials of Computational Chemistry Theories and Models*, John Wiley & Sons, England, **2013**.

(13) Trip ovi ć, V.; S úla son, E.; Siahrostami, S.; Nørs ov, J . K.; Rossmeisl, J. *Electrochim. Acta* **2010**, *55*, 7975.

Chapter 5. (Solvent, Structure)-Engineered CO_2 Electroreduction over Transition Metal Sulfide Nanowires

Abstract: Electroreduction of CO_2 incorporates the utilization of CO_2 and the storage of intermittent renewable energy. However, present electrocatalysts usually suffer from sluggish kinetics, high overpotential, low selectivity and energy efficiency. Herein, we successfully prepared Ag_2S nanowires (NWs) using a facile one-step method and utilized it as an electrocatalyst for electrochemical CO_2 reduction reaction (CO_2RR). Both the electrolyte- and structure-dependent catalytic activities in aqueous and ionic liquid (IL) media were investigated.
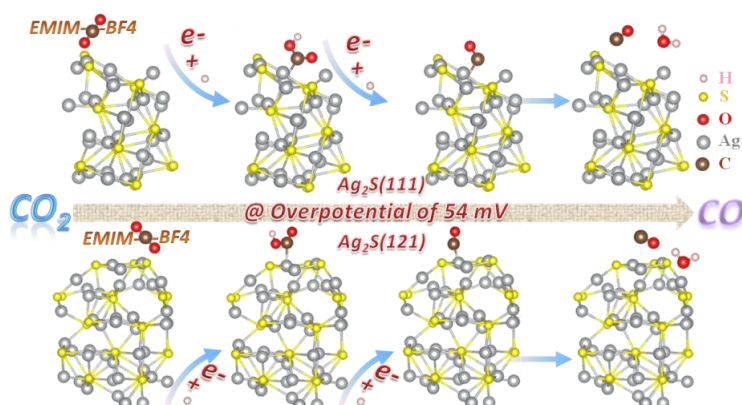
Ag_2S NWs in IL possess a partial current density of 12.37 mA cm^{-2}, ~14- and ~17.5-fold higher than those of Ag_2S NWs and bulk Ag in $KHCO_3$. Moreover, it shows significantly higher selectivity with a value of 92.0% at η of -0.754 V. More importantly, the CO formation begins at an ultralow overpotential (η) of 54 mV. The superior performance originates from not only the presence of [EMIM-CO_2]$^+$ complexes, which increase the solubility of CO_2 and the probability of substantial collision of CO_2 with catalyst, but also the structure-dependent contribution. The partial density of states (PDOS) and work functions reveal that d band center of the

surface Ag atom of Ag$_2$S(121) is closer to the Fermi energy level and have a higher d-electron density than those of Ag(111) and Ag55, which lowers transition state energy for CO$_2$ electroreduction. Besides, density functional theory (DFT) calculations indicate that the CO$_2^{\cdot-}$ formation over Ag$_2$S is energetically favorable on (111) and (121) facets. Instead, the CO desorption on these facets determines the reaction rate. Therefore, we conclude that the excellent performance of Ag$_2$S NWs in IL is synergistically derived from electrolyte-assisted and structure-engineered contributions. This distinguishes Ag$_2$S NWs in IL as an excellent and selective platform for CO$_2$RR.

5.1. Introduction

Growing concerns on global warming and environmental issues arising from the anthropogenic CO$_2$ emissions have prompted the search of environmentally friendly technologies to convert CO$_2$ back to fuels and/or value-added chemicals in a sustainable manner.[1, 2] Electrochemical CO$_2$ reduction reaction (CO$_2$RR) is an advantageous approach to produce valuable products (e.g. CO, CH$_4$, etc.), and has been considered as an attractive strategy to lower global carbon footprint since it artfully incorporates the utilization of anthropogenic CO$_2$ and the storage of intermittent renewable energy (e.g., from wind, solar and tidal).[3, 4] However, CO$_2$RR usually suffers from sluggish kinetics due to the thermodynamic inertness of CO$_2$, the coupled multiple proton and electron transfer processes and the competition with the inevitable hydrogen evolution reaction (HER),[5, 6] particularly in aqueous media. These consequently lead to the poor electrocatalytic activity (partial current density, j), high overpotential (η) and uncontrollable selectivity (Faraday efficiency, FE) towards the aimed product.

In response, various materials, such as metal oxide (e.g., SnO_2[7, 8]), heteroatom-doped carbon materials (e.g., N-doped carbon nanotube[9] and nanofiber[10]) and metal organic complexes (e.g., molecular Cu[6] and Re[4] catalysts), have been identified to be electrochemically active for CO_2RR. Of all the electrocatalysts investigated to date, metals (e.g., Au,[11] Ag[12] and Cu[13]), particularly well-designed metal nanoparticles, have significantly improved the catalytic activity and selectivity for CO_2RR by modifying the metals to nanostructured architecture. Extensive studies experimentally and computationally suggest that certain structural and morphological features, such as specific facets,[14] grain boundaries[15] and edge-to-corner ratios,[12] can selectively contribute to the electrochemical performance for CO_2RR since the binding energies of reaction intermediates on these featured sites are relatively weaker than that of H* originated from the competitive HER. This builds up a platform to accurately understand and correlate the electrocatalytic activities with their physicochemical properties. However, the high η derived from the weak binding interactions between the reaction intermediates and catalyst as well as the low exchange current densities resulted from the slow electron transfer kinetics depends not only on the intrinsic electronic properties and structure of the developed material,[7, 16] but also on the employed solvent. Organic solvents, such as imidazolium-based ionic liquid (IL)[17, 18] and acetonitrile[19, 20] serving as co-electrocatalysts have shown nontrivial effect upon the improvement of catalytic activity. Compared with aqueous media, organic solvents, particularly imidazolium-based IL with high pKa as the proton donors, considerably promote the CO_2RR by lowering the energy barrier for electron transfer, increasing the CO_2 solubility, stabilizing the intermediate species and hampering the competitive HER.[5, 18, 19, 20, 21] The utilization of organic solvent in CO_2RR allows the occurrence of CO_2 conversion to fuels even on some inexpensive earth-abundant

62

metal catalysts (e.g., Bi,[19] Sn and Pb[20]). Despite the remarkable progress in CO_2RR studies, steering the reaction pathway towards desirable product and further lowering η are still a great challenge, which necessitates the exploration of better electrocatalyst with higher selectivity and electrocatalytic activity. Silver sulfide (Ag_2S), as a bulk material, is a narrow-band gap semiconductor with many intriguing properties, including good chemical stability and excellent optical limiting properties as well as an unusual solid ionic conductivity showing both electronic and ionic conductivities at room temperature.[22, 23, 24] However, there have been very limited studies over dichalcogenide (e.g. Ag_2S) in electrochemical fields, particularly in CO_2RR.

This study reports a facile one-step method[25] for the synthesis of Ag_2S nanowires (NWs) and its application for CO_2RR in 1-ethyl-3-methylimidazoliumtetrafluoroborate (EMIM-BF$_4$) to investigate the (solvent, structure)-promoted electrocatalytic performance. It was found that Ag_2S NWs were highly active for CO_2RR towards CO formation in IL at an ultralow η as compared to the one in aqueous media. DFT calculations were utilized to further rationalize the significantly improved catalytic activity and selectivity of Ag_2S NWs towards CO_2RR.

5.2 Results and Discussion

The Ag_2S NWs were synthesized by simply mixing $AgNO_3$ and mercaptoacetic acid solution, followed by shaking the mixture for ~1 min and waiting for another ~20 min at room temperature (see supporting information for detailed procedures). The scanning electron microscopy (SEM) investigation indicates the abundant and highly purified formation of well-aligned Ag_2S NWs with diameters in the range of 150~200 nm and lengths up to several micrometers (Figures 5.1a and b), as also confirmed by the atomic force microscope measurements (AFM, Figure 5.1c). The high-resolution transmission electron microscopy (HRTEM) image (Figure 5.1d) and the electron

energy-loss spectroscopy (EELS) elemental mapping show homogeneous distributions of Ag and S in the Ag_2S NWs, which further verifies the successful preparation of Ag_2S NWs. Moreover, the TEM image (Figure 5.1e) and the corresponding fast Fourier transformation pattern (FFT, Figure 5.1f) demonstrate that the as-obtained Ag_2S NWs are well crystallized, where the lattice fringes with an interplanar distance of ~0.2444 nm are perpendicular to the NW axis. The fringe spacing corresponds to the (121) plane of the monoclinic Ag_2S crystal phase, suggesting that the growth direction of Ag_2S NWs is along [121]. To further determine the structure of the Ag_2S NWs, X-ray diffraction (XRD) was conducted and the Bragg reflections indicate the formation of monoclinic a-phase Ag_2S (JCPDS 14-0072) of the synthesized sample (Figure S5.2). Furthermore, the diffraction peak indexed as (121) is comparably more intense than the others, as confirmed by the previous studies.[23] This demonstrates that the as-prepared Ag_2S NWs are well oriented and well consistent with the analysis of HRTEM. In addition, the as-obtained Ag_2S NWs possess a surface area of ~26.2 m^2 g^{-1} and numerous mesopores with the size of ~1.6 nm (Figure 5.1g), both of which ensure the substantial active sites for CO_2RR.

The electrochemical CO_2RR activities of Ag_2S NWs in both aqueous (0.1 M $KHCO_3$) and IL media were examined on a glassy carbon electrode (GCE, 0.785 cm^2) (Note: the IL medium is an electrolyte containing 50 vol% of $EMIM-BF_4$ and 50 vol% of deionized water, which contributes to the maximum CO_2RR activity[21]). All the electrochemical measurements were carried out in a custom-built two-compartment cell separated by Nafion 117 membrane. The polarization curves of all samples were obtained in a sweeping potential range of $-0.144 \sim -1.156$ V vs. reversible hydrogen

electrode (RHE, all reported potentials are based on RHE) for aqueous media and $-0.136 \sim -1.164$ V for IL media at a scan rate of 50 mV s^{-1}.
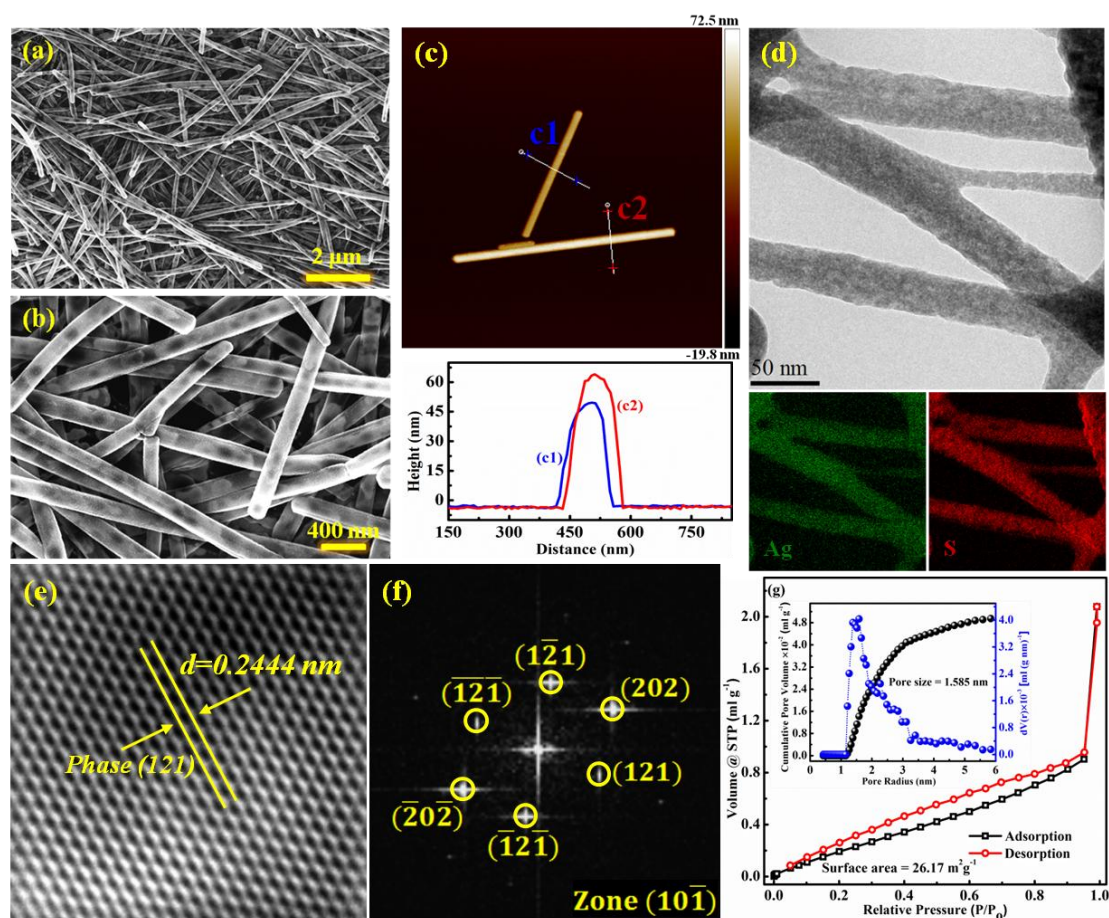
Figure 5.1 (a, b) high-resolution SEM images of as-prepared Ag$_2$S NWs; (c) AFM image and corresponding height profile of Ag$_2$S NWs; (d) High-resolution TEM image and the corresponding electron energy-loss spectroscopy (EELS) mapping showing elemental distributions of Ag and S; (e) TEM image and (f) corresponding fast Fourier transformation; (g) N$_2$ adsorption-desorption isotherm of Ag$_2$S NWs, the inset shows the pore size distribution.

Figure 5.2a shows the linear sweep voltammetry (LSV) results of Ag$_2$S NWs in both KHCO$_3$ and IL media with bulk Ag in KHCO$_3$ as a representative noble-metal catalyst and GCE in KHCO$_3$ as a reference to differentiate its own contribution to CO$_2$RR. The Ag$_2$S NWs in IL show roughly 4-fold higher current densities than that in aqueous media (6.9 mA cm^{-2}, normalized by geometrical surface area), and ~10.5

times higher than the bulk Ag. More importantly, the CO_2RR of Ag_2S NWs in IL occurred at a much more positive onset potential as compared to the Ag_2S NWs in $KHCO_3$ and Bulk Ag (see the inset in Figure 5.2a). The significant increase in the current density for Ag_2S NWs in IL is an indication of a remarkable solvent-promoted cathodic kinetics for CO_2RR since the IL enables the lowering of the energy barrier for the electron transfer and the increase in the CO_2 solubility. However, the LSV results normally are an inconclusive evidence to verify the high catalytic activity of Ag_2S NWs towards CO_2RR since HER and CO_2RR are often simultaneously interconnected. To further distinguish the occurrence of preferred CO_2RR other than HER and the highly solvent-promoted CO_2RR activity of Ag_2S NWs in IL, the catalyst was further investigated under various applied potentials (Figure S5.4). The accurate compositions of the products at each potential were analyzed by a gas chromatography (GC) and a 1H nuclear magnetic resonance (NMR). Figure 5.2b shows the overall FEs of products as a function of potential. It indicates that CO, H_2 and CH_4 are the products with a combined FE of ~100% over the entire potential range and no other products were detected by NMR or GC. As seen, this system is highly selective towards CO_2RR for CO formation at the potentials between -0.564 and -1.164 V, where a maximum FE of ~92% towards CO at a potential of -0.864 V was obtained. However, at lower potentials than -0.564 V, a mixture of CO and H_2 was produced due to the gradually enhanced HER competition. In comparison, Ag_2S NWs, bulk Ag and GCE in $KHCO_3$ were also tested under the same experimental conditions, and the corresponding FEs for CO formation are shown in Figure 5.2c. As a substrate and reference, bare GCE, despite weak current densities, achieved a maximum FE of 6.7% for CO formation at the potential of -1.056 V (Figure 5.2c). Concurrently, Ag_2S NWs and bulk Ag in $KHCO_3$ show much lower FEs in the

applied potential range and reached their maximum values of 41.7% and 57.2% at the potentials of −0.756 and −1.056 V, respectively, as compared to Ag_2S NWs in IL (92.0% at −0.864 V). At the fixed potential of −0.864 V where Ag_2S NWs in IL achieves its maximum FE, Ag_2S NWs in $KHCO_3$ (38.9%) and bulk Ag (31.9%) exhibit a FE of 2.4- and 2.9-fold lower than that of Ag_2S NWs in IL. More importantly, the onset potential of CO formation for Ag_2S NWs in IL is observed at −0.164 V (also confirmed by the LSV result in Figure 5.2a), indicating an η of ~54 mV over the equilibrium potential of −0.11 V. This η corresponds to a FE of ~2.4% for Ag_2S NWs in IL, whereas the Ag_2S NWs and bulk Ag in $KHCO_3$ did not proceed CO_2RR at this η. To achieve an equivalent FE (~2.4%) for the formation of CO, Ag_2S NWs and bulk Ag in $KHCO_3$ require a remarkably higher η of 246 mV (potential of −0.456 V) and 546 mV (potential of −0.656 V), respectively. Figure 5.2d shows the CO partial current densities of GCE, Ag_2S NWs, bulk Ag in $KHCO_3$ and Ag_2S NWs in IL on the basis of steady-state current densities and CO FEs at various potentials. It clearly demonstrates the exclusive catalytic activities of all samples towards CO formation during CO_2RR. Ag_2S NWs in IL possess a partial current density of 12.37 mA cm^{-2}, which is ~14- and ~17.5-fold higher than those of Ag_2S NWs (0.89 mA cm^{-2}) and bulk Ag (0.71 mA cm^{-2}) in $KHCO_3$ at the potential of −1.156 V, further confirming the solvent-promoted effect for CO_2RR to CO.

To gain better kinetic insights into Ag_2S NWs for CO_2RR in both solvents, the CO partial current densities at various overpotentials were measured and a Tafel plot is shown in Figure 5.3a. It has been identified that the single-electron transfer (i.e. $CO_2 + e^- \rightarrow CO_2^-$) determines the reaction rate for CO_2RR since it strides over a higher energy barrier as compared to other elementary steps.[26] Tafel slopes of 197 mV dec^{-1} for bulk Ag and 150 mV dec^{-1} for Ag_2S NWs in $KHCO_3$ were observed,

which in turn confirms the fact that the rate-determining step in aqueous media is dependent on the initial single-electron transfer.
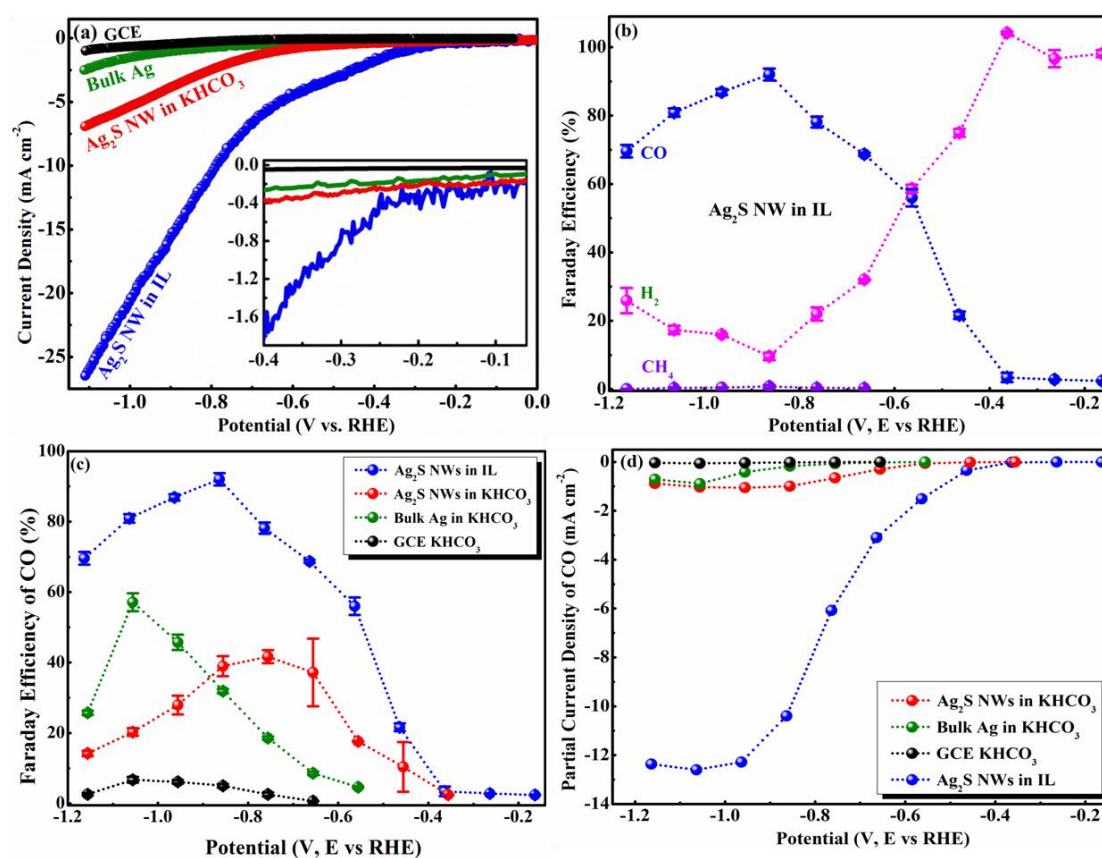
Figure 5.2 (a) Cathodic LSV results scanning at 50 mV s^{-1}; (b) overall FEs (i.e. CO, CH$_4$ and H$_2$) for Ag$_2$S NWs in IL; (c) CO FEs of different catalysts at various potentials and (d) the corresponding CO partial current densities.

However, a Tafel slope of 115 mV dec^{-1} was obtained on Ag$_2$S NWs in IL, slightly less than the theoretical value of 118 mV dec^{-1} expected for the rate-determining single-electron transfer at the electrode,[27] implying that the formation of the adsorbed CO$_2^{\cdot-}$ intermediate is not the rate-determining step. As demonstrated by Monhammad et. al,[21] the strong binding of CO on the transition metal dichalcogenide inhibits desorption of CO in IL, which consequently determines the reaction rate. The exchange current density (i_o) derived from Tafel plot (Figure 5.3b), a reflection of intrinsic rate of electron transfer as well as a measure of the energy required for

CO_2RR to CO, is 2.2×10^{-4} mA cm^{-2} for Ag$_2$S NWs in IL, which is 7- and 3.1-fold higher than that for bulk Ag (3.1×10^{-5} mA cm^{-2}) and Ag$_2$S NWs (6.9×10^{-5} mA cm^{-2}) in KHCO$_3$, respectively. Additionally, as an evaluation parameter of electrocatalyst in renewable energy storage, the maximum values of energy efficiency (EE) of Ag$_2$S NWs in IL, Ag$_2$S NWs and bulk Ag in KHCO$_3$ were calculated and the results are shown in Figure 5.3b. The combination of high FE for the desired product (i.e. CO) and low η of Ag$_2$S NWs in IL jointly contribute to an EE of ~58.5%, considerably higher than Ag$_2$S NWs (~27.9%) and bulk Ag (~33.2%) in KHCO$_3$. These evidences make Ag$_2$S NWs in IL stand out among the state-of-the-art electrocatalysts and support the claim that it is a promising system towards CO_2RR for CO formation. Moreover, Ag$_2$S NWs in IL exhibits significantly higher CO mass activities (Figure 5.3c), e.g. 2.37 to 19.28 A g^{-1}, than that of Ag$_2$S NWs (0.09 to 1.65 A g^{-1}) and bulk Ag (0.01 to 0.66 A g^{-1}) in KHCO$_3$ at the selected potential range of -0.56 to -0.96 V. To evaluate the stability of Ag$_2$S NW in IL, potentiostatic measurement at a fixed potential of -0.864 V was carried out over an extended period of 20 h (Figure 5.3d). The current density fluctuated slightly throughout the durability test, and the Ag$_2$S NWs in IL showed no morphological change after the stability test (Figures 5.1a and S5.5), suggesting that the Ag$_2$S NWs in IL are stable for CO_2RR. The X-ray photoelectron spectroscopy (XPS) results of this catalyst before and after electrolysis further verified its superior long-term stability (Figure S5.6 and Table S5.2).

Understanding the reasons credited for the excellent CO_2RR performance (e.g. ultralow onset potential, high CO selectivity at a lowered η) of Ag$_2$S NWs in IL is of prime significance in discovering mechanism and designing desirable materials. As mentioned, the presence of EMIM+ cations in CO_2-saturated media has demonstrated

formation of [EMIM-CO$_2$]$^+$ complexes,[28] which could physically adsorb on the negatively charged catalyst and subsequently increase the solubility of CO$_2$ and the probability of substantial close collision of CO$_2$ with catalyst.[18, 28]
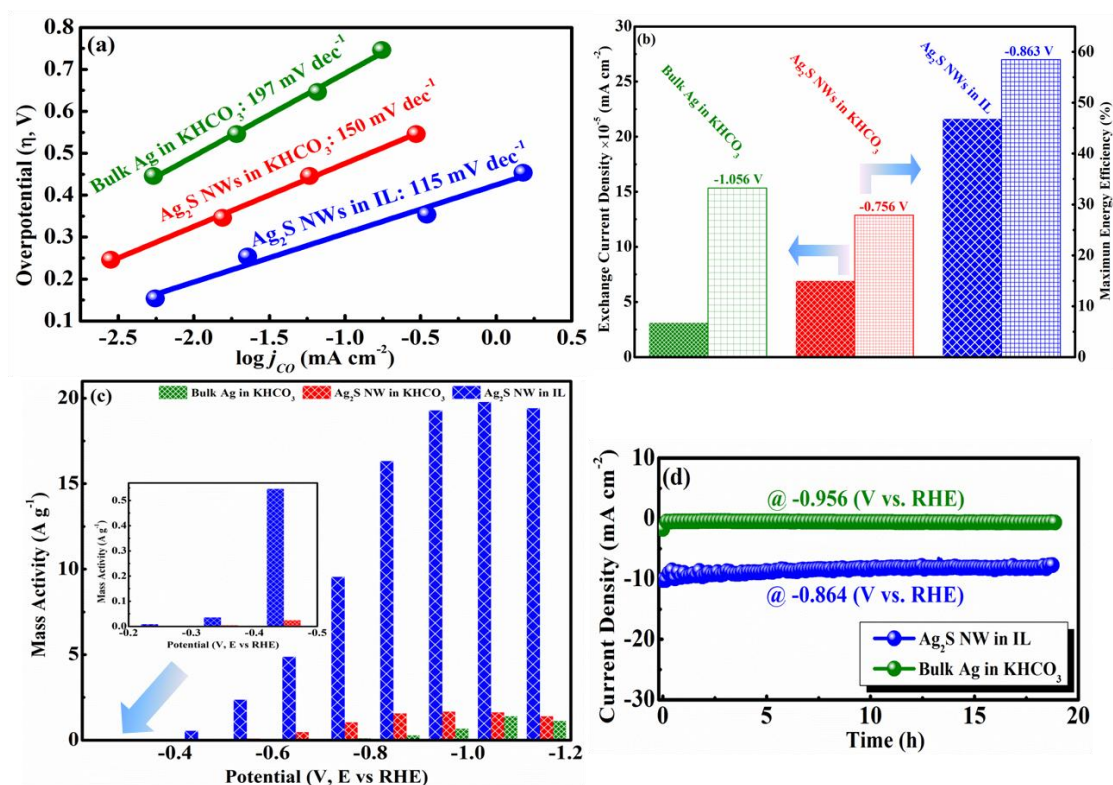
Figure 5.3 (a) Tafel plots and (b) exchange current densities and maximum EEs of all catalysts; (c) CO mass activity as a function of potential; (d) long-term stabilities of Ag$_2$S NWs in IL and bulk Ag in KHCO$_3$.

Moreover, the [EMIM-CO$_2$]$^+$ complexes significantly lower the energy barrier of electron-transfer process, which consequently reduces the η towards CO$_2$RR.[29] However, we conjecture that the significantly enhanced CO$_2$RR performance originates not only from the solvent-assisted contribution, but also the specific structure-engineered promotion. To confirm this, construction of Gibbs free energy diagram through DFT calculations were performed based on the computational hydrogen electrode model.[14] Figures 5.4a and S5.7 show the calculated Gibbs free energy (ΔG) diagram for CO$_2$RR and HER on the facets of (111) and (121) for Ag$_2$S,

versus (111) and 55-cluster for Ag, respectively. It is confirmed that the single-electron transfer (i. e. $CO_2 + e^- \rightarrow CO_2^{\cdot-}$) is the rate-determining step and considerably endergonic for Ag(111) and Ag55. This consequently explains the high η of bulk Ag, as confirmed by the analysis of i_o in Figure 5.3b and the previous studies.[12] However, the $CO_2^{\cdot-}$ formation over Ag$_2$S NWs is energetically favored as compared to bulk Ag due to the strong binding on the facets of (111) and (121). Instead, the strong binding of CO on these facets restrains desorption of CO and determines the reaction rate (see Figure 5.4b), as demonstrated by Asadi et al.[21] that the metal edges of transition metal possibly show high CO coverage. Concurrently, transition metal-terminated edges of dichalcogenide are demonstrated to have a higher d-electron density and a similarly metallic property since d band center of the surface metal atoms are closer to the Fermi energy level relative to those of bulk transition metal.[28] Therefore, we also calculated the partial density of states (PDOS) of the surface Ag atoms of bulk Ag and Ag$_2$S, as shown in Figures 5.4c and d. The results verify that d band center of the surface Ag atom of Ag$_2$S(121) is closer to the Fermi energy level and shows a higher d-electron density than those of Ag(111) and Ag55. This lowers transition state energy for CO$_2$RR over Ag$_2$S NWs and subsequently enhances the electrocatalytic activity. In addition, the work functions of bulk Ag and Ag$_2$S NWs were experimentally and computationally calculated by ultraviolet photoelectron spectroscopy (UPS) (Figure S5.8) and DFT simulations (Figure 5.4e), respectively. Our results indicate a comparable work function of Ag$_2$S NWs relative to that of bulk Ag. Both the UPS and DFT simulations as well as the i_o confirm the superior electronic properties of Ag$_2$S NWs in comparison to bulk Ag, which contribute to a faster electron transfer and consequently a higher electrocatalytic activity. Therefore,

we conclude that the exceptional performance of Ag₂S NWs in IL is attributed to a synergistic effect of solvent-assisted and structure-engineered contributions.
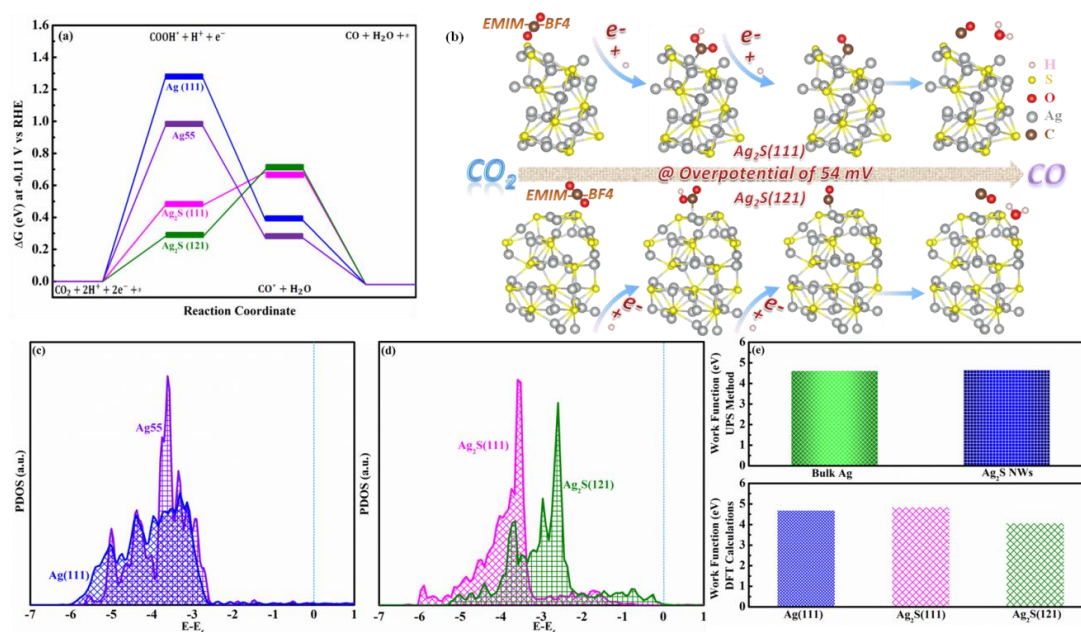
Figure 5.4 (a) Free energy diagrams for CO₂RR on different facets of Ag [i.e. (111) and 55-cluster] and Ag₂S [i.e. (111) and (121)]; (b) Proposed mechanism for (electrolyte, structure)-engineered CO₂RR on Ag₂S NWs; calculated PDOS of the surface Ag atom of (c) bulk Ag [i.e. Ag55 and Ag(111)] and (d) Ag₂S NWs [i.e. Ag₂S(111) and Ag₂S(121)]; (e) work functions of bulk Ag and Ag₂S NWs based on DFT and experimental calculations.

5.3 Conclusion

In summary, Ag₂S NWs were successfully synthesized using a facile one-step method and utilized to investigate both electrolyte- and structure-dependent electroreduction of CO_2 to CO in aqueous and IL media. Ag₂S NWs in IL possess a partial current density of 12.37 mA cm⁻², ~14- and ~17.5-fold higher than those of Ag₂S NWs (0.89 mA cm⁻²) and bulk Ag (0.71 mA cm⁻²) in KHCO₃, respectively. Moreover, it shows significantly higher selectivity with a value of 92.0% at η of −0.754 V as compared to Ag₂S NWs (41.7%) and bulk Ag (57.2%) in KHCO₃ at η of −0.646 V and −0.946 V, respectively. More importantly, the formation of CO begins at an ultralow η of 54 mV,

confirming the superior catalytic activity of Ag_2S NWs in IL. In addition, only slight degradation was observed over 20 h, further verifying the excellence of Ag_2S NWs as an electrocatalyst for CO_2RR in IL. The superior electrochemical performance originates from the presence of $[EMIM-CO_2]^+$ complexes, which not only physically adsorb on the negatively charged catalyst and subsequently increase the solubility of CO_2 and the probability of substantial close collision of CO_2 with catalyst, but also significantly lower the energy barrier of electron-transfer process, which consequently reduce the η towards CO_2RR. Besides, DFT calculations indicate that the CO_2^- formation over Ag_2S NWs is energetically favored on the facets of (111) and (121). Instead, the strong binding of CO on these facets restrains desorption of CO and determines the reaction rate, as confirmed by the results of UPS and PDOS. Therefore, the exceptional performance of Ag_2S NWs in IL is attributed to a synergistic effect of solvent-assisted and structure-engineered contributions. These findings can serve as progressive steps in advancing our understanding on CO_2RR mechanism and exploring new electrocatalysts for efficient CO_2RR.

5.4 References

(1) Faunce, T.; Styring, S.; Wasielewski, M. R.; Brudvig, G. W.; Rutherford, A. W.; Messinger, J.; Lee, A. F.; Hill, C. L.; Fontecave, M.; MacFarlane, D. R. *Energ. Environ. Sci.* **2013**, *6*, 1074.

(2) Wang, Z.-L.; Li, C.; Yamauchi, Y. *Nano Today* **2016**, *11*, 373.

(3) Costentin, C.; Robert, M.; Sav ant, J.-M. *Accounts Chem. Res.* **2015**, *48*, 2996.

(4) Oh, S.; Gallagher, J. R.; Miller, J. T.; Surendranath, Y. *J. Am. Chem. Soc.* **2016**, *138*, 1820.

(5) Zhang, Z.; Chi, M.; Veith, G. M.; Zhang, P.; Lutterman, D. A.; Rosenthal, J.; Overbury, S. H.; Dai, S.; Zhu, H. *ACS Catal.* **2016**, *6*, 6255.

(6) Weng, Z.; Jiang, J.; Wu, Y.; Wu, Z.; Guo, X.; Materna, K. L.; Liu, W.; Batista, V. S.; Brudvig, G. W.; Wang, H. *J. Am. Chem. Soc.* **2016**, *138*, 8076.

(7) Li, F.; Chen, L.; Knowles, G. P.; MacFarlane, D. R.; Zhang, J. *Angew. Chem. Int. Edit.* **2017**, *56*, 505.

(8) Kumar, B.; Atla, V.; Brian, J. P.; Kumari, S.; Nguyen, T. Q.; Sunkara, M.; Spurgeon, J. M. *Angew. Chem. Int. Edit.* **2017**, *56*, 3645.

(9) Wu, J.; Yadav, R. M.; Liu, M.; Sharma, P. P.; Tiwary, C. S.; Ma, L.; Zou, X.; Zhou, X.-D.; Yakobson, B. I.; Lou, J. *ACS Nano* **2015**, *9*, 5364.

(10) Kumar, B.; Asadi, M.; Pisasale, D.; Sinha-Ray, S.; Rosen, B. A.; Haasch, R.; Abiade, J.; Yarin, A. L.; Salehi-Khojin, A. *Nat. Commun.* **2013**, *4*.

(11) Zhu, W.; Michalsky, R.; Metin, O.; Lv, H.; Guo, S.; Wright, C. J.; Sun, X.; Peterson, A. A.; Sun, S. *J. Am. Chem. Soc.* **2013**, *135*, 16833.

(12) Liu, S.; Tao, H.; Zeng, L.; Liu, Q.; Xu, Z.; Liu, Q.; Luo, J. L. *J. Am. Chem. Soc.* **2017**, *139*, 2160.

(13) Ma, M.; Djanashvili, K.; Smith, W. A. *Angew. Chem. Int. Edit.* **2016**, *55*, 6680.

(14) Back, S.; Yeom, M. S.; Jung, Y. *ACS Catal.* **2015**, *5*, 5089.

(15) Feng, X.; Jiang, K.; Fan, S.; Kanan, M. W. *J. Am. Chem. Soc.* **2015**, *137*, 4606.

(16) Li, Y.; Cui, F.; Ross, M. B.; Kim, D.; Sun, Y.; Yang, P. *Nano Lett.* **2017**, *17*, 1312.

(17) Liu, M.; Pang, Y.; Zhang, B.; De Luna, P.; Voznyy, O.; Xu, J.; Zheng, X.; Dinh, C. T.; Fan, F.; Cao, C.; de Arquer, F. P.; Safaei, T. S.; Mepham, A.; Klinkova, A.; Kumacheva, E.; Filleter, T.; Sinton, D.; Kelley, S. O.; Sargent, E. H. *Nature* **2016**, *537*, 382.

(18) Rosen, B. A.; Salehi-Khojin, A.; Thorson, M. R.; Zhu, W.; Whipple, D. T.; Kenis, P. J.; Masel, R. I. *Science* **2011**, *334*, 643.

(19) DiMeglio, J. L.; Rosenthal, J. *J. Am. Chem. Soc.* **2013**, *135*, 8798.

(20) Medina-Ramos, J.; Pupillo, R. C.; Keane, T. P.; DiMeglio, J. L.; Rosenthal, J. *J. Am. Chem. Soc.* **2015**, *137*, 5021.

(21) Asadi, M.; Kim, K.; Liu, C.; Addepalli, A. V.; Abbasi, P.; Yasaei, P.; Phillips, P.; Behranginia, A.; Cerrato, J. M.; Haasch, R. *Science* **2016**, *353*, 467.

(22) Sahu, A.; Qi, L.; Kang, M. S.; Deng, D.; Norris, D. J. *J. Am. Chem. Soc.* **2011**, *133*, 6509.

(23) Wang, D.; Hao, C.; Zheng, W.; Peng, Q.; Wang, T.; Liao, Z.; Yu, D.; Li, Y. *Adv. Mater.* **2008**, *20*, 2628.

(24) Terabe, K.; Hasegawa, T.; Nakayama, T.; Aono, M. *Nature* **2005**, *433*, 47.

(25) Lee, U.; Ham, S.; Han, C.; Jeon, Y. J.; Myung, N.; Rajeshwar, K. *Mater. Chem. Phys.* **2010**, *121*, 549.

(26) Chen, Y.; Li, C. W.; Kanan, M. W. *J. Am. Chem. Soc.* **2012**, *134*, 19969-19972.

(27) Zhang, S.; Kang, P.; Ubnoske, S.; Brennaman, M. K.; Song, N.; House, R. L.; Glass, J. T.; Meyer, T. J. *J. Am. Chem. Soc.* **2014**, *136*, 7845.

(28) Asadi, M.; Kumar, B.; Behranginia, A.; Rosen, B. A.; Baskin, A.; Repnin, N.; Pisasale, D.; Phillips, P.; Zhu, W.; Haasch, R.; Klie, R. F.; Kral, P.; Abiade, J.; Salehi-Khojin, A. *Nat. Commun.* **2014**, *5*, 4470.

(29) Rosen, B. A.; Haan, J. L.; Mukherjee, P.; Braunschweig, B.; Zhu, W.; Salehi-Khojin, A.; Dlott, D. D.; Masel, R. I. *J. Phys. Chem. C* **2012**, *116*, 15307.

5.5 Supporting information

5.5.1 The specifications of chemicals and gases

Silver nitrate ($AgNO_3$), potassium bicarbonate (> 99.99% trace metal basis) and isopropanol were all purchased from Fisher Scientific Company. Mercaptoacetic acid ($C_2H_4O_2S$) was purchased from Alfa Aesar. 1-ethyl-3-

methylimidazoliumtetrafluoroborate (EMIM-BF$_4$, >98%, HPLC) and bulk Ag (25 μm) were purchased from Sigma Aldrich.

Nafion perfluorinated ion-exchange resin solution (5 wt.% in mixture of lower aliphatic alcohol & H$_2$O) was purchased from Sigma-Aldrich. Nafion® N-117 membrane (0.18 mm thick) was purchased from Alfa Aesar; The glassy carbon electrode (GCE 10 mm) was purchased from AIDA Science Technology Company, China. Deionized water was taken from a Millipore Autopure system. All chemicals are of analytical grade and used without further purification. Hydrogen (H$_2$, 99.99%), argon (Ar, 99.99%), compressed air (extra dry) and carbon dioxide (CO$_2$, 99.99%) were purchased from Prexair.

5.5.2 One-step facile synthesis of Ag$_2$S nanowires (Ag$_2$S NWs).

For the synthesis of Ag$_2$S NWs, 300 mL of MAA (5mM) was added to the 150 mL of 5 mM AgNO$_3$ solution. After shaking the mixture for 1 min and waiting another 20 min at room temperature, the mixture was centrifuged and washed three times with deionized water to remove residual acid. The products could be transformed to crystalline Ag$_2$S NWs without changing dimensions by a thermal anneal at ~300 $^{\circ}$C.

5.5.3 Electrochemical measurements

Linear sweep voltammetry (LSV): 20 mg of powders (10 mg of catalyst and 10 mg of carbon black) were dispersed in 1 ml mixed solvent containing 700 μl isopropanol, 100 μl of 5 wt% Nafion solution and 200 μl deionized water to form a homogeneous ink after at least 3 hours ultrasonic. Then 50.0 μl of the catalyst ink was loaded onto a glassy carbon electrode (GCE) of 10 mm in diameter (loading catalyst ~ 0.637 mg cm^{-2}), the GCE were mechanically polished with alumina paste before loading the catalyst suspension, then the GCE was dried overnight in air at room temperature

before testing. The LSV curves were conducted with a Solartron 1255 frequency response analyzer and a Solartron 1286 electrochemical interface instrument in a home-made electrochemical cell using saturated calomel electrode as the reference electrode, a platinum gauze as the counter electrode and the catalyst coated GCE as the working electrode. Electrolyte was saturated by bubbling CO_2 prior to the start of each experiment at a flow rate of 20 ml min^{-1} for 2 h until a saturated CO_2 condition was reached to ensure that all the oxygen was removed from the electrolyte [note: the IL media is an electrolyte containing 50% of EMIM-BF$_4$ and 50% of deionized water in volume ratio (pH of CO_2-saturated IL media is 6.68), where it contributes to the maximum CO_2RR activity]. The flow of CO_2 was maintained over the solution during the recording of LSV curves in order to ensure its continued CO_2 saturation. The working electrode was repeated at least 20 times before data were recorded at a scan rate of 50 mVs^{-1}. All potentials are reported with respect to the reversible hydrogen electrode (RHE). All measurements are independently conducted where a freshly deposited ink was used.

$$\text{Potential (V vs. RHE)} = \text{Applied potential (V vs. SCE)} + 0.241\ V + 0.0592 \times pH$$

Product analysis of the three-electrode setup for CO_2 reduction: 50 μl of the catalyst ink was loaded onto the GCE (0.785 cm^2) (loading ~0.637 mg cm^{-2}) and a fresh catalyst was employed for each potential. The gas products from the cathode compartment were analyzed using a Hewlett-Packard model Agilent 6890N gas chromatograph (GC) equipped with a packed bed column (HaySep D) operated at 80 °C with a thermal conductivity detector and a flame ionization detector. Argon (Air liquid 5.0) was employed as carrier gas with a flow rate of 30 ml min^{-1}. The gaseous products H_2, CH_4 and CO were separated in a molecular sieve column

(Alltech, part no. 57732, 1.65 m × 1/8 in., molecular sieve 13X, 60/80 mesh) and hydrocarbons and CO_2 in a HaySep column (Alltech, part no. 14487, 3.5 m × 1/8 in., HaySep D, 80/100 mesh). NMR was used to quantify the concentration of liquid-phase products.

5.5.4 Density Functional Theory (DFT) Calculations

Periodic density functional theory (DFT) calculations using Vienna Ab-initio Simulation Package (VASP)[1–4] were carried out to study the carbon dioxide reduction reactions on representative surfaces of Ag_2S (111) and Ag_2S (121). Density of valence electrons involved in the simulation system were described with plane wave basis set. All through the simulation, projected augmented wave (PAW) method developed by Blöchl[5,6] was selected as the pseudopotential to describe the ion-electron interaction. The revised Perdew-Burke-Ernzerhof (RPBE)[7] within the generalized gradient approximation (GGA) as implemented in VASP was used to calculate the exchange and correlation energies. During the calculation, plane wave energy cutoff was set at 450eV and spin polarization was switched on. Structures of interest were subjected to geometry optimization until force on each atom is smaller than 0.05eV/Å. Gaussian smearing method with a small width of 0.02eV was employed and the final energy values were extrapolated to 0K.

Experimental lattice parameters (Space group: P21/n; Cell: a=4.229Å, b=6.931Å, c= .862Å, α= 0.0°, β= .61°, γ= 0.0°) were adopted to build the unit cell of Ag_2S which is one of the commonly used methods[8]. Based on the unit cell, surface models with Miller Indies of (111) and (121) were cleaved. Thickness requirement for subsequent work function calculation was considered through adjusting thickness of the slab. Also, to minimize the surface interaction originating from the periodicity, vacuum layer with thickness of 15Å was added on top of the slab and the surface

models were then optimized. The total thicknesses along z direction was 25.2Å for Ag$_2$S(111) surface unit cell and 27.05Å for Ag$_2$S(121) surface unit cell. During the geometry optimization, the bottom layers with thickness of 4.74Å for Ag$_2$S(111) and 5.56Å for Ag$_2$S(121) which were about half thickness of the slab[9] were fixed and kept constant, while remaining atoms were allowed to relax. Adsorbed molecules and intermediate were firstly optimized in box of 15Å×15Å×15Å with k-point grid of 1×1×1 within the Monkhorst-Pack division scheme[10] for sampling of the Brillouin zone, and were then transferred to the surfaces studied. The k-point grid of 2×2×1 was used for both of the Ag$_2$S(111) and Ag$_2$S(121) surface unit cell. Different adsorption configurations of the adsorbates on Ag$_2$S(111) and Ag$_2$S(121) surfaces were tested and among which the most stable ones characterized with the lowest energy were selected.
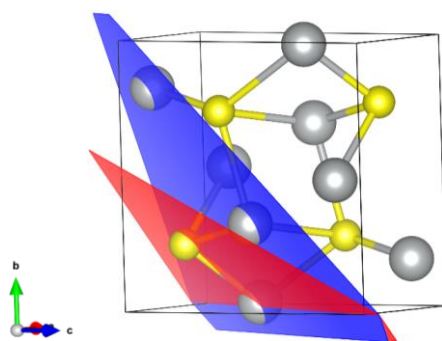
Figure S5.1 Ag$_2$S(111) (blue) and Ag$_2$S(121)(red) illustrated in unit cell of Ag$_2$S

To further explore the underlying catalytic mechanism related to carbon dioxide reduction reaction, an investigation of electronic structure of the optimized Ag$_2$S(111) and Ag$_2$S(121) surfaces has been conducted[11]. Partial density of states (PDOS) of d orbital of the adsorption site Ag on the surface was extracted and plotted. Work function was evaluated through comparing the values of Fermi energy and that of the xy-averaged electrostatic potential in the middle of the vacuum along z direction.

Relevant structure models listed in this paper were built and visualized with package of Visualization for Electronics and Structural Analysis (VESTA) Ver. 3.4.0[12].

To build Gibbs free energy diagram, computational hydrogen electrode (CHE) model[7,13,14] where each electrochemical reaction step is treated as a simultaneous transfer of the proton-electron pair as a function of the applied potential. Gibbs free energies at 298.15K for relevant species were calculated with the expression:

$$G = E_{DFT} + E_{ZPE} + \int C_p dT - TS$$

Where E_{DFT} is the DFT calculated electronic energy in VASP, E_{ZPE} is the zero-point vibrational energies, T is temperature (298.15K), $\int CpdT$ is the enthalpic correction and TS is the entropy contribution which are calculated from vibrational analysis and standard statistical mechanics equations. More details about the method to build Gibbs free energy diagram can be referred to the paper published before[15] and relevant data of Ag nanoparticle and Ag(111) is also referred from that paper.

Table S5.1 DFT calculated energies and relevant thermodynamic data.

Species/adsorbate	E_{ZPE} /eV	$\int C_p dT$ /eV	-TS /eV	$G-E_{elec}$ /eV
111_CO	0.171	0.092	-0.241	0.021
111_COOH	0.590	0.117	-0.292	0.415
111_H	0.139	0.024	-0.038	0.124
121_CO	0.171	0.092	-0.241	0.021
121_COOH	0.597	0.118	-0.279	0.436
121_H	0.167	0.005	-0.006	0.165

5.5.5 Supporting Figures
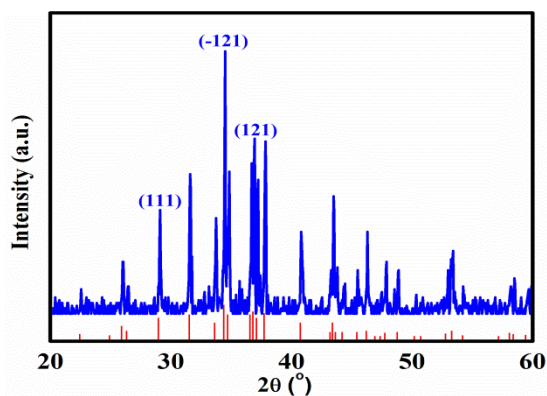
Figure S5.2 XRD pattern of as-prepared Ag_2S NWs.
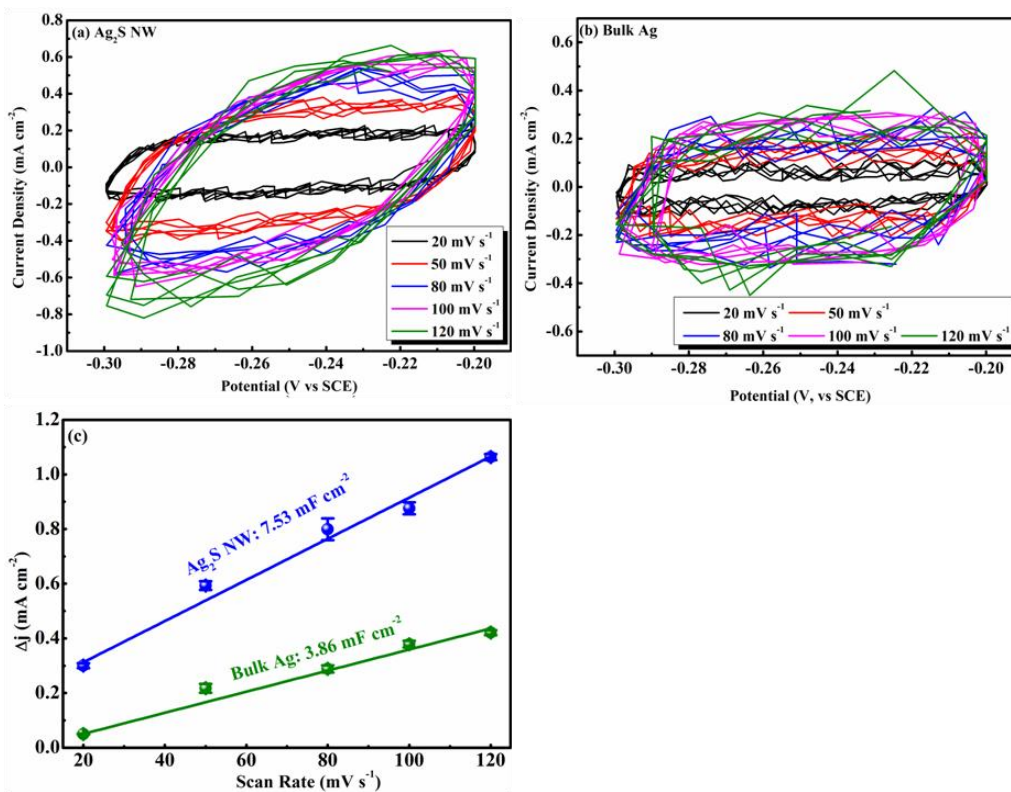
Figure S5.3 Cyclic voltammetry (CV) curves of (a) Ag_2S NWs and (b) bulk Ag at different scan rates. The experiments were performed at 0.1 M $KHCO_3$ by sweeping potential between -0.2 to -0.3 V vs SCE (non-faradic region). (c) Current density of CV experiments at potential -0.25 V vs SCE as a function of scan rates. The slope of this line shows double layer capacitor for each catalyst.
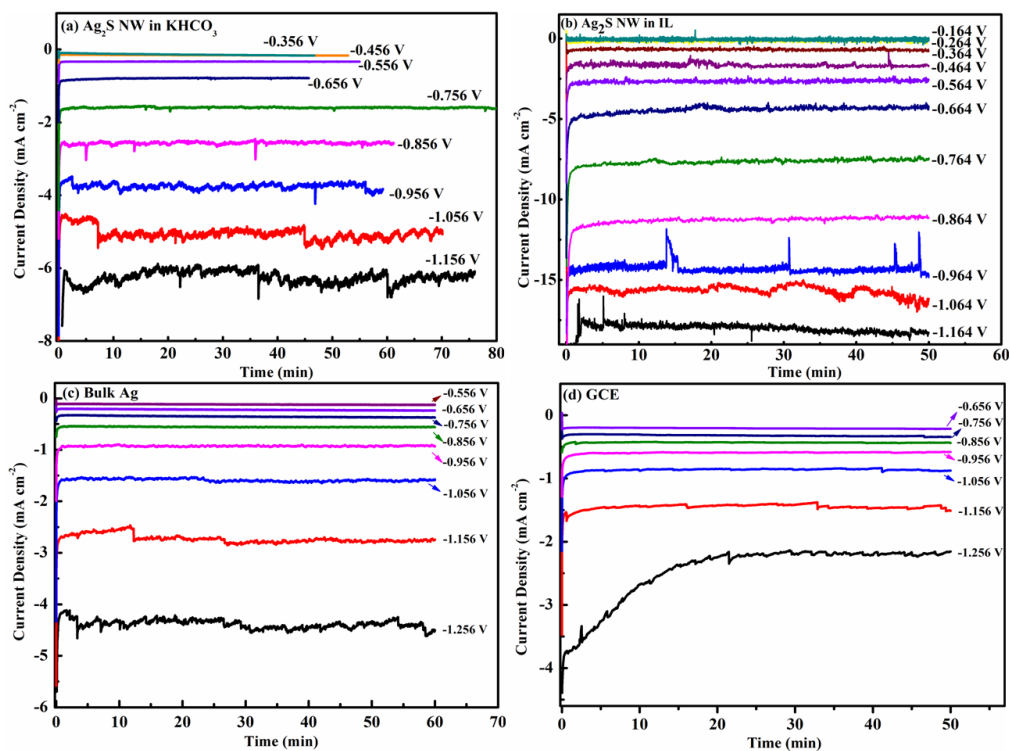
Figure S5.4 Plots of current densities over time of different catalysts (Ag$_2$S NWs in IL, Ag$_2$S NWs, bulk Ag and bare GCE in KHCO$_3$) for CO$_2$ electroreduction.
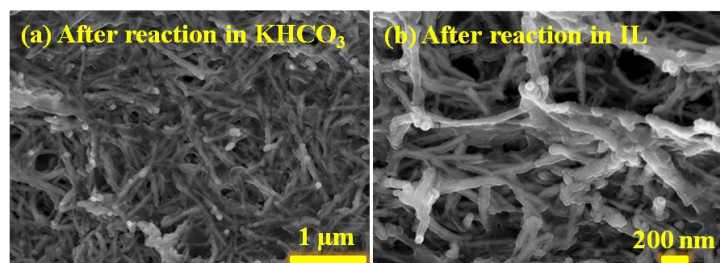
Figure S5.5 SEM images of Ag$_2$S NWs after electroreduction in (a) KHCO$_3$ and (b) IL for CO$_2$RR.
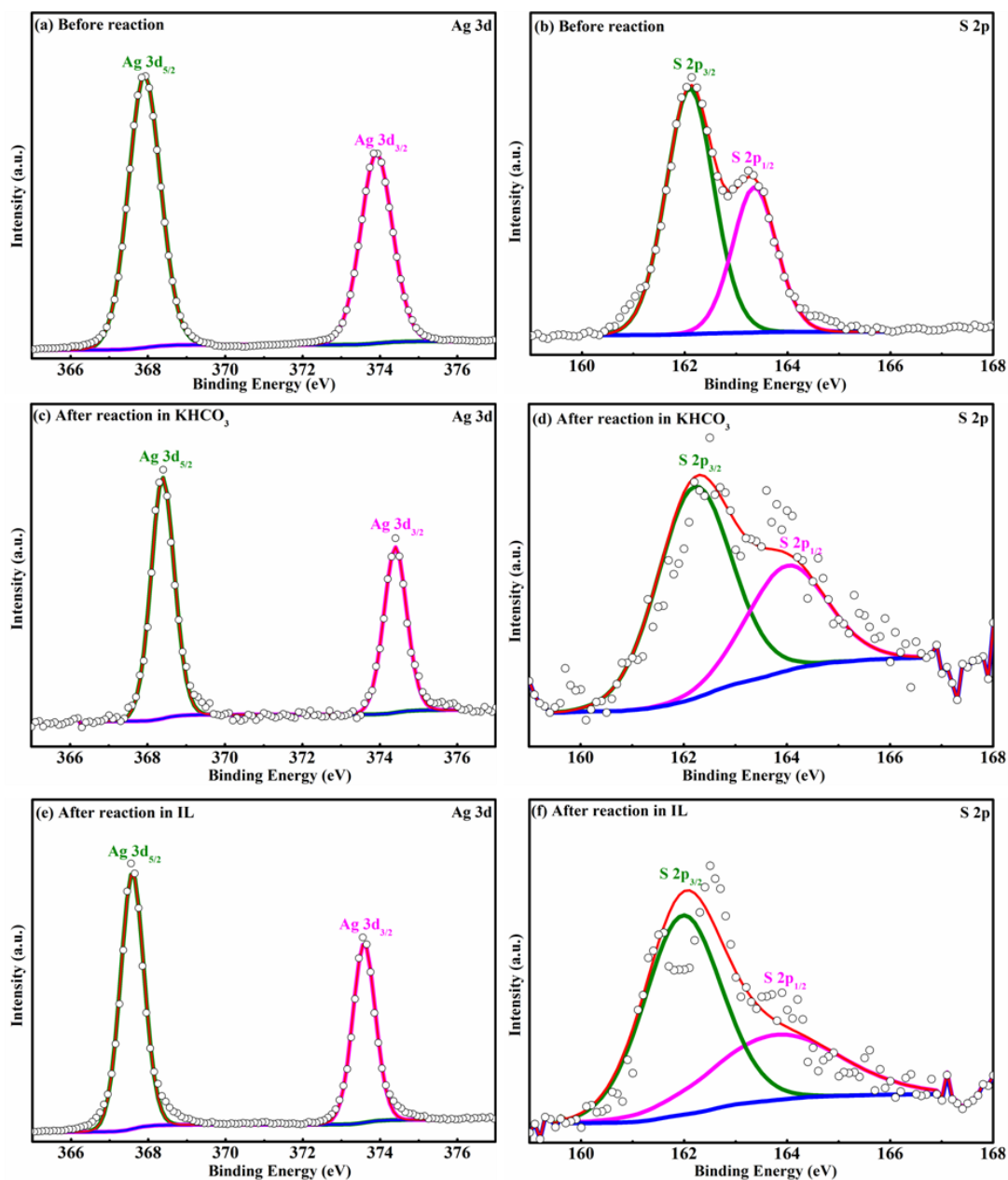
Figure S5.6 X-ray photoelectron spectroscopy (XPS) spectra of Ag_2S NWs (a) before and after electroreduction in (b) $KHCO_3$ and (c) IL. The spectra (c and e) show standard Ag $3d_{3/2}$ and $3d_{5/2}$ peaks, match well with the presence of Ag3d (a) in Ag_2S NWs before electroreduction. The spectra (d and f) show standard $S2p_{1/2}$ and $S2p_{3/2}$ peaks, consistent with the presence of S2p (b) in Ag_2S NWs before electroreduction.

Table S5.2 Quantitative analysis of Ag (i.e. $3d_{5/2}$ and $3d_{3/2}$) and S (i.e. $2p_{3/2}$ and $2p_{1/2}$) of Ag$_2$S NWs before reduction, after reduction in KHCO$_3$ and after reduction in IL.

Ag$_2$S NWs		Before reduction (%)	After reduction in KHCO$_3$ (%)	After reduction in IL (%)
Ag	$3d_{5/2}$	59.065	59.714	59.676
	$3d_{3/2}$	40.935	40.286	40.324
S	$2p_{3/2}$	64.743	64.995	64.691
	$2p_{1/2}$	35.257	35.005	35.309
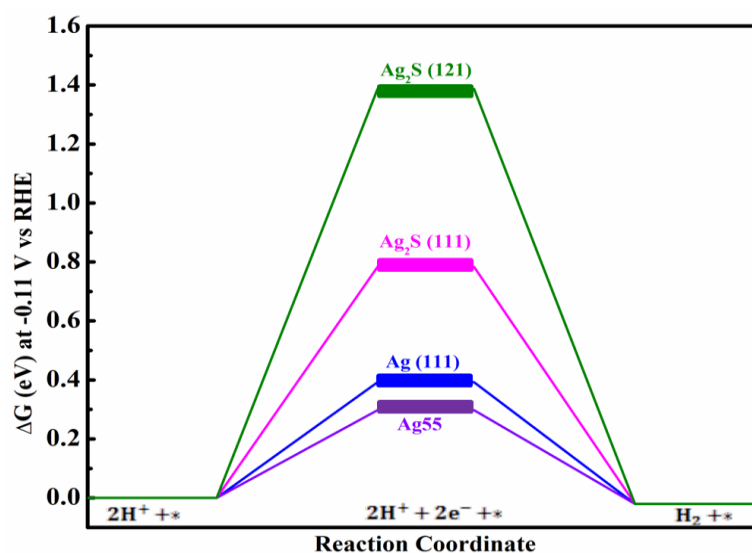
Figure S5.7 Free energy diagrams for hydrogen evolution reaction (HER) on different facets of Ag [i.e. (111) and 55-cluster] and Ag$_2$S [i.e. (111) and (121)].
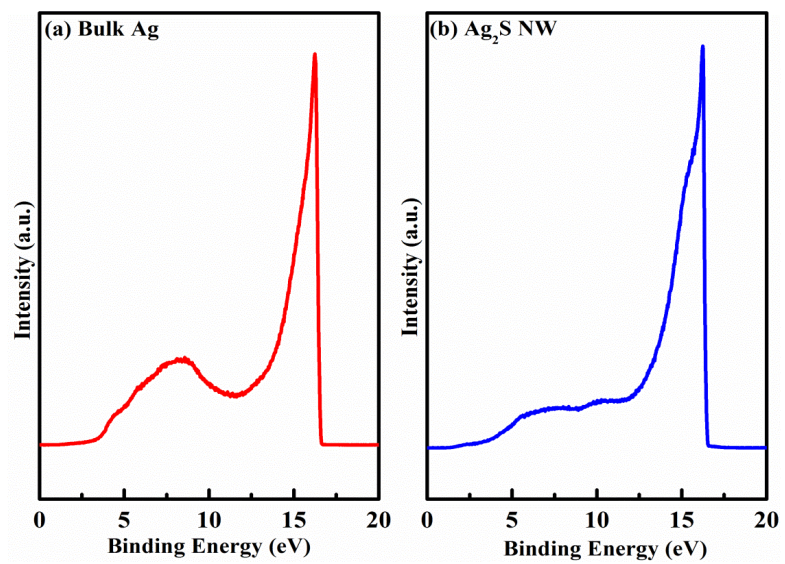
Figure S5.8 Experimental work function measurements for (a) bulk Ag and (b) Ag$_2$S NWs.

5.5.6 References

(1)   Kresse, G.; Hafner, J. *Phys. Rev. B* **1993**, *47*, 558.

(2)   Kresse, G.; Hafner, J. *Phys. Rev. B* **1994**, *49*, 14251.

(3)   Kresse, G.; Furthmüller, J. *Phys. Rev. B* **1996**, *54*, 11169.

(4)   Kresse, G.; Furthmüller, J. *Comput. Mater. Sci.* **1996**, *6*, 15.

(5)   Blöchl, P. E. *Phys. Rev. B* **1994**, *50,* 17953.

(6)   Kresse, G. *Phys. Rev. B* **1999**, *59*, 1758.

(7)   Hammer, B.; Hansen, L.; Nørskov, J. *Phys. Rev. B* **1999**, *59*, 7413.

(8)   Ping, Y.; Galli, G.; Goddard, W. a. *J. Phys. Chem. C* **2015**, *119*, 11570.

(9)   Sandupatla, A. S.; Alexopoulos, K.; Reyniers, M.-F.; Marin, G. B. *J. Phys. Chem. C* **2015**, *119*, 18380.

(10)   Monkhorst, H. J.; Pack, J. D. *Phys. Rev. B* **1976**, *13*, 5188.

(11)   Yang, H. G.; Sun, C. H.; Qiao, S. Z.; Zou, J.; Liu, G.; Smith, S. C.; Cheng, H. M.; Lu, G. Q. *Nature* **2008**, *453*, 638.

(12)   Momma, K.; Izumi, F. *J. Appl. Crystallogr.* **2011**, *44*, 1272.

(13)   Durand, W. J.; Peterson, A. A.; Studt, F.; Abild-Pedersen, F.; Nørskov, J. K. *Surf. Sci.* **2011**, *605*, 1354.

(14)   Rosen, J.; Hutchings, G. S.; Lu, Q.; Rivera, S.; Zhou, Y.; Vlachos, D. G.; Jiao, F. *ACS Catal.* **2015**, *5*, 4293.

(15)   Liu, S.; Tao, H.; Zeng, L.; Liu, Q.; Xu, Z.; Liu, Q.; Luo, J.-L. *J. Am. Chem. Soc.* **2017**, *139*, 2160.

Chapter 6. The Excellence of La(Sr)Fe(Ni)O$_3$ as an Active and Efficient Cathode for Direct CO$_2$ Electrochemical Reduction at Elevated Temperatures

Abstract: To effectively reduce and utilize the atmospheric CO$_2$, electrochemically converting it to CO with an efficient and stable cathode in a high temperature solid oxide electrolyzer attracts extensive interest. A composite cathode based on lanthanum nickelate potentially opens up a possibility for CO$_2$ electrolysis. We herein developed a new Ni-doped La(Sr)FeO$_{3-\delta}$ material which is firstly fabricated as cathode for CO$_2$ electrolysis in a solid oxide electrolysis cell (SOEC).
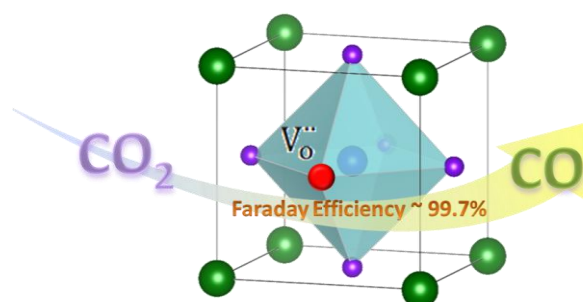
The ultralow total polarization resistance, together with an impressive current density of 1.21 A cm^{-2} at a potential of 1.55 V and 850 °C, demonstrates the superior electrocatalytic activity of La$_{0.6}$Sr$_{0.4}$Fe$_{0.8}$Ni$_{0.2}$O$_{3-\delta}$ (LSFN) for stably and effectively promoting cathodic kinetics for CO$_2$ electrolytic reaction. An ultrahigh Faraday efficiency of ~99.7% was also achieved at an applied potential of 1.0 V (vs OCV) and 850 ℃ . The comparable cell performance for CO$_2$ electrolysis benefits from the extension of reactive sites due to the improved mixed ionic and electronic conductivity, together with an accelerated adsorption and diffusion of adsorbed active species resulted from the high oxygen vacancy introduced on the LSFN backbone

surface. Besides the comparable electrochemical performance, the excellent redox reversibility between reduction and re-oxidation as well as considerable coking tolerance towards CO-enriched gas reveals that this newly prepared La(Sr)Fe(Ni) is a potential cathode material for SOEC, particularly for direct carbon-abundant cell.

6.1 Introduction

The level of atmospheric carbon dioxide (CO_2) increases significantly as a result of anthropogenic accumulation at an accelerating rate in the past few decades, aggravating climate change and environmental issues consequently.[1] To weaken the greenhouse effects, the development of technologies for reducing CO_2 emission or utilizing CO_2 has attracted extensive studies worldwide. As an alternative artificial method of reducing carbon footprint, high temperature CO_2 reduction in an oxygen ion conducting solid oxide electrolysis cell (SOEC) draws a promising path on the blueprint for future environmental sustainability and energy storage.[2] As compared with electrochemical CO_2 reduction at room temperature, SOEC is of great interest because of their advantages: (1) it possesses an incomparable high Faraday efficiency since CO is the only product from CO_2 reduction, (2) high abundance, environmentally friendly and cost-effective transition metal oxides (perovskites) provide the possibility for practical utilization. Moreover, by using electrical power generated from renewable sources, such as solar cells and wind turbines, CO_2 electrolysis reaction can convert these intermittent renewable energy sources into chemical in the form of CO.[3] Meanwhile, the produced CO and O_2, as the by-products from CO_2 electrolysis, are generated in two different streams because of the spatial separation by a dense electrolyte, and both of them have wide range applications in industrial processes.[4, 5] The challenge of this process lies in the design of a highly

stable and effective catalyst which can accelerate the electrode reaction rate and consequently, increase the current utilization efficiency. The state-of-the-art Ni/YSZ cermet H_2 electrode has been widely studied as anode in solid oxide fuel cell (SOFC) owing to its impressive catalytic properties.[6] Because of the similarity to SOFC, progresses have been made in the development of high temperature SOEC by using Ni-based cathodes.[7, 8] The Ni-based cermet also shows excellent electrochemical performance for the conversion of CO_2 with desired electrocatalytic activity.[9] Nevertheless, a fundamental material issue regarding the non-optimal redox stability of Ni-based cermet should be noticed as this will possibly lead to the loss of the electrical conductivity, performance degradation and delamination of electrode and electrolyte.[10-12] To avoid these issues, some perovskite oxide materials, which were reported to be promising anode materials with good redox stability in SOFC, have been utilized as potential cathode materials in SOEC. Perovskite-type oxides, such as La(Sr)Cr(M)$O_{3-\delta}$ (M = Fe, Mn and Ni),[10, 13-18] and La(Sr)N$O_{3-\delta}$ (N = Mn, Ti and Cr),[11, 19-21] have been demonstrated to be the good cathode materials for CO_2 or H_2O electrolysis at elevated temperatures due to their sufficient electronic conductivity. However, the electrochemical performances of these materials are still poor as compared with Ni-based materials because of the limited number of active sites (low electrocatalytic activity and insufficient electrical conductivity). Tatsumi *et al.* investigated many oxide materials with different structures as cathode materials for CO_2 electrolysis and found that the La$_{0.6}$Sr$_{0.4}$Fe$O_{3-\delta}$ with a perovskite structure showed much higher electrocatalytic activity than others.[22] This is probably due to the high mixed ionic and electronic conductivity and surface activity for electrochemical dissociation of CO_2.[23] However, the electrochemical performance of La$_{0.6}$Sr$_{0.4}$Fe$O_{3-\delta}$ is still less satisfactory as compared with those of Ni-based materials at elevated

temperatures. The relative low electronic conductivity of $La_{0.6}Sr_{0.4}FeO_{3-\delta}$ limits its further application as electrode material in both SOFC[24] and SOEC.[22] If Fe is partially substituted by Ni ($La_{0.6}Sr_{0.4}Ni_{1-x}Fe_xO_{3-\delta}$), especially when x>0.5, this material shows high electronic conductivity and thermal expansion coefficient which are close to these of YSZ electrolytes.[25, 26] The high mixed ionic and electronic conductivity, good compatibility with electrolyte and thermal stability of $La_{0.6}Sr_{0.4}Ni_{1-x}Fe_xO_{3-\delta}$ make it a potential electrode for SOFC.[25, 26] Nevertheless, $La_{0.6}Sr_{0.4}Ni_{1-x}Fe_xO_{3-\delta}$ has not been applied for CO_2 electrolysis yet. On the basis of its properties, it may be a promising cathode material for CO_2 electrolysis at elevated temperatures.

In this work, we evaluated the potential of perovskite oxide $La_{0.6}Sr_{0.4}Fe_{0.8}Ni_{0.2}O_{3-\delta}$ (LSFN) as a cathode material for CO_2 electrolysis at elevated temperatures with the aim of improving its electrocatalytic activity. The LSFN was fabricated as cathode in an yttria stabilized zirconia (YSZ) electrolyte supported SOEC. The redox stability, electrocatalytic activity, Faraday efficiency and coking resistance of the LSFN for CO_2 electrolysis at 800 °C and 850 °C were investigated, respectively.

6.2 Experimental Procedure

6.2.1 Preparation of Materials and Characterization

Perovskite oxide powders of LSFN were prepared by a modified sol-gel method as described elsewhere.[27] Stoichiometric amounts of $La(NO_3)_3 \cdot 6H_2O$, $Sr(NO_3)_2$, $Fe(NO_3)_3 \cdot 9H_2O$ and $Ni(NO_3)_2 \cdot 6H_2O$ were first dissolved in deionized water under continuous stirring, and EDTA-NH_3H_2O combined solution was added, followed by the addition of citric acid. The molar ratio of EDTA : citric acid : total metal ions was controlled to be around 1 : 1.5 : 1. Subsequently, NH_3H_2O was added to adjust the pH value to around 8. The solution was stirred and heated on a hot plate at 80 °C until the

formation of organic resins. The synthesized gel was decomposed at 300 °C for 4 h to remove the organic components and the nitrates. The precursor powders were then fired at 1100 °C for 10 h in air to obtain the final electrode materials. $(La_{0.60}Sr_{0.40})_{0.95}Co_{0.20}Fe_{0.80}O_{3-\delta}$ (LSCF) and $Gd_{0.2}Ce_{0.8}O_{2-\delta}$ (GDC) powders were purchased from fuelcellmaterials Company ("fuelcellmaterials.com"). The electrode pastes were prepared by mixing electrode materials and GDC with a weight ratio of 1:1 with a glue containing 1-butanol, benzyl butyl phthalate (BBP), ethyl cellulose and α-terpineol, followed by ball milling for 3 h.

The crystalline structure of synthesized powders was identified by X-ray diffraction (XRD) with Riga u Rotaflex Cu Kα radiation (40 kV, 44 mA). Thermogravimetric analysis (TA SDT Q600) was conducted at a heating/cooling rate of 10 °C min^{-1} in different atmospheres from 20 to 900 °C to characterize the thermophysical properties. Microstructures were determined with a high-resolution Zeiss Sigma FE-SEM equipped with an EDX detector. The LSFN powders were also analyzed using a JEOL JEM 2100 transmission electron microscope (TEM) at an accelerating voltage of 300 kV. X-ray photoelectron spectroscopy (XPS, Kratos AXIS Ultra) was used to investigate the surface chemistry of the LSFN powders with the adventitious carbon (C 1s) at the binding energy (BE) of 284.6 eV as the reference.

6.2.2 Cell Fabrication and Tests

The dimensions of the as-received commercial YSZ discs ("fuelcellmaterials.com") are 250~300 μm in thickness and 25 mm in diameter. The GDC pastes were screen-printed on both sides of the YSZ disc and co-sintered at 1300 °C for 5 h to form GDC buffer layers. Both the cathode pastes and anode pastes were screen-printed onto corresponding surfaces of the YSZ disc to form a membrane electrode assembly

(MEA). The MEA was sintered at 1100 °C for 4 h in air. Gold paste was painted onto the surfaces of both anode and cathode to form current collectors. The CO_2 electrolysis cell was built by fixing the MEA between coaxial pairs of alumina tubes with a ceramic sealant (AREMCO 552). Dry CO_2/CO (70:30) was fed to the cathode side at a flow rate of 40 mL min^{-1}.

The electrochemical measurements were conducted by using a four-probe method on a Solartron 1255 frequency response analyzer and a Solartron 1286 electrochemical interface instrument after the temperature was slowly increased to the elevated temperatures. The polarization resistance of the CO_2 electrolysis cell was determined from electrochemical impedance spectroscopy (EIS) measured under an ac potential with a frequency range of 1 MHz to 0.1 Hz and an amplitude of 10 mV at the stable open circuit voltage (OCV). The gases from the cathode stream were analyzed using a Hewlett-Packard model HP5890 gas chromatograph (GC) equipped with a packed column. Nicolet Almega XR Dispersive Raman Microscope was used to evaluate the level of coke deposition and the formation of secondary phase on the LSFN cathode after CO_2 electrolysis.

6.3 Results and Discussion

6.3.1 Characterizations of as-obtained LSFN

Figure 6.1a shows the XRD pattern of the as-prepared LSFN powder after firing in air at 1100 °C for 10 h; the inset shows the enlarged region at the phase of (200). The as-prepared LSFN showed a single phase without any impurity phases, as identified by XRD analysis and previously reported results.[25, 26] When compared with the standard structure of La(Sr)Fe(Mn)O$_3$ (PDF # 54-1292), the diffraction peaks of LSFN after sintering in air were shifted to higher angles, as confirmed by the enlarged zone at the

phase of (200), where the diffraction angle increases from 46.73° to 46.95°. Normally, the substitutions of high spin Mn^{3+} (0.645 Å) and Mn^{4+} (0.53 Å) by Ni^{2+} (0.69 Å) of larger ionic radius cause lower 2ϴ angles and consequently, increases unit cell parameter. However, the reflection shift of LSFN to higher diffraction angles is an indication of decreased cell parameters with respect to the undoped material.[28, 29] This is due to the tensile or compressive strain formation derived from the defects created (vacancies, interstitials and local structure transformations) after the doping of Ni. A closer inspection of the (200) reflection shows peak shoulder formation, which in turn confirms the increased lattice distortion generation.[30] In the meantime, the substitution of B-site by lower valence cation of Ni gives corner-shared strings of BO_6 octahedra and causes the formation of oxygen vacancies to maintain the electroneutrality (see the crystal structure in Figure 6.1b, d). The Ni(Ⅳ)/Ni(III) and Fe(II)/Fe(III) redox couples in $(Ni)O_6$ and $(Fe)O_6$ octahedral units can accept electrons while losing lattice oxygen, which is beneficial for electrical conductivity and catalytic activity. More importantly, the introduced oxygen vacancies could effectively improve the chemical adsorption ability of CO_2 on the catalyst surface since oxygen vacancies act as host sites to accommodate and consequently activate CO_2 molecules.[11, 31] SEM and TEM analyses were also performed to acquire the surface morphological and compositional information, respectively. The microstructure of the as-obtained porous materials with a glossy surface is shown in Figure 6.1c, the well interconnected nanoparticles with an average diameter of ~200 nm ensure sufficient gas diffusion pathways and mechanical strength. The crystal lattice analysis of LSFN in conjunction with the diffractogram of the selected domain in Figure 6.1d was further conducted and shown in Figure 6.1e. The measured lattice space of 0.292 nm corresponds to the value determined by the XRD analysis at the (110) planes of the LSFN perovskite. It is

indexed as a cubic crystalline structure in the space group of Pm-3m (221). Therefore, the high-resolution analysis combined with the diffractogram confirms the structure of the as-prepared LSFN after firing in air.
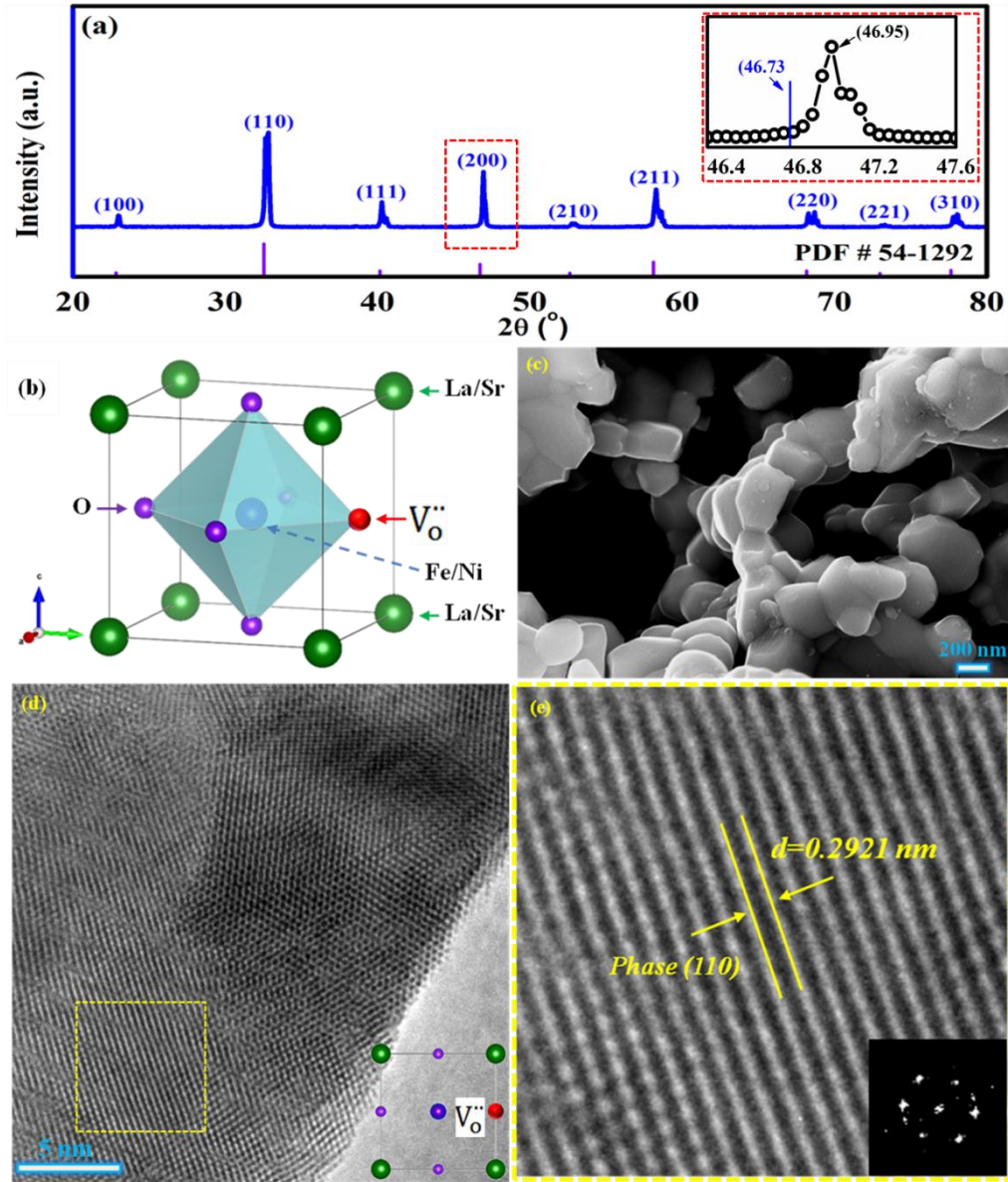
Figure 6.1 Characterizations of as-obtained LSFN. (a) X-ray diffraction pattern and (b) the corresponding crystal structure; (c) SEM image; (d) High-resolution TEM image and (e) corresponding crystal lattice, the inset shows the diffractogram of the selected domain.

6.3.2 Redox stability evaluation

For a typical high temperature SOEC for CO_2 electrolysis, the local CO_2 starvation resulted from the insufficient adsorption of the linear CO_2 molecules on the catalyst surface always leads to an increased electrode polarization,[12] and consequently degrades the cell performance and current utilization efficiency, especially at a high applied potential.[11, 32] The non-polar CO_2 molecules are chemically difficult to be adsorbed and activated on active sites at elevated temperatures. Currently, the bottleneck for direct CO_2 electrolysis is how to improve CO_2 chemical adsorption on the surface of catalyst backbone and the redox stability. Recently, introducing oxygen vacancies on the surface of catalyst backbone has been proposed to raise the potential for accommodating and activating CO_2 molecules on these defective sites.[11, 31] Moreover, it has also been demonstrated that oxygen vacancies can promote absorption of small molecules, such as CO_2, if they tend to get ordered in a special manner.[33] A lower oxidation state of B-site cations in the cubic structure is expected to have more oxygen vacancies and more space for accommodating CO_2 molecules.[34] Because the Ni-enriched regions have relatively large oxygen deficiency due to the lower average coordination number of Ni in the lattice, this will lead to a decrease in the average valence state, and consequently improve the chemical absorption ability of CO_2 in these defect-rich sites.[35] To evaluate the content of oxygen vacancy and redox stability of LSFN, TGA measurements were conducted in different atmospheres from 20 to 900 °C. The weight losses of LSFN in Ar and CO_2 as a function of temperature were recorded in Figure 6.2a. The gradual weight loss (~0.24 wt%) below 200 °C can be attributed to the desorption of H_2O. When continuously increasing temperature (< 375 °C), LSFN suffers from weight loss in both Ar and CO_2 flows. However, the weight change of LSFN in CO_2 experienced slightly faster

decrease as compared to that in Ar, which can be attributed to the combination of the partial loss of lattice oxygen since Cheng [36] reported that the presence of CO_2 causes the loss of lattice oxygen, and the CO_2 desorption on continuously heating.[37] With the temperature increasing, the adsorption and desorption rates of CO_2 on LSFN reach equilibrium, resulting in the almost overlapped curves for both Ar and CO_2. On the basis of Wagner's theory and decreased weight of LSFN,[38] the calculated non-stoichiometry δ is 0.17, which indicates that oxygen vacancies will further generate in CO_2 flow at high temperatures. Currently, the majority of cathode materials employed in SOEC predominately originates from anode materials in more technologically advanced SOFC, but operated in reverse mode.[39, 40] Therefore, it is more desirable if the developed materials have good redox stability for efficient operation in both SOEC and SOFC modes at reducing and oxidizing conditions, respectively. The reversibility of LSFN during redox cycle was established to evaluate the stability of LSFN in both reducing and oxidizing atmospheres by TGA. The as-prepared LSFN was reduced in a 5% H_2/N_2 flow at an elevated temperature up to 900 °C and cooled down in the same gas flow to room temperature, and subsequently re-oxidized when back to 900 °C in air, as shown in Figure 6.2b. The thermogravimetric analysis indicates that a weight loss of 4.84% and a weight gain of 4.79% were observed in reduction and re-oxidation conditions, respectively, corresponding to a loss and uptake of oxygen vacancy (δ) of 0.67. X-ray photoelectron spectroscopy (XPS) measurements were also conducted to analyze the adsorbed oxygen and lattice oxygen before and after stability test for over 36 h, as shown in Figures 6.2c,d. The XPS survey spectra confirm the presence of La, Sr, Fe and Ni for both samples, as shown in Figure 6.2c. The partial difference of XPS spectra after test (Figure 6.2c2) mainly originates from the contributions of GDC and current collector (Au) since GDC was

mixed with LSFN in a weight ratio of 1:1 to further increase the triple phase boundaries, and Au was employed as the current collector. Typically, the peaks at the binding energies of ~528 eV and ~531 eV correspond to the lattice oxygen and adsorbed oxygen on the surface of measured samples, as marked in Figure 6.2d. Moreover, the adsorbed oxygen is related to the surface oxygen vacancies. Apparently, a decrease in the lattice oxygen was observed after the test (Figure 6.2 d2) as compared to the one before the test (Figure 6.2 d1). This confirms the analysis of TGA that oxygen vacancies will further generate under the experimental conditions in the mixture gas of CO_2/CO. Quantitative analysis of lattice oxygen and adsorbed oxygen on the surface of LSFN before and after stability is summarized in Table 2.

Table 6.1 Quantitative analysis of lattice oxygen and adsorbed oxygen on the surface of LSFN before and after tests.

LSFN	Area of lattice oxygen	Area of adsorbed oxygen
Before test	1115.4 (31.64%)	2409.6 (68.36%)
After test	1649.5 (22.81%)	5580.6 (77.19%)

It is found that the adsorbed oxygen increased by 8.83% after the stability test, which exactly matches the decrease in the lattice oxygen (8.83%). This indicates that the increased oxygen vacancies were all derived from the decrease in lattice oxygen, and consequently contributed to the high electrochemical performance (see the analysis for Figure 6.3). Meanwhile, the symmetry of the weight change of LSFN suggests an excellent redox stability between the reduction and re-oxidation cycles.
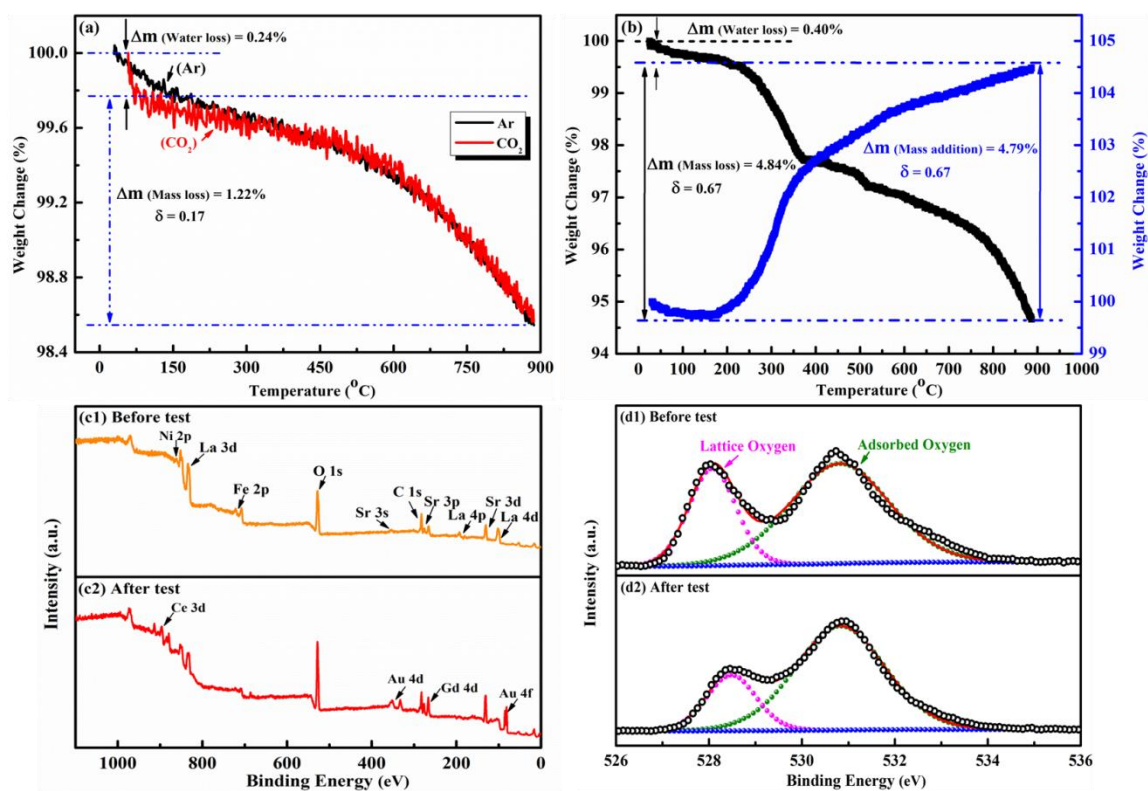
Figure 6.2 Thermogravimetric analysis tests. (a) Weight loss of LSFN as a function of temperature in Ar and CO_2 atmospheres, and (b) Redox cycling ability test of LSFN. XPS analyses of LSFN before and after stability test: (c) Representative XPS of all elements, and (d) O 1s spectra.

6.3.3 Electrochemical performance for CO_2 electrolysis

Its remarkable variability in oxygen vacancy content and good reversibility under cyclic conditions make LSFN a potential candidate for the application in SOEC. To evaluate the feasibility and electrochemical performance of LSFN as cathode for CO_2 electrolysis, we exemplify its application for a YSZ electrolyte support SOEC operating at elevated temperatures. The cathode side was fed with CO_2/CO (70:30) as feedstock at a flow rate of 40 mL min^{-1}, and the anode was exposed to ambient air. Figure 6.3a shows the temperature dependent I-V curves for CO_2 electrolysis at 800 °C and 850 °C. The current density sharply increased with the rising applied potential for the cell with LSFN at 800 °C and 850 °C, and reached a maximum current density of approximately 0.85 A cm^{-2} and 1.21 A cm^{-2} at the potential of 1.55

V, respectively. These values are comparable to those reported recently for cells using PrBaMn$_2$O$_{5+\delta}$ (0.85 A cm^{-2}) [40] and La(Sr)Cr(Fe)-based materials (0.82 A cm^{-2}) [41] at 850 °C at the same applied potential, indicating the effectiveness of LSFN for CO$_2$ electrolysis. This in turn verifies that the partial substitution of Fe by Ni improves the electrical conductivity and electrocatalytic activity, as discussed in Figures 6.1 and 6.3. Additionally, the accelerated reaction rate at 850 °C can be attributed to an increase in the temperature dependent ionic conductivity of both LSFN and electrolyte, which consequently leads to the better performance at a higher temperature. More importantly, the *I-V* curves transiting smoothly from the SOFC mode to the SOEC mode further indicate that the developed LSFN material possesses good redox reversibility under reduction and oxidation conditions, which is good agreement with the analysis in Figure 6.2b. To further investigate the factors credited for the enhanced electrochemical performance, ac impedance spectroscopy was carried out at different temperatures. The impedance spectra of the cell with LSFN at 800 °C and 850 °C under open circuit condition, together with the simulated results by using the attached equivalent circuit, are shown in Figure 6.3b. Apparently, a feasible fitting was achieved with two parallel circuits of resistor and capacitor connected in series with another resistor, where the Rs and Rp correspond to the series resistance and total electrode polarizations (R$_1$+R$_2$) of the cell, respectively. The corresponding simulated values of each element are summarized in Table 1.

Table 6.2 Simulated results of the electrolysis cell with LSFN at 800 °C and 850 °C

Temperature (°C)	R$_s$ (Ω cm^2)	R$_1$ (Ω cm^2)	R$_2$ (Ω cm^2)	R$_P$ (Ω cm^2)
800 °C	0.4395	0.1461	0.0133	0.1594
850 °C	0.4099	0.0977	0.0007	0.0984

As seen, the positive imaginary part of the Nyquist plot stretches from a linear response at high frequency region to two overlapped small semi-circular arcs. In the meantime, both R_s and R_p decrease with rising temperature, which consequently results in the remarkable improvement of cell performance. The high frequency arc (R_1) drops slightly from 0.1461 Ω cm^2 at 800 °C to 0.0977 Ω cm^2 at 850 °C, whereas the low frequency arc (R_2) falls significantly when temperature increases, where R_2 is only 0.0007 Ω cm^2 at 850 °C, 20 times lower than that at 800 °C. More importantly, it has been proposed that the low frequency arc probably reflects the adsorption and diffusion of adsorbed active species on the cathode surface for CO_2 electrolysis.[42] Dissimilarly, the high frequency arc is a sign for the charge transfer in the electrolysis reaction. As previously discussed, the LSFN is a mixed conductor cathode,[24] suggesting that both electron and oxygen ions can possibly pass through the cathode. This means that the decrease in the total polarizations derives from the extension of the reactive sites (related to R_1) in conjunction with the accelerated adsorption and diffusion of adsorbed active species (related to R_2) on the LSFN backbone surface. As a result, the increased active species on the LSFN and the accelerative charge transfer contribute to the enhanced electrochemical performance when the operating temperature increases. To evaluate the current utilization efficiency, potential static tests at different applied potentials (vs OCV) were also carried out. The responses of current densities at different applied potentials were recorded as a function of time, as presented in Figure 6.3c. It is discernible that the current densities increased in step with an increase in the corresponding applied potentials. However, the tendency of increase reduces gradually, which is attributed to the starvation effect of CO_2 in the feedstock and the restrained oxygen evolution at the anode side.[43] Additionally, electrolytic products at different applied potentials were also analyzed with online GC.
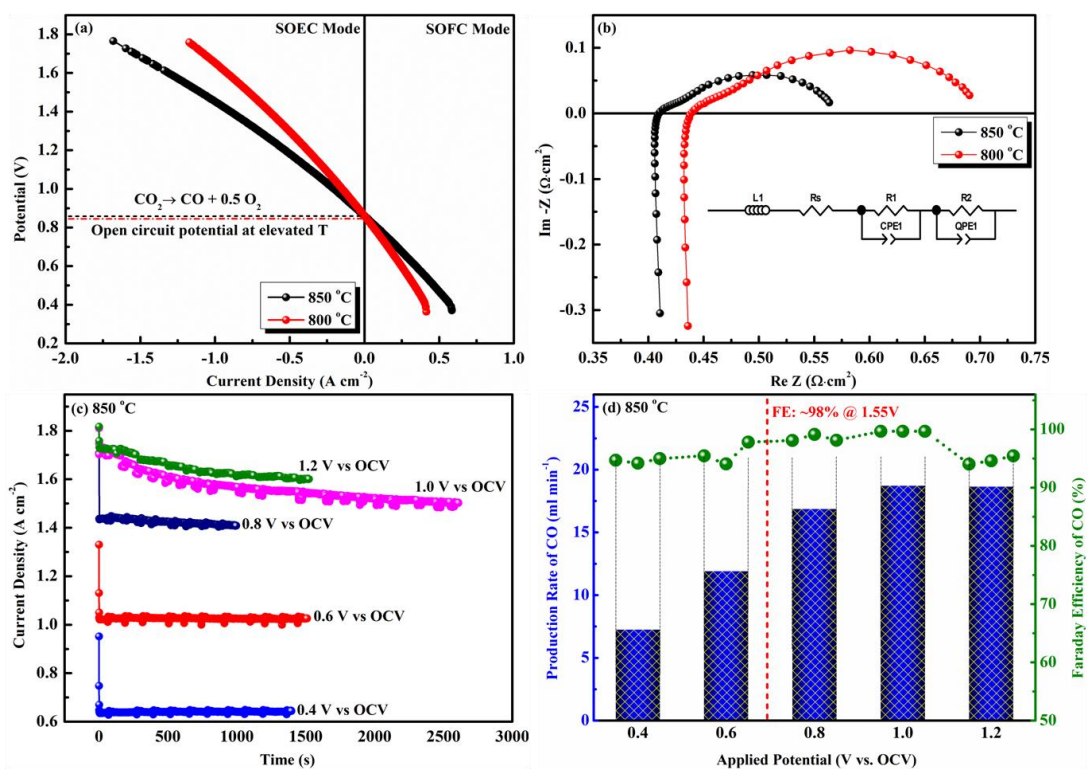
Figure 6.3 Electrochemical performances of the cell with LSFN electrode. (a) *I-V* curves and (b) the corresponding EIS curves of CO_2 electrolysis at 800 °C and 850 °C. The filled symbols are measured data and the lines are the simulated data using the inserted equivalent circuit. (c) Potentiostatic tests of SOEC at different applied potentials at 850 °C; (d) Production rates of CO and the corresponding Faraday efficiencies at different applied potentials at 850 °C.

The formation rates of CO and corresponding Faraday efficiencies at different applied potentials were calculated, as indicated in Figure 6.3d. It can be seen that the formation rates of CO reached 16.8 and 18.7 mL min^{-1} at the potentials of 0.8 and 1.0 V (vs OCV), respectively. However, slight decrease was observed at 1.2 V (vs OCV) because of the starvation of CO_2 in the feedstock, which matches the analysis of Figure 6.3c. The corresponding calculated Faraday efficiencies of the cell with LSFN at 850 °C increased from 94.6% at 0.4 V (vs OCV) to 98.4% at 0.8 V (vs OCV), and reached a peak value of 99.7% at 1.0 V (vs OCV). In contrast to most studies in the literature,[16, 41, 44] the Faraday efficiencies are considerably higher than those reported values so far. The remarkable electrocatalytic ability for effectively converting CO_2 to

CO and corresponding comparable current utilization efficiency of the cell further verify the promising use of LSFN as a cathode material for CO_2 electrolysis at elevated temperatures.

6.3.4 Durability Test and Coking Resistance Evaluation

The degradation of electrode materials over time for both SOEC and SOFC still remains as a challenge, therefore, durability is critical for their commercialization in the energy market and industrial applications, especially when taking hydrocarbon or carbon-enriched gas as feedstock. To examine the stability towards CO-abundant mixture gas, the potentiostatic test was conducted for over 36 h under a constant applied potential load of 0.6 V (vs OCV) at 850 °C, and the corresponding curve of current density as a function of time is presented in Figure 6.4a.
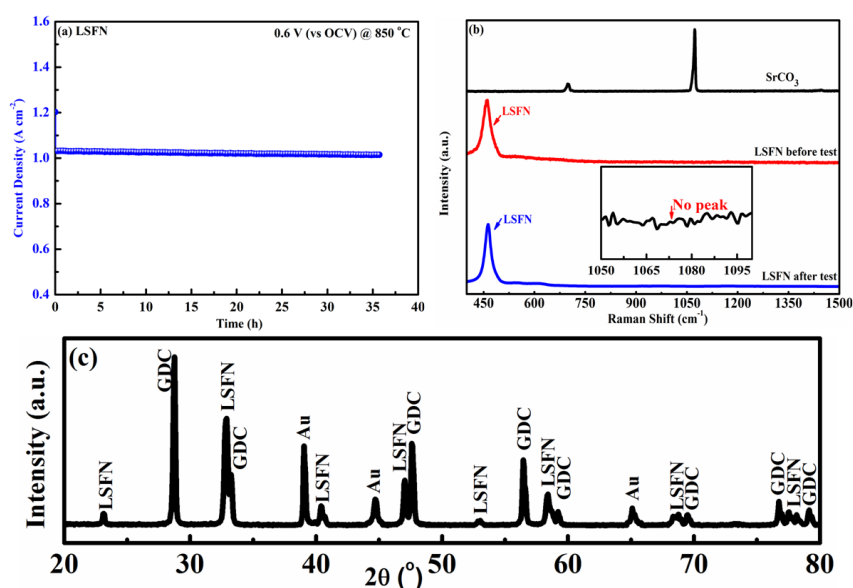
Figure 6.4 (a) Short-term stability of the CO_2 electrolysis cell with LSFN cathode at a constant applied potential of 0.6 V (vs OCV) at 850 °C; (b) Raman spectra collected from cathode surface before and after the short-term stability test; (c) XRD pattern of cathode side after stability test.

When the mixture gas of CO_2/CO (70:30) was supplied to the cathode compartment, the cell achieved a stable response of current density of ~1.02 A cm^{-2} without noticeable degradation for more than 36 h, indicating that the LSFN cathode has good

stability under the experimental conditions. Besides the requirement of good stability, cathode materials in SOEC also require strong tolerance towards carbon formation under the operating conditions. The good durability of LSFN without performance degradation also demonstrates its excellent coking resistance, unlike the conventional Ni-based catalyst on which carbon can easily build up when directly operating in CO-enriched gas with the consequent degradation of the electrode performance.[5, 45] To further verify this, *ex-situ* Raman spectroscopy was carried out on the cathode side of the cell with LSFN before and after the stability test. Representative Raman spectra on the cathode surfaces were recorded in Figure 6.4b. Apparently, no observable carbon peaks were detected for the cell after the stability test at 1346 cm^{-1} and 1561 cm^{-1} as they are correlated with defect-induced Raman features and sp^2-bonded carbons,[46] respectively. The obtained spectra for LSFN after the test are almost the same as the referential one before test, further suggesting that LSFN possesses good coking resistance towards the gas mixture. Recently, the group of Tatsumi Ishihara found that small peaks were assigned to $SrCO_3$ based on the Raman spectra when investigating the La(Sr)Fe(Mn) as an active catalyst for CO_2 electrolysis.[5] It has also been suggested that for La(Sr)Co(Fe) perovskites,[47] the surface segregation of Sr in these materials might explicate the reason. However, no peaks were observed for our material after the stability test at the peak of 1100 cm^{-1} in Figure 6.4 when compared with these peaks of pure $SrCO_3$, as clearly shown in the inset. This means that $SrCO_3$ was not formed on the surface of the cathode during the short-term stability test of CO_2 electrolysis, which was further confirmed by XRD pattern collected on the cathode side after stability test (Figure 6.4c). Therefore, it is concluded that LSFN is stable under the experimental conditions, and the reduction of CO_2 proceeds stably in the electrolysis mode for the cell with LSFN cathode at the elevated temperatures.

6.4 Conclusions

In summary, a new Ni-doped La(Sr)FeO$_{3-\delta}$ cathode material was developed using modified sol-gel method, and firstly fabricated as the cathode for high temperature CO$_2$ electrolysis in a SOEC. It demonstrates superior electrocatalytic activity for stably and effectively promoting SOEC cathode performance. The total polarization resistance reaches as low as 0.0984 Ω cm^2 at 850 °C, reflecting an extension of reactive sites, an accelerated adsorption and diffusion of adsorbed active species on the LSFN backbone surface. This consequently contributes to the comparable performance with an impressive current density of 1.21 A cm^{-2} at a potential of 1.55 V. More importantly, the current utilization efficiency achieves an ultrahigh value of ~99.7% at an applied potential of 1.0 V (vs OCV) and 850 ℃ . The improved mixed ionic and electronic conductivity resulted from the high content of introduced oxygen vacancy, and the increased activated CO$_2$ molecules collectively contribute to the enhanced electrocatalytic activity for CO$_2$ electrolysis. Particularly, the excellence of redox reversibility between reduction and re-oxidation cycles suggests a good redox stability in both SOFC and SOEC modes. Also, no degradation was observed during the stability test, indicative of high coking tolerance towards CO-enriched gas. We, therefore, conclude that La(Sr)Fe(Ni) can potentially be used to fabricate electrode in solid oxide cells, especially for directly hydrocarbon-fueled or carbon-enriched cells.

6.5 References

1. T. M. Letcher, *Climate change: observed impacts on planet Earth*, Elsevier, 2015.

2. J. T. S. Irvine, D. Neagu, M. C. Verbraeken, C. Chatzichristodoulou, C. Graves and M. B. Mogensen, *Nat. Energy*, **2016**, *1*, 15014.

3. D. Raciti, K. J. Livi and C. Wang, *Nano Lett.*, **2015**, *15*, 6829.

4. S. Wang and T. Ishihara, *ISIJ International*, **2015**, *55*, 381.

5. S. Wang, H. Tsuruta, M. Asanuma and T. Ishihara, *Adv. Energy Mater.*, **2015**, *5*.

6. S. D. Ebbesen, S. H. Jensen, A. Hauch and M. B. Mogensen, *Chem. Rev.*, **2014**, *114*, 10697.

7. S. D. Ebbesen and M. Mogensen, *J. Power Sources*, **2009**, *193*, 349.

8. P. Kim-Lohsoontorn and J. Bae, *J. Power Sources*, **2011**, *196*, 7161.

9. Z. Zhan and L. Zhao, *J. Power Sources*, **2010**, *195*, 7250.

10. X. Yue and J. T. S. Irvine, *J. Electrochem. Soc.*, **2012**, *159*, F442.

11. W. Qi, Y. Gan, D. Yin, Z. Li, G. Wu, K. Xie and Y. Wu, *J. Mater. Chem. A*, **2014**, *2*, 6904.

12. A. Hauch, S. D. Ebbesen, S. H. Jensen and M. Mogensen, *J. Mater. Chem.*, **2008**, *18*, 2331.

13. X. Yang and J. T. Irvine, *J. Mater. Chem.*, **2008**, *18*, 2349.

14. W. Yao, T. Duan, Y. Li, L. Yang and K. Xie, *New J. Chem.*, **2015**, *39*, 2956.

15. H. Li, G. Sun, K. Xie, W. Qi, Q. Qin, H. Wei, S. Chen, Y. Wang, Y. Zhang and Y. Wu, *Int. J. Hydrogen Energy*, **2014**, *39*, 20888.

16. S. Xu, S. Li, W. Yao, D. Dong and K. Xie, *J. Power Sources*, **2013**, *230*, 115.

17. Y. Li, Y. Wang, W. Doherty, K. Xie and Y. Wu, *ACS Appl. Mater. Interfaces*, **2013**, *5*, 8553.

18. N. Danilovic, A. Vincent, J.-L. Luo, K. T. Chuang, R. Hui and A. R. Sanger, *Chem. Mater.*, **2009**, *22*, 957.

19. S. Li, Y. Li, Y. Gan, K. Xie and G. Meng, *J. Power Sources*, **2012**, *218*, 244.

20. K. Chen, N. Ai and S. P. Jiang, *Int. J. Hydrogen Energy*, **2012**, *37*, 1301.

21. Y. Li, J. Zhou, D. Dong, Y. Wang, J. Jiang, H. Xiang and K. Xie, *Phys. Chem. Chem. Phys.*, **2012**, *14*, 15547.

22. T. Ishihara, K.-T. Wu and S. Wang, *ECS Transactions*, **2015**, *66*, 197.

23. M. Patrakeev, J. Bahteeva, E. Mitberg, I. Leonidov, V. Kozhevnikov and K. R. Poeppelmeier, *J. Solid State Chem.*, **2003**, *172*, 219.

24. G. Zhu, X. Fang, C. Xia and X. Liu, *Ceram. Int.*, **2005**, *31*, 115.

25. R. Chiba, F. Yoshimura and Y. Sakurai, *Solid State Ionics*, **2002**, *152*, 575.

26. R. Chiba, F. Yoshimura and Y. Sakurai, *Solid State Ionics*, **1999**, *124*, 281.

27. C. Duan, J. Tong, M. Shang, S. Nikodemski, M. Sanders, S. Ricote, A. Almansoori and R. O'Hayre, *Science*, **2015**, *349*, 1321.

28. M. Kerstan, M. Müller and C. Rüssel, *Solid State Sci.*, **2014**, *38*, 119.

29. P. Liu, J. Kong, Q. Liu, X. Yang and S. Chen, *J. Solid State Electr.*, **2014**, *18*, 1513.

30. G. Tsekouras, D. Neagu and J. T. S. Irvine, *Energ. Environ. Sci.*, 2013, *6*, 256-266.

31. S. Liu, Q. Liu and J.-L. Luo, *ACS Catal.*, **2016**, *6*, 6219.

32. X. Yue and J. T. Irvine, *Solid State Ionics*, **2012**, *225*, 131.

33. V. Esposito, M. Søgaard and P. V. Hendriksen, *Solid State Ionics*, **2012**, *227*, 46-56.

34. K. Nomura, Y. Ujihira, T. Hayakawa and K. Takehira, *Appl. Catal. A-Gen.*, **1996**, *137*, 25.

35. X. Tan, N. Liu, B. Meng, J. Sunarso, K. Zhang and S. Liu, *J. Membrane Sci.*, **2012**, *389*, 216.

36. A. Yan, B. Liu, Y. Dong, Z. Tian, D. Wang and M. Cheng, *Appl. Catal. B-Environ.*, **2008**, *80*, 24.

37. J. C. Hicks, J. H. Drese, D. J. Fauth, M. L. Gray, G. Qi and C. W. Jones, *J. Am. Chem. Soc.*, **2008**, *130*, 2902.

38. C. Wagner, *Prog. Solid State Ch.*, **1971**, *6*, 1.

39. N. Minh and M. C. Williams, *ECS Transactions*, **2015**, *68*, 3301.

40. T. H. Shin, J. H. Myung, M. Verbraeken, G. Kim and J. T. Irvine, *Faraday Discuss.*, **2015**, *182*, 227.

41. Y. Q. Zhang, J. H. Li, Y. F. Sun, B. Hua and J. L. Luo, *ACS Appl. Mater. Interfaces*, **2016**, *8*, 6457.

42. X. Yue and J. T. S. Irvine, *Electrochem. Solid St.*, **2012**, *15*, B31.

43. S. Li, Y. Li, Y. Gan, K. Xie and G. Meng, *J. Power Sources*, **2012**, *218*, 244.

44. J. Zhang, K. Xie, H. Wei, Q. Qin, W. Qi, L. Yang, C. Ruan and Y. Wu, *Sci. Rep-UK*, **2014**, *4*, 7082.

45. S. Sengodan, S. Choi, A. Jun, T. H. Shin, Y. W. Ju, H. Y. Jeong, J. Shin, J. T. Irvine and G. Kim, *Nat. Mater.*, **2015**, *14*, 205.

46. S. Liu, K. T. Chuang and J.-L. Luo, *ACS Catal.*, **2015**, *6*, 760.

47. J. A. Kilner, S. J. Skinner and H. H. Brongersma, *J. Solid State Electr.*, **2011**, *15*, 861.

Chapter 7. Highly Stable and Efficient Catalyst with *in Situ* Exsolved Fe-Ni Alloy Nanospheres Socketed on an Oxygen Deficient Perovskite for Direct CO$_2$ Electrolysis

Abstract: The massive emission of carbon dioxide (CO$_2$), the major portion of greenhouse gases, has negatively affected our ecosystem. Developing new technologies to effectively reduce CO$_2$ emission or convert CO$_2$ to useful products has never been more imperative. In response to this challenge, we herein developed a novel *in situ* exsolved Fe-Ni alloy nanospheres uniformly socketed on an oxygen deficient perovskite [La(Sr)Fe(Ni)] as a highly stable and efficient catalyst for the effective conversion of CO$_2$ to carbon monoxide (CO) in a high temperature solid oxide electrolysis cell (HT-SOEC).
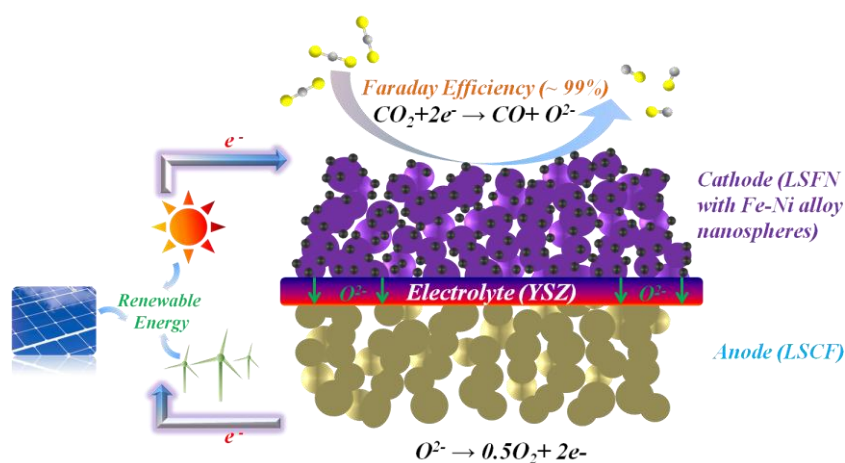
The symmetry between the reduction and re-oxidation cycles of this catalyst indicates its good redox reversibility. The cathodic reaction kinetics for CO$_2$ electrolysis is significantly improved with a polarization resistance as low as 0.272 Ω cm^2. In addition, a remarkably enhanced current density of 1.78 A cm^{-2}, along with a high

Faraday efficiency (~98.8%), was achieved at 1.6 V and 850 °C. Moreover, the potentiostatic stability test of up to 100 h showed that the cell was stable without any noticeable coking in a CO_2/CO (70:30) flow at an applied potential of 0.6 V (vs. OCV) and 850 °C. The increased oxygen vacancies, together with the *in situ* exsolved nanospheres on the perovskite backbone ensures sufficiently active sites and consequently improves the electrochemical performance for the efficient CO_2 conversion. Therefore, this newly developed perovskite can be a promising cathode material for HT-SOEC. More generally, this study points to a new direction to develop highly efficient catalysts in the form of the perovskite oxides with perfectly *in situ* exsolved metal/bimetal nanospheres.

7.1 Introduction

The ever-increasing consumption of fossil fuels has caused the record-breaking emissions of carbon dioxide (CO_2), accelerating global warming and climate change. This issue has attracted growing attention in the past few decades.[1-3] Hence, it is of great interest to convert CO_2 emitted, particularly from anthropogenic sources, to useful products. However, CO_2 is an extremely stable molecule, the conversion of which is an energy-intensive process.[4] Currently, the high-temperature CO_2 solid oxide electrolysis cell (HT-SOEC) has been intensively investigated as a highly efficient electrolyzer (not limited by the Carnot Cycle) for the direct conversion of CO_2 to carbon monoxide (CO) ($CO_2 \rightarrow CO + 0.5O_2$).[5-7] The generated CO can then be used as a fuel gas, converted to syngas or used to reduce oxides to pure metal in iron-making process;[8] the conversion of waste heat from these processes to electricity can further decrease the electrical energy required for the CO_2 electrolysis. Therefore, CO_2 electrolysis has been considered to be a promising energy storage method for dramatically reducing CO_2 concentration.[4] For a typical CO_2 electrolysis cell, CO_2 is

electrochemically converted to CO at the cathode compartment under an external applied potential, and oxygen ions pass through the oxygen-ion conducting electrolyte to the anode compartment, where gaseous oxygen (O_2) is formed. Both products (CO and O_2) are useful products and largely utilized in industrial processes.[9, 10] HT-SOEC, despite using electricity, can provide fast electrode reaction kinetics as well as high electrolysis efficiency. However, cathode materials currently used for HT-SOEC have not met the requirements of satisfactory electrochemical performance and high electrolysis efficiency. In this case, it is highly desirable to develop catalysts with high catalytic activity capable of efficient conversion of CO_2 to CO.

The prerequisites for being an ideal cathode material for CO_2 electrolysis in an HT-SOEC are as follows: (1) excellent catalytic activity for the CO_2 conversion, (2) durable reversibility and redox stability, (3) stable and good coking resistance, (4) high electrical conductivity to provide electrons for CO_2 reduction and high oxygen ions transportation and (5) superior porous structure for gas diffusion. To our best knowledge, most HT-SOECs that have been investigated are based on the currently preferred Ni-based cathodes because of their high catalytic activity for the conversion of CO_2 to CO.[11-14] However, these cathodes suffer from severe electrical conductivity loss and deactivation because of the facile re-oxidation of Ni (Ni $\rightarrow$ NiO) and carbon deposition in an atmosphere with highly concentrated CO_2/CO.[8, 15, 16] In this situation, Ni-based cathode materials fail to be directly utilized in HT-SOEC for CO_2 electrolysis.[17] As previously reported, several perovskite oxides, in the form of La(Sr)MO$_3$ (M=Fe, Mn, Cr), have been intensively investigated as the cathode materials for CO_2 electrolysis. These materials have shown varying levels of enhanced coking resistance although they are accompanied with lower electrochemical performance than that of HT-SOEC using Ni-based cathode materials,

because of inadequate conductivity and/or low catalytic activity for CO_2 electrolysis.[15, 18-20] Recently, a cermet cathode, made by physically mixing NiO and Fe_2O_3 with La(Sr)Fe(Mn), has been found to exhibit high catalytic activity for CO_2 electrolysis.[8] However, those results could be more convincing if, when demonstrating no coking formation in the long-term stability test, the cathode side was not treated with a steam flow for 2 h at the initial stage of every 24 h to remove the deposited carbon.

The addition of a second metal as a promoter to optimize Ni-based anode catalyst in solid oxide fuel cell (SOFC) has been intensively studied. The added second metal can coordinate and promote the catalytic activity of the host catalyst material by altering and modifying the electronic and/or structural parameters of the host metal.[21-23] Theoretically, the host metal forms a bimetallic alloy with the guest metal, which can synergistically promote the catalytic activity.[24-26] Among the reported promoters, significant efforts have been devoted to the investigation of Fe because of its abundance, low cost and effective enhancement of catalytic activity.[27] The addition of Fe also effectively improves the coking resistance.[28] Furthermore, the tailed anode in SOFC, homogenously coated with *in situ* exsolved metallic nanoparticles (NPs) on the surface, can greatly improve the catalytic activity and coking resistance in hydrocarbon fuels.[29-31] Thus, it is expected to have more desirable performance if bimetallic alloy NPs can be uniformly exsolved *in situ* onto the surface of the catalyst backbone in HT-SOEC for CO_2 electrolysis.

In this work, the newly developed Fe-Ni bimetallic alloy nanospheres were successfully exsolved *in situ* and uniformly socketed on the oxygen deficient perovskite backbone by reducing the Sr and Ni doped $LaFeO_3$ perovskite powders,

$La_{0.6}Sr_{0.4}Fe_{0.8}Ni_{0.2}O_{3-\delta}$ (LSFN), in a 5% H_2/N_2 flow at 850 °C. The Fe-Ni bimetallic alloy nanospheres socketed on LSFN perovskite backbone (Fe-Ni-LSFN) were used as the cathode in an yttria stabilized zirconia (YSZ) electrolyte supported HT-SOEC. The catalytic activity and Faraday efficiency of the Fe-Ni-LSFN for CO_2 electrolysis at 850 °C in HT-SOEC, its reversibility and redox stability were investigated. The mechanism of the high electrochemical performance was also explored.

7.2 Experimental procedure

7.2.1 Preparation of Materials and Characterization

Polycrystalline perovskite powders of LSFN were prepared using a modified sol-gel method as described elsewhere.[32] Stoichiometric amounts of $La(NO_3)_3 \cdot 6H_2O$, $Sr(NO_3)_2$, $Fe(NO_3)_3 \cdot 9H_2O$ and $Ni(NO_3)_2 \cdot 6H_2O$ were dissolved in $EDTA-NH_3H_2O$ combined solution under continuous heating and stirring, then citric acid was introduced. The molar ratio of EDTA acid : citric acid : total metal ions was controlled to be around 1 : 1.5 : 1. Subsequently, NH_3H_2O was added to adjust the pH value to around 8. The solution was stirred and heated on a hot plate at 80 °C until the formation of organic resins containing the homogeneously distributed cations because of the slow evaporation of the solvent. The synthesized gel was decomposed at 300 °C for 4 h to remove the organic components and the nitrates. The precursor powders were then fired at 1100 °C for 10 h in air to obtain the raw materials, followed by heating in a tubular furnace at 850 °C for 10 h in a reducing gas flow, thus forming the *in situ* exsolved Fe-Ni-LSFN. $(La_{0.60}Sr_{0.40})_{0.95}Co_{0.20}Fe_{0.80}O_{3-\delta}$ (LSCF) and $Gd_{0.2}Ce_{0.8}O_{2-\delta}$ (GDC) powders were fabricated using a conventional solid state reaction method.[33] The cathode pastes were prepared by mixing LSFN and GDC (weight ratio of 1:1) with a glue containing 1-butanol, benzyl butyl phthalate (BBP),

ethyl cellulose and α-terpineol, followed by ball milling for 3 h. The weight ratio of total powders to glue was 1.7:1. The anode pastes comprised of LSCF and GDC were prepared using the same method as the cathode pastes.

Thermogravimetric analysis (TA SDT Q600) were performed from 20 to 900 °C at a heating/cooling rate of 10 °C min^{-1} in air or 5% H_2/N_2 to characterize the thermophysical properties. The crystalline structure of all the synthesized powders was identified by X-ray diffraction (XRD) with Riga u Rotaflex Cu Kα radiation (40 kV, 44 mA) and the raw data were analyzed with JADE version 6.5. Microstructures were determined with a high-resolution Zeiss Sigma FE-SEM equipped with an EDX detector and an EBSD detector. The LSFN and Fe-Ni-LSFN powders were also analyzed using a JEOL JEM 2100 transmission electron microscope (TEM) at an accelerating voltage of 200 kV. X-ray photoelectron spectroscopy (XPS, Kratos AXIS Ultra) was used to investigate the surface chemistry of the LSFN and Fe-Ni-LSFN powders with the adventitious carbon (C 1s) at the binding energy (BE) of 284.5 eV as the reference.

7.2.2 Cell Fabrication and Testing

The cells investigated in this work were YSZ electrolyte supported (polished before the cell fabrication); the dimensions of the polished YSZ discs are ~220 μm in thickness and 25 mm in diameter. The GDC pastes were screen-printed on both anode and cathode sides of the YSZ electrolyte disc and co-sintered at 1300 °C for 5 h to form GDC buffer layers with a thickness of ~20 μm. Both the cathode pastes and anode pastes were screen-printed onto corresponding surfaces of the YSZ disc to form a membrane electrode assembly (MEA) with a circular area of ~0.946 cm^2. The MEA was sintered at 1100 °C for 4 h in air. Gold paste was painted onto the surfaces of

both anode and cathode to form current collectors. The CO_2 electrolysis cell was built by fixing the MEA between coaxial pairs of alumina tubes with a sealant, which was fastened in a vertical tubular furnace (Thermolyne F79300). Dry CO_2/CO (70:30) was fed to the cell with a flow rate of 50 ml min^{-1} via the cathode compartment located at the bottom, while the anode was placed on the top and exposed to air.

The electrochemical performance of the CO_2 electrolysis cell was measured by employing a four-probe method with Au wires as the leads. The temperature of the CO_2 electrolysis cell was slowly increased to 850 °C and a 5% H_2/N_2 reducing gas flow was continuously pumped into the cathode compartment. The temperature was maintained for 2 h to complete the further reduction and exsolution of the cathode material. The electrochemical measurements were conducted with a Solartron 1255 frequency response analyzer and a Solartron 1286 electrochemical interface instrument. The polarization resistance of the CO_2 electrolysis cell was determined from electrochemical impedance spectroscopy (EIS) measured under an ac potential with a frequency range of 1 MHz to 0.1 Hz and an amplitude of 10 mV at the stable open circuit voltage (OCV). A stability test in dry CO_2/CO (70:30) was performed under a constant applied potential of 0.6 V (vs. OCV) at 850 °C. The outlet gases from the cathode compartment were analyzed using a Hewlett-Packard model HP5890 gas chromatograph (GC) equipped with a packed column (Porapak QS) operated at 80 °C with a thermal conductivity detector and a flame ionization detector. Nicolet Almega XR Dispersive Raman Microscope with 532 nm laser and X50 objective was used to determine the level of coke deposition on the Fe-Ni-LSFN cathode after CO_2 electrolysis.

7.3. Results and Discussion

7.3.1 Identification of the *in situ* exsolved Fe-Ni alloy nanospheres

Figure 7.1A shows the XRD patterns of (a) the LSFN powders after firing in air at 1100 °C and (b) the Fe-Ni-LSFN powders after reducing in a 5% H_2/N_2 flow at 850 °C. Both LSFN and Fe-Ni-LSFN were obtained as well-crystallized powders. Apparently, no impurity phases were detected in the as-prepared LSFN [Figure 7.1A (a)], but the diffraction angles of the peaks for LSFN after sintering in air were shifted right to those for $LaFeO_3$, the shift of the reflections to higher diffraction angles is indicative of a significant decrease in the cell parameters and lattice distortion with respect to the undoped material.[34-36] After reducing the LSFN to Fe-Ni-LSFN in the 5% H_2/N_2 flow at 850 °C for 2 h, the XRD pattern showed the same diffraction peaks as the LSFN powders, as indicated in Figure 7.1A (b). However, the reflections shifted to lower 2Θ angles after reduction, indicative of increased unit cell parameter and lattice distortion. The peaks labeled as "★" in Figure 7.1A (b) were assigned to the diffraction peaks of $Fe_{0.64}Ni_{0.36}$ (PDF # 47-1405), which was the *in situ* exsolved NPs from the LSFN backbone. It is well known that Fe and Ni can easily form a solid solution phase in various atomic ratios as they are adjacent to each other in the periodic table.[37] Based on the phase diagram of a bimetallic Fe-Ni system,[38] at least one regular alloy could be formed under our experimental conditions. Moreover, it has been identified that the metallic Fe and Ni were first formed on the surface of the backbone, followed by the generation of the Fe-Ni alloy.[39] The two splitting peaks appeared in Figure 7.1A (b), which were assigned to La_2O_3 since the exsolution is typically accompanied by undesirable A-site cation-containing phases.[29, 40] However, the catalyst retains predominantly a perovskite structure after reduction. The XRD patterns with the appearance of the labeled peaks in Figure 7.1A (b) support the fact

that Fe, together with Ni, can undoubtedly be *in situ* exsolved in the form of alloy NPs. Besides, the Fe-Ni-LSFN powders were also analyzed with EDS line scan by crossing one NP socketed on the LSFN backbone to quantitatively describe the variations in the concentration of each element (La, Sr, Fe and Ni) and the results are presented in Figure 7.1B. The magnitudes of the Fe and Ni signals increased sharply while La and Sr showed an opposite tendency over the selected NP, indicating that the *in situ* exsolved NPs should be bimetallic Fe-Ni alloy. To further confirm that the *in situ* exsolved NPs are the bimetallic Fe-Ni alloy, XPS analysis were conducted to investigate the surface chemistry as well as the electronic parameters. The peak appearing at a BE of 284.6 eV corresponded to the C1s. The XPS survey spectra shown in Figures 7.1C and S7.1A confirmed the presence of La, Sr, Fe and Ni in the Fe-Ni-LSFN and LSFN powders, respectively. Based on the quantitative analysis from the XPS curve, the Fe^0/Ni^0 atomic ratio was around 72.8/27.2, which was quite close to 64/36 from $Fe_{0.64}Ni_{0.36}$. This in turn confirms the XRD result that an alloy solid solutions was formed. Generally, the peak located at the BE of ~528 eV was related to the lattice oxygen, whereas the one at the BE of ~531 eV was associated with the adsorbed or loosely bonded oxygen which was correlated to the surface oxygen vacancies.[41] It is worth noting that the O 1s spectra in Figure 7.1D (b) shows a decrease in the lattice oxygen on the Fe-Ni-LSFN surface with respect to the one in Figure 7.1D (a) on the LSFN surface. This can be attributed to the formation of oxygen vacancies and the reduction of Fe- and/or Ni-oxides to lower oxidation state.[42] The electronic effects of the bimetallic Fe-Ni alloy NPs were determined by analyzing the BEs of Fe^0 and Ni^0. The peaks of Fe^0 and Ni^0 are obviously shown in Figures 7.1E and 7.1F, respectively, whereas in Figures S7.1B and S7.1C, no peaks for Fe^0 and Ni^0

are identified. Typically, the $2p_{3/2}$ orbital of Fe^0 and the $2p_{1/2}$ orbital of Ni^0 are located at the BEs of ~706.4 eV [43] and ~870 eV,[44] respectively.
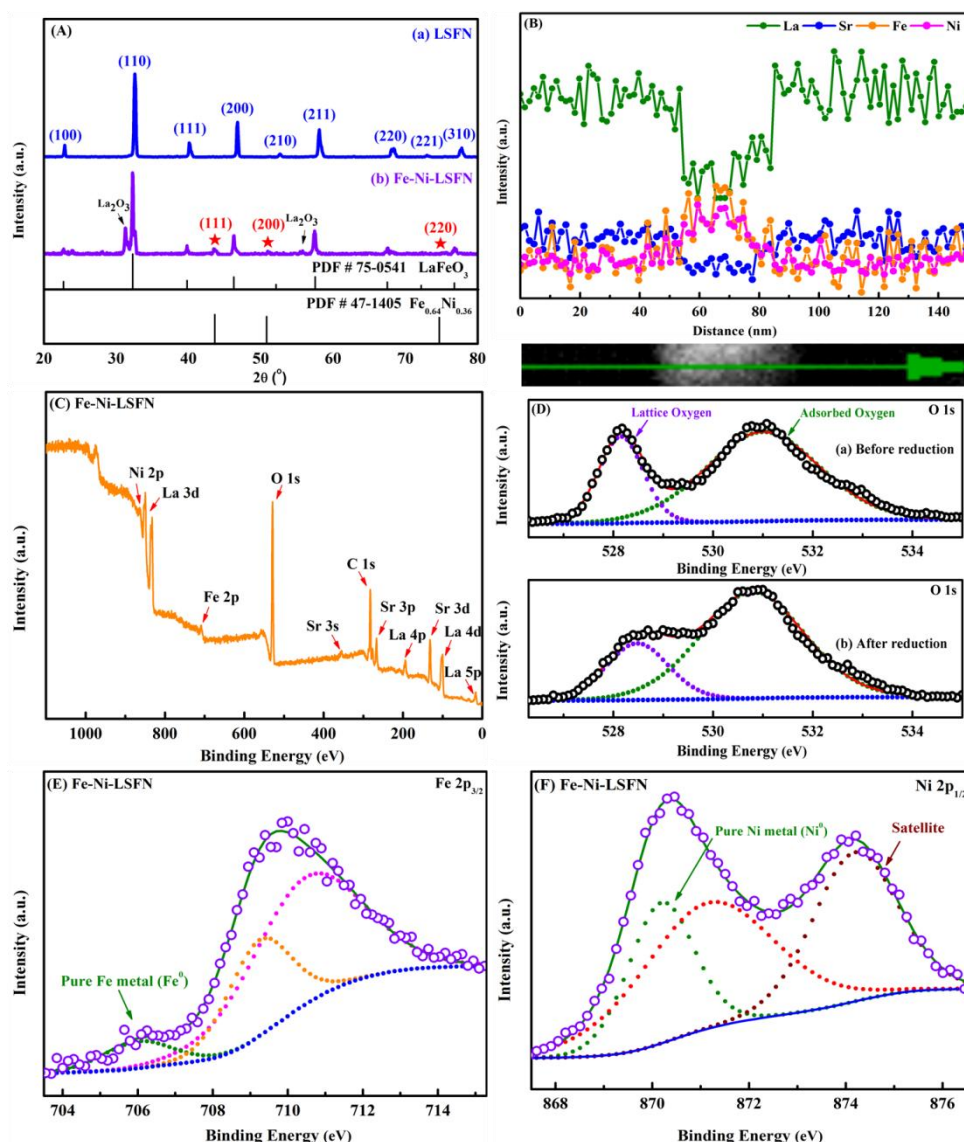
Figure 7.1 (A) X-ray diffraction patterns of LSFN (a) before and (b) after sintering at 850 °C in 5% H_2/N_2 atmosphere for 2 h. (B) EDX line scan of the exsolved Fe-Ni alloy nanosphere. (C) Representative XPS of Fe-Ni-LSFN powders, (D) O 1s spectra of (a) before and (b) after reduction, (E) Fe $2p_{3/2}$ spectra and (F) Ni $2p_{1/2}$ spectra after the reduction.

However, once an alloy is formed, the BE of Ni^0 moves to a lower value, which implies an increased electron density and electronegativity; the BE of Fe^0 will shift to a higher value in a reverse process.[45, 46] In fact, this is actually an effective way to

improve the catalytic activity towards CO_2 electrolysis via fine-tuning the electronic structure by the formation of Fe-Ni alloy NPs. The results in Figures 7.1E and 7.1F suggest that Fe^0 and Ni^0 were only partially *in situ* exsolved from the LSFN backbone, as the majority of Fe and Ni were in the form of oxides.[39]

To further acquire the morphological characteristics and compositional information of the LSFN and Fe-Ni-LSFN powders, SEM and TEM analysis were performed. SEM images of the as-prepared LSFN powders before and after reduction are shown in Figures 7.2A and 7.2B, respectively. Obviously, no metallic NPs could be found on the surface of the raw materials before reduction (Figure 7.2A). Figure 7.2B clearly shows that Fe-Ni alloy NPs were *in situ* exsolved and uniformly socketed on the surface of the LSFN backbone with the average diameter of ~30 nm. The morphologies of LSFN and Fe-Ni-LSFN associated with *in situ* exsolved Fe-Ni alloy nanospheres were further studied with TEM. From the low-resolution TEM images shown in Figures 7.2C and 7.2D, Fe-Ni alloy NPs can be clearly observed and were well dispersed with almost the same size under the bright field condition after the reduction. Figure 7.2E, together with Figures S7.2A and S7.2B, shows that those *in situ* exsolved Fe-Ni alloy NPs were all in perfect spherical shapes and well distributed on the edge of the LSFN backbone. The crystal lattice analyses associated with fast Fourier transformation of the Fe-Ni alloy nanosphere (Figure 7.2F), LSFN before (Figure 7.2G) and after reduction (Figure 7.2H) were further studied. The lattice space between the two parallel planes of the Fe-Ni alloy nanospheres was 0.2097 nm (Figure 7.2F), which is in close accordance with the calculated value of 0.2074 nm in (111) planes in the P space group of the $Fe_{0.64}Ni_{0.36}$ alloy. Meanwhile, the distance between two parallel planes of LSFN before reduction was 0.2731 nm which corresponded to the lattice constant of (110) planes, as shown in Figure 7.2G.
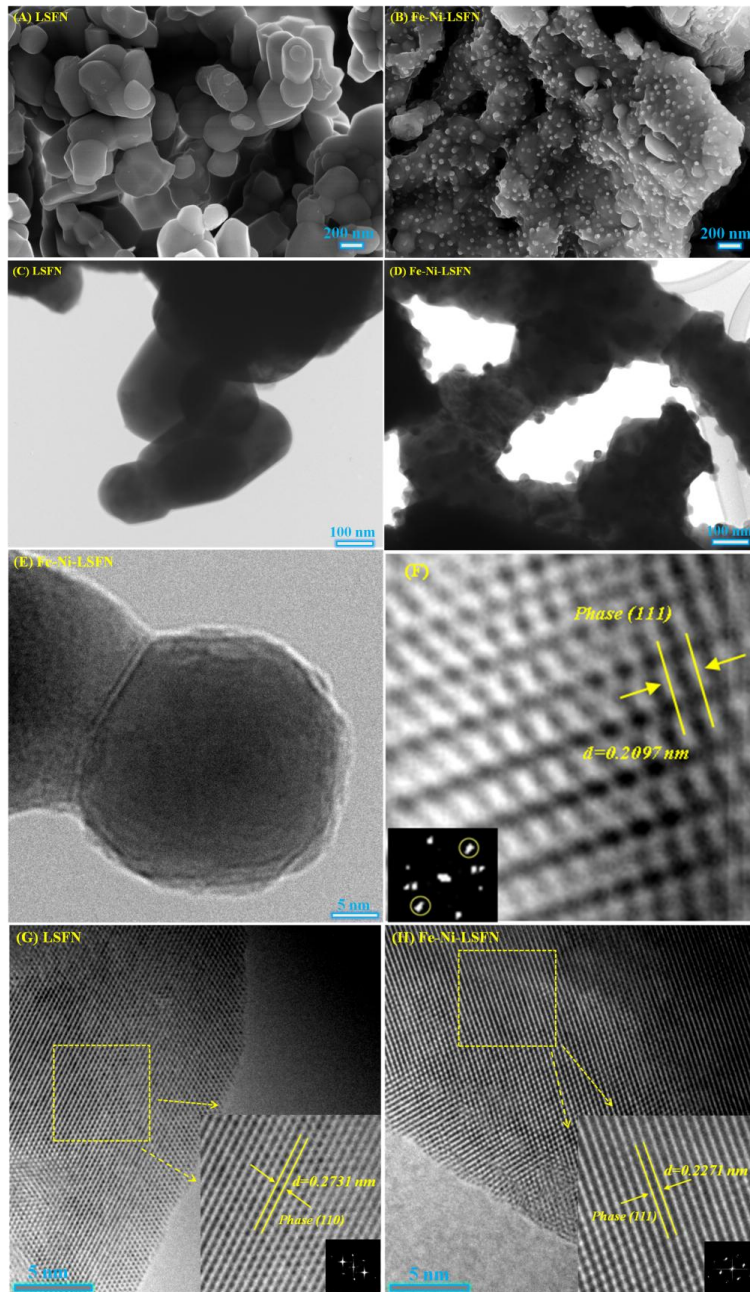
Figure 7.2 SEM images of LSFN powders (A) before and (B) after reduction in 5% H_2/N_2 at 850 °C for 2 h. Low-resolution Bright-field TEM images of LSFN powders (C) before and (D) after reduction. High-resolution TEM images of (E) LSFN after reduction and (F) corresponding crystal lattices of Fe-Ni alloy nanosphere. The crystal lattice analyses associated with fast Fourier transformation of LSFN (G) before and (H) after the reduction.

It was consistent with the value of 0.2749 nm, determined by XRD calculation at the angle of 32.5° with the Bragg's law. After the reduction, the measured inter-planar

spacing of LSFN backbone is 0.2271 nm, much closer to the value of 0.2243 nm for the lattice constant of (111) planes (Figure 7.2H). Therefore, the TEM analyses agreed well with the XRD results, an indication of the same crystal structure of LSFN backbone before and after the reduction.

7.3.2 Redox stability evaluation

Up to now, direct CO_2 electrolysis has still faced various challenges, including the restrictions of CO_2 adsorption and CO desorption on the surface of the cathode materials, which results in a decrease in CO_2 electrolysis performance. Grafting a solid amine to produce an alkaline surface is a preferred way to increase the chemical adsorption of CO_2 on the solid materials at a temperature below 300 °C. However, the temperature is far below the operating temperature of HT-SOEC.[47, 48] Recently, defected sites with oxygen vacancies on the surface of ceramic materials have been considered to be a promising route for the chemical adsorption of CO_2 since oxygen vacancies act as the host sites to accommodate the non-polar CO_2. Moreover, the chemically adsorbed CO_2 can be activated on oxygen vacancy sites, which favors CO_2 electrolysis.[49] We conducted TGA measurements from 20 to 900 °C in a 5% H_2/N_2 flow to confirm the oxygen vacancy formation of the as-prepared LSFN powders. The weight loss, together with the differential thermal analysis, was recorded in Figure 7.3A. The gradual weight loss (~0.24 wt%) below 378 °C can be ascribed to the desorption of H_2O. When the temperature was further increased, the weight of LSFN powders experienced a sharp drop followed by a continuous decrease during the ramping process. This region is referred to the oxygen vacancy formation or the decrease in the oxygen content because of the reduction of Ni- and Fe-containing oxides to the *in situ* exsolved Fe-Ni alloy. The sharp exothermic peaks in Figure 7.3A marked with "★" further confirm that oxygen vacancies were formed and the Fe-Ni

alloy was *in situ* exsolved from the LSFN backbone. After cooling down to room temperature, the gas was switched to air and the temperature was increased again to measure the stability during redox cycle (Figure S7.3). Apparently, the Fe-Ni-LSFN powders showed a prodigious weight gain during the ramping process, which is attributed to the re-oxidation of the Fe-Ni-LSFN to LSFN accompanied by an increase in oxygen content.

Table 7.1 Quantitative analysis of lattice oxygen and adsorbed oxygen on the surface of LSFN and Fe-Ni-LSFN.

Catalyst	Area of lattice oxygen	Area of adsorbed oxygen
LSFN	1073.8 (27.497%)	2831.9 (72.503%)
Fe-Ni-LSFN	921.4 (24.256%)	2877.7 (75.744%)

Figure 7.3B shows the weight analysis where a weight change of 3.68 wt% was observed in both the reduction and the re-oxidation processes, which corresponds to an oxygen loss and uptake tendency. On the basis of Wagner's theory,[50] the calculated non-stoichiometry δ is 0.485. It was further confirmed by the O 1s quantitative analysis of the surface oxygen vacancies with respect to lattice oxygen, as summarized in Table 7.1, where the percentage difference in the surface oxygen vacancies of LSFN and Fe-Ni-LSFN was 3.241% with a corresponding δ value of 0.451. This symmetry between the reduction and re-oxidation cycles suggests an excellent redox stability.[51]
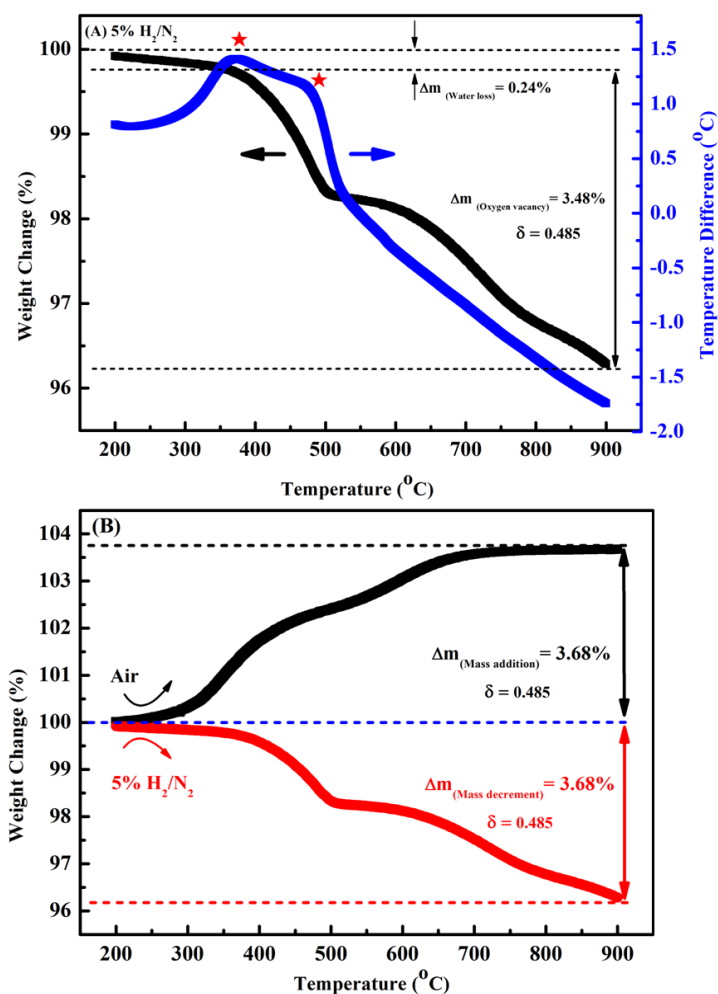
Figure 7.3 Thermogravimetric analysis testing. (A) Weight loss and differential thermal analysis of LSFN powders in 5% H_2/N_2 reducing atmosphere, and (B) Redox cycling ability test of LSFN powders, conducted first in a 5% H_2/N_2 reducing atmosphere in the ascending temperature range. After it cooled down, switched to air flow in the same ascending temperature range.

7.3.3 Catalytic activity and reversibility evaluation for CO_2 electrolysis

Since Fe-Ni-LSFN shows superior redox stability, the application of Fe-Ni-LSFN as a potential cathode material for CO_2 electrolysis in a YSZ supported electrolyte SOEC was investigated. CO_2/CO (70:30) was fed through the cathode compartment at a flow rate of 50 ml min^{-1} (the flow rate measured by a flow meter at the exit of the cell was around 40 ml min^{-1}), and the anode was exposed to ambient air. The measured OCVs of the HT-SOEC were 0.898 V and 0.872 V at 800 and 850 °C, respectively. Both

were slightly lower than the corresponding standard potentials [$E^o(T)$= 0.980 V at 800 °C and 0.957 V at 850 °C] for CO_2 electrolysis (Summarized in Table S7.1). Figure 7.4A presents the temperature dependent I-V curves for CO_2 electrolysis under the applied potential from -0.5 to -1.0 V (vs. OCV) at 800 and 850 °C. It was found that the Fe-Ni-LSFN with in $situ$ exsolved Fe-Ni alloy nanospheres was very effective to increase the cell performance for CO_2 electrolysis with a remarkable current density of 1.78 A cm^{-2} at 1.6 V and 850 °C, which is much higher than the reported values of ~0.9 A cm^{-2} in Ce-doped La(Sr)Cr(Fe) [52] and ~0.84 A cm^{-2} in PrBaMnO [7] at the same experimental conditions. Moreover, the I-V curves transitioned smoothly from SOFC mode to SOEC mode, indicating a good reversibility of the HT-SOEC with this catalyst. However, the current densities in the same potential range were much smaller at 800 °C than those obtained at 850 °C, especially at lower applied potentials. This suggests quite slow electrode reaction kinetics for CO_2 electrolysis at 800 °C, or that the CO_2 electrolysis reaction did not even proceed because of a large overpotential on the cathode.[7] To differentiate the contribution of different components in the cathode, Fe-Ni alloy, GDC (since it has been reported to be active for CO_2 reduction [53]) and LSFN were all fabricated for CO_2 electrolysis under the same experimental conditions, as shown in Figure 7.4B. It was found that LSFN was also very effective for increasing the cell performance for CO_2 electrolysis with a cathodic current density of 1.31 A cm^{-2} at 1.6 V and 850 °C. However, poor performances were observed for the cells with the GDC and Fe-Ni alloy materials, which are probably due to the low electronic conductivity of GDC and limited triple phase boundaries of Fe-Ni under the same conditions, respectively. To better understand the factor credited for the excellent electrochemical performance, EIS was conducted under the stable OCV conditions in CO_2/CO atmosphere. The Nyquist

plots obtained at 800 and 850 °C, together with the simulated data analyzed using ZSimpwin software and based on the inserted equivalent circuit, are shown in Figures 7.4C (a) and (b), respectively. Obviously, the experimentally measured results are all in consistence with the simulated ones, indicating the suitability of the equivalent circuit model proposed for the cell. Table 7.2 summarizes the values of the parameters of the equivalent-circuit, obtained by simulating the circuit model with EIS data at 800 and 850 °C.

Table 7.2 Simulated results of the electrolysis cell with the Fe-Ni-LSFN cathode in CO_2/CO (70:30) at 800 °C and 850 °C

Temperature (°C)	R_s (Ω cm^2)	R_1 (Ω cm^2)	R_2 (Ω cm^2)	R_P (Ω cm^2)
850 °C	0.317	0.126	0.146	0.272
800 °C	0.781	1.052	0.026	1.078

The real-axis intercept corresponds to the ohmic polarization of the cell, which is denoted as R_s and is mainly contributed by the resistance from ionic transportation in the electrolyte. The loops correspond to the R-CPE models of the anode activation kinetics (R_1) and the cathode activation kinetics (R_2), respectively. Remarkably, the total activation polarization (R_p) value of the cell in CO_2/CO (70:30) was as low as 0.272 Ω cm^2 at 850 °C, suggesting that the Fe-Ni-LSFN materials with *in situ* exsolved Fe-Ni alloy nanospheres provide fast electrode kinetics to proceed the CO_2 electrolysis reaction, this might confirm the potential use of Fe-Ni-LSFN for CO_2 electrolysis at high temperature (over 850 °C). When the temperature was decreased to 800 °C, polarization resistance of the cell increased dramatically to 1.078 Ω cm^2 whereas the value of R_s also rose to 0.781 Ω cm^2. This indicates that changes occurred

physically and chemically for both the electrolyte and the Fe-Ni-LSFN material between 800 and 850 °C, which resulted in fast electrode kinetics that largely accelerated the CO_2 electrolysis reaction at 850 °C. Consequently, the current density increased from 0.67 to 1.78 A cm^{-2} at 1.6 V.

Potential static tests for CO_2 electrolysis at different applied potentials (vs. OCV) at 800 and 850 °C were also performed. The products collected from the cathode compartment were analyzed with on-line GC in 20 min intervals. Apparently, the current densities of the cell increased in step with an increase in the applied potentials at 800 °C as shown in Figure S7.4A. The current densities at 850 °C displayed the same tendency as that at 800 °C at the potentials below 1.0 V (vs. OCV). However, a significant drop of the current density occurred at the potential of 1.2 V (vs. OCV) (Figure 7.4D), which is attributed to the effect of growing concentration polarization (large overpotential) because of the starvation of CO_2 in the feedstock and the restrained oxygen evolution at the anode compartment.[9] Figures 7.4E and S7.4B clearly show that CO_2 conversion increased as a function of applied potential (vs. OCV) for the CO_2 electrolysis. At the applied potential of 1.0 V (vs. OCV), the conversion of CO_2 to CO with the Fe-Ni-LSFN catalyst reached ~58.48% with a CO percentage of 70.93% in the outlet gases at 850 °C, which was over 2-fold higher than that achieved at 800 °C. Furthermore, production rates of CO and Faraday efficiencies at different applied potentials and temperatures were also calculated, as shown in Figure 7.4F. At 850 °C, the CO production rate reached 13.5 and 16.4 ml min^{-1} at the potentials of 0.8 and 1.0 V (vs. OCV), respectively. The production rate drops at 1.2 V (vs. OCV) is believed to be due to the starvation of CO_2 in the feedstock.
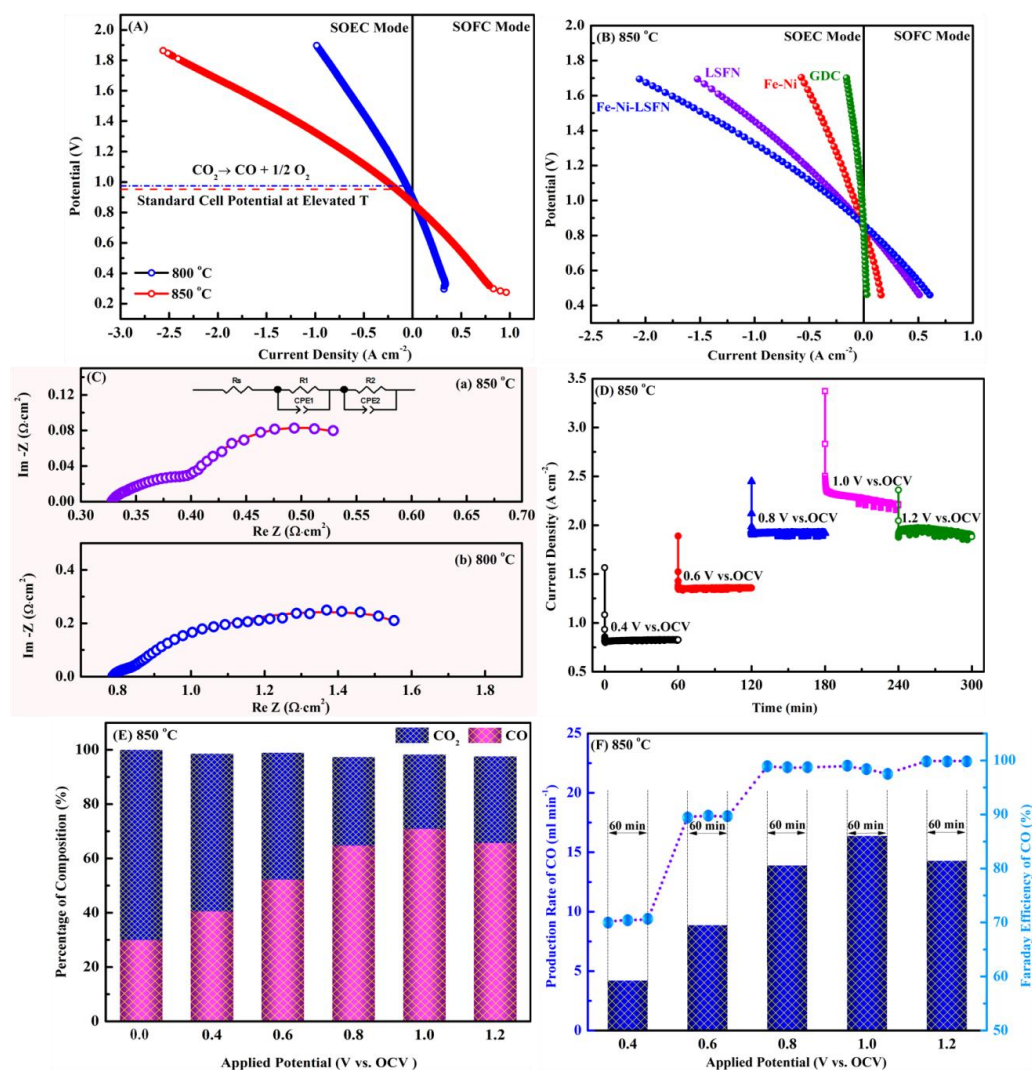
Figure 7.4 Electrochemical performances of the CO$_2$ electrolysis cell with Fe-Ni-LSFN cathode material. (A) Current-voltage curves of CO$_2$ electrolysis at 800 °C and 850 °C. (B) The comparison of current-voltage curves for CO$_2$ electrolysis using the Fe-Ni-LSFN, LSFN, GDC and Fe-Ni as cathode catalysts at 850 °C. (C) EIS curves of the cell with Fe-Ni-LSFN at 800 °C and 850 °C. The filled symbols reflect measured results and the lines represent the simulated results using the equivalent circuit inserted in the plot. (D) Potential static tests for CO$_2$ electrolysis at different applied potentials at 850 °C and (E) corresponding CO$_2$/CO compositions in the outlet gases. (F) Production rates and Faraday efficiencies of CO$_2$ electrolysis at different applied potentials at 850 °C. A GC run repeated every 10 min in 1 hour. The average value of two measurements was taken as the gas volumetric concentration for Faraday efficiency calculation, three average values are used for the plot.

126

To evaluate the electricity utilization efficiency, Faraday efficiencies were calculated based on the current densities and CO production rates. A GC run repeated every 10 min in 1 hour. The average value of two measurements was taken as the gas volumetric concentration for Faraday efficiency calculation. Clearly, the Faraday efficiencies undulated at ~89% at potentials below 0.8 V (vs. OCV). Nonetheless, they dramatically increased at potentials above 0.8 V (vs. OCV) and reached a peak value of ~99.5%, which is remarkably higher than the reported values with La(Sr)Cr(Mn) and La(Sr)Cr(Fe) cathode materials.[54-56] The extremely high conversion of CO_2 and Faraday efficiency with the Fe-Ni-LSFN cathode proves the excellent catalytic activity of the Fe-Ni-LSFN for the CO_2 electrolysis at high temperatures.

7.3.4 Stability and carbon deposition evaluation

Carbon deposition normally builds up on a conventional Ni-based catalyst in the form of carbon fibers,[57] which then simultaneously grows at the interface of the metal/perovskite backbone, resulting in the metal NPs uplifting from their original locations. This finally leads to the degradation of cell performance.[58] To assess the coking resistance and long-term durability of the cell with the Fe-Ni-LSFN cathode for CO_2 electrolysis, the cell current densities were recorded as a function of time at a constant applied potential of 0.6 V (vs. OCV) in a CO_2/CO (70:30) flow at 850 °C, as shown in Figure 7.5A. The current densities plateaued at ~1.37 A cm^{-2} for over 100 h, suggesting negligible degradations during the testing period. Meanwhile, corresponding gas composition in the cathode effluent was detected at intervals of 10 h with on-line GC, and corresponding Faraday efficiencies were found to fluctuate slightly at around 89.5%, indicating that the cell's capability for converting CO_2 to CO did not degrade. This long-term stability is owed to the excellent coking

resistance of the Fe-Ni-LSFN catalyst in the CO_2/CO atmosphere. The cathode cross section of the cell after the long-term stability test was further analyzed with the high-resolution SEM. Figure 7.5B clearly shows the excellent adhesions of the cathode, buffer layer and electrolyte. No delamination was observed in the interface region after the long term tests, which ensured efficient charge transfer during the cell operation. Moreover, the *in situ* exsolved Fe-Ni nanospheres were still uniformly socketed on the LSFN backbone without much agglomeration and no visible carbon deposition was found in the interface of the Fe-Ni alloy nanospheres and the LSFN perovskite backbone and elsewhere (Figure 7.5C). (Note: The backbones without socketed Fe-Ni alloy nanospheres were GDC since the cathode pastes were prepared by mixing LSFN with GDC in the weight ratio of 1:1 to further increase triple phase boundaries). *Ex-situ* Raman spectroscopy was also employed to further verify if there was any carbon deposition that had formed. Normally, two typical carbon features located at 1338 (D band) and 1568 cm^{-1} (G band) will be observed in the Raman spectra if coking occurs. D band is the defect-induced Raman feature, while G band refers to the C-C stretching which is common to all sp^2-bonded carbons.[31] Based on the Raman spectra collected from the cathode surface before [Figure 7.5D (a)] and after [Figure 7.5D (b)] the long-term stability test, no notable carbon peaks were detected. The small peak at 1100 cm^{-1} can be assigned to $SrCO_3$,[8] indicating that trace amounts of $SrCO_3$ formed on the surface of the cathode. This is correlated to the surface segregation of Sr in LSFN as it has recently been suggested for $La_{0.6}Sr_{0.4}Co_{0.2}Fe_{0.8}O_3$ perovskites.[59, 60] However, the main phase of LSFN is still $LaFeO_3$ perovskite. These results confirm that the CO_2 electrolysis cell with Fe-Ni-LSFN cathode has an excellent coking resistance and good stability towards CO_2 conversion.
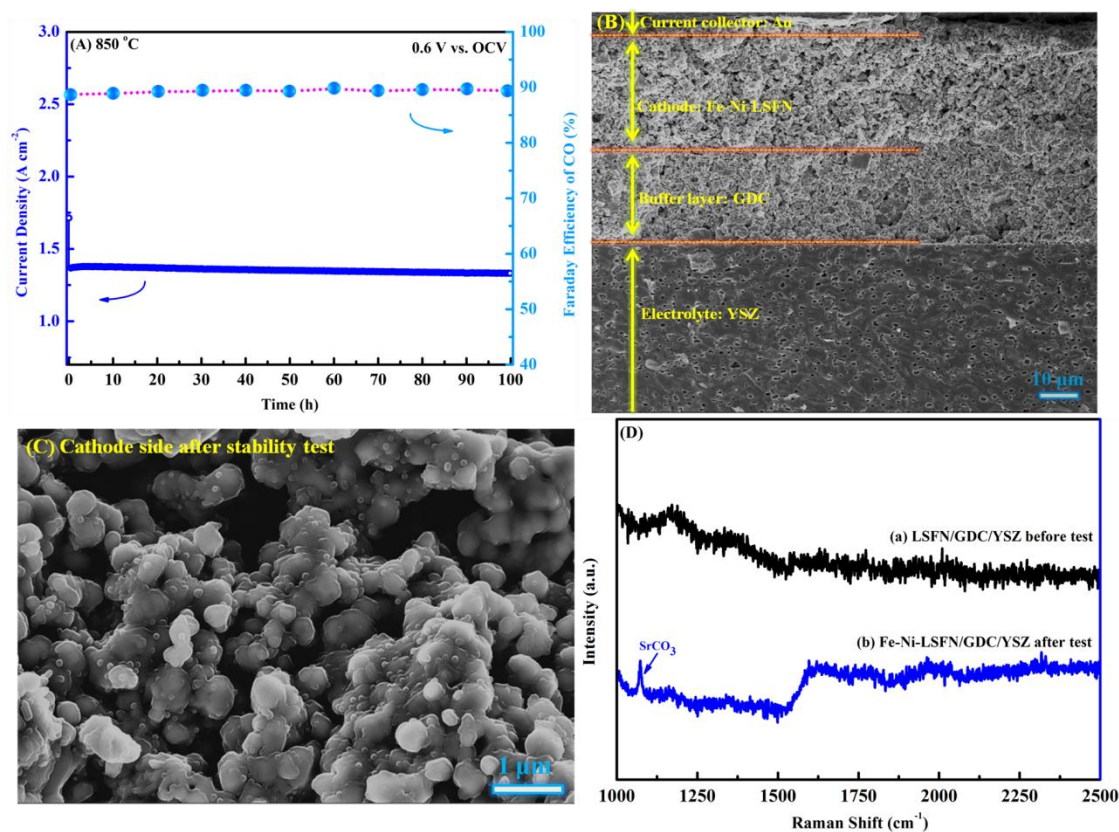
Figure 7.5 (A) Long-term stability of the CO_2 electrolysis cell with Fe-Ni-LSFN cathode material under a constant applied potential of 0.6 V (vs. OCV) at 850 °C and corresponding Faraday efficiencies with the interval of 10 h, the flow rate of CO_2 was 50 ml min^{-1} and the anode was exposed to air. (B) SEM images of cathode cross section and (C) cathode catalyst after stability test and (D) Raman spectra collected from cathode surface (a) before and (b) the long-term stability test.

Finally, we explored the mechanism credited for the excellent electrochemical performance and coking resistance of the Fe-Ni-LSFN cathode for the CO_2 electrolysis. It is well known that the CO_2 electrolysis reaction can only occur at the triple phase boundaries (TPBs), where the three important phases (CO_2, the electronic conductor and ion conductor) are all in contact. For the purpose of proceeding the CO_2 electrolysis reaction effectively, three essential aspects can be attempted to maximize the number of reactive sites, including 1) increasing the activated reactant (CO_2), 2) enhancing the ionic conductivity and 3) improving the electronic conductivity. The XRD results have verified that the substitution of Sr and Ni in the

lattice of $LaFeO_3$ resulted in the shift of reflections to higher diffraction angles after annealing in air, indicative of increased unit cell parameter and lattice distortion. More importantly, oxygen vacancies were continuously introduced until a limit in the number of introduced oxygen vacancies ($\delta = 0.485$) was reached during the reduction, as confirmed by the TGA analysis and the O 1s quantitative analysis of the surface oxygen vacancies. The introduced oxygen vacancies could effectively enhance the chemical adsorption CO_2, because CO_2 molecules could be easily incorporated into the oxygen vacancy sites and form chemical bonding at high temperatures [48] with oxygen vacancies acting as host sites to accommodate the non-polar CO_2. The chemically adsorbed CO_2 can also be activated on oxygen vacancy sites.[48] What's more important is that the introduced high concentration of oxygen vacancies allows LSFN backbone to exhibit high ionic conductivity. Another noteworthy aspect is the enhancement of electronic conductivity. As reported, the larger A-site cations in the lattice terminate at the AO surface, which was further confirmed by the atomic ratios of Fe/Sr derived from XPS survey spectra. The corresponding values of Fe/Sr for LSFN and Fe-Ni-LSFN were respectively around 1/3 and 5/9, both of which were less than the stoichiometric ratio of 2/1. Qualitatively this means that the surface region is A-site enrichment, which effectively obstructs B-sites from contacting with CO_2. Generally, the less exposed B-sites transition metal cations are responsible for the catalytic activity and electron transfer.[61] Therefore, the terminated AO surface inhibits electron transfer from the perovskite to CO_2 species, resulting in a poor cell performance. However, the continued reduction results in the exsolution of a proportion of the B-site dopants (Fe and Ni) and their simultaneous reduction to metal after a limit in the number of introduced oxygen vacancies is reached since the LSFN backbone can not accommodate any more vacancies.[62] The surface nucleation process

drains exsolved ions from the nearby perovskite lattice, which makes the additional reducible ions diffuse to the surface to balance out the compositional gradient and promote the growth of the metal clusters. The exsolving process directly results in the enhancement of the electronic conductivity.[61] These three aspects synergistically ensure the sufficient reactive sites of the Fe-Ni-LSFN and consequently, the cell performance, as confirmed by the current densities' comparison of LSFN (1.31 A cm^{-2}) and Fe-Ni-LSFN (1.78 A cm^{-2}). Furthermore, the exsolved bimetallic nanospheres maintain crystallographic coherence with the host lattice, exhibiting a stronger adhesion with the host lattice backbone.[58] The strong interaction between the *in situ* exsolved Fe-Ni alloy nanospheres and the perovskite backbone prevents carbon formation and the subsequent Fe-Ni alloy nanospheres uplifting. Thus, we concluded that the perovskite backbone, together with the *in situ* exsolved Fe-Ni alloy nanospheres, can synergistically act as a highly stable and efficient catalyst, further boosting the catalytic performance and coking resistance of the HT-SOEC for CO_2 electrolysis.

7.4 Conclusions

The present work demonstrates that the newly developed *in situ* exsolved Fe-Ni alloy nanospheres uniformly socketed on the oxygen deficient perovskite acted as a highly stable and efficient catalyst to effectively boost the catalytic performance of CO_2 electrolysis in a HT-SOEC. The cathode kinetics for CO_2 electrolysis was significantly improved with a remarkably enhanced current density of 1.78 A cm^{-2}, together with a high Faraday efficiency (98.8%), achieved at 1.6 V and 850 °C. Moreover, the symmetry between reduction and re-oxidation cycles of this material indicates its exceptional redox reversibility. It was also verified that the CO_2 electrolysis cell with the Fe-Ni-LSFN cathode could be steadily conducted for over

100 h without any discernible carbon deposition. This study, herein, demonstrates that the novel *in situ* exsolved Fe-Ni alloy nanospheres uniformly socketed on the oxygen deficient perovskite catalyst are highly effective for CO_2 electrolysis, and could be used as a promising cathode material.

7.5 References

(1) Hester, R. E.; Harrison, R.M. *Carbon capture: sequestration and storage*, RSC Publishing **2010**, *1*.

(2) Vasireddy, S.; Morreale, B.; Cugini, A.; Song, C. S.; Spivey, J. J. Energy Environ. Sci. **2011**, *4*, 311.

(3) Xie, K.; Zhang, Y.; Meng, G.; Irvine, J. T. Energy Environ. Sci. **2011**, *4*, 2218.

(4) Mao, X.; Hatton, T. A. Ind. Eng. Chem. Res. **2015**, *54*, 4033.

(5) Graves, C.; Ebbesen, S. D.; Jensen, S. H.; Simonsen, S. B.; Mogensen, M. B. Nat. Mater. **2015**, *14*, 239.

(6) Bierschenk, D. M.; Wilson, J. R.; Barnett, S. A. Energy Environ. Sci. **2011**, *4*, 944.

(7) Shin, T. H.; Myung, J. H.; Verbraeken, M.; Kim, G.; Irvine, J. T. Faraday Discuss. **2015**, *182*, 227.

(8) Wang, S.; Tsuruta, H.; Asanuma, M.; Ishihara, T. Adv. Energy Mater. **2015**, *5*.

(9) Ebbesen, S. D.; Jensen, S. H.; Hauch, A.; Mogensen, M. B. Chem. Rev. **2014**, *114*, 10697.

(10) Bidrawn, F.; Kim, G.; Corre, G.; Irvine, J. T. S.; Vohs, J. M.; Gorte, R. J. Electrochem. Solid-State Lett. **2008**. *11*, 167.

(11) Jensen, S. H.; Larsen, P. H.; Mogensen, M. Int. J. Hydrogen Energ. **2007**, *32*, 3253.

(12) Ebbesen, S. D.; Mogensen, M. J. Power Sources **2009**, *193*, 349.

(13) Pihlatie, M. H.; Kaiser, A.; Mogensen, M.; Chen, M. Solid State Ionics **2011**, *189*, 82.

(14) Pihlatie, M. H.; Frandsen, H. L.; Kaiser, A.; Mogensen, M. J. Power Sources **2010**, *195*, 2677.

(15) Yue, X.; Irvine, J.T. J. Electrochem. Soc. **2012**, *159*, 442.

(16) Murray, E. P.; Tsai, T.; Barnet, S. Nature **1999**, *400*, 649.

(17) McIntosh, S.; Gorte, R.J. Chem. Rev. **2004**, *104*, 4845.

(18) Yue, X.; Irvine, J.T. Solid State Ionics **2012**, *225*, 131.

(19) Tao, S.; Irvine, J.T. Nat. Mater. **2003**, *2*, 320.

(20) Yue, X.; Irvine, J.T. Electrochem. Solid-State Lett. **2012**. *15*, 31.

(21) Kitla, A.; Safonova, O. V.; Föttinger, K. Catal. Lett. **2013**, *143*, 517.

(22) Gonzalez-delaCruz, V. M.; Pereniguez, R.; Ternero, F.; Holgado, J. P.; Caballero, A. J. Phys. Chem. C **2012**. *116*, 2919.

(23) Tao, F. F. Chem. Soc. Rev. **2012**. *41*, 7977.

(24) Lu, Z. G.; Zhu, J. H.; Bi, Z. H.; Lu, X. C. J. Power Sources **2008**, *180*, 172.

(25) An, W.; Gatewood, D.; Dunlap, B.; Turner, C. H. J. Power Sources **2011**, *196*, 4724.

(26) Yang, C.; Yang, Z.; Jin, C.; Xiao, G.; Chen, F.; Han, M. Adv. Mater. **2012**, *24*, 1439.

(27) Fu, C. J.; Chan, S. H.; Ge, X. M.; Liu, Q. L.; Pasciak, G. Int. J. Hydrogen Energ. **2011**, *36*, 13727.

(28) Min, J. -S.; Mizuno, N. Catal. Today **2001**. *66*, 47.

(29) Neagu, D.; Tsekouras, G.; Miller, D. N.; Ménard, H.; Irvine, J. T. Nat. Chem. **2013**, *5*, 916.

(30) Yang, C.; Li, J.; Lin, Y.; Liu, J.; Chen, F.; Liu, M. Nano Energy **2015**, *11*, 704.

(31) Liu, S.; Chuang, K.T.; Luo, J.-L. ACS Catal. **2016**, *6*, 760.

(32) ua n, C.; Tong, J.; Shang, M.; Ni ode ms i , S.; Sanders, M.; Ricote, S.; O'Hayre, R. Science **2015**, *349*, 1321.

(33) Yang, L.; Liu, Z.; Wang, S.; Choi, Y.; Zuo, C.; Liu, M. J. Power Sources **2010**, *195*, 471.

(34) Montini, T.; Bevilacqua, M.; Fonda, E.; Casula, M.; Lee, S.; Tavagnacco, C.; Gorte, R.; Fornasiero, P. Chem. Mater. **2009**, *21*, 1768.

(35) Kerstan, M.; Müller, M.; Rüssel, C. Solid State Sci. **2014**, *38*, 119.

(36) Liu, P.; Kong, J.; Liu, Q.; Yang, X.; Chen, S. J. Solid State Electr. **2014**, *18*, 1513.

(37) Jiang, X. Z.; Stevenson, S. A.; Dumesic, J. J. Catal. **1985**, *91*, 11.

(38) Munroe, P.; Hatherly, M. Scripta Metall. Mater. **1995**, *32*, 93.

(39) Sun, Y. F.; Li, J. H.; Cui, L.; Cui, S. H.; Li, J.; Luo, J. L. Nanoscale **2015**, *7*, 11173.

(40) Nishihata, Y.; Mizuki, J.; Akao, T.; Tanaka, H.; Uenishi, M.; Kimura, M.; Okamoto, T.; Hamada, N. Nature 2002, *418*, 164.

(41) Yin, J. W.; Yin, Y. M.; Zhang, C.; Minh, N. Q.; Ma, Z. F. J. Phys. Chem. C 2014, *118*, 13357.

(42) Jin, F.; Xu, H.; Long, W.; Shen, Y.; He, T. J. Power Sources **2013**, *243*, 10.

(43) Devaux, R.; Vouagner, D.; De Becdelievre, A. M.; Duret-Thual, C. Corros. Sci., **1994**, *36*, 171.

(44) Mansour, A. N. Surf. Sci. Spectra **1994**. *3*, 221.

(45) Zhang, J.; Wang, H.; Dalai, A.K. J. Catal. **2007**. *249*, 300.

(46) Takanabe, K.; Nagaoka, K.; Nariai, K.; Aika, K. I. J. Catal. **2005**. *232*, 268.

(47) Hicks, J. C.; Drese, J. H.; Fauth, D. J.; Gray, M. L.; Qi, G.; Jones, C. W. J. the Am. Chem. Soc. **2008**, *130*, 2902.

(48) Qi, W.; Gan, Y.; Yin, D.; Li, Z.; Wu, G.; Xie, K.; Wu, Y. J. Mater. Chem. A **2014**, *2*, 6904.

(49) Nolan, M. J. Phys. Chem. C **2009**. *113*, 2425.

(50) Wagner, C. Prog Solid State Ch. **1971**, *6*, 1.

(51) Sengodan, S.; Choi, S.; Jun, A.; Shin, T. H.; Ju, Y. W.; Jeong, H. Y.; Kim, G. Nat. Mater. **2015**, *14*, 205.

(52) Zhang, Y. Q.; Li, J. H.; Sun, Y. F.; Luo, J. L. ACS Appl. Mater. Interfaces **2016**, *8*, 6457.

(53) Green, R. D.; Liu, C.-C; Adler, S. B. Solid State Ionics, **2008**, *179*, 647.

(54) Xu, S.; Chen, S.; Li, M.; Xie, K.; Wang, Y.; Wu, Y. J. Power Sources **2013**. *239*, 332.

(55) Li, H.; Sun, G.; Xie, K.; Qi, W.; Qin, Q.; Wei, H.; Wu, Y. Int. J. Hydrogen Energ. **2014**. *39*, 20888.

(56) Yao, W.; Duan, T.; Li, Y.; Yang, L.; Xie, K. New J. Chem. **2015**. *39*, 2956.

(57) Blinn, K. S.; Abernathy, H.; Li, X.; Liu, M.; Bottomley, L. A.; Liu, M. Energy Environ. Sci. **2012**. *5*, 7913.

(58) Neagu, D.; Oh, T. S.; Miller, D. N.; Ménard, H.; Bukhari, S. M.; Gamble, S. R.; Irvine, J. T. Nat. Commun. **2015**, *6*, 8120.

(59) Ten Elshof, J.; Lankhorst, M.; Bouwmeester, H. J. Electrochem. Soc. **1997**, *144*, 1060.

(60) Ten Elshof, J.; Bouwmeester, H.; Verweij, H. Solid State Ionics **1996**, *89*, 81.

(61) Irvine, J. T. S.; Neagu, D.; Verbraeken, M. C.; Chatzichristodoulou, C.; Graves, C.; Mogensen, M. B. Nat. Energ. **2016**, *1*, 15014.

(62) Tsekouras, G.; Neagu, D.; Irvine, J. T. Energy Environ. Sci. **2013**, *6*, 256.

7.6 Supporting information

7.6.1 The specifications of chemicals and gases:

$La(NO_3)_4 \cdot 6H_2O$ (Fisher Scientific Company, 99.995%); $Sr(NO_3)_2$ (Fisher Scientific Company, Crystalline); $Fe(NO_3)_3 \cdot 9H_2O$ (Fisher Scientific Company, Crystalline); $Co(NO_3)_3 \cdot 6H_2O$ (ACROS ORGANICS, 99+%); $Ni(NO_3)_2 \cdot 6H_2O$ (Fisher Scientific Company, 99.9%); NH_3H_2O (ACROS ORGANICS, 28-30%);

Citric acid (Fisher Scientific Company, 99.9%); Alpha-terpineol (ACROS ORGANICS, 99+%); Cellulose (ACROS ORGANICS, 99%); 2-isopropanol (Fisher Scientific Company, 70%); 1-butanol (Sigma Aldrich, 99.4+%); Benzyl butyl phthalate (BBP, ACROS ORGANICS, 97%); Ethylenediamine tetraacetic acid (EDTA, Fisher Scientific Company, 99.6%);

CO_2/CO in the ratio of 70:30 (Prexair Company, Canada); 5% H_2/N_2 (Prexair Company, Canada).

7.6.2 Preparation of the electrode catalyst pastes

Both cathode and anode pastes were prepared by ball milling the powders and a home-made glue with a weight ratio of 1.7:1 for 3 h at a rotation speed of 300 r/min. The home-made glue was prepared via mixing 1-butanol (2g), Benzyl butyl phthalate (BBP) (2g), Ethyl cellulose (0.7g), and α-terpineol (15g) together. The full dissolution of cellulose was obtained by heating the mixture to 80 °C under vigorous agitation.

7.6.3 Supporting table and figures

Table S7.1 Thermodynamic data for CO_2 electrolysis at different temperatures from the HSC software

CO$_2$ Electrolysis: CO (g) + 0.5 O$_2$ (g) → CO$_2$ (g)				
T (°C)	ΔH (kJ)	ΔG (kJ)	Equilibrium constant K	Reversible potential E (V)
800	-282.316	-189.206	1.623E+9	0.980
850	-282.111	-184.873	3.969E+08	0.957
900	-281.899	-180.548	1.095E+08	0.936
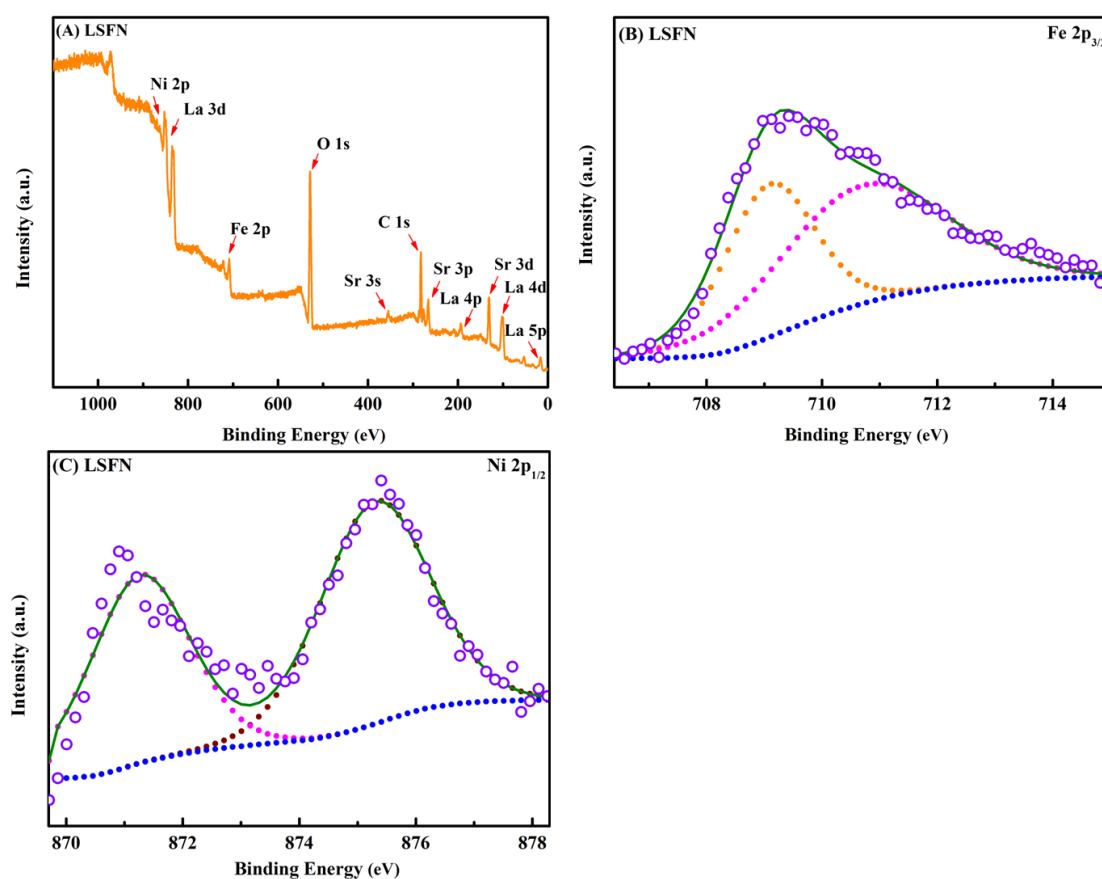
Figure S7.1 (A) Representative XPS of LSFN powders, (B) Fe 2p$_{3/2}$ spectra and (C) Ni 2p$_{1/2}$ spectra before the reduction.
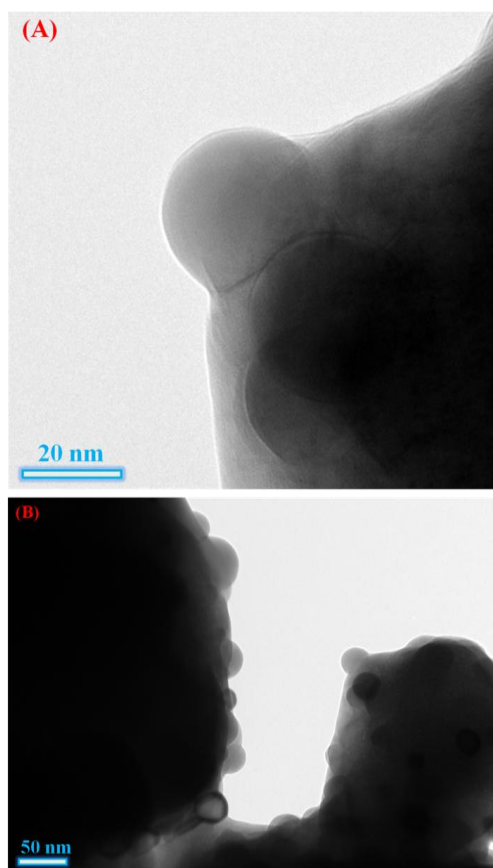
Figure S7.2 High-resolution TEM images of Fe-Ni-LSFN powders after reduction with the scale bar of (A) 20 nm and (B) 50 nm.
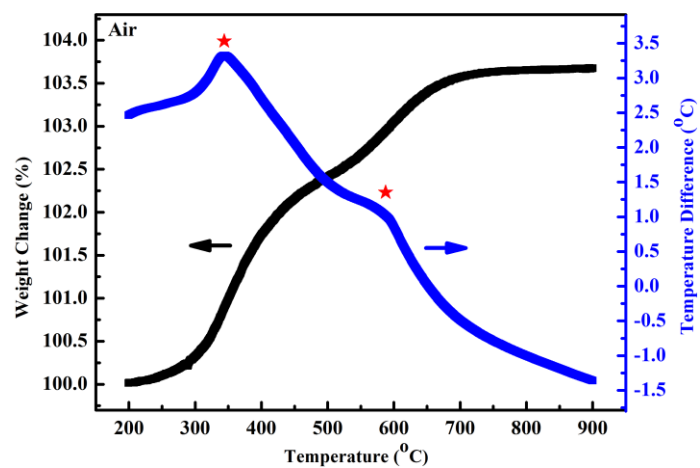
Figure S7.3 Thermogravimetric analyses testing. Weight loss and differential thermal analyses of Fe-Ni-LSFN powders in air from 20 to 900 °C.
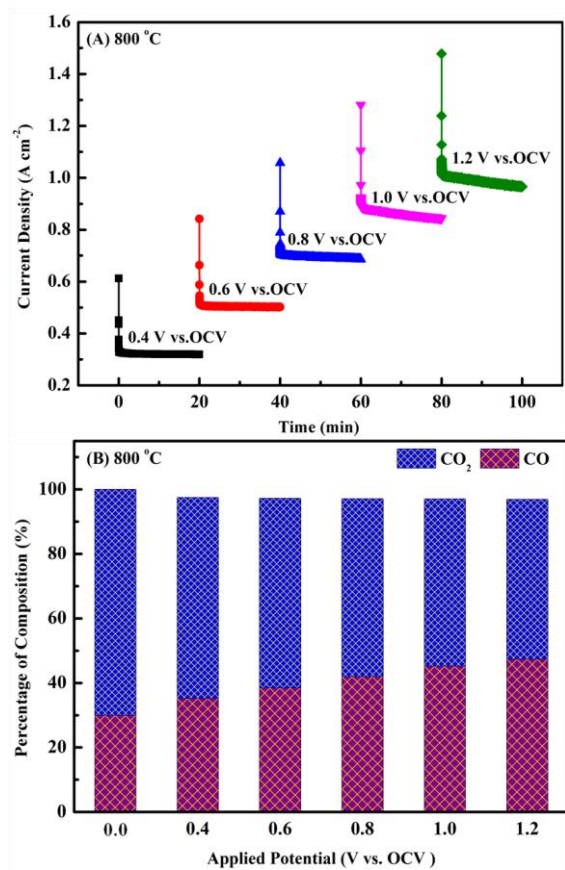
Figure S7.4 Electrochemical performances of the CO_2 electrolysis cell with Fe-Ni-LSFN cathode material. (A) Potential static tests for CO_2 electrolysis at different applied potentials at 800 °C and (B) the corresponding CO_2/CO compositions in the outlet gases.

Chapter 8. CO$_2$-to-CO Conversion on Layered Perovskite with *in Situ* Exsolved Co-Fe Alloy Nanoparticles: An Active and Stable Cathode for Solid Oxide Electrolysis Cell

Abstract: To relieve the greenhouse effects due to the massive emission of CO$_2$, efficient reduction on carbon footprint and effective utilization of CO$_2$ have been a crucial research field worldwide in the past few decades. Novel catalysts efficiently facilitating the conversion of CO$_2$ into target chemicals are highly desirable. Herein, we developed a new cathode with *in situ* exsolved Co-Fe alloy nanoparticles embedded in an active $(Pr_{0.4}Sr_{0.6})_3(Fe_{0.85}Mo_{0.15})_2O_7$ (PSFM) double-layered perovskite backbone (Co-Fe-PSFM), which acts as a more stable and efficient catalyst to promote the CO$_2$ electrolysis in a high temperature solid oxide electrolysis cell (SOEC) compared to the $Pr_{0.4}Sr_{0.6}Co_{0.2}Fe_{0.7}Mo_{0.1}O_{3-\delta}$ (PSCFM) cubic perovskite.
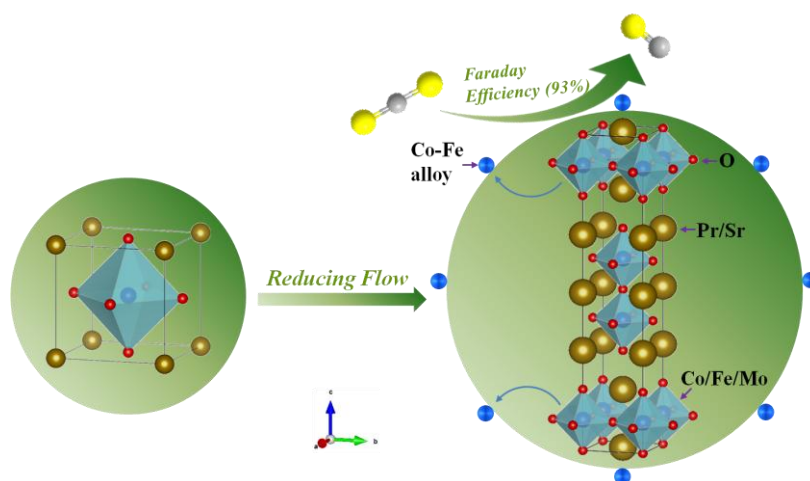
This newly developed material shows a superb redox reversibility between reduction and re-oxidation cycles. Additionally, a remarkable current density of 1.01 A cm^{-2} of the SOEC with Co-Fe-PSFM cathode in conjunction with an impressive polarization area-specific resistance (ASR) as low as 0.455 Ω cm^2 of the cathode was achieved at

1.6 V and 850 °C. In particular, a high value of Faraday efficiency (~93%) was achieved at 0.8 V (vs. OCV) and 850 °C. More importantly, the cell with the new cathode shows no observable degradation and carbon formation at 850 °C over a period of 100 h at a constant applied potential. The improved oxygen vacancies resulted from the exsolving process, and phase change (cubic perovskite to double-layered perovskite), together with the exsolved Co-Fe alloy nanoparticles, contribute to the improved catalytic activity, high Faraday efficiency, good stability, and excellent coking resistance for CO_2 electrolysis. In light of the properties above, double-layered PSFM socketed with Co-Fe alloy nanoparticles is an attractive ceramic material for intermediate/high temperature applications, especially for CO_2 electrolysis.

8.1. Introduction

The increasing utilization of fossil fuels has brought about a record-breaking level of atmospheric CO_2, which adversely and uncontrollably impacts the global climate. Global warming, which is attributed to the significantly rising level of the atmospheric CO_2, has become a serious environmental concern [1]. To attenuate the greenhouse effects, efficient technologies to significantly reduce CO_2 emission and effectively utilize CO_2 have been the focus of recent research. Some of the traditional CO_2 conversion methods are infeasible for large-scale industrial implementations, mainly because of their high energy consumption and/or low conversion efficiency [2, 3]. Therefore, highly selective and energy-efficient CO_2 conversion method is a great stride towards the effective CO_2 capturing and utilization. Recently, solid oxide electrolysis cell (SOEC) has been considered to be advantageous for the efficient electrochemical conversion of CO_2 into CO because it utilizes renewable energy, such as wind power and solar energy. Conventionally, highly active anode materials

employed in solid oxide fuel cell (SOFC) are preferentially considered as the potential cathodes in SOEC [4, 5]. However, it is not always feasible to use the SOFC anode materials directly for SOEC. For example, the Ni/YSZ composite anode, an active catalyst for H_2 oxidation in SOFC, suffers from the inherent redox instability, because Ni is oxidized to NiO when exposed to oxidizing flow, which leads to a loss of the electrical conductivity [6]. Additionally, carbon accumulation lowers the cell performance and even causes the delamination of the cathode from the electrolyte [7]. Therefore, developing new catalysts for CO_2 electrolysis in high temperature SOEC capable of efficient conversion of CO_2 to CO is highly desirable.

Cathode materials based on doped lanthanum chromates and lanthanum ferrites have been widely studied for direct CO_2 electrolysis, such as La(Sr)Fe(Mn) [12, 13], La(Sr)Cr(Mn) [8-11], La(Sr)Cr(Fe) [14] and Ce [15] or Ti [16] doped La(Sr)Cr(Fe). These cathode materials have been demonstrated to be the potential catalysts for CO_2 electrolysis because of their good stability in carbon-abundant environment. However, insufficient catalytic activity and low electrical conductivity consequently lead to poor electrochemical performances. Recently, double-layered perovskite, $PrBaMn_2O_{5+\delta}$, was found to enhance electrocatalytic activity for CO_2 electrolysis. Since it contains the multivalent transition metal cation (Mn), which can provide higher electrical conductivity and maintain a larger content of oxygen vacancy than perovskite-type materials, it contributes a faster oxygen ion diffusion [17]. On one hand, oxygen vacancies that act as host sites to accommodate the non-polar CO_2 could effectively facilitate CO_2 chemical adsorption at high temperature [18]. On the other hand, the chemically adsorbed CO_2 can be activated on oxygen vacancy sites, which favors the CO_2 electrolysis.

It is well-known that the transition metal cations on the B-site are responsible for the catalytic activity and electron transfer [19]. However, the larger A-site cations in the lattice (both cubic perovskite and double-layered perovskite) are energetically favorable to be terminated at the AO surface [20, 21], and A-sites effectively block B-sites from contacting with CO_2 because less B-sites are exposed to the free surface [19]. Consequently, this contributes to a poor electrochemical performance. To tackle this issue, we proposed to exsolve metal/bimetal nanoparticle *in situ* on the surface of the host lattice because the exsolved ions from the double-layered perovskite lattice promote the diffusion of reducible ions to the surface, thus facilitating the growth of the metal/bimetal nanoparticle. The *in situ* exsolved metal/bimetal nanoparticles improve both the electronic conductivity and the catalytic activity. Co-Fe bi-metallic alloy, acting as an excellent electrochemical catalyst, has been widely studied as anode materials in SOFC, since both Co and Fe have been considered as effective alloying elements to improve the electrochemical performance in SOFC [22-24]. Co possesses almost the same catalytic activity as Ni and has less possibility towards carbon formation. Another well-studied element, Fe, also shows excellent coking resistance [25]. According to the binary Co-Fe phase diagram [26], a complete solid solution in the form of Co-Fe alloy is obtainable at the temperature range of 730-985 °C and upon cooling to below 730 °C, an ordering reaction occurs. Such ordering reactions could modify the catalytic activity of the alloy [23]. More importantly, electrical conductivity and stability can be largely enhanced in a wide range of oxygen partial pressures by the introduction of Mo at intermediate temperature [27]. Besides, Mo-doping can strongly affect the iron oxidation states and the simultaneous formation of oxygen defects in the perovskite which are responsible for the catalytic activity [28].

Herein, we developed a $(Pr_{0.4}Sr_{0.6})_3(Fe_{0.85}Mo_{0.15})_2O_7$ (PSFM) double-layered perovskite with *in situ* exsolved Co-Fe alloy nanoparticles (Co-Fe-PSFM) for CO_2 electrolysis by reducing $Pr_{0.4}Sr_{0.6}Co_{0.2}Fe_{0.7}Mo_{0.1}O_{3-\delta}$ (PSCFM) in a 5% H_2/N_2 flow at 850 °C. Both PSCFM and Co-Fe-PSFM were fabricated as the cathodes in an yttria stabilized zirconia (YSZ) electrolyte supported SOEC. The catalytic activities and Faraday efficiencies of the PSCFM and Co-Fe-PSFM for CO_2 electrolysis at 850 °C were studied. The redox stability and coking resistance of the Co-Fe-PSFM were also evaluated.

8.2. Results and Discussion

8.2.1 Characterizations of Synthesized Materials

Polycrystalline perovskite powders of PSCFM were prepared using a modified sol-gel method, as described elsewhere [29]. The as-prepared PSCFM showed a pure single phase without any impurities, as confirmed by X-ray diffraction (XRD) in Figure 8.1A(a). It has a cubic structure [space group: Pm-3m(221)] with a lattice constant of a = b = c = 3.8762 Å. Comparing the XRD patterns of PSFM after reduction in H_2 flow for 2 h with those of PSCFM (Figure 8.1A(b)), it is found that the PSFM possesses a tetragonal structure with lattice parameters of a = b = 3.853 Å, c = 20.149 Å, and a space group of I4/mmm (139). The splitting of the diffraction peaks observed in Figure 8.1A(b) indicates a different phase structure of the PSFM. The two weak peaks, marked with "Δ", correspond to the crystal faces of (110) and (200) of the Co-Fe alloy, respectively [30]. The lattice space between the two parallel planes derived from the local magnification region of the Co-Fe alloy nanoparticles in Figure 8.1B is 0.212 nm, as shown in Figure 8.1C. It is quite close to the calculated value of 0.202 nm at (1 1 0) planes of the Co-Fe alloy in the space group of [Pm-3m (221)]. This in

turn confirms that Co in conjunction with Fe could be *in situ* exsolved in the form of alloy.
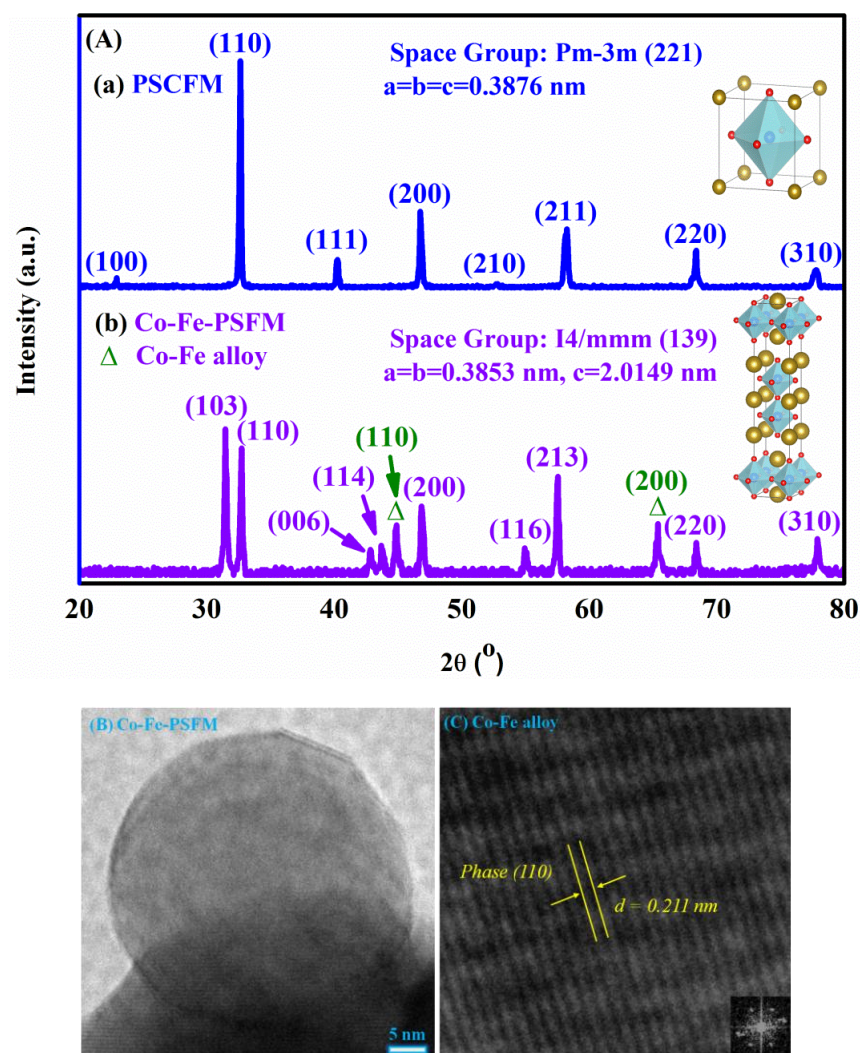
Figure 8.1 (A) X-ray diffraction patterns of PSCFM (a) before and (b) after sintering at 850 °C in 5% H_2/N_2 atmosphere for 2 h. (B) High-resolution TEM image of Co-Fe-PSFM powders and (C) the corresponding crystal lattice of Co-Fe alloy nanoparticle.

The differences in structure and lattice parameters of the two materials support the fact that the cubic PSCFM was phase-changed to double-layered PSFM during the exsolving process under a reducing flow [30]. Figures 8.2A and 8.2B show the microstructures of the as-obtained porous PSCFM and Co-Fe-PSFM, respectively. Apparently, the PSCFM particles with an average diameter of ~300 nm are well

interconnected (Figure 8.2A). This ensures the high mechanical strengths and fast gas diffusivity. After its exposure in H_2 at 900 °C for 2 h, it clearly shows that the morphology of the material differs from that of the one sintered in air (Figure 8.2A), some nanoparticles with an average diameter of ~50 nm exsolved and socketed on the double-layered PSFM backbone, as shown in Figure 8.2B. The morphologies and compositions of the Co-Fe-PSFM were also characterized by low-resolution transmission electron microscope (TEM) and high resolution TEM with the results shown in Figures 8.2(C-D). The low-resolution TEM image of the Co-Fe-PSFM revealed that the surface of the PSFM backbone was embedded with some nanoparticles (Figure 8.2C). A selected nanoparticle was magnified with high resolution, which further confirmed that the *in situ* exsolved particle was well socketed on the host perovskite (Figure 8.2D). This phenomenon was verified by the energy-dispersive X-ray spectroscopy (EDS) elemental mappings (Figures 8.2D and S8.1) and EDS spectra (Figure 8.2E). The EDS spectrum confirmed the presence of Pr, Sr, Co, Fe and Mo in the Co-Fe-PSFM, as shown in Figure 8.2E. It can be seen in Figures 8.2D and S8.1, both Co (magenta) and Fe (red) elements were distributed uniformly in the exsolved nanoparticle. This is consistent with the XRD result, indicating that only Co and Fe nanoparticles can be exsolved *in situ* from the PSFM backbone under the reducing condition. In contrast, the signals of element distributions of Pr (dark cyan), Sr (green) and Mo (yellow) were infinitesimal and thus negligible. On the basis of above analysis, we concluded that the Co-Fe exsolving process on the surface of the PSFM backbone and the phase change occurred simultaneously under the reducing flow at elevated temperature. Besides the crystallographic structure and morphology, X-ray photoelectron spectroscopy (XPS) measurements were conducted to analyze the chemical valence states of Co and Fe on

the surface as well as the oxygen (adsorbed oxygen and lattice oxygen), as shown in Figures 8.3(A-D).
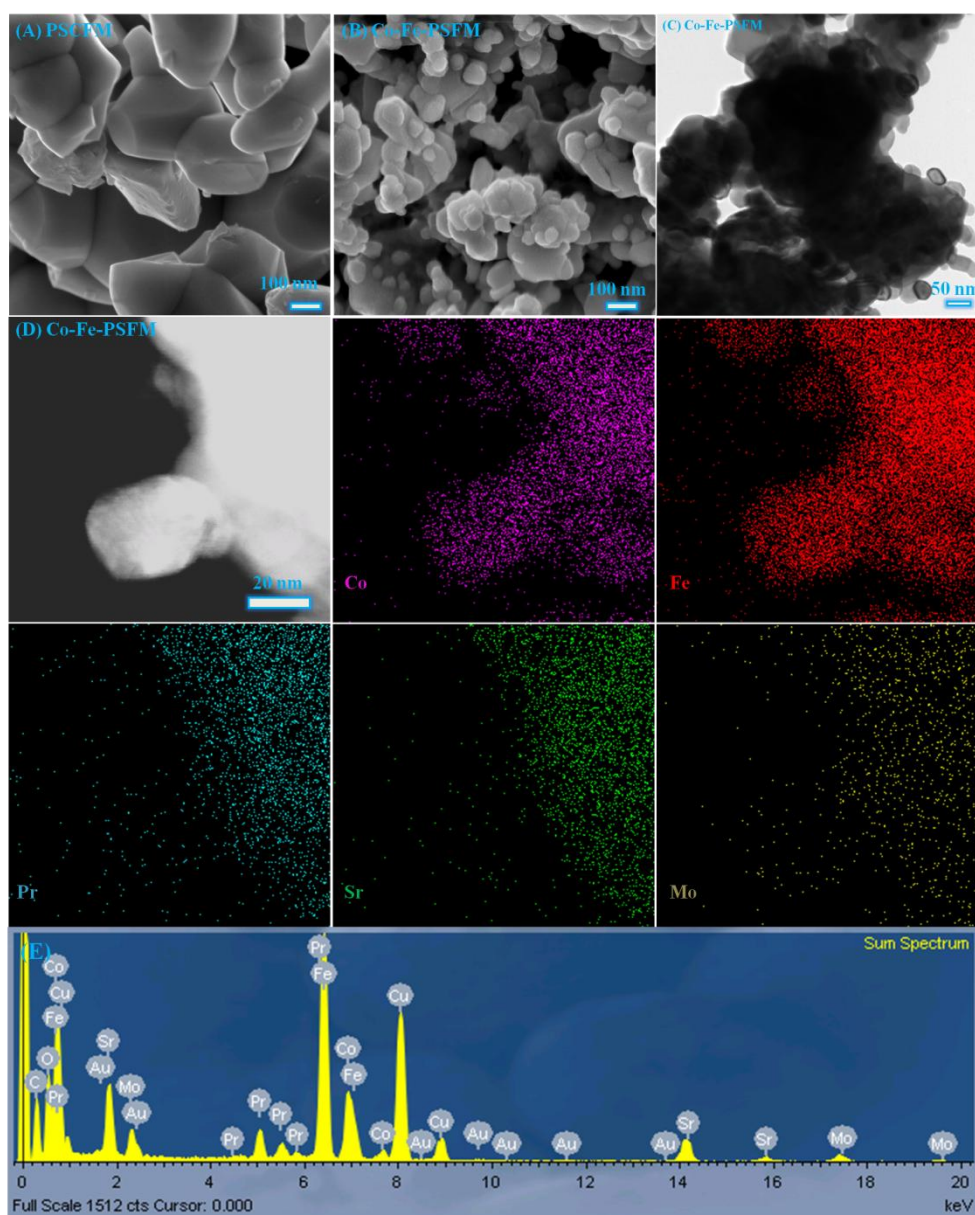
Figure 8.2 SEM images of PSCFM powders (A) before and (B) after reduction. TEM images of Co-Fe-PSFM powders with (C) Low-resolution and (D) High-resolution and the corresponding EDS elemental mappings (Pr, Sr, Co, Fe, Mo) of the morphology of the Co-Fe-PSFM powder, and (E) the EDS spectrum.

The adventitious carbon (C 1s) at the binding energy (BE) of 284.6 eV is regarded as the reference. The XPS survey spectra shown in Figures 8.3A and S8.2A confirmed the presence of Pr, Sr, Co, Fe and Mo in both PSCFM and Co-Fe-PSFM powders,

respectively. The spectra of Co and Fe were analyzed in Figures 8.3B and 8.3C. It can be seen that the peaks of Co^0 and Fe^0 were obviously shown, whereas in Figures S8.2B and S8.2C, no noticeable peaks for Co^0 and Fe^0 were identified. Two weak peaks of Co^0, located at 777.8 (Co $2p_{3/2}$) and 792.5 eV (Co $2p_{1/2}$) [31] for the Co-Fe-PSFM perovskite unambiguously verified that Co existed after the exsolving reaction. Also, as compared to the Fe 2p spectra in Figure S8.2C, the splitting sub-peaks of Fe 2p spectra are located at 706.2 (Fe $2p_{3/2}$) [32] and 719.2 eV (Fe $2p_{1/2}$) [33] in Figure 8.3C after reduction, revealing the successful exsolution of Fe. Based on the quantitative analysis with XPS, the atomic ratio of Co^0/Fe^0 was around 32/68.
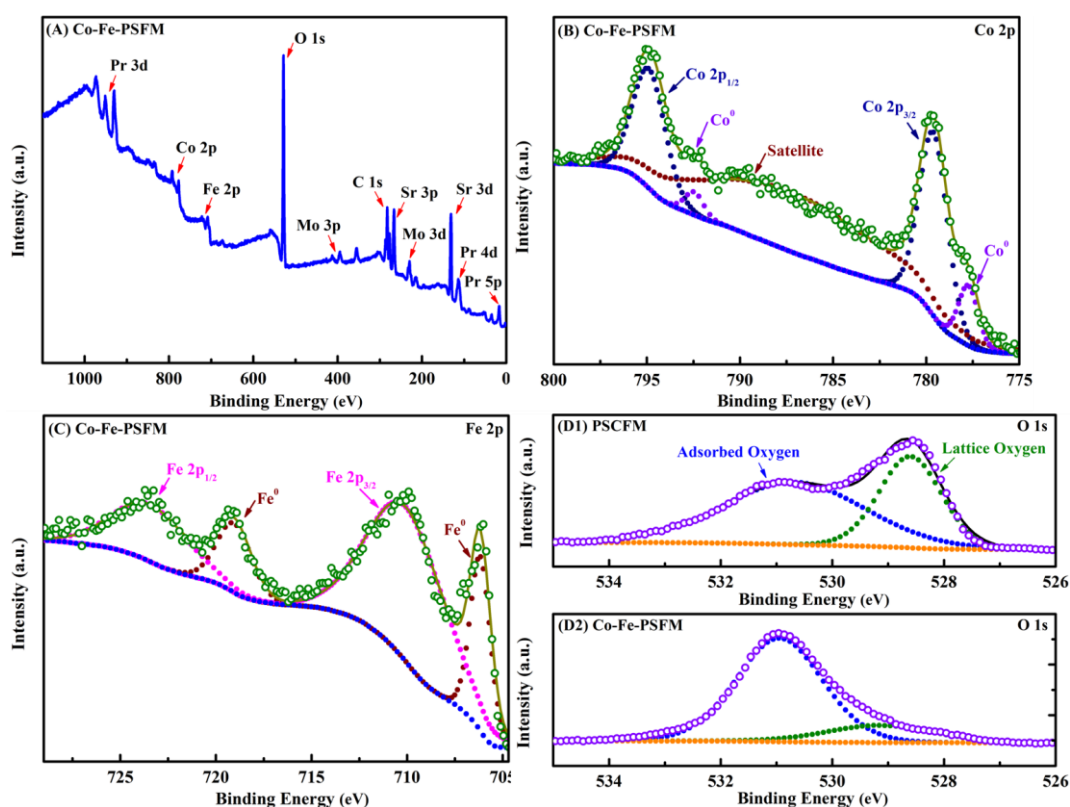
Figure 8.3 (A) Representative XPS of Co-Fe-PSFM powders, (B) Co 2p spectra and (C) Fe 2p spectra. (D) O 1s spectra of (D1) before and (D2) after reduction.

Our results are consistent with the report that during reduction, the metallic Co and Fe were at first formed on the surface of the backbone, followed by the formation of the Co-Fe alloy [34]. As mentioned before, the oxygen vacancy could effectively improve

the ability of CO_2 chemical adsorption and activate CO_2 on those defective sites [18]. The O 1s spectra of both materials were presented in Figures 8.3D1 and D2. Two partially superimposed peaks at 528.7 and 531.0 eV were deconvoluted, corresponding to the lattice oxygen and the adsorbed or loosely bonded oxygen (correlated with surface oxygen vacancies), respectively [35]. Apparently, the PSFM backbone possessed a higher proportion of adsorbed oxygen species at the surface with respect to lattice oxygen than that of PSCFM. In addition, a prominent decrease in the lattice oxygen on the Co-Fe-PSFM surface was observed when comparing with that on the PSCFM surface. This was caused by the exsolution of Co and Fe from oxides as pure metals in conjunction with the continuous formation of oxygen vacancies, suggesting that oxygen vacancies can be further generated in the exsolving process. The high surface oxygen vacancies make double-layered PSFM a promising electrochemically active catalyst.

8.2.2 Evaluation of Redox Stability

Michael Nolan [36] reported that doping of transition metal cation could modify reactivity of ceramic materials with respect to oxygen vacancy formation and molecular adsorption. The doped cations result in strong structural distortion and lower oxygen vacancy formation energy. While oxygen vacancies generated on the perovskite oxides have been considered to be able to effectively improve the chemical adsorption of CO_2. The chemically adsorbed CO_2 is strongly activated on the oxygen vacancy-related defective sites, which favors the electrochemical CO_2 electrolysis at elevated temperatures [18].

To further evaluate the oxygen vacancy formation and to investigate redox stability of the obtained materials, the PSCFM powders were reduced in a H_2 flow at elevated ramping temperature range from 20 to 1000 °C, and cooled down to room

temperature and re-oxidized up to 1000 °C in air (10 °C min^{-1}). The weight loss under the reducing condition in conjunction with the differential thermal analysis was recorded in Figure 8.4A. The gradual weight loss of ~0.30 wt% below 380 °C (Step 1) was attributed to the loss of H_2O [22, 37]. The weight experienced a sharp drop between 380℃ and 520 ℃ (Step 2) during the ramping process. This was mostly attributed to the oxygen vacancy formation and/or a decrease in oxygen content during the phase change process under the reducing condition. The inset is the differential thermal analysis curve, which clearly shows the presence of a sharp exothermic peak on heating at 463.2 °C, confirming the phase change within the temperature range. After that, a continuous decrease of the weight during the ramping process was referred to the further loss of lattice oxygen because of the reduction of Co- and Fe-containing oxides to the *in situ* exsolved Co and Fe (Step 3). The reversibility of the phase change during redox cycle is shown in Figure 8.4B. Clearly, the weight of the Co-Fe-PSFM sharply increased during re-oxidation in air during the ramping process, which was attributed to the re-oxidation of the Co-Fe-PSFM to PSCFM. A weight gain and decrease of 6.62 wt % and 6.67 wt % were observed on re-oxidation and reduction processes, respectively, corresponding to an uptake and a loss of oxygen. Moreover, XRD pattern shows that the powders after re-oxidation retain the same cubic structure (Figure S8.3). The double-layered perovskite Co-Fe-PSFM with high oxygen mobility possesses a remarkable variability in terms of oxygen content under redox conditions, indicating that a reversible oxygen switchover in the lattice takes place [17]. This symmetry between reduction and re-oxidation cycles suggests an excellent redox reversibility.
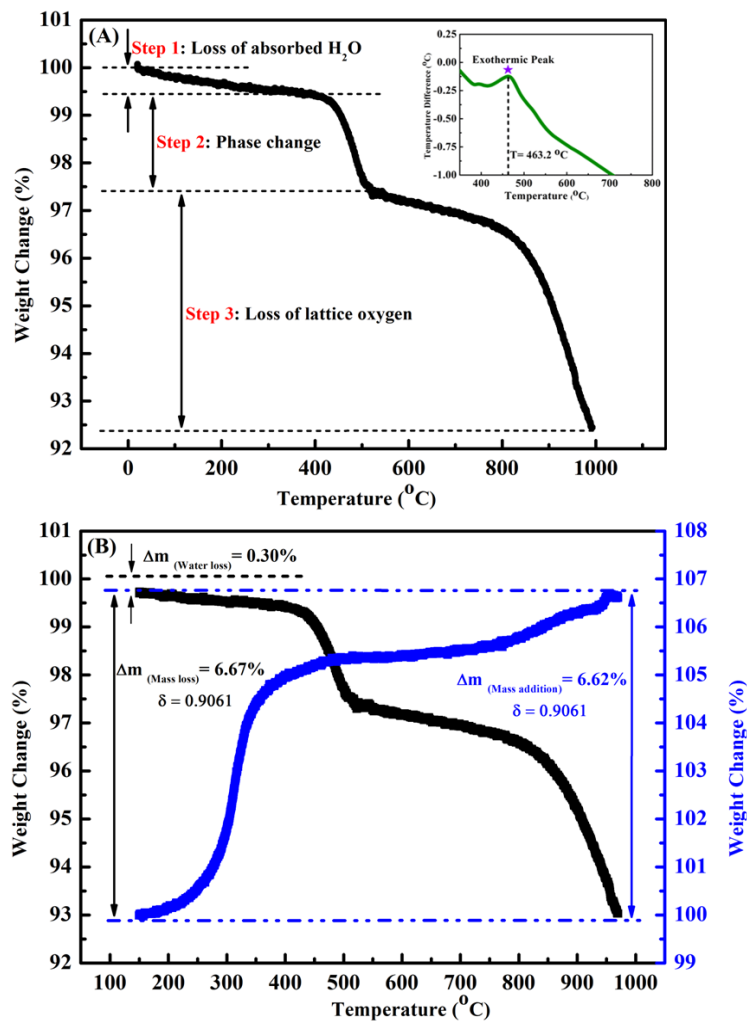
Figure 8.4 Thermogravimetric analyses. (A) Weight loss of PSCFM powders in 5% H_2/N_2 flow, the inset is the differential thermal analyses. (B) Redox stability test of PSCFM powders, carried out firstly in a reducing flow. After it cooled down, switched to air flow. Both are in the same temperature range.

8.2.3 Evaluation of Electrochemical Performance

To evaluate the electrochemical performance, both Co-Fe-PSFM/GDC (cell 1) and PSCFM/GDC (cell 2) composite cathodes were separately fabricated in a YSZ electrolyte supported SOEC. The CO_2/CO with the ratio of 70/30 continuously flowed through the cathode side at a rate of 30 ml min^{-1} (the flow rates measured at the outlets of cells 1 and 2 were 29.0 and 26.0 ml min^{-1}, respectively). Figure 8.5A shows the polarization curves (*I-V*) of cells 1 and 2 in the potential range from -0.5 to -1.0 V (vs. OCV) at 850 °C. The *I-V* curves went smoothly from the SOFC mode (positive

X-axis) to SOEC mode (negative X-axis), suggesting that both cells had good reversibility and besides SOEC, the newly developed material could also be potentially used in SOFC field. An impressive current density of 0.80 A cm^{-2} at 1.6 V and 850 °C was observed (cell 2). It is comparable, under the same condition, with 0.9 and 0.84 A cm^{-2} in the materials of cubic perovskite Ce-doped La(Sr)Cr(Fe) [15] and double-layered PrBaMnO [17], respectively. In contrast, cell 1 with the Co-Fe-PSFM shows a 20% increase in the value of current density at 1.6 V and 850 °C. The enhanced current density can be ascribed to the effects of the increased adsorbed oxygen on the surface of PSFM and the high catalytic activity of the exsolved Co-Fe alloy. To better understand the factors credited for the remarkable electrochemical performance of cell 1, electrochemical impedance spectroscopy (EIS) was used to examine the electrochemical activity of the material for CO_2 electrolysis at stable open circuit voltage at 850 °C. The Nyquist plots of the impedance spectra together with the simulated curves of cells 1 and 2 are presented in Figure 8.5B. The inset is the equivalent circuit. Clearly, the simulated values are all in consistence with the experimental measurements, proving the suitability of the equivalent circuit simulating both cells. The difference between the real axes intercepts at the high and low frequencies of each impedance loop represents the electrode polarization resistance (Rp = R1 + R2) [38]. The resistance, after normalizing with the electrode area, is called area-specific resistance (ASR) which is an indicator to assess the catalytic activity for the CO_2 electrolysis. A lower ASR value means a higher catalytic activity. The simulated values of the parameters of the equivalent circuit for both cells are summarized in Table 8.1. As expected, the total activation polarization (Rp) value of cell 1 was as low as 0.455 Ω cm^2 at 850 °C, about 0.1 Ω cm^2 lower as compared to that of cell 2, indicating that the Co-Fe-PSFM effectively promoted proceed the

electrode kinetics reaction as a result of its high oxygen vacancy concentration, enhanced electrical conductivity and catalytic activity.

Table 8.1 Simulated results of the electrolysis cell with the PSCFM and Co-Fe-PSFM cathodes in CO_2/CO (70:30) under OCV condition at 850 °C.

Catalyst	R_s (Ω cm^2)	R_1 (Ω cm^2)	R_2 (Ω cm^2)	R_P (Ω cm^2)
Co-Fe-PSFM (Cell 1)	0.427	0.104	0.351	0.455
PSCFM (Cell 2)	0.464	0.240	0.314	0.554

To examine the electrolysis performance, potentiostatic tests for both cells 1 and 2 were conducted at different applied potentials (vs. OCV) at 850 °C. The outlet products were analyzed with on-line gas chromatography (GC) in 30 min intervals (a GC run repeated every 10 min for three measurements) at each potential. The average value of every three runs was taken as the CO volume concentration with the 30 min interval for each potential. The volume concentration of CO as a function of applied potential (vs. OCV) for the CO_2 electrolysis were recorded in Figures 8.5C and S8.4A to evaluate the current utilization efficiency (Faraday efficiency, FE). Apparently, the conversion of CO_2 to CO of both cells increased with the rising applied potential. At the potential of 0.8 V (vs. OCV) for cells 1 and 2, the corresponding CO volume concentrations reached the values of ~51.6% and ~50.3% in the outlet gases at 850 °C, respectively. Upon continuously increasing the applied potential, a slight drop of CO percentage in the outlet gases occurred, resulting from the local starvation of CO_2 in the inlet gas and the restrained oxygen evolution at the anode side [4]. Normally, this will lead to a large electrode polarization and low current efficiency for the electrolysis of CO_2 at high temperature. Additionally, production rates of CO and FEs at different applied potentials for both cells were also calculated, as shown in Figures

8.5(D) and S8.4(B). The CO production rates of cells 1 and 2 reached 6.33 and 5.36 ml min^{-1} at the potentials of 0.8 V (vs. OCV), respectively. The decreased production rates after 0.8 V (vs. OCV) are believed to be caused by the local starvation of CO_2. To evaluate the current utilization efficiency, FEs were calculated using the current densities and CO production rates and the results are also shown in Figures 8.5D and S8.4(B).
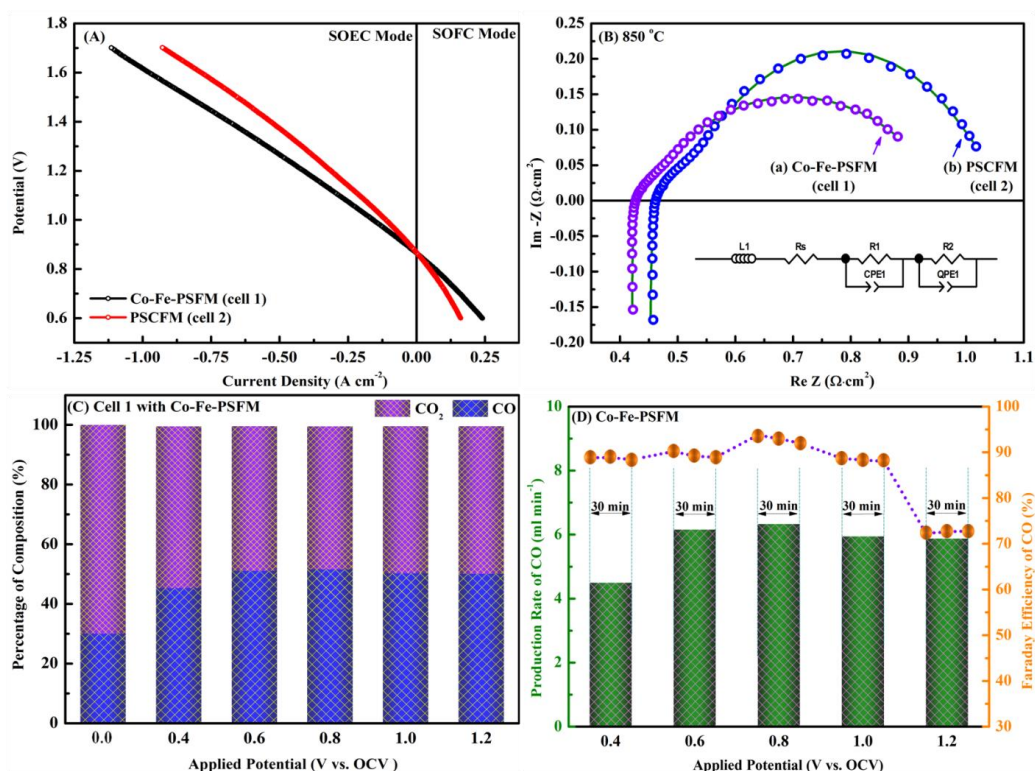
Figure 8.5 Electrochemical performances of the CO_2 electrolysis cell. (A) Current-voltage curves of CO_2 electrolysis fabricated with Co-Fe-PSFM (cell 1) and PSCFM (cell 2), and (B) the corresponding EIS curves at 850 °C. The solid symbols reflect measured results and the lines represent the simulated results using the equivalent-circuit inserted in the plot. (C) The percentages of CO_2/CO composition in the outlet gases during the potentiostatic tests for CO_2 electrolysis at different applied potentials at 850 °C and (D) the corresponding production rates and Faraday efficiencies. A GC run repeated every 10 min. The average value of three measurements was taken as the gas volumetric concentration for Faraday efficiency calculation, three average values are used for the plot. The flow rate of CO_2 in the cathode side was 30 ml min^{-1} and the anode was exposed to air.

The FE of cell 1 increased and reached a peak value of ~93% at the potentials below 0.8 V (vs. OCV). This is considerably higher than the reported values of ~85% in both Mn-doped La(Sr)Ti [18] and La(Sr)Cr(Mn) embedded with exsolved Cu nanoparticles [8], and 89% in La(Sr)Cr(Fe) with exsolved Fe nanoparticles [14]. The impressive high conversion of CO_2 in conjunction with the high FE of the new material fabricated in this work in confirms the excellent catalytic activity of Co-Fe-PSFM for CO_2 electrolysis at high temperature.

8.2.4 Evaluation of Long-term Stability and Coking Resistance

To assess the coking resistance of PSFM with the Co-Fe alloy nanoparticles, a constant potential of 0.4 V (vs. OCV) was applied to the cell for the long-term stability test, the cell current densities were recorded as a function of time in a CO_2/CO (70:30) flow at 850 °C, as shown in Figure 8.6A. The current densities of the cell with Co-Fe-PSFM stabilized at the value of ~0.4 A cm^{-2} after the initial transition stage, the corresponding FEs were found to fluctuate slightly at an average value of 87.7% with the testing interval of 10 h between each run. Normally, carbon can be easily generated on a conventional Ni-based cathode when directly operating in such a carbon-abundant atmosphere [39, 40]. Significantly, no degradation was observed and the cell 1 showed a slight increase in the current density instead in CO_2/CO environment at the constant applied potential of 0.4 V (vs. OCV) and 850 °C for the testing period of 100 h, indicating that no coking occurs. The cathode cross-section of the cell after the long-term stability test was examined by the high-resolution SEM, as seen in Figure 8.6B. The porous cathode attached firmly to the YSZ electrolyte, an indication of the good thermal compatibility between the newly developed cathode and the YSZ electrolyte. Based on the XRD pattern of PSCFM/GDC in Figure S8.5A, the phases in the cathode layer were still GDC and PSCFM. No other obvious peaks

related to the cathode were observed, and this in turn indicated that the material was quite stable under the feed-gas conditions. Additionally, the compositional line profile clearly demonstrated that the GDC buffer layer successfully prevented the inter-diffusion of ionic species between the cathode layer and the YSZ electrolyte (Figure 8.6B). Also, the EDS mapping verified the uniform distribution of Co-Fe alloy nanoparticles through the entire cathode layer (Figure S8.5B). In addition, the Co-Fe alloy nanoparticles were still uniformly embedded on the surface of the PSFM backbone after the cell testing. They still kept their nanoparticle shape with the size of ~50 nm as compared to the ones before testing, and no visible carbon deposition was observed on the surface of the backbone (Figure 8.6C). This suggests that the Co-Fe nanoparticles were in stable presentence under the cell operating conditions. The cathode surfaces of PSCFM/GDC, Co-Fe-PSFM/GDC and Ni/GDC after exposure to CO_2/CO, were analyzed with *ex-situ* Raman spectroscopy. Representative Raman spectra collected on these cathodes were recorded in Figure 8.6 D. The D band at ~1346 cm^{-1} is associated with the disordered graphite, while the G band at ~1561 cm^{-1} corresponds to the highly ordered graphite [41]. As seen, no carbon formation was detected on both PSCFM/GDC and Co-Fe-PSFM/GDC cathode surfaces [Figures 8.6D(b) and (c)]. However, two typical carbon features in the Raman spectra located at ~1339.2 and ~1571.0 cm^{-1} were observed for the Ni/GDC cathode surface [Figure 8.6D(a)]. This confirms that both Co-Fe-PSFM and PSCFM have an excellent coking resistance towards co-presence of CO_2/CO. Particularly, the Co-Fe-PSFM not only shows high catalytic activity for CO_2 electrolysis but also possesses an excellent coking resistance, which makes it a potential cathode material suitable for direct CO_2 electrolysis at high temperatures.
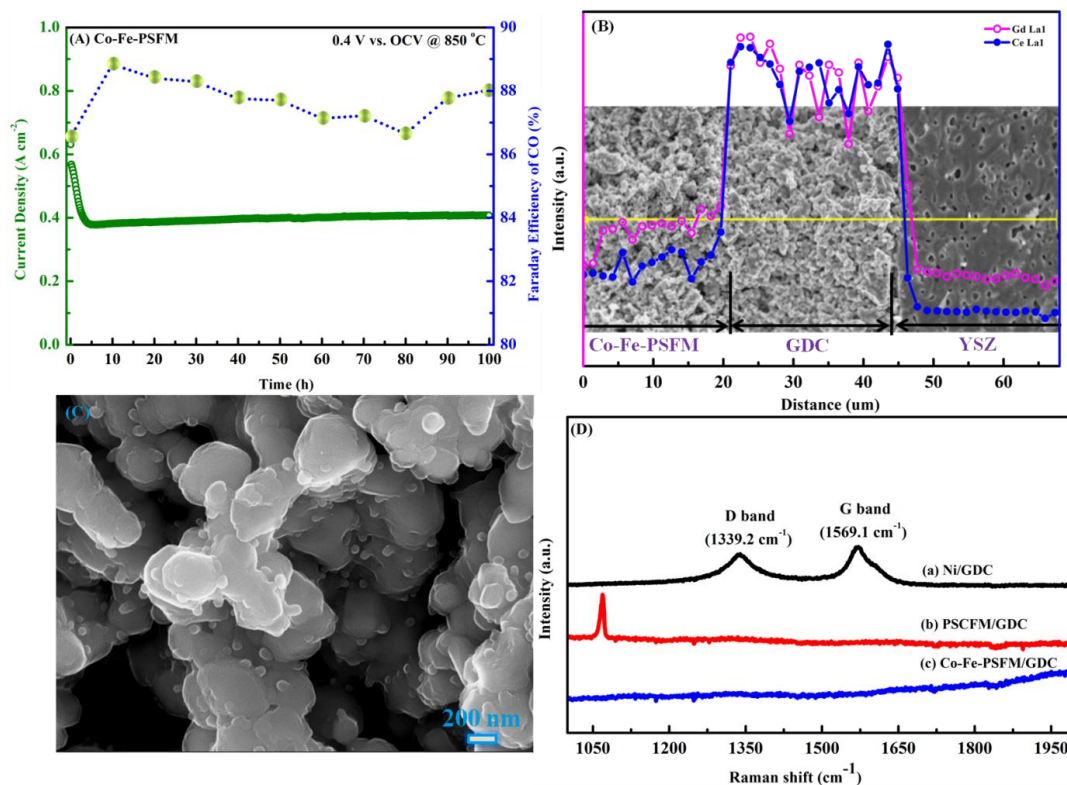
Figure 8.6 (A) Long-term stability of the CO_2 electrolysis cell with Co-Fe-PSFM cathode at the constant applied potential of 0.4 V (vs. OCV) at 850 °C and the corresponding Faraday efficiencies with the interval of 10 h. (B) SEM images of cathode cross section and the corresponding EDS line profile. (C) Cathode layer interface after stability test and (D) Raman spectra collected from cathode surface of (a) Ni/GDC, (b) PSCFM/GDC and (c) Co-Fe-PSFM/GDC after testing.

8.3. Conclusions

In summary, we developed a new cathode material with *in situ* exsolved Co-Fe alloy nanoparticles embedded on an active double-layered perovskite backbone, which acts as a stable and efficient catalyst to promote the electrochemical performance of CO_2 electrolysis in a SOEC. This material exhibits a superb redox reversibility between reduction and re-oxidation cycles. In addition, an enhanced oxygen vacancy content, in comparison with PSCFM, was achieved after both exsolving process and phase change. Furthermore, the PSFM with Co-Fe alloy nanoparticles has rather low polarization ASR (~0.455 Ω cm^2 at 850 °C). A considerably high current density of

157

1.01 A cm^{-2} for SOEC with the Co-Fe-PSFM cathode was achieved at 1.6 V and 850 °C. The performance of the cell with the new cathode showed excellent coking resistance and no degradation was observed at 850 °C for 100 h. More importantly, the FE reached a value as high as ~93% at an applied potential of 0.8 V (vs. OCV) and 850 ℃. As compared with PSCFM, the improved oxygen vacancies of PSFM, together with the exsolved Co-Fe alloy nanoparticles, contributed to the excellent catalytic activity, high FE and good stability for CO_2 electrolysis. Therefore, this design concept may point to a new direction towards fabrication of the cathodes with high performance and stability for high temperature CO_2 electrolysis.

8.4. References

(1) J. T. Randerson, K. Lindsay, E. Munoz, W. Fu, J. K. Moore, F. M. Hoffman, N. M. Mahowald and S. C. Doney, *Global Biochem. Cy.*, **2015**, *29*, 744.

(2) J. Albo, M. Alvarez-Guerra, P. Castano and A. Irabien, *Green Chem.*, **2015**, *17*, 2304.

(3) X. Mao and T. A. Hatton, *Ind.& Eng. Chem. Res.*, **2015**, *54*, 4033.

(4) S. D. Ebbesen, S. H. Jensen, A. Hauch and M. B. Mogensen, *Chem. Rev.*, **2014**, *114*, 1069710.

(5) S. D. Ebbesen and M. Mogensen, *J. Power Sources*, **2009**, *193*, 349.

(6) X. Yue and J. T. S. Irvine, *J. Electrochem. Soc.*, **2012**, *159*, F442.

(7) F. Bidrawn, G. Kim, G. Corre, J. T. S. Irvine and J. M. Vohs, *Electrochem. Solid St.*, **2008**, *11*, B167.

(8) S. Wang, H. Tsuruta, M. Asanuma and T. Ishihara, *Adv. Energy Mat.*, **2015**, *5*.

(9) S. Wang and T. Ishihara, *ISIJ Int.*, **2015**, *55*, 381.

(10) H. Li, G. Sun, K. Xie, W. Qi, Q. Qin, H. Wei, S. Chen, Y. Wang, Y. Zhang and Y. Wu, *Int. J. Hydrogen Energ.*, **2014**, *39*, 20888.

(11) S. Xu, S. Li, W. Yao, D. Dong and K. Xie, *J. Power Sources*, **2013**, *230,* 115.

(12) S. Xu, S. Chen, M. Li, K. Xie, Y. Wang and Y. Wu, *J. Power Sources*, **2013**, *239*, 332.

(13) X. Yue and J. T. S. Irvine, *Electrochem. Solid St.*, **2012**, *15*, B31.

(14) Y. Li, Y. Wang, W.O. Doherty, K. Xie and Y. Wu, *ACS Appl. Mater. Interfaces*, **2013**, *5*, 8553.

(15) Y. -Q. Zhang, J. -H Li, Y.-F Sun, B. Hua and J. -L. Luo*, ACS Appl. Mater. Interfaces*, **2016**, *8*, 6457.

(16) W. Yao, T. Duan, Y. Li, L. Yang and K. Xie, *New J. Chem.*, **2015**, *39*, 2956.

(17) T. H. Shin, J. -H. Myung, M. Verbraeken, G. Kim and J. T. S. Irvine, *Faraday Discuss.*, **2015**, *182*, 227.

(18) W. Qi, Y. Gan, D. Yin, Z. Li, G. Wu, K. Xie and Y. Wu, *J. Mater. Chem. A*, **2014**, *2*, 6904.

(19) J. T. S. Irvine, D. Neagu, M. C. Verbraeken, C. Chatzichristodoulou, C. Graves and M. B. Mogensen, *Nat. Energy*, **2016**, *1*, 15014.

(20) H. Dulli, P. A. Dowben, S. -H Liou and E. W. Plummer, *Phys. Rev. B*, **2000**, *62*, R14629.

(21) J. Druce, H. Tellez, M. Burriel, M. D. Sharp, L. J. Fawcett, S. N. Cook, D. S. McPhail, T. Ishihara, H. H. Brongersma and J. A. Kilner, *Energ Environ Sci.*, **2014**, *7*, 3593.

(22) S. Liu., K. T. Chuang and J. -L. Luo, *ACS Catal.*, **2016**, *6*, 760.

(23) Z. G. Lu, J. H. Zhu, Z. H. Bi and X. C. Lu, *J. Power Sources*, **2008**, *180*, 172.

(24) A. A. Mirzaei, A. B. Babaei, M. Galavy and A. Youssefi, *Fuel Process. Technol.*, **2010**, *91*, 335.

(25) T. Horita, N. Sakai, T. Kawada, H. Yokokawa and M. Dokiya, *J. Electrochem. Soc.*, **1996**, *143*, 1161.

(26) T. B. Massalski, J. L. Murray, L. H. Bennett and H. Baker, *American Society for Metals*, Metals Park, OH. **1986**.

(27) A. Aguadero, D. Perez-Coll, J. A. Alonso, S. J. Skinner and J. Kilner, *Chem. Mater.*, **2012**, *24*, 2655.

(28) Q. Liu, X. Dong, G. Xiao, F. Zhao and F. Chen, Adv. Mater., **2010**, *22*, 5478.

(29) C. Duan, J. Tong, M. Shang, S. Nikodemiski, M. Sanders, S. Ricote, A. Almansoori and R. O'Hayre, *Science*, **2015**, *349*, 1321.

(30) C. Yang, J. Li, Y. Lin, J. Liu, F. Chen and M. Liu, *Nano Energy*, **2015**, *11*, 704.

(31) C. D. Wagner and G. E. Muilenberg, *Handbook of X-ray photoelectron spectroscopy*, **1979**.

(32) R. Devaux, D. Vouagner, C. Duret-Thual and A. M. de Becdelievre, *Corrosion Sci.*, **1994**, *36*, 171.

(33) D. J. Joyner, O. Johnson and D. M. Hercules, *J. Am. Chem. Soc.*, **1980**, *102*, 1910.

(34) Y. -F. Sun, J. -H. Li, L. Cui, B. Hua, S. -H. Cui, J. Li and J. -L. Luo, *Nanoscale*, **2015**, *7*, 11173.

(35) J. -W. Yin, Y. Yin, J. Lu, C. Zhang, Z. -F. Ma and N. Q. Minh, *J. Phys. Chem. C*, **2014**, *118*, 13357.

(36) M. Nolan, *J. Phys. Chem. C*, **2009**, *113*, 2425.

(37) Y. -F. Sun, Y. -Q. Zhang, B. Hua, Y. Behanamian, J. Li, S. -H. Cui, J. -H. Li and J. -L. Luo, *J. Power Sources*, **2016**, *301*, 237.

(38) Y. Zhu, W. Zhou, R. Ran, Y. Chen, Z. Shao and M. Liu, *Nano Lett.*, **2016**, *16*, 512.

(39) S. Sengodan, S. Choi, A. Jun, T. H. Shin, Y. -W. Ju, H. Y. Jeong, J. Shin, J. T. S. Irvine and G. Kim, *Nat. Mater.*, **2015**, *14*, 205.

(40) D. Neagu, T. -S. Oh, D. N. Miller, H. Menard, S. M. Bukhari, S. R. Gamble, R. J. Gorte, J. M. Vohs and J. T. S. Irvine, *Nat. Commun.*, **2015**, *6*, 8120.

(41) M. D. McIntyre, D. M. Neuburger and R. A.Walker, *ECST*, **2015**, *66*, 11.

8.5. Supporting information

8.5.1 The specifications of chemicals and gases

$Pr(NO_3)_3 \cdot 5H_2O$ (Fisher Scientific Company, 99.995%); $Sr(NO_3)_2$ (Fisher Scientific Company, Crystalline); $Fe(NO_3)_3 \cdot 9H_2O$ (Fisher Scientific Company, Crystalline); $Co(NO_3)_3 \cdot 6H_2O$ (ACROS ORGANICS, 99+%); $(NH_4)_6Mo_7O_{24} \cdot 4H_2O$ (Fisher Scientific Company, 99.9%); NH_3H_2O (ACROS ORGANICS, 28-30%);

Citric acid (Fisher Scientific Company, 99.9%); Alpha-terpineol (ACROS ORGANICS, 99+%); Cellulose (ACROS ORGANICS, 99%); 2-isopropanol (Fisher Scientific Company, 70%); 1-butanol (Sigma Aldrich, 99.4+%); Benzyl butyl phthalate (BBP, ACROS ORGANICS, 97%); Ethylenediamine tetraacetic acid (EDTA, Fisher Scientific Company, 99.6%);

CO_2/CO in the ratio of 70:30 (Prexair Company, Canada); 5% H_2/N_2 (Prexair Company, Canada).

8.5.2 Materials preparation

Polycrystalline perovskite powders of $Pr_{0.4}Sr_{0.6}Co_{0.2}Fe_{0.7}Mo_{0.1}O_{3-\delta}$ (PSCFM) were prepared using a modified sol-gel method as described elsewhere.[1] Stoichiometric amounts of $Pr(NO_3)_3 \cdot 5H_2O$, $Sr(NO_3)_2$, $Co(NO_3)_2 \cdot 6H_2O$, $Fe(NO_3)_3 \cdot 9H_2O$ and $(NH_4)_6Mo_7O_{24} \cdot 4H_2O$ were dissolved in $EDTA-NH_3H_2O$ combined solution under continuous heating and stirring, then citric acid was introduced. The molar ratio of

EDTA acid : citric acid : total metal ions was controlled to be around 1 : 1.5 : 1. Subsequently, NH_3H_2O was added to adjust the pH value to 8~9. The solution was stirred and heated on a hot plate at 80 °C until the formation of organic resins containing the homogeneously distributed cations due to the slow evaporation of the solvent. The synthesized gel was decomposed at 300 °C for 4 h to remove the organic components and the nitrates. The raw powders were then fired at 1100 °C for 10 h in air to obtain the raw materials, followed by heating in a tubular furnace at 850 °C for 10 h in a 5% H_2/N_2 reducing gas flow, thus forming the Co-Fe *in-situ* exsolved $(Pr_{0.4}Sr_{0.6})_3(Fe_{0.85}Mo_{0.15})_2O_7$ (Co-Fe-PSFM). $(La_{0.60}Sr_{0.40})_{0.95}Co_{0.20}Fe_{0.80}O_{3-\delta}$ (LSCF) and $Gd_{0.2}Ce_{0.8}O_{2-\delta}$ (GDC) powders were fabricated using a conventional solid state reaction method.[2] The cathode pastes were prepared by mixing Co-Fe-PSFM and GDC (weight ratio 1:1) with a glue containing 1-butanol, benzyl butyl phthalate (BBP), ethyl cellulose and α-terpineol, followed by ball milling for 3 h. The weight ratio of total powders to glue was 1.7:1. The anode pastes comprised of LSCF and GDC were prepared using the same method as the cathode pastes.

8.5.3 Supporting figures
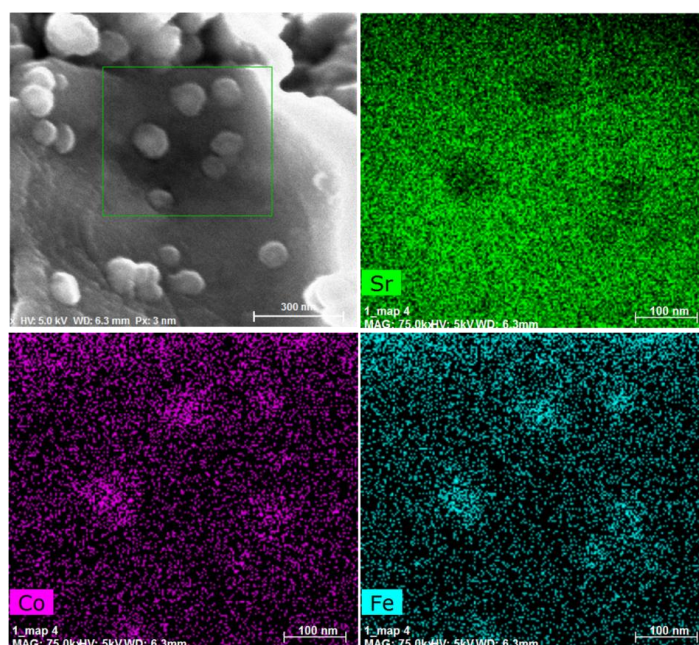
Figure S8.1 The morphology of the Co-Fe-PSFM powder and the corresponding EDS elemental mappings (Sr, Co, Fe).
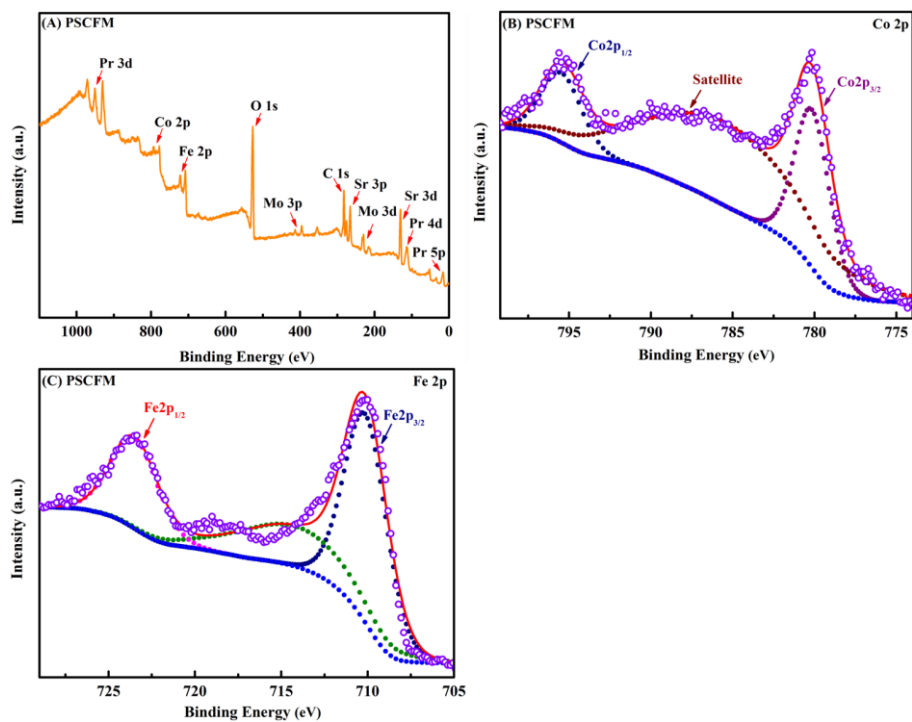
Figure S8.2 (A) Representative XPS of PSCFM powders, (B) Co 2p spectra and (C) Fe 2p spectra.
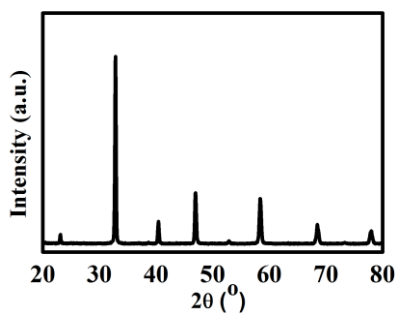
Figure S8.3 XRD pattern for the powders after re-oxidation.
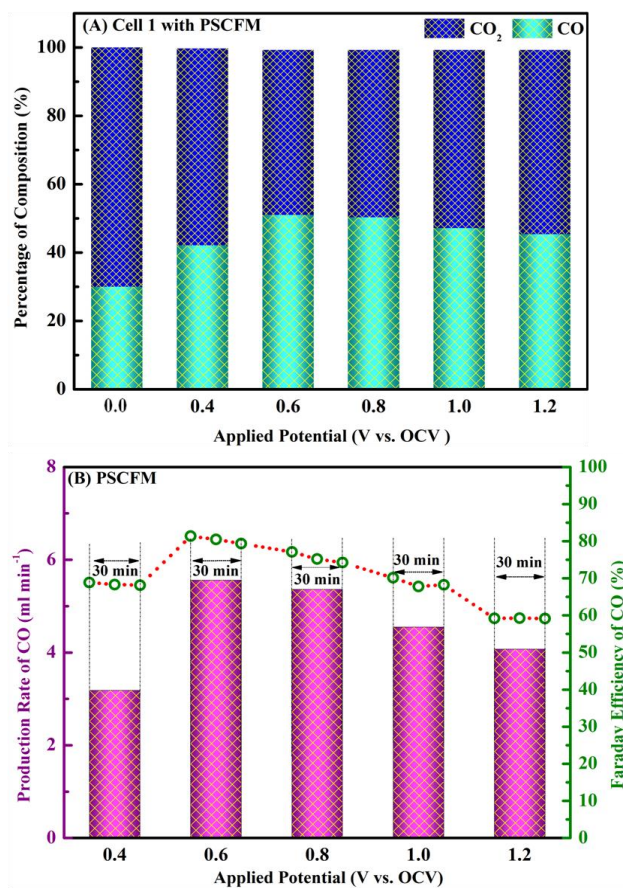
Figure S8.4 Electrochemical performances of cell 1 with PSCFM cathode material. (A) CO_2/CO compositions in the outlet gases at different applied potentials and 800 °C. (B) the corresponding production rates and Faraday efficiencies of CO_2 electrolysis at different applied potentials and 850 °C. A GC run repeated every 10 min. The average value of two measurements was taken as the gas volumetric concentration for Faraday efficiency calculation. The flow rate of CO_2 in the anode compartment was 30 ml min^{-1} (the flow rate measured by a flow meter at the exit of the cell was around 26 ml min^{-1}) and the anode was exposed to air.
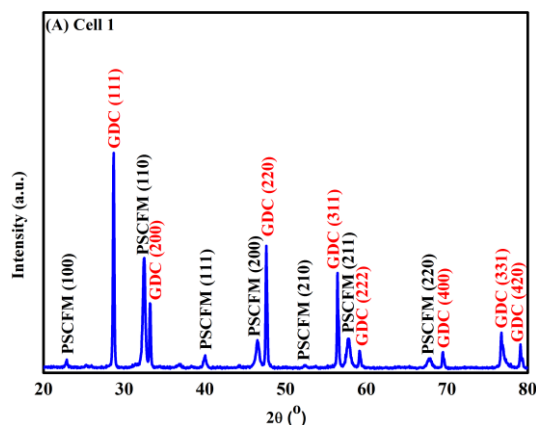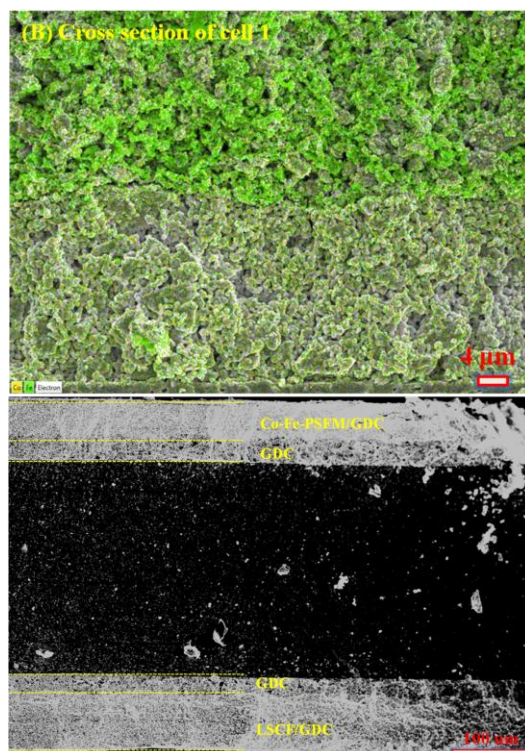
Figure S8.5 (A) XRD pattern for the cathode surface of cell 2 with PSCFM after the stability test. (B) EDS elemental mapping of cathode side cross section of cell 2 with Co-Fe-PSFM.

8.5.4 References

(1) C. Duan, J. Tong, M. Shang, S. Nikodemski, M. Sanders, S. Ricote, A. Almansoori, R. O'Hayre, Science **2015**, *349*, 1321.

(2) L. Yang, Z. Liu, S. Wang, Y. Choi, C. Zuo, M. Liu, J. Power Sources **2010**, *195*, 471.

Chapter 9. Summary and future prospects

9.1 Summary

The work presented in this dissertation explored the electrochemical CO_2RR at room temperature and elevated temperatures. Tri-Ag-NPs were successfully prepared and investigated in terms of the shape-dependent electrocatalytic activity towards CO_2RR in 0.1 M $KHCO_3$. Tri-Ag-NPs exhibit considerably higher selectivity as compared to SS-Ag-NPs and bulk Ag. Moreover, the formation of CO starts to be detected at an ultralow onset potential, confirming the excellent catalytic activity of Tri-Ag-NPs towards CO_2RR. In addition, the durability test without observable degradation of over 7 days further confirms the excellence of Tri-Ag-NPs as a cathode for efficient CO_2RR. DFT calculations indicate that the high selectivity of Tri-Ag-NPs at an decreased η, together with a significantly lowered onset potential, is a consequence of both the optimum edge-to-corner ratio (edge sites are active for CO_2RR, while corner sites are preferable for HER) and the predominant Ag(100) facet in the shape-controlled synthesized Tri-Ag-NPs. Meanwhile, it requires the lowest energy to initiate the rate determining single-electron transfer step. To further investigate the solvent and structure effects, Ag_2S NWs were successfully synthesized using a facile one-step method and employed to investigate both electrolyte- and structure-dependent electroreduction of CO_2 to CO in aqueous and IL media. Ag_2S NWs in IL possess much higher partial current density and selectivity than those of Ag_2S NWs and bulk Ag in $KHCO_3$. More importantly, the formation of CO begins at an ultralow η of 54 mV, confirming the superior catalytic activity of Ag_2S NWs in IL. In addition, only slight degradation was observed over 20 h, further verifying the excellence of Ag_2S NWs as an electrocatalyst for CO_2RR in IL. The superior electrochemical performance originates from the presence of $[EMIM-CO_2]^+$ complexes, which not

only physically adsorb on the negatively charged catalyst and subsequently increase the solubility of CO_2 and the probability of substantial close collision of CO_2 with catalyst, but also significantly lower the energy barrier of electron-transfer process, which consequently reduce the η towards CO_2RR. Besides, DFT calculations indicate that the CO_2^- formation over Ag_2S NWs is energetically favored on the facets of (111) and (121). Instead, the strong binding of CO on these facets restrains desorption of CO and determines the reaction rate, as confirmed by the results of UPS and PDOS. Therefore, the exceptional performance of Ag_2S NWs in IL is attributed to a synergistic effect of solvent-assisted and structure-engineered contributions. These findings can serve as progressive steps in advancing our understanding on CO_2RR mechanism and exploring new electrocatalysts for efficient CO_2RR.

For the purposing of exploring the CO_2RR at elevated temperatures, a new Ni-doped $La(Sr)FeO_{3-δ}$ cathode material was developed using modified sol-gel method, and firstly fabricated as the cathode for high temperature CO_2 electrolysis in a SOEC. It demonstrates superior electrocatalytic activity and negligible degradation for stably and effectively promoting SOEC cathode performance. Therefore, it is concluded that La(Sr)Fe(Ni) can potentially be used to fabricate electrode in solid oxide cells, especially for directly hydrocarbon-fueled or carbon-enriched cells. To further improve the cell performance with this material, the as-obtained material was pre-reduced under reducing flow to achieve in situ exsolved metal/bimetal nanoparticles since the coated nanoparticles can significantly improve the catalytic activity. The *in situ* exsolved Fe-Ni alloy nanospheres uniformly socketed on the oxygen deficient perovskite acted as a highly stable and efficient catalyst to effectively boost the catalytic performance of CO_2 electrolysis in a HT-SOEC. The cathode kinetics for CO_2 electrolysis was significantly improved together with a high Faraday efficiency

at elevated temperatures. Moreover, the symmetry between reduction and re-oxidation cycles of this material indicates its exceptional redox reversibility. It was also verified that the CO_2 electrolysis cell with the Fe-Ni-LSFN cathode could be steadily conducted without any discernible carbon deposition. This study, herein, demonstrates that the novel *in situ* exsolved Fe-Ni alloy nanospheres uniformly socketed on the oxygen deficient perovskite catalyst are highly effective for CO_2 electrolysis, and could be used as a promising cathode material. To further confirm this concept, a new cathode material with *in situ* exsolved Co-Fe alloy nanoparticles was embedded on an active double-layered perovskite backbone, which also acts as a stable and efficient catalyst to promote the electrochemical performance of CO_2RR in a SOEC as compared with the one without *in situ* exsolve bimetal nanoparticles. The improved oxygen vacancies together with the exsolved alloy nanoparticles contribute to the excellent catalytic activity, high FE and good stability for CO_2RR. Therefore, this design concept may point to a new direction towards fabrication of the cathodes with high performance and stability for high temperature CO_2RR at elevated temperatures.

9.2 Future prospects

Several suggestions are listed as follows. It is my hope that this dissertation and these suggested areas will serve as guidance and inspiration for the researchers who will continuously conduct CO_2RR investigation in the near future.

1) Highly effective and stable electrocatalysts for CO_2RR at room and elevated temperatures.

Carbides have been extensively studied for oxygen reduction reaction due to its easy preparation procedure and lower price than those of metals. However, carbides have not been reported for CO_2RR so far, while perovskite oxides have been demonstrated

to have high catalytic for oxygen reduction reaction and CO_2RR at elevated temperatures. But limited reports are available for CO_2RR at room temperature.

2) The mechanism for CO_2RR at room and elevated temperatures.

Currently, the mechanistic understanding associated with CO_2RR is still lacking. The development of new catalytic materials should be accompanied by concomitant theoretical investigation (e.g., molecular dynamics simulation and electronic calculation). To elucidate the structure-property relationship and the detailed mechanisms for CO_2RR, density functional theory (DFT) can be performed.

3) Further fundamental understanding of degradation mechanisms and material behaviors in CO_2RR process.

4) Development of effective electrolyte for room temperature CO_2RR.

The electrolyte that is currently being used is $KHCO_3$ solution. It has been reported that EMIM-BF4 solution reduced the activation energy for CO_2RR. More organic solvents or ionic liquids can be explored for CO_2RR.

5) Electrolytic cell set up with flowing electrolyte.

To further increase the current density, designing and constructing a device with flow electrolyte is necessary for the purpose of reducing concentration overpotential. It is expected that increasing the flow rate of the solution will reduce the thickness of the diffusion layers, thus, will increase the limiting current density.

Bibliography

1. Omer, A. M. *Renew. Sust. Energ. Rev.* **2008**, *12*, 2265.

2. Outlook, W. E. **2009**.

3. Asif, M.; Muneer, T. *Renew. Sust. Energ. Rev.* **2007**, *11*, 1388.

4. Keeling, C.; Whorf, T. *Carbon Dioxide Information Analysis Center* **2009**.

5. Liu, Z.; Guan, D.; Wei, W.; Davis, S. J.; Ciais, P.; Bai, J.; Peng, S.; Zhang, Q.; Hubacek, K.; Marland, G. *Nature* **2015**, *524*, 335.

6. https://kodukant.kovtp.ee/documents/1727611/3730742/Käsiraamat.pdf/32b40e cd-fc0c-410a-96ff-cda1c375c7ca

7. Goldemberg, J.; Johansson, T. B.; Reddy, A. K.; Williams, R. H. *Energy for a sustainable world*; Wiley New York, **1988**.

8. Meinshausen, M.; Meinshausen, N.; Hare, W.; Raper, S. C.; Frieler, K.; Knutti, R.; Frame, D. J.; Allen, M. R. *Nature* **2009**, *458*, 1158.

9. Revesz, R. L.; Howard, P. H.; Arrow, K.; Goulder, L. H.; Kopp, R. E.; Livermore, M. A.; Oppenheimer, M.; Sterner, T. *Nature* **2014**, *508*, 173.

10. Zachos, J. C.; Dickens, G. R.; Zeebe, R. E. *Nature* **2008**, *451*, 279.

11. http://www.globalcarbonproject.org/carbonbudget/archive/2014/GCP_budget_2 014_lowres_v1.02.pdf

12. IPCC, Climate Change. **2007**. *The Physical Science Basis*. Contribution of Working Group I to the Fourth Assessment Report of the Intergovernmental Panel on Climate Change, Cambridge University Press. Cambridge, United Kingdom and New York, NY, USA, **2007**.

13. Molina, M. J.; Molina, L. T. *J. Air Waste Manage.* **2004**, *54*, 644.

14. Crutzen, P. J. *Atmos. Environ.* **2004**, *38*, 3539.

15. Hidalgo, J.; Masson, V.; Baklanov, A.; Pigeon, G.; Gimeno, L. *Ann. N.Y. Acad. Sci.* **2008**, *1146*, 354.

16. Boot-Handford, M. E.; Abanades, J. C.; Anthony, E. J.; Blunt, M. J.; Brandani, S.; Mac Dowell, N.; Fernández, J. R.; Ferrari, M.-C.; Gross, R.; Hallett, J. P.; Haszeldine, R. S.; Heptonstall, P.; Lyngfelt, A.; Makuch, Z.; Mangano, E.; Porter, R. T. J.; Pourkashanian, M.; Rochelle, G. T.; Shah, N.; Yao, J. G.; Fennell, P. S. *Energy Environ. Sci.* **2014**, *7*, 130.

17. Leung, D. Y.; Caramanna, G.; Maroto-Valer, M. M. *Renew. Sust. Energ. Rev.* **2014**, *39*, 426.

18. Krebs, F. C. *Energ. Environ. Sci.* **2012**, *5*, 7238.

19. MacDowell, N.; Florin, N.; Buchard, A.; Hallett, J.; Galindo, A.; Jackson, G.; Adjiman, C. S.; Williams, C. K.; Shah, N.; Fennell, P. *Energy Environ. Sci.* **2010**, *3*, 1645.

20. Huang, C.-H.; Tan, C.-S. *Aerosol Air Qual. Res.* **2014**, *14*, 480.

21. Centi, G.; Perathoner, S. *Green carbon dioxide: advances in CO$_2$ utilization*; John Wiley & Sons, **2014**.

22. Halmann, M. *Ann Arbor: CRC Press*.

23. Halmann, M. M.; Steinberg, M. *Greenhouse gas carbon dioxide mitigation: science and technology*; CRC press, **1998**.

24. Aresta, M. *Carbon dioxide as chemical feedstock*; John Wiley & Sons, **2010**.

25. Sridhar, N.; Hill, D.; Agarwal, A.; Zhai, Y.; Hektor, E. *Det Norske Veritas* **2011**.

26. DOE, U. *US Department of Energy, Morgantown, WV, 39,* **2006**.

27. http://www.pennenergy.com/articles/pennenergy/2014/09/petra-nova-CO$_2$-emissions-capture-enhanced-oil-recovery-project-underway.html.

28. http://www.thinkgeoenergy.com/university-spin-off-plans-on-using-co2-for-the-extraction-of-geothermal-heat/.

29. Bauen, A.; Berndes, G.; Junginger, M.; Londo, M.; Vuille, F.; Ball, R.; Bole, T.; Chudziak, C.; Faaij, A.; Mozaffarian, H. *Bioenergy: a sustainable and reliable energy source. A review of status and prospects.* **2009**.

30. Lanzafame, P.; Centi, G.; Perathoner, S. *Chem. Soc. Rev.* **2014**, *43*, 7562.

31. Mao, X.; Hatton, T. A. *Ind. Eng. Chem. Res.* **2015**, *54*, 4033.

32. Qiao, J.; Liu, Y.; Hong, F.; Zhang, J. *Chem. Soc. Rev.* **2014**, *43*, 631.

33. Zhu, D. D.; Liu, J. L.; Qiao, S. Z. *Adv. Mater.* **2016**, *28*, 3423.

34. Costentin, C.; Robert, M.; Savéant, J.-M. *Chem. Soc. Rev.* **2013**, *42*, 2423.

35. Jiang, Z.; Xiao, T.; Kuznetsov, V. á.; Edwards, P. á. *Philosophical Transactions of the Royal Society of London A: Mathematical, Phys. Eng. Sci.* **2010**, *368*, 3343.

36. Graves, C.; Ebbesen, S. D.; Jensen, S. H.; Simonsen, S. B.; Mogensen, M. B. *Nat. Mater.* **2015**, *14*, 239.

37. Kharecha, P. A.; Hansen, J. E. *Global Biogeochem. Cy.* **2008**, *22*.

38. Banos, R.; Manzano-Agugliaro, F.; Montoya, F.; Gil, C.; Alcayde, A.; Gómez, J. *Renew. Sust. Energ. Rev.* **2011**, *15*, 1753.

39. Dincer, I. *Renew. Sust. Energ. Rev.* **2000**, *4*, 157.

40. Jacobson, M. Z.; Delucchi, M. A. *Energ. Policy* **2011**, *39*, 1154.

41. Fthenakis, V.; Mason, J. E.; Zweibel, K. *Energ. Policy* **2009**, *37*, 387.

42. White, J. L., Princeton University, **2016**.

43. Aresta, M.; Dibenedetto, A.; Angelini, A. *Chem. Rev.* **2013**, *114*, 1709.

44. Lim, R. J.; Xie, M.; Sk, M. A.; Lee, J.-M.; Fisher, A.; Wang, X.; Lim, K. H. *Catal. Today* **2014**, *233*, 169.

45. Albo, J.; Alvarez-Guerra, M.; Castaño, P.; Irabien, A. *Green Chem.* **2015**, *17*, 2304.

46. Ebbesen, S. D.; Jensen, S. H.; Hauch, A.; Mogensen, M. B. *Chem. Rev.* **2014**, *114*, 10697.

47. National Institute of Standards and Technology (NIST). NIST Chemistry WebBook. http://webbook.nist.gov/chemistry/.

48. Delacourt, C.; Ridgway, P. L.; Kerr, J. B.; Newman, J. *J. Electrochem. Soc.* **2008**, *155*, B42.

49. Kuhl, K. P.; Cave, E. R.; Abram, D. N.; Jaramillo, T. F. *Energ. Environ. Sci.* **2012**, *5*, 7050.

50. Liu, S.; Liu, Q.; Luo, J.-L. *ACS Catal.* **2016**, 6, 6219.

51. Liu, S.; Liu, Q.; Luo, J.-L. *J. Mater. Chem. A* **2016**, 4, 17521.

52. Liu, S.; Liu, Q.; Luo, J.-L. *J. Mater. Chem. A* **2017**, *5*, 2673.

53. Liu, S.; Tao, H.; Zeng, L.; Liu, Q.; Xu, Z.; Liu, Q.; Luo, J. L. *J. Am. Chem. Soc.* **2017**, *139*, 2160.

54. Zhu, W.; Michalsky, R.; Metin, O.; Lv, H.; Guo, S.; Wright, C. J.; Sun, X.; Peterson, A. A.; Sun, S. *J. Am. Chem. Soc.* **2013**, *135*, 16833.

55. Li, F.; Chen, L.; Knowles, G. P.; MacFarlane, D. R.; Zhang, J. *Angew. Chem.* **2017**, *56*, 505.

56. Jhong, H.-R. M.; Ma, S.; Kenis, P. J. A. *Curr. Opin. Chem Eng.* **2013**, *2*, 191.

57. Bard, A. J.; Faulkner, L. R. *Electrochem. Methods* **2001**, *2*.

58. Baruch, M. F. **2016**.

59. Oloman, C.; Li, H. ChemSusChem 2008, 1, 385.

60. Magdesieva, T.; Yamamoto, T.; Tryk, D.; Fujishima, A. *J. Electrochem. Soc.* **2002**, *149*, 89.

61. Gao, D.; Zhou, H.; Wang, J.; Miao, S.; Yang, F.; Wang, G.; Wang, J.; Bao, X. *J. Am. Chem. Soc.* **2015**, *137*, 4288.

62. Kortlever, R.; Balemans, C.; Kwon, Y.; Koper, M. T. M. *Catal. Today* **2015**, *244*, 58.

63. Li, Y.; Cui, F.; Ross, M. B.; Kim, D.; Sun, Y.; Yang, P. *Nano Lett.* **2017**, *17*, 1312.

64. Wang, Z.; Yang, G.; Zhang, Z.; Jin, M.; Yin, Y. *ACS Nano* **2016**, *10*, 4559.

65. Mistry, H.; Varela, A. S.; Bonifacio, C. S.; Zegkinoglou, I.; Sinev, I.; Choi, Y. W.; Kisslinger, K.; Stach, E. A.; Yang, J. C.; Strasser, P.; Cuenya, B. R. *Nat. Commun.* **2016**, *7*, 12123.

66. Loiudice, A.; Lobaccaro, P.; Kamali, E. A.; Thao, T.; Huang, B. H.; Ager, J. W.; Buonsanti, R. *Angew. Chem. In. Edit.* **2016**, *55*, 5789.

67. Reske, R.; Mistry, H.; Behafarid, F.; Roldan Cuenya, B.; Strasser, P. *J. Am. Chem. Soc.* **2014**, *136*, 6978.

68. Kim, C.; Jeon, H. S.; Eom, T.; Jee, M. S.; Kim, H.; Friend, C. M.; Min, B. K.; Hwang, Y. J. *J. Am. Chem. Soc.* **2015**, *137*, 13844.

69. Back, S.; Yeom, M. S.; Jung, Y. *ACS Catal.* **2015**, *5*, 5089.

70. Fang, Y.; Flake, J. C. *J. Am. Chem. Soc.* **2017**.

71. Kapusta, S.; Hackerman, N. *J. Electrochem. Soc.* **1983**, *130*, 607.

72. Ding, C.; Li, A.; Lu, S.-M.; Zhang, H.; Li, C. *ACS Catal.* **2016**, *6*, 6438.

73. Medina-Ramos, J.; Pupillo, R. C.; Keane, T. P.; DiMeglio, J. L.; Rosenthal, J. *J. Am. Chem. Soc.* **2015**, *137*, 5021.

74. Cui, C.; Wang, H.; Zhu, X.; Han, J.; Ge, Q. *Sci. China Chem.* **2015**, *58*, 607.

75. Subramanian, K.; Asokan, K.; Jeevarathinam, D.; Chandrasekaran, M. *J. Appl. Electrochem.* **2007**, *37*, 255.

76. Lee, C. H.; Kanan, M. W. *ACS Catal.* **2015**, *5*, 465.

77. Zhang, Z.; Chi, M.; Veith, G. M.; Zhang, P.; Lutterman, D. A.; Rosenthal, J.; Overbury, S. H.; Dai, S.; Zhu, H. *ACS Catal.* **2016**, *6*, 6255.

78. Murata, A.; Hori, Y. *B. Chem. Soc. Jpn.* **1991**, *64*, 123.

79. Wu, J.; Yang, X.; He, Z.; Mao, X.; Hatton, T. A.; Jamison, T. F. *Angew. Chem. Int. Edit.* **2014**, *53*, 8416.

80. Schizodimou, A.; Kyriacou, G. *Electrochimi. Acta* **2012**, *78*, 171.

81. Luc, W.; Collins, C.; Wang, S.; Xin, H.; He, K.; Kang, Y.; Jiao, F. *J. Am. Chem. Soc.* **2017**, *139*, 1885.

82. Ma, S.; Sadakiyo, M.; Heima, M.; Luo, R.; Haasch, R. T.; Gold, J. I.; Yamauchi, M.; Kenis, P. J. *J. Am. Chem. Soc.* **2017**, *139*, 47.

83. Torelli, D. A.; Francis, S. A.; Crompton, J. C.; Javier, A.; Thompson, J. R.; Brunschwig, B. S.; Soriaga, M. P.; Lewis, N. S. *ACS Catal.* **2016**, *6*, 2100.

84. Studt, F.; Sharafutdinov, I.; Abild-Pedersen, F.; Elkjaer, C. F.; Hummelshoj, J. S.; Dahl, S.; Chorkendorff, I.; Norskov, J. K. *Nat. Chem.* **2014**, *6*, 320.

85. Sarfraz, S.; Garcia-Esparza, A. T.; Jedidi, A.; Cavallo, L.; Takanabe, K. *ACS Catal.* **2016**.

86. Xu, Z.; Lai, E.; Shao-Horn, Y.; Hamad-Schifferli, K. *Chem. Commun.* **2012**, *48*, 5626.

87. Zhao, W.; Yang, L.; Yin, Y.; Jin, M. *J. Mater. Chem. A* **2014**, *2*, 902.

88. Guo, X.; Zhang, Y.; Deng, C.; Li, X.; Xue, Y.; Yan, Y.-M.; Sun, K. *Chem. Commun.* **2015**, *51*, 1345.

89. Rasul, S.; Anjum, D. H.; Jedidi, A.; Minenkov, Y.; Cavallo, L.; Takanabe, K. *Angew. Chem. Int. Edit.* **2015**, *54*, 2146.

90. Chen, Y.; Li, C. W.; Kanan, M. W. *J. Am. Chem. Soc.* **2012**, *134*, 19969.

91. Ma, M.; Trzesniewski, B. J.; Xie, J.; Smith, W. A. *Angew. Chem.* **2016**, *55*, 9748.

92. Zhang, S.; Kang, P.; Ubnoske, S.; Brennaman, M. K.; Song, N.; House, R. L.; Glass, J. T.; Meyer, T. J. *J. Am. Chem. Soc.* **2014**, *136*, 7845.

93. Chen, Y.; Kanan, M. W. *J. Am. Chem. Soc.* **2012**, *134*, 1986.

94. Baruch, M. F.; Pander III, J. E.; White, J. L.; Bocarsly, A. B. *ACS Catal.* **2015**, *5*, 3148.

95. Li, C. W.; Kanan, M. W. *J. Am. Chem. Soc.* **2012**, *134*, 7231.

96. Li, C. W.; Ciston, J.; Kanan, M. W. *Nature* **2014**, *508*, 504.

97. Kim, D.; Lee, S.; Ocon, J. D.; Jeong, B.; Lee, J. K.; Lee, J. *Phys. Chem. Chem. Phys.* **2015**, *17*, 824.

98. Zhang, S.; Kang, P.; Meyer, T. J. *J. Am. Chem. Soc.* **2014**, *136*, 1734.

99. Kumar, B.; Atla, V.; Brian, J. P.; Kumari, S.; Nguyen, T. Q.; Sunkara, M.; Spurgeon, J. M. *Angew. Chem.* **2017**, *56*, 3645.

100. Ren, D.; Deng, Y.; Handoko, A. D.; Chen, C. S.; Malkhandi, S.; Yeo, B. S. *ACS Catal.* **2015**, *5*, 2814.

101. Oh, Y.; Vrubel, H.; Guidoux, S.; Hu, X. *Chem. Commun.* **2014**, *50*, 3878.

102. Sekimoto, T.; Deguchi, M.; Yotsuhashi, S.; Yamada, Y.; Masui, T.; Kuramata, A.; Yamakoshi, S. *Electrochem. Commun.* **2014**, *43*, 95.

103. Gao, D.; Zhang, Y.; Zhou, Z.; Cai, F.; Zhao, X.; Huang, W.; Li, Y.; Zhu, J.; Liu, P.; Yang, F.; Wang, G.; Bao, X. *J. Am. Chem. Soc.* **2017**, *139*, 5652.

104. Asadi, M.; Kumar, B.; Behranginia, A.; Rosen, B. A.; Baskin, A.; Repnin, N.; Pisasale, D.; Phillips, P.; Zhu, W.; Haasch, R.; Klie, R. F.; Kral, P.; Abiade, J.; Salehi-Khojin, A. *Nat. Commun.* **2014**, *5*, 4470.

105. Asadi, M.; Kim, K.; Liu, C.; Addepalli, A. V.; Abbasi, P.; Yasaei, P.; Phillips, P.; Behranginia, A.; Cerrato, J. M.; Haasch, R. *Science* **2016**, *353*, 467.

106. Li, F.; Zhao, S.-F.; Chen, L.; Khan, A.; MacFarlane, D. R.; Zhang, J. *Energy Environ. Sci.* **2016**, *9*, 216.

107. Chan, K.; Tsai, C.; Hansen, H. A.; Nørskov, J. K. *ChemCatChem* **2014**, *6*, 1899.

108. Li, R.; Wei, Z.; Gou, X.; Xu, W. *RSc Adv.* **2013**, *3*, 9978.

109. Gong, K.; Du, F.; Xia, Z.; Durstock, M.; Dai, L. *Science* **2009**, *323*, 760.

110. Yang, S.; Zhi, L.; Tang, K.; Feng, X.; Maier, J.; Müllen, K. *Adv. Funct. Mater.* **2012**, *22*, 3634.

111. Wu, J.; Liu, M.; Sharma, P. P.; Yadav, R. M.; Ma, L.; Yang, Y.; Zou, X.; Zhou, X. D.; Vajtai, R.; Yakobson, B. I.; Lou, J.; Ajayan, P. M. *Nano Lett.* **2016**, *16*, 466.

112. Wu, J.; Yadav, R. M.; Liu, M.; Sharma, P. P.; Tiwary, C. S.; Ma, L.; Zou, X.; Zhou, X.-D.; Yakobson, B. I.; Lou, J. *ACS Nano* **2015**, *9*, 5364.

113. Usseglio-Viretta, F.; Laurencin, J.; Delette, G.; Villanova, J.; Cloetens, P.; Leguillon, D. *J. Power Sources* **2014**, *256*, 394.

114. Zheng, Y.; Wang, J.; Yu, B.; Zhang, W.; Chen, J.; Qiao, J.; Zhang, J. *Chem. Soc. Rev.* **2017**, *46*, 1427.

115. Jensen, S. H.; Larsen, P. H.; Mogensen, M. *Int. J. Hydrogen Energ.* **2007**, *32*, 3253.

116. Ebbesen, S. D.; Mogensen, M. *J. Power Sources* **2009**, *193*, 349.

117. Pihlatie, M.; Kaiser, A.; Mogensen, M.; Chen, M. *Solid State Ionics* **2011**, *189*, 82.

118. Pihlatie, M.; Frandsen, H. L.; Kaiser, A.; Mogensen, M. *J. Power Sources* **2010**, *195*, 2677.

119. Wang, S.; Tsuruta, H.; Asanuma, M.; Ishihara, T. *Adv. Energ. Mater.* **2015**, *5*, 1401003.

120. Yue, X.; Irvine, J. T. *J. Electrochem. Soc.* **2012**, *159*, F442.

121. Murray, E. P.; Tsai, T.; Barnett, S. *Nature* **1999**, *400*, 649.

122. Ishihara, T.; Kannou, T. *Solid State Ionics* **2011**, *192*, 642.

123. Bidrawn, F.; Kim, G.; Corre, G.; Irvine, J.; Vohs, J. M.; Gorte, R. J. *Electrochem. Solid St.* **2008**, *11*, B167.

124. Yang, X.; Irvine, J. T. *J. Mater. Chem.* **2008**, *18*, 2349.

125. Chen, S.; Xie, K.; Dong, D.; Li, H.; Qin, Q.; Zhang, Y.; Wu, Y. *J. Power Sources* **2015**, *274*, 718.

126. Ge, X.; Zhang, L.; Fang, Y.; Zeng, J.; Chan, S. H. *RSC Adv.* **2011**, *1*, 715.

127. Li, S.; Li, Y.; Gan, Y.; Xie, K.; Meng, G. *J. Power Sources* **2012**, *218*, 244.

128. Marina, O. A.; Pederson, L. R.; Williams, M. C.; Coffey, G. W.; Meinhardt, K. D.; Nguyen, C. D.; Thomsen, E. C. *J. Electrochem. Soc.* **2007**, *154*, B452.

129. Liu, Q.; Yang, C.; Dong, X.; Chen, F. *Int J of Hydrogen Energ.* **2010**, *35*, 10039.

130. Liu, Q.; Dong, X.; Xiao, G.; Zhao, F.; Chen, F. *Adv. Mater.* **2010**, *22*, 5478.

131. Yang, L.; Xie, K.; Xu, S.; Wu, T.; Zhou, Q.; Xie, T.; Wu, Y. *Dalton T.* **2014**, *43*, 14147.

132. u , .; hao, H.; i , S.; ia , .; Gong, .; hang, .; Cheng, .; Li, .; Gu, L.; wierc e , K. *ACS Nano* **2016**, *10*, 8660.

133. Shao, Z.; Haile, S. M.; Ahn, J.; Ronney, P. D.; Zhan, Z.; Barnett, S. A. *Nature* **2005**, *435*, 795.

134. Kan, W. H.; Thangadurai, V. *Ionics* **2015**, *21*, 301.

135. Tsekouras, G.; Neagu, D.; Irvine, J. T. S. *Energy Environ. Sci.* **2013**, *6*, 256.

136. Druce, J.; Téllez, H.; Burriel, M.; Sharp, M. D.; Fawcett, L. J.; Cook, S. N.; McPhail, D. S.; Ishihara, T.; Brongersma, H. H.; Kilner, J. A. *Energy Environ. Sci.* **2014**, *7*, 3593.

137. Myung, J.-h.; Neagu, D.; Miller, D. N.; Irvine, J. T. *Nature* **2016**.

138. Zhou, J.; Shin, T.-H.; Ni, C.; Chen, G.; Wu, K.; Cheng, Y.; Irvine, J. T. *Chem. Mater.* **2016**, *28*, 2981.

139. Yang, C.; Li, J.; Lin, Y.; Liu, J.; Chen, F.; Liu, M. *Nano Energy* **2015**, *11*, 704.

140. Neagu, D.; Oh, T. S.; Miller, D. N.; Menard, H.; Bukhari, S. M.; Gamble, S. R.; Gorte, R. J.; Vohs, J. M.; Irvine, J. T. *Nat. Commun.* **2015**, *6*, 8120.

141. Zhang, Q.; Li, N.; Goebl, J.; Lu, Z.; Yin, Y. *J. Am. Chem. Soc.* **2011**, *133*, 18931.

142. Metraux, G. S.; Mirkin, C. A. *Adv. Mater.* **2005**, *17*, 412.

143. Duan, C.; Tong, J.; Shang, M.; Nikodemski, S.; Sanders, M.; Ricote, S.; Almansoori, A.; O'Hayre, R. *Science* **2015**, *349*, 1321.

144. Buitenwerf, R.; Rose, L.; Higgins, S. I. *Nat. Clim. Change* **2015**, *5*, 364.

145. Goeppert, A.; Czaun, M.; May, R. B.; Prakash, G. S.; Olah, G. A.; Narayanan, S. *J. Am. Chem. Soc.* **2011**, *133*, 20164.

146. Koh, J. H.; Jeon, H. S.; Jee, M. S.; Nursanto, E. B.; Lee, H.; Hwang, Y. J.; Min, B. K. *J. Phys. Chem. C* **2015**, *119*, 883.

147. Hatsukade, T.; Kuhl, K. P.; Cave, E. R.; Abram, D. N.; Jaramillo, T. F. *Phys. Chem. Chem. Phys.* **2014**, *16*, 13814.

148. Salehi-Khojin, A.; Jhong, H.-R.; Rosen, M. B. A.; Zhu, W.; Ma, S.; Kenis, P. J. A.; Masel, R. I. *J. Phys. Chem. C* **2013**, *117*, 1627.

149. Yoon, Y.; Hall, A.S.; Surendranath, Y. *Angew. Chem. Int. Edit.* **2016**, 128, 15508.

150. Lu, Q.; Rosen, J.; Zhou, Y.; Hutchings, G.S.; Kimmel, Y.C.; Chen, J.G.; Jiao, F. *Nat. Commun.* **2014**, *5,* 3242.

151. Liu, M.; Pang, Y.; Zhang, B.; De Luna, P.; Voznyy, O.; Xu, J.; Zheng, X.; Dinh, C.T.; Fan, F.; Cao, C.; de Arquer, F.P. *Nature* **2016**, *537*, 382.

152. Xia, Y.; Xiong, Y.; Lim, B.; Skrabalak, S. E. *Angew. Chem. Int. Edit.* **2009**, *48*, 60.

153. Zeng, J.; Xia, X.; Rycenga, M.; Henneghan, P.; Li, Q.; Xia, Y.; *Angew. Chem.Int. Edit.* **2011**, *50*, 244.

154. Kumar, B.; Asadi, M.; Pisasale, D.; Sinha-Ray, S.; Rosen, B. A.; Haasch, R.; Abiade, J.; Yarin, A. L.; Salehi-Khojin, A. *Nat. Commun.* **2013**, *4,* 3819.

155. Hsieh, Y.C.; Senanayake, S.D.; Zhang, Y.; Xu, W.; Polyansky, D.E. *ACS Catal.* **2015**, *5*, 5349.

156. Rosen, B. A.; Salehi-Khojin, A.; Thorson, M. R.; Zhu, W.; Whipple, D. T.; Kenis, P. J.; Masel, R. I. *Science* **2011**, *334*, 643.

157. J. Rosen, G. S. Hutchings, Q. Lu, S. Rivera, Y. Zhou, D. G. Vlachos and F. Jiao, *ACS Catal.* **2015**, *5*, 4293.

158. Kresse, G.; Hafner, J. *Phys. Rev. B* **1993**, *47*, 558.

159. Kresse, G.; Hafner, J. *Phys. Rev. B* **1994**, *49*, 14251.

160. Kresse, G.; Furthmüller, J. *Comput. Mater. Sci.* **1996**, *6*, 15.

161. Kresse, G.; Furthmüller, J. *Phys. Rev. B* **1996**, *54*, 11169.

162. Blöchl, P. E. *Phys. Rev. B* **1994**, *50*, 17953.

163. Kresse, G. *Phys. Rev. B* **1999**, *59*, 1758.

164. Hammer, B.; Hansen, L.; Nørskov, J. *Phys. Rev. B* **1999**, *59*, 7413.

165. Durand, W. J.; Peterson, A. A.; Studt, F.; Abild-Pedersen, F.; Nørskov, J. K. *Surf. Sci.* **2011**, *605*, 1354.

166. Cramer, C. J. *Essentials of Computational Chemistry Theories and Models*, John Wiley & Sons, England, **2013**.

167. Trip ovi ć, V.; S úlason, E.; Siahrostami, S.; Nørs ov, J. K.; Rossmeisl, J. *Electrochim. Acta* **2010**, *55*, 7975.

168. Faunce, T.; Styring, S.; Wasielewski, M. R.; Brudvig, G. W.; Rutherford, A. W.; Messinger, J.; Lee, A. F.; Hill, C. L.; Fontecave, M.; MacFarlane, D. R. *Energ. Environ. Sci.* **2013**, *6*, 1074.

169. Wang, Z.-L.; Li, C.; Yamauchi, Y. *Nano Today* **2016**, *11*, 373.

170. Costentin, C.; Robert, M.; Sav ant, J.-M. *Accounts Chem. Res.* **2015**, *48*, 2996.

171. Oh, S.; Gallagher, J. R.; Miller, J. T.; Surendranath, Y. *J. Am. Chem. Soc.* **2016**, *138*, 1820.

172. Weng, Z.; Jiang, J.; Wu, Y.; Wu, Z.; Guo, X.; Materna, K. L.; Liu, W.; Batista, V. S.; Brudvig, G. W.; Wang, H. *J. Am. Chem. Soc.* **2016**, *138*, 8076.

173. Ma, M.; Djanashvili, K.; Smith, W. A. *Angew. Chem. Int. Edit.* **2016**, *55*, 6680.

174. Feng, X.; Jiang, K.; Fan, S.; Kanan, M. W. *J. Am. Chem. Soc.* **2015**, *137*, 4606.

175. DiMeglio, J. L.; Rosenthal, J. *J. Am. Chem. Soc.* **2013**, *135*, 8798.

176. Sahu, A.; Qi, L.; Kang, M. S.; Deng, D.; Norris, D. J. *J. Am. Chem. Soc.* **2011**, *133*, 6509.

177. Wang, D.; Hao, C.; Zheng, W.; Peng, Q.; Wang, T.; Liao, Z.; Yu, D.; Li, Y. *Adv. Mater.* **2008**, *20*, 2628.

178. Terabe, K.; Hasegawa, T.; Nakayama, T.; Aono, M. *Nature* **2005**, *433*, 47.

179. Lee, U.; Ham, S.; Han, C.; Jeon, Y. J.; Myung, N.; Rajeshwar, K. *Mater. Chem. Phys.* **2010**, *121*, 549.

180. Rosen, B. A.; Haan, J. L.; Mukherjee, P.; Braunschweig, B.; Zhu, W.; Salehi-Khojin, A.; Dlott, D. D.; Masel, R. I. *J. Phys. Chem. C* **2012**, *116*, 15307.

181.Kresse, G.; Hafner, J. *Phys. Rev. B* **1993**, *47*, 558.

182.Kresse, G.; Hafner, J. *Phys. Rev. B* **1994**, *49*, 14251.

183.Kresse, G.; Furthmüller, J. *Phys. Rev. B* **1996**, *54*, 11169.

184.Kresse, G.; Furthmüller, J. *Comput. Mater. Sci.* **1996**, *6*, 15.

185.Blöchl, P. E. *Phys. Rev. B* **1994**, *50*, 17953.

186.Kresse, G. *Phys. Rev. B* **1999**, *59*, 1758.

187.Hammer, B.; Hansen, L.; Nørskov, J. *Phys. Rev. B* **1999**, *59*, 7413.

188.Ping, Y.; Galli, G.; Goddard, W. a. *J. Phys. Chem. C* **2015**, *119*, 11570.

189.Sandupatla, A. S.; Alexopoulos, K.; Reyniers, M.-F.; Marin, G. B. *J. Phys. Chem. C* **2015**, *119*, 18380.

190.Monkhorst, H. J.; Pack, J. D. *Phys. Rev. B* **1976**, *13*, 5188.

191.Yang, H. G.; Sun, C. H.; Qiao, S. Z.; Zou, J.; Liu, G.; Smith, S. C.; Cheng, H. M.; Lu, G. Q. *Nature* **2008**, *453*, 638.

192.Momma, K.; Izumi, F. *J. Appl. Crystallogr.* **2011**, *44*, 1272.

193.T. M. Letcher, *Climate change: observed impacts on planet Earth*, Elsevier, 2015.

194.J. T. S. Irvine, D. Neagu, M. C. Verbraeken, C. Chatzichristodoulou, C. Graves and M. B. Mogensen, *Nat. Energy*, **2016**, *1*, 15014.

195.D. Raciti, K. J. Livi and C. Wang, *Nano Lett.*, **2015**, *15*, 6829.

196.S. Wang and T. Ishihara, *ISIJ International*, **2015**, *55*, 381.

197.S. Wang, H. Tsuruta, M. Asanuma and T. Ishihara, *Adv. Energy Mater.*, **2015**, *5*.

198.P. Kim-Lohsoontorn and J. Bae, *J. Power Sources*, **2011**, *196*, 7161.

199.Z. Zhan and L. Zhao, *J. Power Sources*, **2010**, *195*, 7250.

200.W. Qi, Y. Gan, D. Yin, Z. Li, G. Wu, K. Xie and Y. Wu, *J. Mater. Chem. A*, **2014**, *2*, 6904.

201. A. Hauch, S. D. Ebbesen, S. H. Jensen and M. Mogensen, *J. Mater. Chem.*, **2008**, *18*, 2331.

202. W. Yao, T. Duan, Y. Li, L. Yang and K. Xie, *New J. Chem.*, **2015**, *39*, 2956.

203. H. Li, G. Sun, K. Xie, W. Qi, Q. Qin, H. Wei, S. Chen, Y. Wang, Y. Zhang and Y. Wu, *Int. J. Hydrogen Energy*, **2014**, *39*, 20888.

204. S. Xu, S. Li, W. Yao, D. Dong and K. Xie, *J. Power Sources*, **2013**, *230*, 115.

205. Y. Li, Y. Wang, W. Doherty, K. Xie and Y. Wu, *ACS Appl. Mater. Interfaces*, **2013**, *5*, 8553.

206. N. Danilovic, A. Vincent, J.-L. Luo, K. T. Chuang, R. Hui and A. R. Sanger, *Chem. Mater.*, **2009**, *22*, 957.

207. K. Chen, N. Ai and S. P. Jiang, *Int. J. Hydrogen Energy*, **2012**, *37*, 1301.

208. Y. Li, J. Zhou, D. Dong, Y. Wang, J. Jiang, H. Xiang and K. Xie, *Phys. Chem. Chem. Phys.*, **2012**, *14*, 15547.

209. T. Ishihara, K.-T. Wu and S. Wang, *ECS Transactions*, **2015**, *66*, 197.

210. M. Patrakeev, J. Bahteeva, E. Mitberg, I. Leonidov, V. Kozhevnikov and K. R. Poeppelmeier, *J. Solid State Chem.*, **2003**, *172*, 219.

211. G. Zhu, X. Fang, C. Xia and X. Liu, *Ceram. Int.*, **2005**, *31*, 115.

212. R. Chiba, F. Yoshimura and Y. Sakurai, *Solid State Ionics*, **2002**, *152*, 575.

213. R. Chiba, F. Yoshimura and Y. Sakurai, *Solid State Ionics*, **1999**, *124*, 281.

214. M. Kerstan, M. Müller and C. Rüssel, *Solid State Sci.*, **2014**, *38*, 119.

215. P. Liu, J. Kong, Q. Liu, X. Yang and S. Chen, *J. Solid State Electr.*, **2014**, *18*, 1513.

216. X. Yue and J. T. Irvine, *Solid State Ionics*, **2012**, *225*, 131.

217. V. Esposito, M. Søgaard and P. V. Hendriksen, *Solid State Ionics*, **2012**, *227*, 46.

218. K. Nomura, Y. Ujihira, T. Hayakawa and K. Takehira, *Appl. Catal. A-Gen.*,

1996, *137*, 25.

219. X. Tan, N. Liu, B. Meng, J. Sunarso, K. Zhang and S. Liu, *J. Membrane Sci.*, **2012**, *389*, 216.

220. A. Yan, B. Liu, Y. Dong, Z. Tian, D. Wang and M. Cheng, *Appl. Catal. B-Environ.*, **2008**, *80*, 24.

221. J. C. Hicks, J. H. Drese, D. J. Fauth, M. L. Gray, G. Qi and C. W. Jones, *J. Am. Chem. Soc.*, **2008**, *130*, 2902.

222. C. Wagner, *Prog. Solid State Ch.*, **1971**, *6*, 1.

223. N. Minh and M. C. Williams, *ECS Transactions*, **2015**, *68*, 3301.

224. T. H. Shin, J. H. Myung, M. Verbraeken, G. Kim and J. T. Irvine, *Faraday Discuss.*, **2015**, *182*, 227.

225. Y. Q. Zhang, J. H. Li, Y. F. Sun, B. Hua and J. L. Luo, *ACS Appl. Mater. Interfaces*, **2016**, *8*, 6457.

226. X. Yue and J. T. S. Irvine, *Electrochem. Solid St.*, **2012**, *15*, B31.

227. J. Zhang, K. Xie, H. Wei, Q. Qin, W. Qi, L. Yang, C. Ruan and Y. Wu, *Sci. Rep-UK*, **2014**, *4*, 7082.

228. S. Sengodan, S. Choi, A. Jun, T. H. Shin, Y. W. Ju, H. Y. Jeong, J. Shin, J. T. Irvine and G. Kim, *Nat. Mater.*, **2015**, *14*, 205.

229. S. Liu, K. T. Chuang and J.-L. Luo, *ACS Catal.*, **2015**, *6*, 760

230. J. A. Kilner, S. J. Skinner and H. H. Brongersma, *J. Solid State Electr.*, **2011**, *15*, 861.

231. Hester, R. E.; Harrison, R.M. *Carbon capture: sequestration and storage*, RSC Publishing **2010**, *1*.

232. Vasireddy, S.; Morreale, B.; Cugini, A.; Song, C. S.; Spivey, J. J. Energy Environ. Sci. **2011**, *4*, 311.

233. Xie, K.; Zhang, Y.; Meng, G.; Irvine, J. T. Energy Environ. Sci. **2011**, *4*, 2218.

234. Bierschenk, D. M.; Wilson, J. R.; Barnett, S. A. Energy Environ. Sci. **2011**, *4*, 944.

235. McIntosh, S.; Gorte, R.J. Chem. Rev. **2004**, *104*, 4845.

236. Tao, S.; Irvine, J.T. Nat. Mater. **2003**, *2*, 320.

237. Kitla, A.; Safonova, O. V.; Föttinger, K. Catal. Lett. **2013**, *143*, 517.

238. Gonzalez-delaCruz, V. M.; Pereniguez, R.; Ternero, F.; Holgado, J. P.; Caballero, A. J. Phys. Chem. C **2012**. *116*, 2919.

239. Tao, F. F. Chem. Soc. Rev. **2012**. *41*, 7977.

240. Lu, Z. G.; Zhu, J. H.; Bi, Z. H.; Lu, X. C. J. Power Sources **2008**, *180*, 172.

241. An, W.; Gatewood, D.; Dunlap, B.; Turner, C. H. J. Power Sources **2011**, *196*, 4724.

242. Yang, C.; Yang, Z.; Jin, C.; Xiao, G.; Chen, F.; Han, M. Adv. Mater. **2012**, *24*, 1439.

243. Fu, C. J.; Chan, S. H.; Ge, X. M.; Liu, Q. L.; Pasciak, G. Int. J. Hydrogen Energ. **2011**, *36*, 13727.

244. Min, J. -S.; Mizuno, N. Catal. Today **2001**. *66*, 47.

245. Neagu, D.; Tsekouras, G.; Miller, D. N.; Ménard, H.; Irvine, J. T. Nat. Chem. **2013**, *5*, 916.

246. Yang, L.; Liu, Z.; Wang, S.; Choi, Y.; Zuo, C.; Liu, M. J. Power Sources **2010**, *195*, 471.

247. Montini, T.; Bevilacqua, M.; Fonda, E.; Casula, M.; Lee, S.; Tavagnacco, C.; Gorte, R.; Fornasiero, P. Chem. Mater. **2009**, *21*, 1768.

248. Jiang, X. Z.; Stevenson, S. A.; Dumesic, J. J. Catal. **1985**, *91*, 11.

249. Munroe, P.; Hatherly, M. Scripta Metall. Mater. **1995**, *32*, 93.

250. Sun, Y. F.; Li, J. H.; Cui, L.; Cui, S. H.; Li, J.; Luo, J. L. Nanoscale **2015**, *7*, 11173.

251. Nishihata, Y.; Mizuki, J.; Akao, T.; Tanaka, H.; Uenishi, M.; Kimura, M.; Okamoto, T.; Hamada, N. Nature 2002, *418*, 164.

252. Yin, J. W.; Yin, Y. M.; Zhang, C.; Minh, N. Q.; Ma, Z. F. J. Phys. Chem. C 2014, *118*, 13357.

253. Jin, F.; Xu, H.; Long, W.; Shen, Y.; He, T. J. Power Sources **2013**, *243*, 10.

254. Devaux, R.; Vouagner, D.; De Becdelievre, A. M.; Duret-Thual, C. Corros. Sci., **1994**, *36*, 171.

255. Mansour, A. N. Surf. Sci. Spectra **1994**. *3*, 221.

256. Zhang, J.; Wang, H.; Dalai, A.K. J. Catal. **2007**. *249*, 300.

257. Takanabe, K.; Nagaoka, K.; Nariai, K.; Aika, K. I. J. Catal. **2005**. *232*, 268.

258. Nolan, M. J. Phys. Chem. C **2009**. *113*, 2425.

259. Wagner, C. Prog Solid State Ch. **1971**, *6*, 1.

260. Green, R. D.; Liu, C.-C; Adler, S. B. Solid State Ionics, **2008**, *179*, 647.

261. Xu, S.; Chen, S.; Li, M.; Xie, K.; Wang, Y.; Wu, Y. J. Power Sources **2013**. *239*, 332.

262. Blinn, K. S.; Abernathy, H.; Li, X.; Liu, M.; Bottomley, L. A.; Liu, M. Energy Environ. Sci. **2012**. *5*, 7913.

263. Ten Elshof, J.; Lankhorst, M.; Bouwmeester, H. J. Electrochem. Soc. **1997**, *144*, 1060.

264. Ten Elshof, J.; Bouwmeester, H.; Verweij, H. Solid State Ionics **1996**, *89*, 81.

265. J. T. Randerson, K. Lindsay, E. Munoz, W. Fu, J. K. Moore, F. M. Hoffman, N. M. Mahowald and S. C. Doney, *Global Biochem. Cy.*, **2015**, *29*, 744.

266. H. Dulli, P. A. Dowben, S. -H Liou and E. W. Plummer, *Phys. Rev. B*, **2000**, *62*,

R14629.

267. A. A. Mirzaei, A. B. Babaei, M. Galavy and A. Youssefi, *Fuel Process. Technol.*, **2010**, *91*, 335.

268. T. Horita, N. Sakai, T. Kawada, H. Yokokawa and M. Dokiya, *J. Electrochem. Soc.*, **1996**, *143*, 1161.

269. T. B. Massalski, J. L. Murray, L. H. Bennett and H. Baker, *American Society for Metals*, Metals Park, OH. **1986**.

270. A. Aguadero, D. Perez-Coll, J. A. Alonso, S. J. Skinner and J. Kilner, *Chem. Mater.*, **2012**, *24*, 2655.

271. C. D. Wagner and G. E. Muilenberg, *Handbook of X-ray photoelectron spectroscopy*, **1979**.

272. R. Devaux, D. Vouagner, C. Duret-Thual and A. M. de Becdelievre, *Corrosion Sci.*, **1994**, *36*, 171.

273. D. J. Joyner, O. Johnson and D. M. Hercules, *J. Am. Chem. Soc.*, **1980**, *102*, 1910.

274. Y. -F. Sun, Y. -Q. Zhang, B. Hua, Y. Behanamian, J. Li, S. -H. Cui, J. -H. Li and J. -L. Luo, *J. Power Sources*, **2016**, *301*, 237.

275. Y. Zhu, W. Zhou, R. Ran, Y. Chen, Z. Shao and M. Liu, *Nano Lett.*, **2016**, *16*, 512.

276. M. D. McIntyre, D. M. Neuburger and R. A.Walker, *ECST*, **2015**, *66*, 11.